



# **XXXV OSTIV CONGRESS**

19 - 23 July 2021



## **Congress Proceedings**

### **Die Deutsche Bibliothek – CIP Einheitsaufnahme**

Die Deutsche Nationalbibliothek verzeichnet diese Publikation in der Deutschen Nationalbibliografie; detaillierte bibliografische Daten sind im Internet unter <http://dnb.d-nb.de> abrufbar.

### **Rolf Radespiel, Till Lindner (Eds.)**

XXXV OSTIV Congress – Congress Program and Proceedings

© 2021

ISBN 978-3-947623-42-6

### **Copyright notice**

The copyright to all contributed articles collected in this volume resides with the authors. Any reproduction – in parts or as a whole, electronically or in print – of material from within this volume requires the written consent of the author(s).

### **Publisher of OSTIV Conference Proceedings:**

TU Braunschweig – Niedersächsisches Forschungszentrum für Luftfahrt

Hermann-Blenk-Straße 42 • 38108 Braunschweig

Tel: 0531-391-9821

Mail: [nfl@tu-braunschweig.de](mailto:nfl@tu-braunschweig.de)

Internet: [www.tu-braunschweig.de/nfl](http://www.tu-braunschweig.de/nfl)



Copyright Title Page Photo: Idaflieg e.V.

## **Abstract**

The XXXV Congress of the International Scientific and Technical Organisation for Gliding (OSTIV) were held as a virtual event from 19 July – 23 July, 2021, as the COVID-19 pandemic did not allow alignment of the Congress with a World Gliding Championship. OSTIV Congresses address all scientific and technical aspects of soaring flight. The Congress 2021 featured 36 presentations from 11 countries. These contributions describe new knowledge in the meteorological fields of atmospheric convection and atmospheric waves. The presentations on sailplane technologies comprise the areas of sailplane design and performance, aerodynamics, aeroelasticity, loads, and propulsion, whereas further contributions cover various aspects of training and safety. These Congress Proceedings lead the participants through the full-week program and make extended abstracts of the presentations accessible to the public.

# Foreword

Welcome to the virtual OSTIV Congress 2021. Every two years the Congress offers new information and latest research results in soaring and sailplane technology of scientists and engineers from all over the world. The meeting presents unique opportunities for scientific exchange and coordination of future activities.

This Congress of the year 2020 was planned to be hosted by the Deutsche Aero Club, along with the 36th FAI World Gliding Championships, in Stendal, Germany. Due to the COVID-19 pandemic the 36<sup>th</sup> FAI World Gliding Championships were postponed to the year 2021, but the Championships has had to be cancelled. OSTIV is particularly thankful to Stendal's WGC organizers, who did everything to overcome the difficulties due to COVID-19.

In the end, OSTIV decided to organize the Congress as a virtual meeting. Our Call for Abstracts generated response by engineers and scientists from 11 countries worldwide. The received extended abstracts were reviewed and are presented in this proceedings booklet. We believe that an excellent program has been generated this way. For their efforts in recruiting high-quality contributions we acknowledge the members of the Program Committee:

Zafer Aslan, Turkey	Götz Bramesfeld, Canada	Richard Carlson, USA
Michael Greiner, Germany	Mark Maughmer, USA	Judah Milgram, USA
Lukáš Popelka, Czech Republic	Rolf Radespiel, Germany	Gerard Robertson, New Zealand

Preparing the Congress took many hours of work by the Organizing Team, consisting of Jennifer Kupke, Rolf Radespiel, Ursula Schamp. We are very thankful for their efforts. Our thanks also go to Till Lindner of Technische Universität Braunschweig for booklet editing.

The OSTIV Congress is the perfect setting to bestow the OSTIV Prize 2021 and the OSTIV Best Student Paper Awards. We look forward to the Prize Ceremony and the Congress Closing Session for presenting the Award Winners.

We wish all Congress participants an exciting and rewarding week.

Prof. Rolf Radespiel

OSTIV President

Prof. Mark Maughmer

OSTIV Vice President

# Table of Abstracts (in order of appearance in Program)

## Monday, 19 July

<i>C. Kenschke</i> : Safety Issues in Lifetime Calculations of Sailplanes .....	1
<i>J. Schwochow</i> : Gust Response of Elastic Sailplanes.....	4
<i>L. M. M. Boermans, E. Lasauskas</i> : On the gust loads of sailplanes.....	8
<i>A. Ultsch</i> : Naïve transfer of ICAO’s Organizational Safety methods, such as SMS, into club-based flying might be either useless or even harmful .....	13
<i>D. Nadler</i> : Improving Motorglider Safety and Reliability.....	14
<i>K. Höck</i> : Investigation about Safety in Winch Launching.....	15
<i>W. Scholz, S. Leis, V. Petters, W. Würz, J. Axthelm, W. Fichter</i> : ASASys – Anti-Stall Assistant System for Sailplanes .....	19

## Tuesday, 20 July

<i>E. Braun</i> : DLR’s latest research sailplane: Discus-2c DLR .....	23
<i>F. Johnke, J. F. Santosa, M. Habermann</i> : fs36 Fly-by-Wire of the Akademische Fliegergruppe Stuttgart .....	27
<i>W. Scholz, J. Schneider, A. Strohmayer, S. Notter, W. Fichter</i> : icaré 2 wtp – Fly with light and control by thrust.....	31
<i>B. Neining</i> : Status report about AlpTherm_2 as a fully revised convection model .....	35
<i>O. Maas, D. Etling</i> : On the influence of moisture on the strength of thermals: A large-eddy simulation case study..	39
<i>A. O. Mut, F. B. Demir, H. Temur, Z. Aslan</i> : Examination of the Microburst Incident in Istanbul, July 2017.....	44

## Wednesday, 21 July

<i>S. Senger, R. Klein</i> : E-ROP electric and rotary engined hybrid plane.....	47
<i>Jan Pytka, A. Rypulak, Z. Czyż, R. Bąbel, K. Gierczak, Jar. Pytka, R. Kliza, K. Hryć</i> : Experimental Verification of the PROPWING Propulsion System – First Tests of a Model Motor Glider.....	49
<i>A. R. Ramesh, K. C. Mallette, H. Kim, B. Bissonnette, G. Bramesfeld</i> : CREATEV: An Exploration of a Solar-Powered, Ultra-Long Endurance UAV .....	53
<i>M. Greiner, W. Würz</i> : Laminar separation bubbles at unsteady inflow conditions – a status report .....	57
<i>F. El Tin</i> : Sink Polar Analysis for Unmanned Aerial Gliders using the USAF Datacom.....	62
<i>L. Metkowski, M. Maughmer</i> : A Design Study on the Application of Slotted, Natural-Laminar-Flow Airfoils on 18-Meter Sailplanes.....	63
<i>I. Weisheit</i> : Microbiological examination of aeroplane control elements .....	69
<i>T. Weigelt</i> : Experiences from Flight Testing in the Idaflieg .....	72

## Thursday, 22 July

<i>T. Lindner, C. Rolffs, N. Dierksen, R. Özküz, S. Scheffler, O. Dorn</i> : Proceedings in the Development of a Crashworthy Glider Cockpit .....	75
<i>L. Fohlmeister, T. J. Adam, B. Schwarz</i> : Optical deformation measurement of a two-seater cockpit under emergency landing conditions during a quasi-static load test .....	78
<i>M. Melville, G. Bramesfeld, J. Cole</i> : An Integrated Flight Dynamic Model for Flexible Aircraft .....	82
<i>B. Neining, A. de Orleans-Borbon</i> : A climatology of soaring conditions in Eurasia .....	87
<i>C. Lindemann</i> : Wave Flying Experiences - Examples of Observations and its Interpretation .....	91
<i>E. Hindman</i> : Ascend Mount Everest via paraglider?.....	93
<i>S. ÇİL, H. Q. Adeeb, R. A. Al-bayati</i> : Satellite Observation of a Deep Convective Storm Top at Kastamonu, Turkey - A Case Study. ....	97

*J.-M. Clément*: Discovering the Tropical Gravity Wave ..... 99

**Friday, 23 July**

*M. Greiner*: Two birds with one stone (and one trailer) ..... 102

*K. Rohde-Brandenburger*: Inflight Measurements of Control Surface Deflection in Circling Flight..... 106

F. Sturm, M. Hornung: Morphing Shell Design of a Sailplane with a Morphing Forward Wing Section ..... 109

*O. P. Neto, G. Pogorzelski, A. M. Neves*:

A numerical method for kinematic and structural optimization of sailplane mechanical flight control systems ..... 113

*J. Condé-Wolter, P. J. Steinbild, P. Kostka, T. Ehrig, A. Winkler, N. Modler, F. Sell*:

Load monitoring for sailplanes utilizing an innovative carbon fibre-based, spatially resolved strain sensor ..... 117



## Safety Issues in Lifetime Calculations of Sailplanes

Christoph Kensche

Stuttgart, christophkenske@aol.com

**Abstract:** Lifetime evaluations for modern sailplanes provide an indication that the possible life of the composite structure will exceed the common limitation of 12.000 flight hours by far. It is demonstrated that this is even the case by the introduction of a very conservative safety factor of life of 80 which results from the combination of an FFA-safety factor of 8 for metals and the conservative anticipation of a damage accumulation factor of 0.1 for composites. The calculations were performed for the tensile- and compression loaded carbon and glass reinforced spar caps of the bending spars in wings as well for the shear loaded glass webs.

**Keywords:** Lifetime, fatigue, s-n curve, composites, Palmgren-Miner rule, damage accumulation factor

### Introduction

The present lifetime allowable for composite sailplanes is in general 12.000 flight hours. Although nowadays many gliders have already reached this limit the high expenses for the experimental work may prevent additional testing. Those gliders must stay on the ground therefore.

However, in the meantime a big number of fatigue tests with spar beam structures using the KoSMOS-life load spectrum and also monotonic one-step tests have been conducted. Comparisons of the results with respect to the stiffness change on the one side and a combination of a lifetime assessment using the respective s-n curves and the linear Palmgren-Miner rule on the other side, have led to the conclusion that the lifetime could be widened up to 50.000 flight hours and more without any signs of fatigue like e.g. stiffness loss [1, 2].

By means of this background knowledge and stimulated by a publication from Soenne about fatigue evaluations for the PIK 20D [3], the author offers a rather practical and robust solution for a lifetime prolongation which is based on numerical calculations reported in [4].

### Lifetime evaluations and results

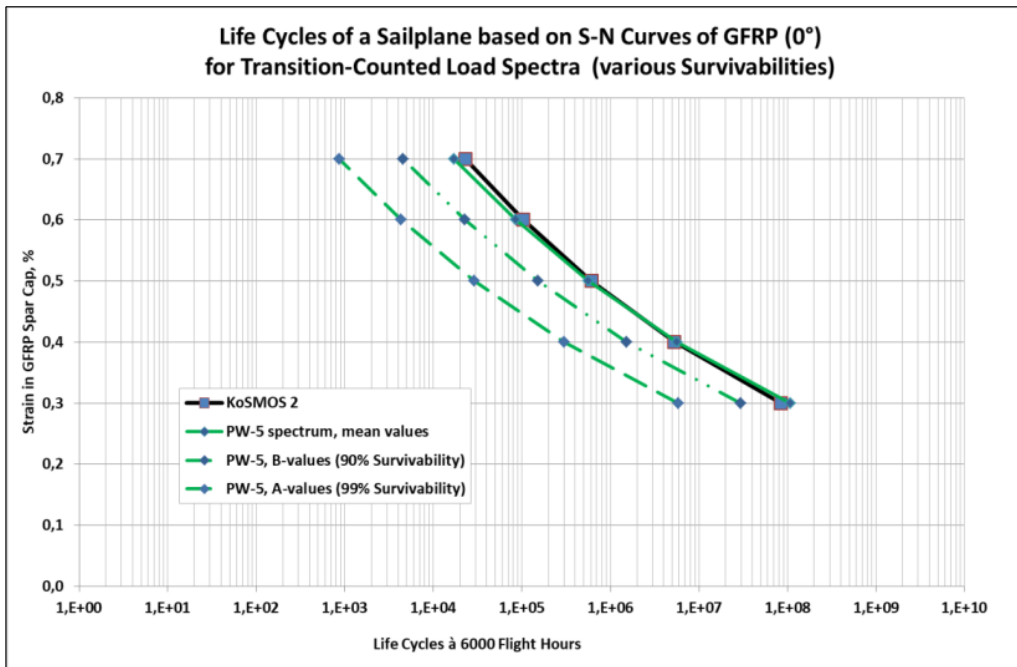
In that paper lifetime calculations were carried out for various service life spectra with similar and most conservative results for the well-known KoSMOS- as well the PW5-service spectra. The plots which show the influence of the design strains applied for different material combinations upon the lifetime demonstrate that there is a gap of some orders of magnitude between a theoretical lifetime and the 12.000 flight hours allowable even at highest strain levels. The calculations were carried out for the s-n curves of following materials commonly used in gliders:

- 0°-oriented GFRP for the life of glass fibre spar caps,
- 0°-oriented CFRP for the life of carbon fibre spar caps,
- ±45° GFRP for the life of the shear webs.

Since the calculations were based on the mean values of the material data, a safety philosophy has to be considered which gives highest confidence to the results and their interpretation.

In a first step, the safe-life-approach was investigated, i.e. a 99% survivability (A-values). In this case no structural fatigue failure must occur. This is in contrast to the fail-safe philosophy (90% survivability, B-values) where, according to the damage tolerance concept, e.g. BVD (barely visible damages) are allowed.

As an example, Figure 1 shows results of the computations for KoSMOS (mean values) and the PW5-spectrum applied on the mean, B- and A-values for 0°-oriented GFRP. It is obvious that for the highest design strain there is still a life cycle gap of about factor 100 between the A-values and the lifetime allowable.



In a second step the afore mentioned Soinne-proposal was introduced to investigate whether the idea behind

**Figure 1: Lifetime calculations for GFRP-spar cap material for 50%, 90% and 99% survivability**

would still show a sufficiently safe distance to the allowable. The proposal combines an FAA-method applying a safety factor of 8 for metals and a rather conservative approach for composites using a damage accumulation factor of  $D=0.1$ , lacking better data, however supporting the experience that also for composites  $D$  can vary between 0.1 and 10. In consequence, the resulting safety factor of life will be 80.

The following computation was performed with the KoSMOS-spectrum for 0°-GFRP material showing the curves of the mean and the A-values in comparison with the curve for the proposed safety factor of life of 80. Figure 2 shows also in this case for the highest design strain a gap of more than an order of magnitude between that curve and certified lifetime limit.

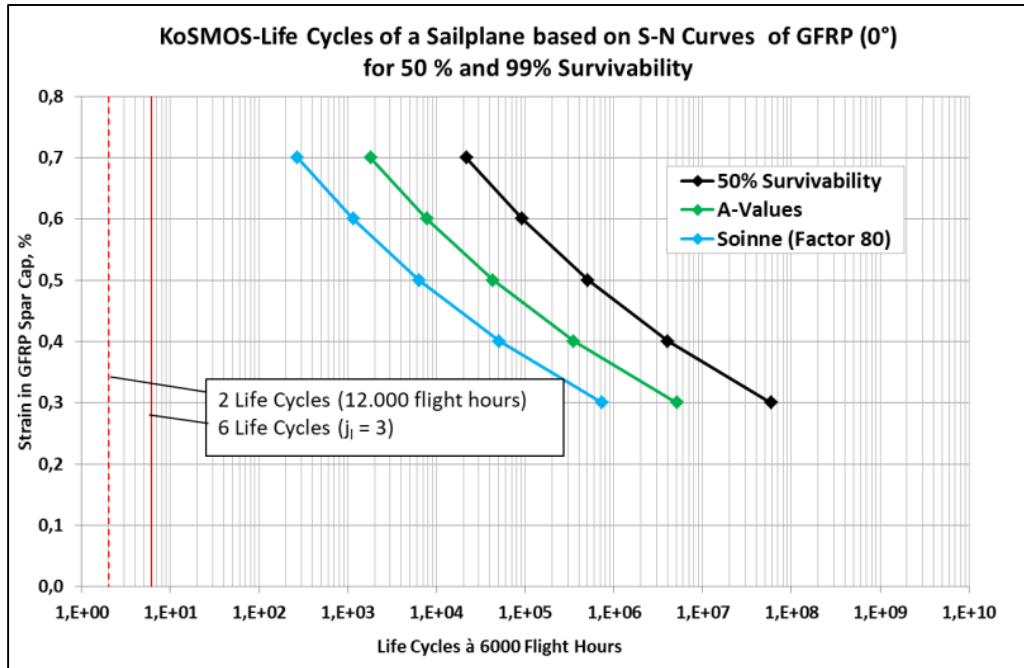


**Figure 2: Lifetime calculation for GFRP-spar cap material for 50%, 99% survivability compared with a curve for a lifetime factor of 80 (Soinne)**

Also the other investigated materials show a satisfying high gap to the certified 12.000 flight hours. It should be mentioned here that the data of the investigated materials have are more than 25 years old. It can be anticipated that the quality will have improved in the meantime. Nevertheless, the space between the certified lifetime of 12.000 flight hours and the theoretical safety factor-penalised lifetimes is still unbelievable high. So the calculations may serve as a well-documented basis for a discussion on an increase of a certified lifetime of up to 50.000 flight hours.

**References**

<sup>1</sup>Ch.W. Kensche, *Proposal for a certification procedure of extended sailplane lifetime*, Technical Soaring, Vol. 26, No. 4 (2002)  
<sup>2</sup>Ch.W. Kensche, A.v. Wingerde, D. Lekou, *Fatigue of Composite Scarf Joints in Wind Energy Rotor Blades and in Spar Beams for Light Aircraft*, Technical Soaring, Vol. 33, NO. 3 (2009)  
<sup>3</sup>Erkki Soinne, *PIK-20D Glider Fatigue Review*, Technical Soaring, Vol 43, No. 1 (2019)  
<sup>4</sup>Ch.W. Kensche, *Numerical Comparison of Glider Load Spectra*, Technical Soaring, Vol 43, No 4 (2019)

## Gust Response of Elastic Sailplanes

Jan Schwochow  
janschwochow@web.de

**Abstract:** For the design of a new sailplane, the load analysis plays a decisive role in dimensioning the lightweight structure and thus also in optimizing the operating weight. The loads comprise maneuver, gust, ground and further special loads. Since in general no structural dynamic model of the sailplane is available, it is difficult to incorporate the structural flexibility of the high aspect ratio wings, which might alleviate gust loads in most cases. In order to keep the compliance procedure simple for the sailplane designer, the assumptions of the relevant paragraph of the CS-22 are based on a rigid model which flies through a unitary gust with one-minus-cosine shape. The analysis of the gust load factor is related to the well-known Pratt-Walker formula, where the gust length is fixed at 25 mean wing chords. For light sailplanes with high aspect ratio wings and microlight glider this criteria might overestimate the gust loads. A new more adaptive simple formula for the gust alleviation factor is suggested by OSTIV Sailplane Development Panel to be introduced in the next amendment of the CS-22. In the following the validity is checked with a more rational gust analysis employing an aeroelastic model consisting of a Finite-Element beam model coupled to unsteady aerodynamic loads formulated in frequency domain.

**Keywords:** Aeroelasticity, discrete gust analysis, load factor, transient response.

### Introduction

The atmospheric gust is formed by random fluctuations in the wind speed and direction caused by a swirling motion of the air. Gust-induced loads can significantly impact the structural integrity. The term dynamic loads is used to represent gust loads that include the inertia forces associated with elastic-mode (free vibration) accelerations. Events with steep gradients of air speed in horizontal or vertical directions are called discrete gusts, which may occur at the edges of thermals and downdrafts, wave streams or at temperature inversions. When an airplane penetrates any of these gradients rapidly, an impulsive change of aerodynamic loads and attitude is generated. The current certification regulations utilize theoretical work undertaken by the NACA where the concept of one-minus-cosine gust was reported by Pratt-Walker in 1954 [1], which was discussed for sailplane configurations in [2]. The simplification of the gust shape is shown in **Figure 1**. An assumption from measurements on large transport aircrafts estimates a representative fixed gust length  $H$  to 25 times the mean wing chord.

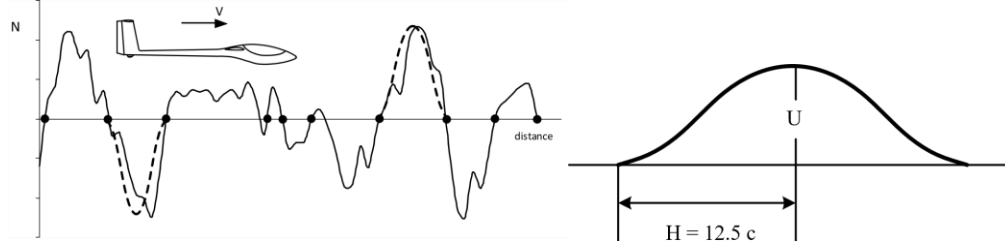


**Figure 1. One-minus-cosine gust**

The certification specifications for sailplanes and powered sailplanes EASA CS-22 [1] implies this discrete gust profile to estimate the loads caused by atmospheric turbulence. The application of the Pratt-Walker formula determines the maximum gust load factors according to flight speed and the gust alleviation factor, which is related to the mass ratio and lift slope. This factor takes into account the lag of the motion-induced aerodynamic forces on the aircraft by evaluating the Wagner function. The contents of the gust load factors paragraph §22.341 reads:

- (a) In the absence of a more rational analysis, the gust load factors  $n$  must be computed as follows:

$$n = 1 \pm \left( \frac{k}{2} \rho_0 U V a \right) / \left( \frac{mg}{S} \right) \quad (1)$$

where:

$\rho_0 =$	density of air at sea-level (kg/m <sup>3</sup> )	$U =$	gust velocity (m/s)
$V =$	equivalent air speed (m/s)	$a =$	slope of wing lift curve per radian
$m =$	mass of the sailplane (kg)	$g =$	acceleration due to gravity (m/s <sup>2</sup> )
$S =$	design wing area (m <sup>2</sup> )		

$$k = 0.88\mu / (5.3 + \mu) \quad \text{gust alleviation factor calculated from the following formula:}$$

$$\mu = \left(2 \frac{m}{S}\right) / \rho_\infty l_m a \quad \text{is the non-dimensional sailplane mass ratio, with } \rho_\infty \text{ is the density of air (kg/m}^3\text{) at}$$

the altitude considered and  $l_m$  is the mean geometric chord of the wing (m)

(b) The value of  $n$  calculated from the expression given above need not exceed:  $n = 1.25(V/V_{s1})^3$

The validity of this underlying assumption for light-weight gliders is being discussed currently in the OSTIV Sailplane Development Panel. A new formula was derived for the gust alleviation factor  $k$  by Boermans and Lasauskas [3], which conservatively reproduces the gust loads from the simulations as a function of the gust length  $H$ :

$$k = \frac{0.96\mu / (H/l_m)}{0.475 + \mu / (H/l_m)} \quad \text{with} \quad \frac{H}{l_m} = 12.17 + 0.191\mu \quad (2)$$

The new formula contains the relation between the occurring gust length  $H$  and the mean wing chord  $l_m$  as input. So far no comprehensive statement about an appropriate gust length covering all relevant meteorological conditions could be found. As a go around the equation on the right is suggested to be introduced in the new CS-22 amendment to provide the same value for the alleviation factor as the 25 times mean wing chord gust length. The validity of the current specification really rests on accumulated experience. Sailplanes with structures designed to the specified load factors have been found to be strong enough in the past, and may therefore be expected to be satisfactory in the future as well. In order to check the validity of the new formula the transient gust response time simulation of a flexible generic open-class sailplane is presented, which follows the methodology in [5] as a more rational analysis.

### Methodology

The Finite-Element model of the complete aircraft structure is set up in global coordinates and represents the structural dynamics of the airframe. Typically, up to several thousand grid points will be used, with three displacement and three rotation coordinates at each. The type of elements used in the finite element analysis (FEA) will depend upon the type of structure. Due to highly slender wings and empennage of the sailplane Euler-Bernoulli beam elements are appropriate to represent the vibration characteristics of the airframe (see **Figure 2**). The global stiffness  $\mathbf{K}$  and mass matrix  $\mathbf{M}$  are calculated from span-wise bending and torsional properties. Instead of using the full problem, solving the dynamic response problem employs a reduced set of normal vibration modes and natural frequencies, which result from solving the eigenvalue problem:

$$[\mathbf{K} - \omega_i^2 \mathbf{M}] \phi_i = \mathbf{0} \quad (3)$$

where  $\omega_i$  is the natural frequency. The columns in the modal matrix  $\Phi_r$  contain the normal modes  $\phi_i$ ,  $i = 1, \dots, r$ , which are  $\mathbf{M}$ -orthonormal, such that  $\hat{\mathbf{M}} = \Phi_r^T \mathbf{M} \Phi_r = \mathbf{I}_r$ . The modal stiffness matrix is  $\hat{\mathbf{K}} = \Phi_r^T \mathbf{K} \Phi_r = \text{diag}(\omega_i^2)$ . Note, that natural frequencies and normal modes can be experimentally determined in the ground vibration test GVT. The following description of the modal transient response analysis reduces the system by a small set of low-frequency normal modes up to the wing torsional mode shape.

The unsteady aerodynamic force matrices are calculated from the whole-aircraft normal mode displacements, using the Doublet Lattice Method DLM [6], which is essentially the conversion to an aerodynamic finite element method. Each element is a portion of the wing surface (quadrilateral box) in which two of its sides are aligned with the incoming flow. The pressure difference  $\Delta C_p$  and the normal downwash  $w(x, y)$  are assumed constant at each box and their value is assigned to the respective control point. Such relation is written in terms of the aerodynamic influence coefficient matrix  $\mathbf{AIC}$ , with as many rows and columns as the number of boxes in the wing surfaces:

$$\frac{\mathbf{w}(kr)}{V_\infty} = \mathbf{AIC}(kr)^{-1} \Delta \mathbf{C}_p(kr) \quad \text{with} \quad kr = \frac{\omega l_m}{2V_\infty} \quad (4)$$

Due to the oscillating downwash, the aerodynamic influence coefficient matrix is a complex nonlinear function of the reduced frequency  $kr$ , where  $\omega$  is the oscillation frequency and  $l_m$  is the reference mean chord. The corner points of the quadrilateral boxes will be different from those used for the structural model, and spline fits are extensively used to interpolate from one to the other (see **Figure 2**). The modal aerodynamic load matrix resulting from mode shape oscillation is written as

$$\mathbf{A}(kr) = \Phi_r^T \mathbf{T}^T \mathbf{S} \mathbf{AIC}(kr) \mathbf{T} \Phi_r, \quad (5)$$

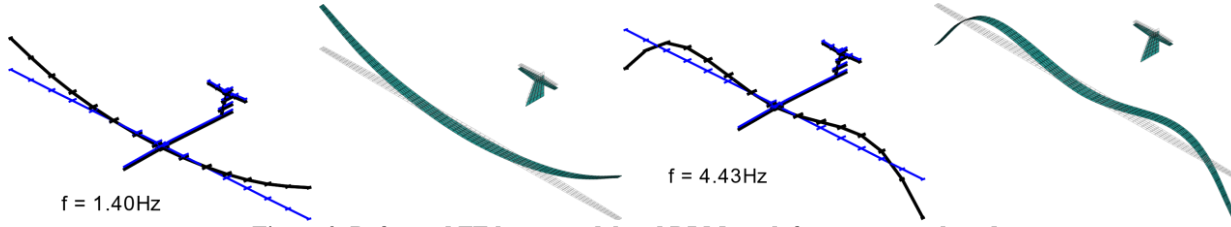


Figure 2. Deformed FE beam model and DLM mesh for two natural modes

where  $\mathbf{T}$  is the load and displacement transfer interpolation matrix and  $\mathbf{S}$  is the integration matrix to convert pressure in forces. For spanwise uniform gust excitation, the vertical gust velocity acting on a certain aerodynamic box can be obtained by the time delay of the gust velocity at a specific gust reference point  $x_0$ , which is expressed as

$$u_{gj} = |u_g| e^{-i\omega((x_j-x_0)/V_\infty)} = |u_g| e^{-ikr((x_j-x_0)/l_m)}, \quad (6)$$

in which,  $u_{g0}$  and  $u_{gj}$  respectively represent the gust velocity at the reference point and the control point of the  $j$ -th aerodynamic box. The resulting complex gust mode vector contains the time delay for all the aerodynamic boxes. The aerodynamic pressures induced by the gust downwashes are obtained by multiplication with the  $AIC$  matrix. Again, the aerodynamic pressures can be converted to the structural equivalent forces via spline interpolation:

$$\mathbf{f}_g = q_\infty \mathbf{T}^T \mathbf{S} \mathbf{AIC}^{-1}(k) \mathbf{\Phi}_g(kr) \frac{u_g}{V_\infty} = q_\infty \mathbf{A}_g(kr) \frac{u_g}{V_\infty} \quad \text{with} \quad q_\infty = 1/2 \rho_\infty V_\infty^2. \quad (7)$$

To obtain the time-domain model of the aeroelastic system, the transient response is obtained by exploiting the fact, that a convolution in the time domain corresponds to a multiplication in the frequency domain. Both aerodynamic force matrices are functions of the reduced frequency, which means that the aeroelastic equations in frequency-domain establish a transfer function of the structural response due to the gust input in frequency-domain.

$$\hat{\mathbf{M}} \dot{\mathbf{q}}(t) + (\hat{\mathbf{K}} - q_\infty \tilde{\mathbf{A}}(t)) \mathbf{q}(t) = \frac{q_\infty}{V_\infty} \tilde{\mathbf{A}}_g(t) u_g(t) \Rightarrow [-\omega^2 \hat{\mathbf{M}} + \hat{\mathbf{K}} - q_\infty \mathbf{A}(kr)] \mathbf{Q}(\omega) = q_\infty \mathbf{A}_g(kr) \frac{U_g(\omega)}{V_\infty} \quad (8)$$

The aeroelastic transfer function reads

$$\mathbf{H}_g(\omega) = 1/2 \rho_\infty V_\infty [-\omega^2 \hat{\mathbf{M}} + \hat{\mathbf{K}} - q_\infty \mathbf{A}(kr)]^{-1} \mathbf{A}_g(kr). \quad (9)$$

The resulting response  $\mathbf{q}(t)$  in time domain can be calculated by Fourier- and inverse Fourier-transformation:

1. Evaluate the Fourier transform of  $w_g(t)$ :  $U_g(\omega) = FFT(u_g(t)) = \int_{-\infty}^{\infty} u_g(t) e^{-i\omega t} dt$  (10)

2. Generate the frequency response by multiplication:  $\mathbf{Q}(\omega) = \mathbf{H}_g(\omega) U_g(\omega)$  (11)

3. Calculate the inverse Fourier transform:  $\mathbf{q}(t) = FFT^{-1}(\mathbf{Q}(\omega)) = \frac{1}{2\pi} \int_{-\infty}^{\infty} \mathbf{Q}(\omega) e^{i\omega t} d\omega$  (12)

4. The overall vertical acceleration in terms of the incremental load factor results from

$$\Delta n(t) = -\frac{1}{mg} \sum_i \mathbf{n}_{z,i} \times \mathbf{f}_i(t), \quad \mathbf{f}(t) = \mathbf{K} \mathbf{\Phi} \mathbf{q}(t) \quad (13)$$

where gust loads in physical coordinates are calculated from the modal response  $\mathbf{q}(t)$ , the matrix of normal modes  $\mathbf{\Phi}$  and the global stiffness matrix  $\mathbf{K}$ . The vector  $\mathbf{n}_z$  contains the vertical direction vector at each grid point.

## Results

The transient incremental gust load factor  $\Delta n$  from Eq. 13 represents the sum of the total loads with contribution of aerodynamic, inertial and flexible forces. It is assumed that the sailplane is in trimmed equilibrium at 1g-level before and after the discrete gust encounter. Depending on the gust length and the flight speed the gust gradient will vary and the additional gust energy introduced into the structure will result in the deformation. The task is to find the gust length which produces the maximum and minimum incremental loads, which is called “the tuned-gust”.

The structural dynamic beam model of a representative open class glider with 25m span is used as an example for the modal transient gust response analysis, which has a total mass of  $m=650\text{kg}$ , a wing area of  $S=16.3\text{m}^2$  and a mean chord of  $l_m=0.83\text{m}$  (see Figure 2). According to CS-22 the maximum positive and negative gust velocity is  $U_g=15\text{m/s}$  at the assumed design gust speed  $V_B=50\text{m/s}$ . To find worst-case gust, the length is varied between 1-200 mean chords. In the upper part of Figure 3 the gust upwind is plotted over time, while in the lower part the transient response of the load

factor  $\Delta n(t)$  at the center of gravity is depicted. The resulting incremental gust load factor  $\Delta n$  in Eq. 15 can be directly compared to the right term in Eq. 1 of the simplified CS-22 estimation based on the Pratt-Walker formula and the new expanded formula with variable gust length in Eq. 2. In

**Figure 4** the envelope of the maximum and minimum load factors are plotted. While the Pratt-Walker formula assumes constant gust length, which results in constant load factor of  $\Delta n = 4.42$  according to Eq.1, the new proposal for §22.341 provides larger values at very short gusts, but converges against zero with longer gust length. The envelope of the transient responses is plotted for two cases: 1) the rigid sailplane with very high stiffness, 2) the flexible sailplane with reasonable stiffness based on GVT-data tuning. As a final conclusion the new gust load factor proposal for §22.341 according to Eq.2 covers the structural dynamics of the flexible sailplane configuration for full range of gust length variation.

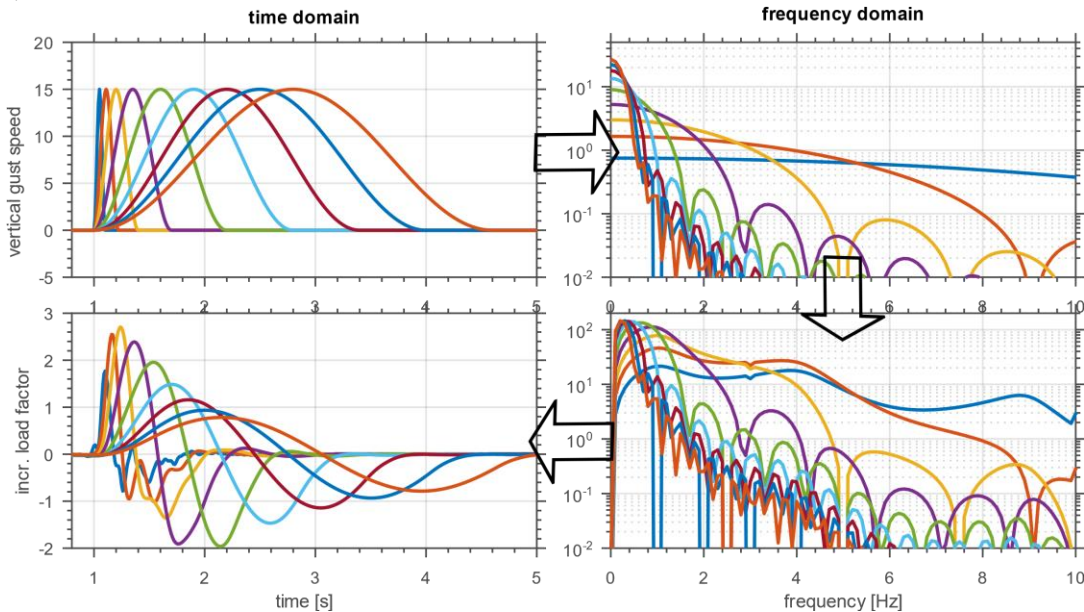


**Figure 3. Gust input and load factor response in time and frequency domain**

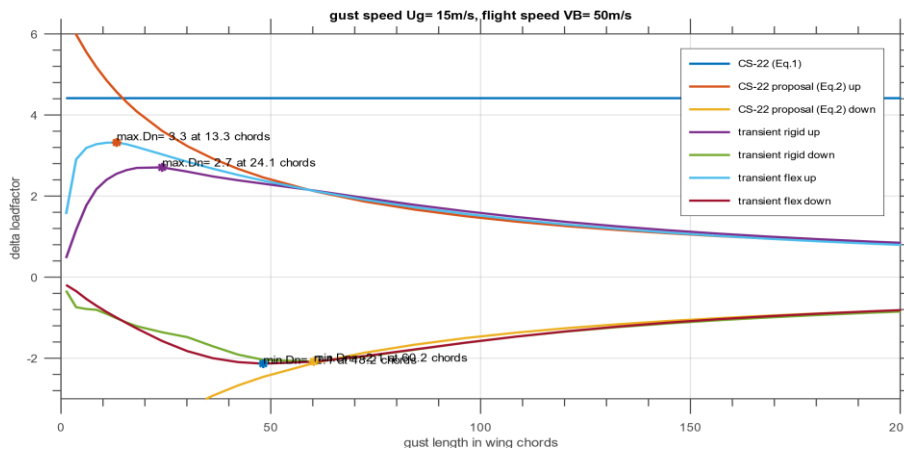


**Figure 4. Comparison of loadfactor envelopes for varying gust length**

**References**

- [1] K. Pratt, W. Walker, A revised gust-load formula and a reevaluation of v-g data taken on civil transport airplanes from 1933 to 1950, NACA Report No.1206, 1954.
- [2] de Jonge, J.B., Gust alleviation factors for sailplanes, 10th OSTIV Congress, South Cemey (England), 1965.
- [3] EASA, Certification Specifications for Sailplanes, CS-22, EASA, 2009.
- [4] Boermans, L.M.M., Lasauskas, E., On the gust loads of sailplanes, OSTIV Congress 2019 Abstracts – 2019.
- [5] Vink, W.J., de Jonge, J.B., A MATLAB program to study gust loading on a simple aircraft model, National Aerospace Laboratory NLR, 1997-07-29, NLR Technical Publication TP 97379 U, 1997.

- [6] Albano, E., Rodden, W. P., A Doublet-Lattice Method for calculating Lift Distributions on oscillating Surfaces in Subsonic Flows, AIAA journal, Vol. 7, No. 2, 1969.

## On the gust loads of sailplanes

L.M.M. Boermans

*TU Delft, Faculty of Aerospace Engineering, The Netherlands, l.m.m.boermans@tudelft.nl*

E. Lasauskas

*Vilnius Gediminas Technical University, Lithuania, Eduardas.lasauskas@vgtu.lt*

**Abstract:** The gust load determination in Certification Specifications for Sailplanes and Powered Sailplanes CS-22 and OSTIV Airworthiness Standards for Sailplanes and Powered Sailplanes OSTIVAS are based on theoretical and experimental investigations performed by NACA in 1951 – 1959. The present paper clarifies that both in the theoretical work and in the data reduction of these gust tests, assumptions are applied that are not valid for sailplanes. An update of the method leads to an improved expression of the alleviation factor and, in combination with an expression for the gust length, leads to the determination of gust loads for new sailplanes that have the same level of safety in gusts as modern sailplanes.

**Keywords:** sailplane design, gust loads, OSTIVAS, CS-22

### Introduction

The determination of gust loads in OSTIVAS and CS-22 is based on Pratt's method and the (1-cos) shaped gust reported in NACA Report 997 (Ref. 1) and NACA Report 1206 (Ref.2), and the maximum gust velocity of 15m/s is reported in NASA TN D-29 (Ref. 3). These reports deal with gust loads on large airplanes and do not cover the parameter range of sailplanes i.e. relatively low wing loadings and small chord lengths. Since the length of the standard design gust profile is defined as 12.5 times the mean chord of the wing, this leads for sailplanes with mean chords between 0.5m and 1m to very short and steep gust profiles with a ratio of the maximum gust velocity and its gradient distance between 1.5 and 3m/s per meter - not measured by NACA as shown in Figure 1 - and consequently to high gust loads at flight speed  $V_B$ . The factor 12.5 reflects that the gradient distance felt by the airplane in its plunge motion depends on how rapidly the airplane weathervanes in pitch. The greater and heavier the plane – roughly represented by the mean chord - the slower the airplane response. For sailplanes the mean chord is not representative for their size and weight. For instance the Baby 11B, MTOM 250kg, span 13.6m has a mean chord of 1.04m and the EB29R, MTOM 850kg, span 28m has a mean chord of 0.58m. Consequently the expression for the standard design gust profile defined as 12.5 times the mean chord of the wing, is not valid for sailplanes.

### Generalized alleviation factor of Pratt

The maximum ratio of gust velocity and its gust gradient distance measured by NACA in Report 997 was 0.81m/s per meter, see Figure 1. This leads for a (1-cos) shaped gust to a maximum gust velocity of 15m/s when the gust gradient length is 23m. A literature study to find a new design gust for airworthiness purpose led to Ref.4 where results are presented of a gust measurement campaign in Russia similar to NACA 997 but performed with sailplanes. The maximum ratio of gust velocity and its gradient was measured as 1.25m/s per meter. This leads to a (1-cos) shaped gust to a maximum gust velocity of 15m/s with a gust gradient length of 15m. In order to calculate the gust load factor for a distinct gust length instead of a gust length of 12.5 times the mean chord of the wing, Pratt's formula for the gust alleviation factor had to be transformed into a generalized expression which is valid for any rigid sailplane flying with constant velocity and pitch angle through a (1-cos) shaped gust of any length to a maximum gust velocity of 15m/s.

In general, the gust alleviation factor depends on airplane properties and atmospheric properties in the dimensionless combination  $\frac{\mu g}{H/\bar{c}}$  (Ref. 7).

By inserting  $\frac{H}{\bar{c}}$  into Pratt's formula and changing the constant 5.3, which is valid for  $\frac{H}{\bar{c}} = 12.5$  only, in  $\frac{5.3}{12.5} = 0.424$

this results in the general expression for the gust alleviation factor: 
$$K_g = \frac{0.88 \cdot \mu_g / (H/\bar{c})}{0.424 + \mu_g / (H/\bar{c})}$$

This expression has been verified successfully by solving the same equation of motion as Pratt, given in Ref. 2 with transient lift functions of Jones and (1-cos) gust shape, using MatLab / Simulink. With this generalized expression for the alleviation factor and the previously mentioned gust lengths of 23m and 15m, loads factors were calculated for 33 sailplanes and compared with the current load factors calculated with  $H=12.5 \cdot \bar{c}$ , see Figure 2 and 3. With current Pratt's method the 33 sailplanes considered have a gust load factor between 5 and 6, and for 2/3 of the sailplanes the gust load factor is higher than the maneuver load factor of 5.3. With the highest gust gradient measured by NACA and corresponding gust gradient length of 23m the gust load factor is about 4 which is nearly identical to the maximum gust load factor specified in the ASTM Standards F2564-14 "Standard Specification for Design and Performance of a Light Sport Glider". It is not known to the authors if this is a coincidence or not.

However, the Russian gust load measurements indicate that sailplanes may encounter steeper gusts. For their steepest gust with gradient distance of  $H = 15m$ , Figure 3 shows that the load factor is between 4 and 5, about 15% lower than those calculated with the method of OSTIVAS and CS-22, and always below the prescribed maneuver load factor of 5.3.

### Generalized alleviation factor of ASWING

In the second part of the paper, the modern integrated aerodynamic/structural/control simulation tool ASWING (Ref. 5), and the tuned discrete gust dynamic load analysis (Ref. 6) has been used to update Pratt's approach. Confidence in ASWING results was obtained from a comparison of gust load results calculated with ASWING and NASTRAN; they were practically identical. With ASWING a rigid sailplane flying with constant velocity and pitch angle through a gust (Pratt's approach) can be calculated, but also a flexible sailplane flying with free velocity and pitch angle, and fixed elevator through a gust. The tuned discrete gust system is a series of discrete (1-cos) shaped gusts with maximum gust velocity 15m/s and varying gust lengths (5m, 10m, 15m ...30m) which is investigated in order to tune the gust to give the maximum response. From the calculated gust loads of 3 typical rigid sailplanes (light and small span, medium weight and 18m span, and heavy and long span), flying through gust gradient lengths from 5m to 30m, the generalized alleviation factor was derived, which is valid for any sailplane in any (1-cos) shaped gust length to a maximum gust velocity of 15m/s. This generalized alleviation factor is somewhat higher - i.e. the alleviation is somewhat less - than Pratt's generalized alleviation factor, Figure 4. Then effects of free velocity and pitch, of a flexible wing, of a forward and rearward c.g position, of a straight quarter chord line or a straight trailing edge, are studied in order to verify if these effects are covered by Pratt's assumption of a rigid wing flying with constant velocity and pitch angle through the new design gust. This turned out to be the case.

### Conclusion

Since the previously mentioned design gust has not been demonstrated to cover the most severe turbulent conditions to be expected in operation of sailplanes, discussions in the OSTIV Sailplane Development Panel led to the idea to use the existing sailplanes, which are generally considered to be safe in gusts, as a calibration tool for the proper value of the gust length. This concept is identical to that underlying the comparative tuned discrete-gust analysis (Ref. 6, p. 78). In other words, to choose a gust length for a new sailplane design that provides the same level of safety in gusts as present sailplanes. By equalizing the ASWING generalized alleviation factor and Pratt's original alleviation factor this gust length can be determined.

In conclusion, in the absence of a more rational analysis, the simple expression of the updated generalized gust alleviation factor K

$$K = \frac{0.96 \cdot \frac{H}{\bar{c}}}{0.475 + \frac{H}{\bar{c}}}$$

in combination with the expression for the length H of the (1-cos) shaped gust length to a maximum gust velocity of 15m/s

$$\frac{H}{\bar{c}} = 12.172 + 0.191 * \mu$$

are proposed for the calculation of the gust load at  $V_B$  for airworthiness requirements purpose that provides the same level of safety in gusts as present sailplanes.

**References**

1. P. Donely; Summary of information relating to gust loads on airplanes. NACA Report 997, 1951.
2. K.G. Pratt, W.G. Walker; A revised gust-load formula and re-evaluation of the V-G data taken on civil transport airplanes from 1933 to 1950. NACA Report 1206, 1954.
3. W.G. Walker and M.R. Copp; Summary of VGH and V-G Data obtained from Piston-Engine Transport Airplanes from 1933 to 1950. NASA TN D-29, 1959.
4. V.V. Chernov; Results of research in the field of structural strength limits for sporting gliders. OSTIV Publication VIII, 1965.
5. M. Drela; Integrated Simulation Model for Preliminary Aerodynamic, Structural, and Control-Law Design of Aircraft. AIAA 99-1394, 1999.
6. F.M. Hobblit; Gust Loads on Aircraft: Concepts and Applications. AIAA Education Series. ISBN 0-930403-45-2, 1988.
7. J.B. de Jonge; A spectral gust alleviation factor for sailplanes. NLR MP 70002U, 1970.

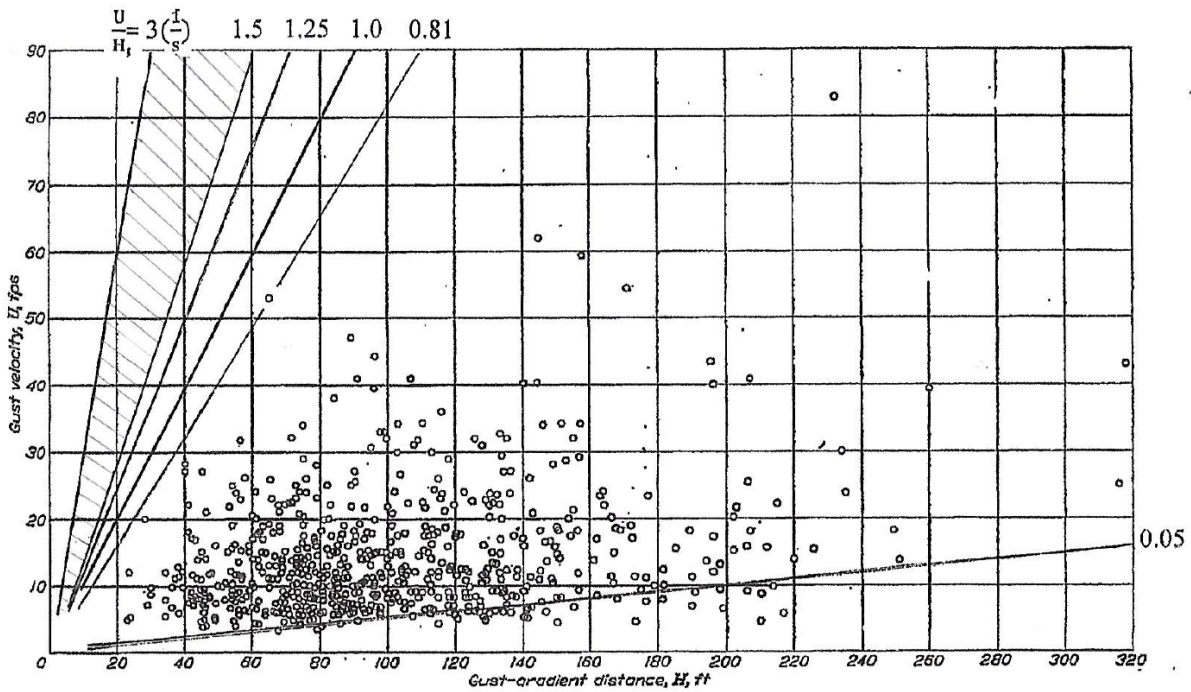


Fig. 1 Gust velocity  $U$  as a function of gust gradient distance  $H_i$  (Ref.1).

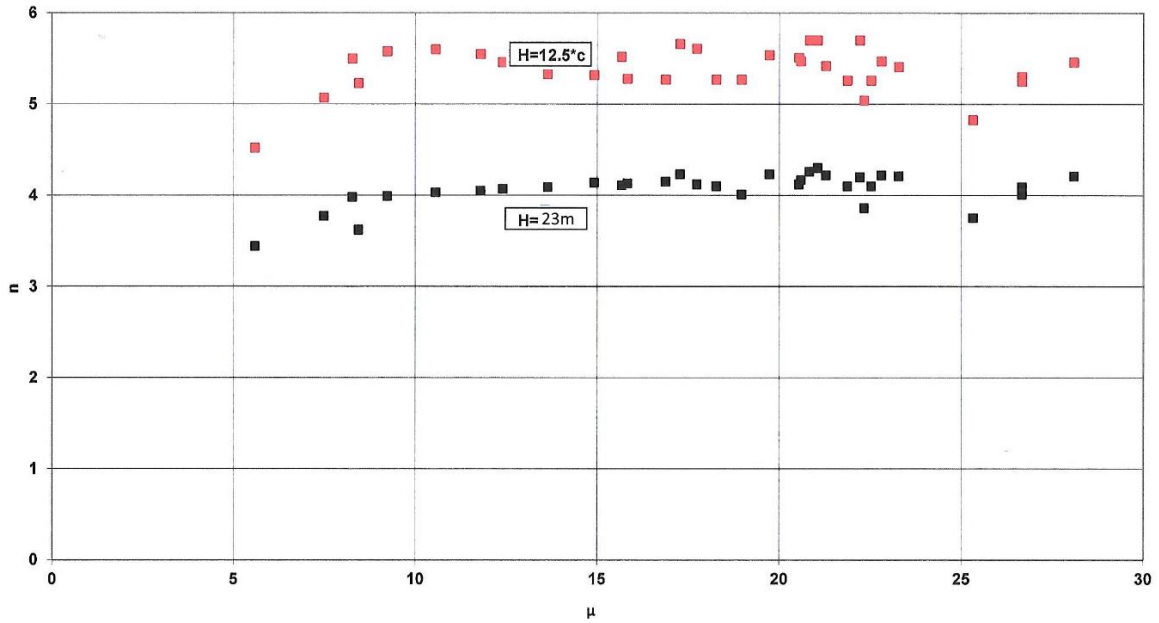


Fig. 2 Gust load factor as a function of the mass ratio parameter for 33 sailplanes in a (1-cos) shaped gust with gradient distance of  $12.5 \cdot \bar{c}$  meter (Pratt) and 23 meter.

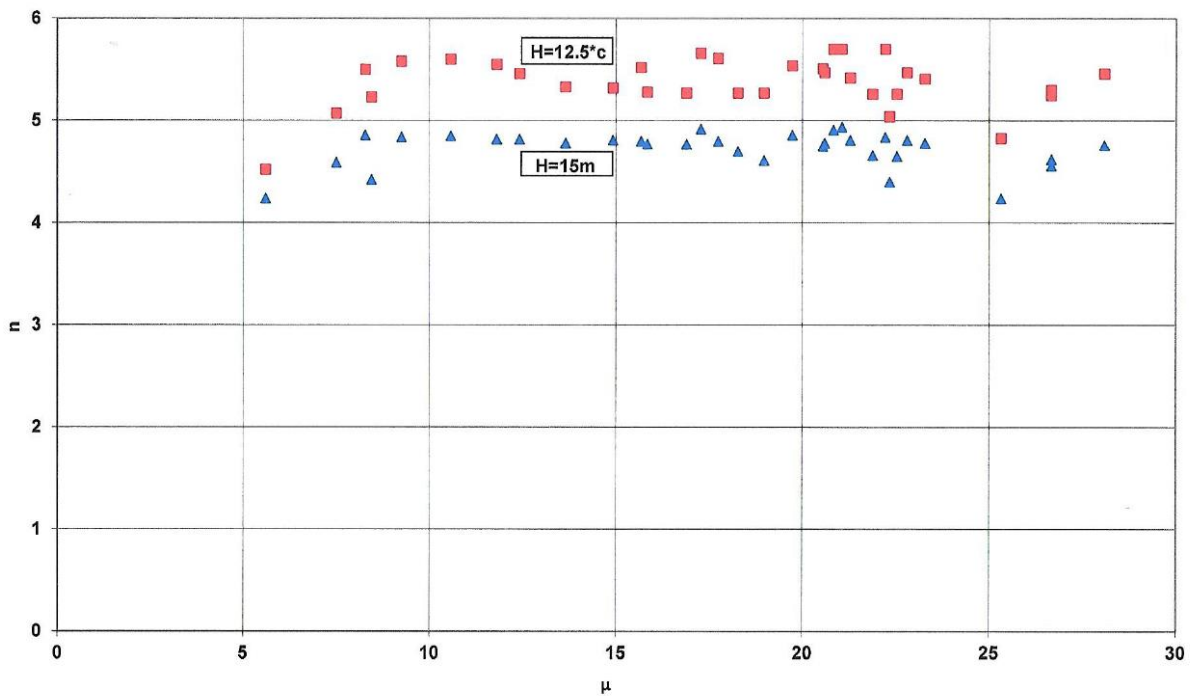


Fig. 3 Gust load factor as a function of the mass ratio parameter for 33 sailplanes in a (1-cos) shaped gust with gradient distance of  $12.5 \cdot \bar{c}$  meter (Pratt) and 15 meter.

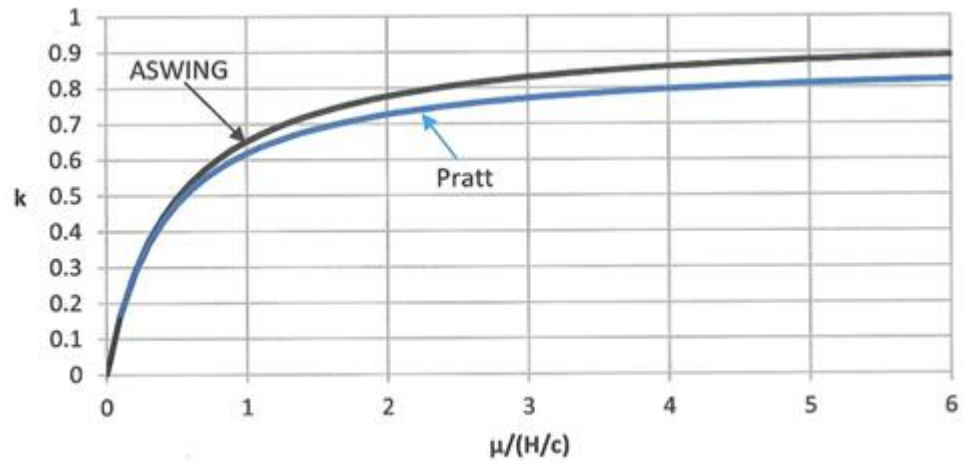


Fig. 4 The Pratt and ASWING generalized alleviation factors.

## **Naïve transfer of ICAO's Organizational Safety methods, such as SMS, into club-based flying might be either useless or even harmful**

Alfred Ultsch

*FLYTOP and University of Marburg, Germany, ultsch@ulweb.de*

**Abstract:** One of the latest safety methods for accident prevention at the commercial side of aviation focusses on the particular organization which actually organizes and operates every day's flights. The worldwide head organization for flying, ICAO, made that variety of Organizational Safety that is most suited for commercial airlines, an international standard. Most of the countries in the world are now obliged to implement ICAO's Organizational Safety in state laws and regulations. The primary organization at the noncommercial field of aviation that could profit from Organizational Safety are flying clubs and their club-based flight schools. However, there is evidence that a naïve one-to-one transfer of ICAO's Organizational Safety methods, such as ICAO's Safety Management System (SMS) or Threat and Error Management (TEM) is in the best case mostly useless. In the worst case it kills people.

We present the results of a first investigation into this problem and point to some key issues for a successful transfer of modern methods based on safety science into club-based glider flying.

## Improving Motorglider Safety and Reliability

*Dave Nadler, drn@nadler.com*

**Abstract:** We are all too aware of motorglider unreliability [1][2][3][4]. Reliability of electric-powered gliders is as bad or worse than gas powered, no panacea here [1]. We will never get Toyota-level reliability for any product without extensive testing, not economically possible for the tiny firms that design and build gliders. However, there are some things we can do to improve the situation. This talk is a discussion of a few simple ways to improve things, and suggested OSTIV projects to move them along.

**Keywords:** Motorglider, Safety, Certification, Standards.

### Introduction

Motorglider certification treats the engine and its systems as an optional accessory – it is certified as a glider. Certification rules expect the pilot to operate the aircraft such that engine failure at any point in flight does not result in an accident. When pilots rely on the engine (as happens far too often), failures cause accidents. Relying on the motor is a training problem and not the main focus of this talk.

EASA/LBA have neither the capacity nor expertise to perform detailed engineering reviews. Because a motor is considered an optional accessory in a glider, official response to problems has been essentially nil, except in extreme cases after major incidents/accidents. Status quo will remain without our action.

### What can OSTIV do?

An outline of possibilities will be discussed, with the hope of kicking off some OSTIV projects:

1. Collect and publicize problem reports to focus attention on existing problems (and possibly solutions)
  - a. Conduct updated DeRese survey
  - b. Create and promote web system for pilots to report problems (and possibly solutions)
  - c. Create improved inspection checklists improving on manufacturer info; create and promote system for consolidating problem info into checklists
2. Advocate updates to certification standards, emphasizing practical and affordable improvements.
  - a. Conformance methods – self-certification with attestation signed by 2 qualified engineers?  
Other ideas?
  - b. Fuel systems
  - c. Wiring and connectors
  - d. Electronics (the problem with small fires, is, that’s how big fires start)
  - e. Battery systems
  - f. Systems
3. Advocate updates to production-authority requirements, emphasizing practical and affordable improvements.
  - a. Protocols for inspection of electrical and fuel systems during production
  - b. Collection and publication of problem data
  - c. Updates of inspection protocols
  - d. Acceptable changes to certified designs, especially electronics
4. Research
  - a. Vibration issues with existing power plants (and possibly look for solutions)
  - b. Fire detection in engine bays
5. Create and promote OSTIV motorglider manufacturer forum to share problems/solutions and advance our common interests of improving the reliability situation.

So, do we want to do a few things, or just be a talking shop?

### References

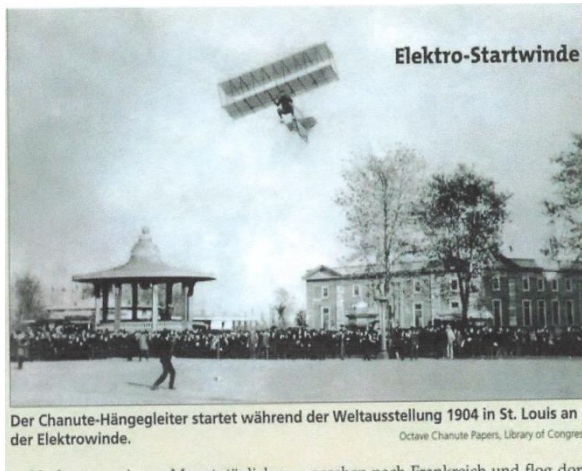
- 1) Dave Nadler: 2020 SSA/OSTIV Convention Presentation: Motor-glider Unreliability: Examples, Systemic Problems, Ideas (YouTube Video); [https://nadler.com/papers/2020\\_OSTIV\\_Motorglider\\_Systemic\\_Problems\\_presented.pdf](https://nadler.com/papers/2020_OSTIV_Motorglider_Systemic_Problems_presented.pdf)
- 2) Jonas De Rese, 2008: Results of the questionnaire: Engines in Sailplanes
- 3) Jean Marie Clement “Problems in Engines for Self Launching Gliders”, Sport Aviation Symposium, Milan, October 21-26, 2005 <http://www.streckenflug.at/download/motorprobleme.pdf>
- 4) Rainer Klein, Segelflugkonferenz Confèrencede volà voile Biel –Bienne 18.11.2017, Electric propulsion in gliders is more than an alternative to traditional combustion engines

## Investigation about Safety in Winch Launching

*Dipl. Ing. Karl Höck, carlo\_hoeck@yahoo.de*

### Introduction

Historically, winch launching was the first manner to bring gliders many metres over the ground. It first happened in the year 1904 on the occasion of the aeronautical concourse in St. Louis, when Frank Avery reached an altitude of 20 m with a Chanute – glider. The drum of the winch was driven by a 10 hp electric engine. Unfortunately, the altitude was not enough to reach the aimed gliding distance of 400 feet.



In the twenties in Europe the construction of winches on the chassis of motorcars, where the engine of car was joined to winch drum, began. Later development of commercial launch winches took aim to a lot of designs on trailers with separate drives. The bandwidth of these drives reached from gasoline to diesel and electric engines and from hydrodynamic to hydrostatic and electric regulations.

In Europe the winch launch became the most popular way for starting gliders, because of their economic and ecologic properties. It is also the most save start, with exception to the self-launch. Nevertheless, we have to take some rules into consideration to avoid typical accidents during this launch procedure. Therefore, it is necessary so simulate of the whole process from the beginning and look at the development of the angle of attack.

Winch launch is a multifactor process, depending on the physical features of glider and winch, as well as on the control of pilot and winch driver. It might be critical, because pilot and winch driver really have no readings about the conditions of their machines.

Efficiency of winch launch depends mostly on the airspeed of the glider. But for the safety of the launch the angle of attack is substantial. This feature follows to a simple summary formula during the process of launching:

$$\alpha = \alpha_0 + \Theta - \beta.$$

$\alpha_0$  = angle of attack by taxi

$\Theta$  = angle of inclination

$\beta$  = angle of track

So we can learn that the first part of the angle of attack depends from the taxi motion of the airplane.

**Angle of attack by taxiing is very important, mainly the distance to the max. angle of attack of the wings airfoil is substantial. This parameter should be published for each type of sailplane.**

Further the movement of rotation and translations are present. In this context we have to look for the forces and torques moving the sailplane and acting on the centre of gravity. The results of process are mainly speeds and angle of attack with by themselves have an influence on the procedure.

Simultaneous the variables “movement of stick and power of winch drive” also regulate the launch. The position of the hook and the centre of gravity and aerodynamic centre represent the parameters. We have to know the angle of attack at the beginning of launching and we must calculate the development of it during the whole process.

### Methodology

To get an idea of the critical issues during launching, we have to simulate the process with all the features. And we must vary some features. We used a spreadsheet for all calculations. Additional to the simulations we performed a statistic investigation about all BFU bulletins and reports from accidents from 2002 to 2020. So we could point out the most critical items for all kinds of starts and use it for certain simulations. We learned that there are three critical phases in the winch launch process.

- *Take-off*
- *climb after maximum inclination*
- *cable breakdown*

The first point is the most important, because there is a risk that the pilot can no longer prevent a stall with a high probably crashing. This problem is increased by the growing mass of airplanes and power of the winches. In the second phase the pilot may prevent the crash by operating right and quickly. That is also true for the cable breakdown.

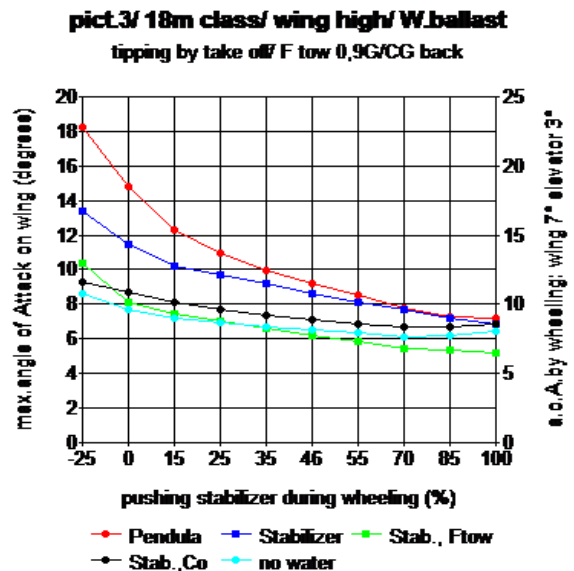
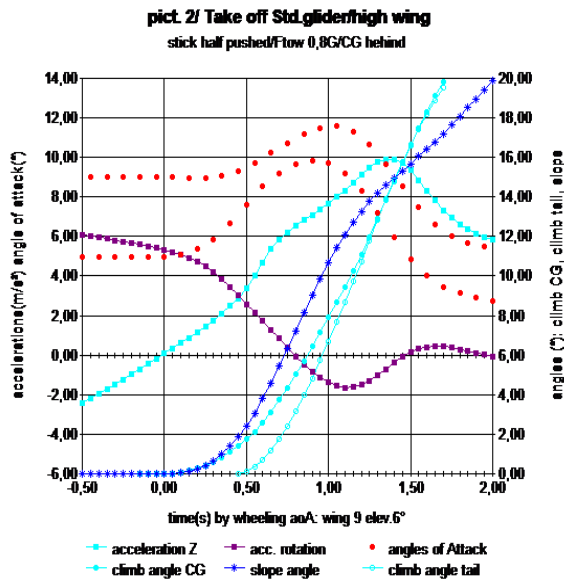
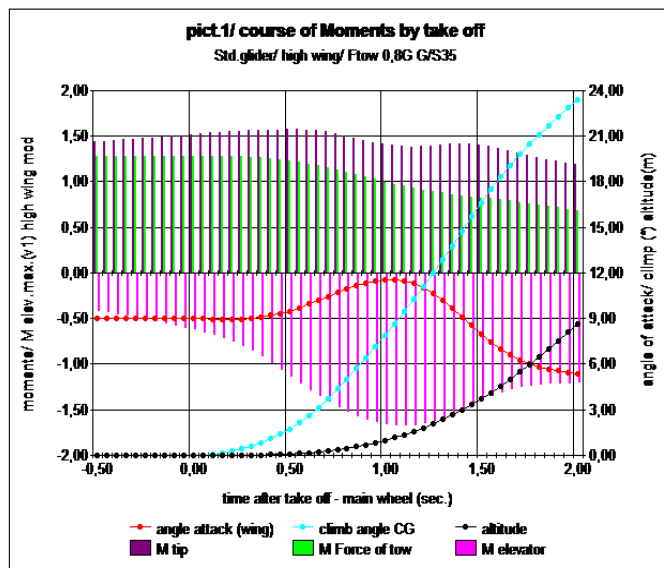
## Results

### 1. Take off phase

In **picture 1** you see the reasons for the critical issues during take-off - phase for a Standard sailplane. It is the result of the moments, tipping the glider and turns it in a critical position with to big slope and angle of attack. Unfortunately, the sailplane has a fixed angle of attack by taxi under less than one degree from stall. That is a problem, because we prefer three degrees for more security.

**Picture 2** shows the two responsible accelerations for the rotation (vertical and turn). Additionally we see the course of the angles of attack and climb. We recognize that climb angle increases more than angle of track. The gap defines the enlargement of the angle of attack on wing, so we catch a critical point there. The angle of attack on the elevator forever increases, because of the rotation of it around the centre of gravity. The data however stay in normal spheres. Because of the small ratio of elevator, the profile allows 17 degrees. The tilt of the airplane depends on a lot of factors. We can learn it, when we take a look on **picture 3**.

The factors are: Design of elevator (pendulum or stabilizer) and wing position, as well as position from hook and the centres of gravity and aerodynamic.



**Very important is deflection of stick, flap and fin while rolling. Pushing the stick during the take-off-phase can be too late!**

Loading of airplane and cable-force are boosting the tilt process. Elasticity of tow material determines the development of cable-force.

**If there is any doubt, push the stick full (80% with flying elevator) when rolling!**

**2. Phase of max. inclination**

If we consider the angle of attack during the whole launch, we can find the second maximum after the max. angle of slope. For this take a look in the simulation showed in **picture 4**. We can recognize there is a very different course of the angle of attack and airspeed. These are general results of the dynamic of rotation and lift.

While rolling the pilot chooses a deflection of ten degrees at the pendulum stabilizer. Six seconds after start in an altitude of 14 m the linear movement of the stabilizer begins. The stop of movement is at a deflection of minus 12 degrees (66 %) after 13 seconds at 300 m. At this point the wing reaches a critical angle of attack of 10 degrees. In the following ten seconds the pilot risks a crash.

The winch driver put the throttle in 3 seconds to full 300 hp - position. After reaching a cable-force of 1,6 G he releases throttle linear till the end of procedure.

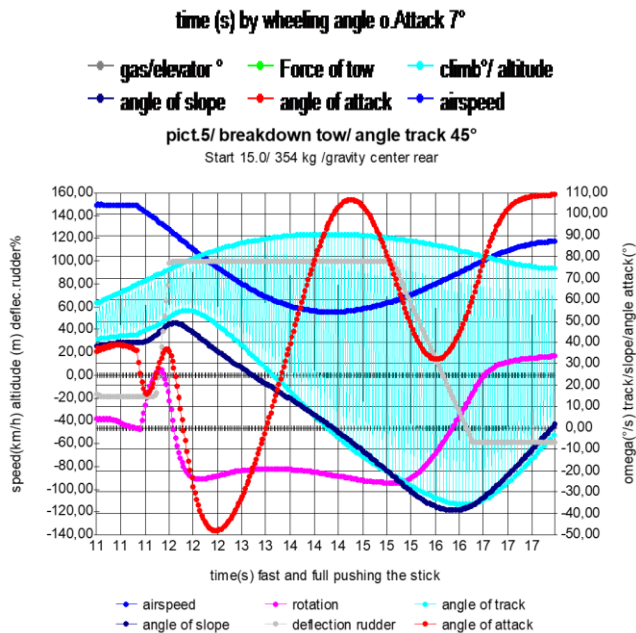
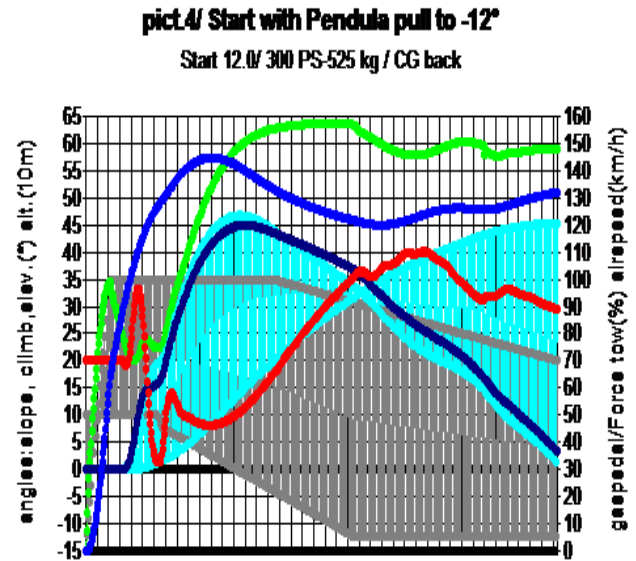
After the end of stabilizer-movement we see a falling force in the tow. That is because of the reduction of lift-coefficient and the torque of the elevator, which must balance the torque of cable-force. At end of launch the torque of cable-force brings the glider out of danger. The critical point in full climb area is after max. slope. There the airspeed naturally reaches a minimum. The pilot can prevent the stall if he pushes stick at this point at the very latest; otherwise pull not more than 10 degrees (55 %). In case of using a stabilizer with rudder, there is less danger for stall in all areas of start. The reason for it is the bigger positive lift coefficient in take-off area and the less negative lift coefficient in climb area.

We recognize not any stability in all the features of the whole procedure. Just the force in the tow could be regulated constant in full climb area, but for it we need a reading for the force. Because of the characteristics of the converter we get no control of output torque with the throttle only.

**3. Cable break down**

This happens mostly after max. slope, where we have the first big enlargement of cable-force. That is the area when speed of cable goes down and the converter output torque is rising. The inertia of drum and cable further increases the cable-force.

**Pict. 5** shows a simulation beginning at an angle of climb near 45 degrees at an altitude of 80 m. In spite the airspeed of 145 km/h speed of airplane falls under minimum at the turning point. Also angle of attack gets too high. During flattening out the airplane, starting at a slope of minus 20 degrees it stalls a second time. The deflection from elevator with minus 60 % was too big.



We learn that breakdown of cable at winch launch is a potential risk. The rotation of minus 20 degrees/sec. is too little for a secure procedure, and this is induced by the small negative lift coefficient of the cambered profile. Certainly this simulation is calculated with the worst factors, but the reaction of pilot is very fast.

There are 3 important handlings in expect of cable breakdown:

- **Pull no slope greater than 45°**
- **After cable-breakdown push fast and fully**
- **Do not release stick before slope is minus 20 degrees, and then pull not more than 50 %**

### **Outlook:**

Winch launch is a very sure procedure, if pilots and winch driver pay attention to some important rules. This is the responsibility from the gliding organisations and their instructors.

Improvement of safety is naturally possible. This could be an installation for reading force of cable at the winches. So winch drivers could control acceleration at the beginning and prevent breakdown of cables. Additionally, a simulator for training students and instructors in handling the dangerous cable breakdown could be efficient.

### **References**

Wayne Johnson, Rotocraft Aerodynamics, Dover, Wash. 1994,1998

## ASASys – Anti-Stall Assistant System for Sailplanes

Werner Scholz<sup>1</sup>, Sebastian Leis<sup>1</sup>, Valentin Petters<sup>2</sup>, Werner Würz<sup>2</sup>, Jan Axthelm<sup>3</sup>, Walter Fichter<sup>3</sup>

<sup>1</sup>*SFL GmbH, Stuttgart, Germany, scholz@sfl-gmbh.de*

<sup>2</sup>*Institute of Aerodynamics and Gas Dynamics (IAG), University Stuttgart, Germany*

<sup>3</sup>*Institute of Flight Mechanics and Controls (iFR), University Stuttgart, Germany*

**Abstract:** The intent, the elements and first results of a research program to develop an anti-stall assistant system called ASASys are described. Focus is on a proposed stall warning sensor using pressure measurements in the wing boundary layer, a proposed new control surface system working with spoiler flaps on the horizontal tail and on the description of the flight test platform, which is a modified sailplane.

**Keywords:** stall prevention, safety, assistant system, stall sensor, spoiler, flight test.

### Introduction

Loss of control, followed by stall and spin is the most lethal type of accident in general aviation, including, glider operations. In order to investigate possible technical means to prevent such accidents, the research project ASASys was started to develop an assistant system to support the pilot accordingly. Partially funded by the German government LuFo aviation research program, the engineering and design company SFL GmbH in Stuttgart, Germany teamed up with the Institute of Aerodynamics and Gas Dynamics (IAG) and the Institute of Flight Mechanics and Controls (iFR) of University Stuttgart to form a research team.

The goal is to develop a system which could be installed in sailplanes and light aircraft for new models or even as retrofit. The research program ASASys has started in 2018 and is expected to end in 2021 and this report focuses on the elements of the system and some first results from wind tunnel and flight testing.

### Methodology

The usage of classic stall warning sensors and/or angle of attack (alfa) sensors has often been proposed for use in gliders to allow the pilot a direct assessment whether a stall is developing. Nevertheless, experience in service has shown that such sensors are seldom used in gliding, despite the clear advantages to have this additional information in the cockpit. The main reason might be that during thermalling gliders are typically already operated very near the critical alfa and a classic stall warning would already start to warn despite the fact that the pilot is turning tight, but perfectly safe under the given circumstances. This is confirmed by the typical training offered by flight instructors which emphasizes turning with safe margin to stalls at low altitude and in the traffic pattern but also tight and slow when circling in the thermals for best climb performance provided the flight situation permits this slow turning near the stall. Therefore, a system acceptable for the typical glider pilot should not warn at a static alfa or speed but should take the flight situation into account. Even more, it would ideally detect a stall still in the developing phase and should then assess whether in the next seconds this could become critical or would stay harmless.

For this purpose, the system proposed in the ASASys program uses a new type of pressure probe on the wing upper side, which is called Embedded Wall Shear Sensor (EWSS) and which is working similar to a Preston probe. In figure 1 on the left side a picture shows the velocity profile in the boundary layer of the wing upper side together with a sketch of the EWSS. The pressure difference between the holes on the forward-facing side and the upper side of the slope-shaped EWSS is measured and normalized against the dynamic pressure taken from the aircraft pitot-static system. The three pictures on the right in figure 1 show the design aspects of the EWSS together with a Euro cent for size comparison. The parts are mainly 3D-printed and combined with commercial electronic pressure sensors, with the EWSS assembly then installed in the upper side of the wing at approx. 65% of the local chord length.

For testing purposes, the flight test platform has one EWSS installed on each wing, at the inner end of the aileron (i.e. the outer flaperon segment) and additionally a classic nose boom air-data probe provides additional alfa measurement which is only taken for comparison and analysis reasons.

With this setup, it is expected that detection of a developing separation of air-flow on the upper side will be possible, allowing also asymmetric flight situation detection and “early warning” against a developing stall. Ideally this would result into a “smart stall warning” which does not only detect a fixed alfa or a fully developed stall.

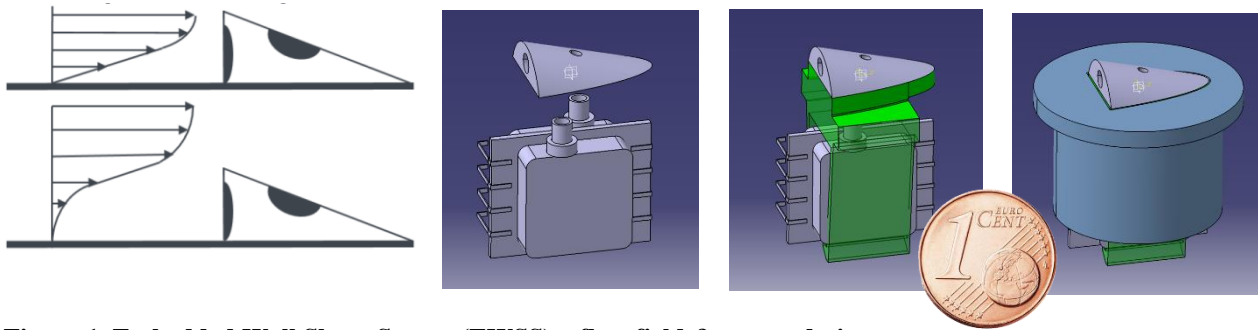


**Figure 1. Embedded Wall Shear Sensor (EWSS) – flow field & sensor design**

In addition to such an improved stall detection, the proposed system should be able to actively support the pilot by assisting stall prevention or even the ability to break a developing stall by inducing a nose down moment upon the aircraft. It was decided early on not to develop a system which is coupled to the primary control systems to avoid all issues coupled with flutter considerations, break-free forces for the pilot inputs and/or certification issues. The solution proposed instead is to use a spoiler-like flap on the horizontal tail on the under side in front of the elevator.

From usage of such spoilers as speed brakes on the upper side of wings or as landing flaps as split flaps on the underside it could already be deduced that the controllability effect of such a spoiler flap would be in the same order of magnitude as for the elevator, allowing this additional control surface to offer enough effect to support the pilot or even to correct a large control input mistake (e.g. when the pilot keeps on pulling back the stick when stalling).

Figure 2 shows the wind tunnel model of the additional spoiler flap on the underside of the horizontal tail (photograph upside down for this picture).

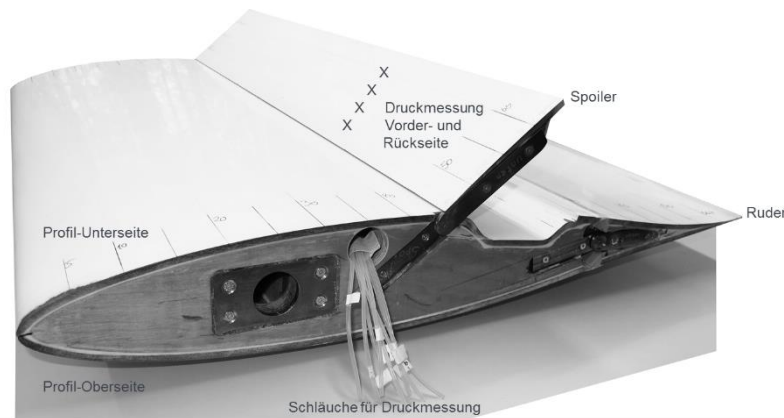


**Figure 2. Wind-tunnel model of elevator section with spoiler flap on underside**

Whereas the development of the stall sensor and the spoiler at the horizontal tail was performed at the Institute of Aerodynamics and Gas Dynamics (IAG) of University Stuttgart, the Institute of Flight Mechanics and Controls (iFR) of University Stuttgart together with SFL GmbH concentrated on the data acquisition system, the control computer and the systems onboard the sailplane which was modified to become the flight test platform. Focus of iFR was here on the system components and the algorithms to be developed for the on-board computer, whereas SFL concentrated on system integration, the air-data system and the planning and operation for the flight tests.

The following figure 3 shows the system architecture on the flight test platform regarding the different systems, which have been installed into the Arcus E sailplane to be operated under the ASASys program. In the nose, an air-data boom with sensors to measure  $\alpha$  and  $\beta$  and the total and static pressures has been installed with an air-data acquisition system in the forward instrument panel. Under the rear seat, sensors are installed to log all control system deflections. The main on-board computer is in the rear baggage compartment with its IMU near the center of gravity. Furthermore, the described stall sensors are installed in both outer wings and the spoilers in the underside of the horizontal tail.

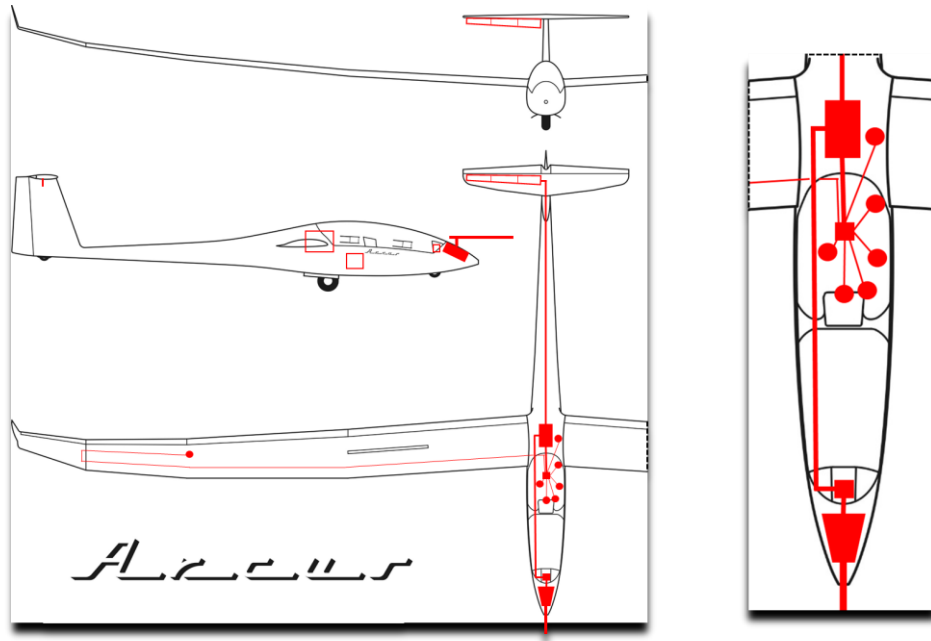


Figure 3. Flight test platform system architecture

### Results

In the time of writing this report, the full planned flight test programme within ASASys has not been fully completed, therefore, the results shown here focus on the wind-tunnel tests done by the Institute of Aerodynamics and Gas Dynamics (IAG) of University Stuttgart and further description of the flight test platform and planned flight tests by SFL.

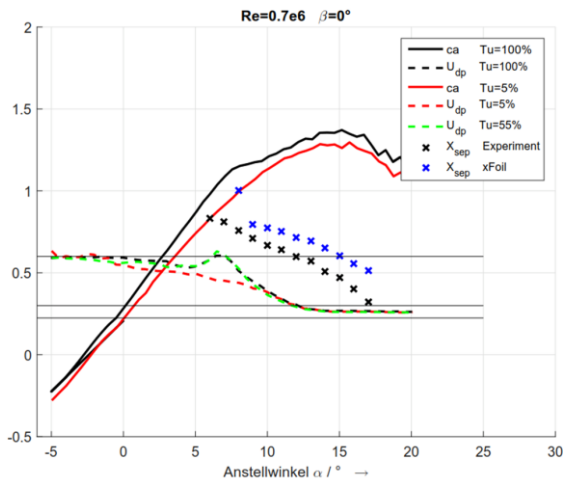


Figure 4a. EWSS measurement at flaps 0°

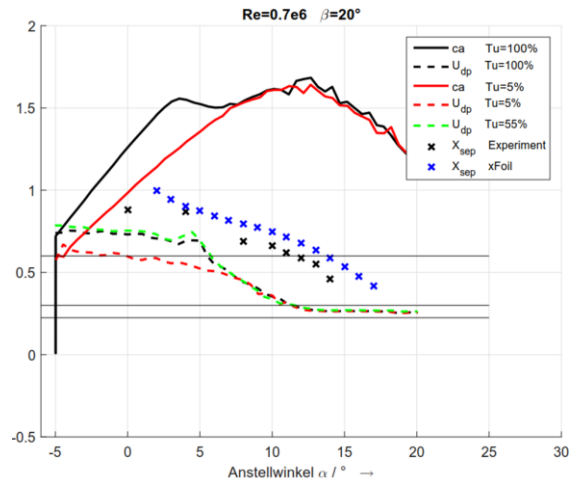


Figure 4b. EWSS measurement at flaps +20°

Figures 4a and 4b show exemplary results from wind-tunnel measurements with the stall sensor mounted in a representative wing section of the flight test platform. Please note that here the y-axis is used for denoting the lift coefficient  $c_L$  (called  $c_a$  in the plots), the relative chord position  $x$  and a sensor signal – all plotted versus angle of attack ( $\alpha$ ). The solid lines show the  $c_L$ - $\alpha$  plots for this airfoil with free transition (black) and full turbulent airflow (red, representative for flight in rain or heavy insect contamination). The left plot is for a neutral flap setting, whereas the right shows a typical thermal flap setting of +20°. The black “x” dots mark the position of flow separation versus  $\alpha$  in the wind-tunnel experiment against the blue “x” which are results of parallel XFOIL calculations. The output of the measured pressure difference from the EWSS is plotted in the dotted lines for free transition (black), fully

turbulent (red) and with transition in front of the sensor (at 55% chord, green). The main take-away of these exemplary results is two-fold:

- with the sensor located at 65%, the measurement pressure becomes 0, when separation is at or forward of 65% which happens at about  $12^\circ$   $\alpha$  for all flap settings – this alone represents a classic stall warning
- but even at much lower  $\alpha$ , the sensor already gives an output which could be used to estimate  $\alpha$  (i.e. the downwind position of the beginning separation), which enables to prognose an onset of a beginning stall

Further measurements in the IAG laminar wind-tunnel showed the expected effectiveness of the spoiler flaps at the horizontal tail which were then used by SFL to design the modification on the flight test platform.

The following figure 5a shows a sketch of this modification of the Arcus empennage in the CAD and 5b shows the modified Arcus E which is used as a flight test platform by SFL GmbH for ASASys and other programs.

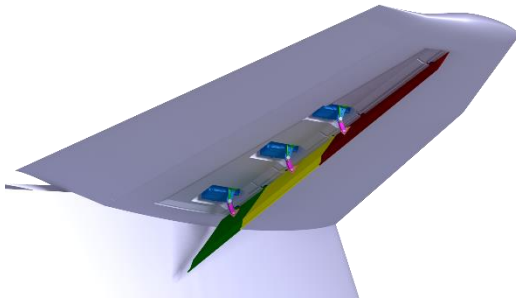


**Figure 5a. Horizontal tail modification**



**Figure 5b. Modified Arcus E sailplane – flight test platform**

First results of the flight test campaign show that the stall sensor indeed allows a good prognosis of the developing stall situation and that this output could be used to calculate a useful  $\alpha$  value which is close to the  $\alpha$  as measured by the nose-boom air-data probe.

The next step is now to implement algorithms into the on-board computer to use this  $\alpha$  / stall prognosis to create an adaptive stall warning for the pilot and to allow this computer also to use the spoiler flaps to prevent the pilot to steer the aircraft into an unwanted stall. The tests with this full functionality are planned for late summer of 2021.

## DLR's latest research sailplane: Discus-2c DLR

Erik BRAUN<sup>1</sup>

<sup>1</sup>DLR, Flight Experiments, Braunschweig, Germany, erik.braun@dlr.de

**Abstract:** Latest in a long line of research sailplanes, the Discus-2c DLR is the successor of the DG-300/17. It is employed as benchmark in evaluating glider performance using the GNSS based comparison method. The higher performance of the 18 m-span base aircraft Discus-2c compared to the DG-300/17 enhances measurement accuracy when testing the newest generation of high performance sailplanes. The DG-300/17 was used almost exclusively as a performance benchmark. The Discus-2c DLR, however, can also be operated as fully-fledged research aircraft for a variety of missions. This presentation will showcase its basic sensors and DAQ equipment as well as several missions that have already been carried out. Lastly, some concepts for possible future research campaigns will be presented.

**Keywords:** *research aircraft, sailplane, airborne research, in-flight measurements.*

### Introduction

DLR operates Europe's largest fleet of research aircraft. Twelve different aircraft make up the fleet, of which four are jet airplanes, two helicopters, and four turboprop airplanes, as well as one single-engine piston airplane and a research sailplane which will be the main topic of this presentation.

DLR and its predecessors have always used research gliders and sailplanes due to their simplicity and very low operating costs. Several different models have been operated over the last decades such as a Ka6E, Cirrus, ASW 15, Kranich, Janus and the specially modified DG300/17. A recurring mission for which the Kranich and Janus were known was the "flying wind tunnel". A test rig made up of a short wing segment and sidewalls was mounted on the nose (Kranich) or above the wing-fuselage junction (Janus) to measure the characteristics of the wing segment, such as drag or pressure distribution. The use of sailplanes was a major benefit for this setup, as the boundary layer could not be influenced by any engine vibrations.



Figure 6: DG-300/17 with ASW28



Figure 5: Janus with flying wind tunnel

Another very important use of sailplanes in aerodynamic research is the measurement of flight performance. There are several methods to determine the glide ratio of an airplane of which the comparison method is the most accurate and least time consuming. By using a sailplane which has been calibrated precisely, so that the glide polar curve is known accurately, and flying in formation with another sailplane which is the test article of the measurement, the unknown polar curve can be determined by measuring the relative vertical velocity at different airspeeds. Thus, ideally any atmospheric disturbance are cancelled out and the polar curve can be determined very accurately in 2-5 flights. The Ka6E, the Cirrus and the DG300/17 were used for these measurements using photogrammetric methods to determine the relative vertical velocity between the two airplanes – GPS was introduced with the DG300/17 and continued with the Discus-2c DLR which now makes use of a moving base differential GNSS technique.

Because of the evolution of high-performance sailplanes with high glide ratios of 1:50 and more, and ever higher wing-loadings, the DG300/17 was at the limit of practicality. So late in the first decade of the new millenium, a new research sailplane was needed, the search for which ended in the Discus-2c DLR. It was introduced into the fleet in 2012 and was fully operational in 2015.

### Aircraft and Systems

The Discus-2c DLR is based on the well-known 18m-class high performance sailplane Discus-2c manufactured by Schempp-Hirth. It has an empty mass of 337 kg, an MTOM of 565 kg, and a wing of 18 m span and 11.39 m<sup>2</sup> area (Schempp-Hirth, 2005). The basic aircraft was modified in several ways to accommodate our special needs. The fuselage is equipped with an engine bay which is usually built into the Ventus series gliders but used as a compartment for measurement equipment in our case. This bay features a removable lid instead to the bay doors of the standard version to minimize drag. The most prominent modification of the fuselage is the large nose-boom in front and above the nose. It is used to collect total and static air pressures as well as angle of attack and sideslip using a five-hole probe at the tip. To complete the set of air data, a total temperature probe combined with a humidity sensor is fitted to the fuselage under the starboard wing. Furthermore, the fuselage has hardpoints in the cockpit area to attach external probes to the sailplane.

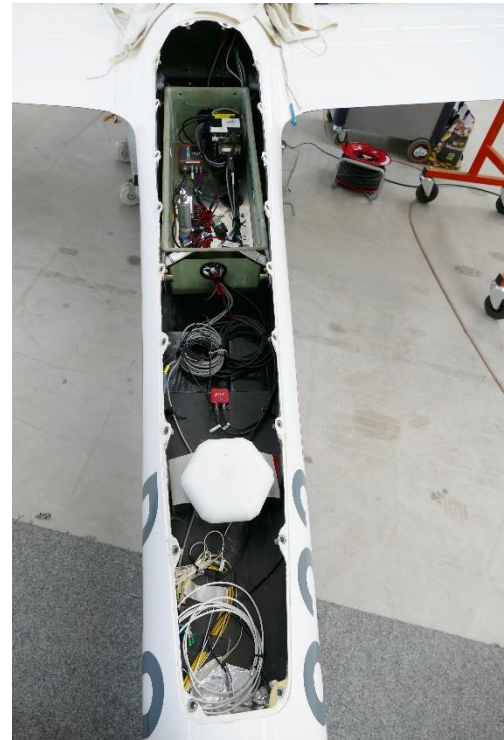


Figure 7: Equipment bay



Figure 8: Discus-2c DLR

48 strain gauges and 22 measuring points using fibre Bragg grating are built into wings and fuselage to determine aerodynamic loads in different flight states. The Discus-2c DLR features magnetometers and accelerometers in various locations which can be used in experiments concerning aeroelastics and flight mechanics. All control surfaces have deflection sensors. The sensor data are recorded using a data acquisition system which is located in the fuselage bay. The DAQ system is powered by a LiFePo4-battery with a capacity for several hours.

To reduce pilot work load and to implement precisely reproducible control inputs, an experimental digital autopilot was integrated into the sailplane. It uses electromagnetic linear actuators on elevator and ailerons. To keep the system simple and to circumvent a complex certification, the actuator can be easily depowered by switching off the power supply. Then they are still connected to the controls but produce virtually no friction in the system.

The measurement of glide polars using the comparison method depends strongly on the determination of the differential vertical sink speeds and relative positions between the Discus-2c DLR and the other sailplane. The measured sink speed difference is added to the known sink speed taken from the polar curve of the Discus. The exact

relative position between the two sailplanes is needed to determine the influence of the Discus' flow field on the performance of the other sailplane. Both values are determined using a moving-base differential GNSS system which is highly accurate and gives sink rate differences in the order of a few cm/s (Rohde-Brandenburger, 2017).



Figure 9: Performance measurement, JS3 and Discus

### Missions

The first experimental campaign for the new research sailplane was the project *iLoads*. The overall goal of this project was to determine loads on an aircraft in flight by measuring the deformation of wings, fuselage and empennage. To achieve this, the Discus is equipped with strain gauges in various parts of the structure. There are 6 in the fuselage, 36 in the wing and 3 in the empennage.

To determine loads in flight by measuring the deformation, the strain gauges had to be calibrated first. This was carried out by loading the wings and other structure of the Discus with predetermined weights and measuring the signals of the different strain gauges. This had to be done in several orientations, most importantly upright and inverted to calibrate for wing bending and torsional loads, and determine sensor hysteresis.



Figure 10: Strain gauge calibration

With the calibrated sensors, a flight test campaign was performed. Over about 25 flight hours, a system identification was carried out by using a variety of control inputs in different conditions while recording the reaction of the aircraft regarding deformation, trajectory and orientation. The result of these experiments is a highly refined model of flight mechanics of the Discus-2c DLR which can be used to calculate different manoeuvres and which will be useful over the life of the sailplane (Viana, 2015).

The latest campaign on the Discus-2c DLR apart from our performance measurements, which are performed each summer in cooperation with the Idaflieg, was the project KonTeKst in which the pressure distribution around the Discus wing was the main interest. As opposed to determining flight loads by measuring deformation, the forces on the wing can also be calculated by integrating the static pressure distribution at several wing sections. This was done by using tiny MEMS pressure sensors which were integrated into a thin wing glove. This glove is a 3D-printed scaled-up part of the wing which was 3D-scanned beforehand to determine the exact shape of the wing in this position. Due to manufacturing inaccuracies the wing airfoil cannot perfectly match the theoretical airfoil shape and this also had to be scaled up. 60 pressure sensors were distributed with 30 each on the upper and lower surfaces of the wing. The results showed a very good agreement with Xfoil calculations of the real airfoil and even the laminar turbulent transition was clearly visible in plots. Due to unsteady measurements with a sampling rate of 200 Hz, the stall behavior of the wing with its corresponding flow fluctuations could be observed. After further miniaturization of the system, it will be used in experiments on our latest research aircraft ISTAR, a modified Falcon 2000 (Raab, 2019).



Figure 12: Measurement glove

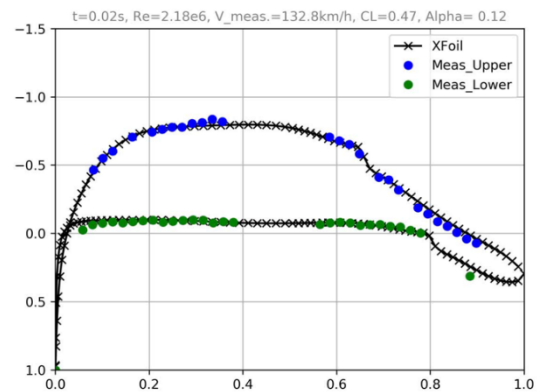


Figure 11: Pressure distribution

### Conclusion and Outlook

The Discus-2c DLR has already shown, that it can be used as a highly flexible and capable research aircraft. This is mainly due to the simplicity in its operation and systems. A very good cooperation with the LBA, the responsible certification authority, also helps, of course. As the Discus has no essential electric or electronic systems needed for a safe flight and is of a very rugged construction typical of most sailplanes, it can be used for a wide variety of experiments with a minimum of effort.

In the future, the Discus will continue to be the main player in the flight performance measurements of sailplanes, but will also fly several new experiments. Next in line is the measurement of atmospheric turbulence to determine its impact on flight performance. This will be done by swapping the total energy probe on the tail for a five-hole probe with pressure sensors directly behind it in the vertical stabilizer to maximize the possible sampling rate by minimizing drag due to long pressure lines. After that, a new pressure rake system will be used to demonstrate the suitability of MEMS pressure sensors for this application. This will also enable the Discus to be the new flying wind tunnel on which airfoils can be tested in flight by using wing gloves. To complete the experimental autopilot system, a rudder actuator will also be fitted later. This will make controlled flight in all three axes possible.

The Discus might be DLR's smallest and lightest research aircraft but is by no means the least capable.

### References

- Raab, C. (2019). *Load Measurements with the Discus-2c - Flight Test Planning and Data Gathering*. Braunschweig: DLR Institut für Flugsystemtechnik.
- Rohde-Brandenburger, K. (2017). *Flight Performance Measurement of Gliders With GNSS System*. Benalla, Australia: OSTIV.
- Schempp-Hirth. (2005). *Wartungshandbuch für Discus-2c DLR*. Kirchheim.
- Viana, M. V. (2015). *Sensor Calibration for Calculation of Loads on the DLR Discus-2c Sailplane*. Braunschweig: DLR Institut für Flugsystemtechnik

## fs36 Fly-by-Wire of the Akademische Fliegergruppe Stuttgart

Felix Johnke, Jan Felix Santosa, Moritz Habermann

*Akaflieg Stuttgart, Germany, felix.johnke@akaflieg.uni-stuttgart.de*

**Abstract:** The fs36 is a sailplane with a fly-by-wire control system and fowler flaps. This control system has many advantages from a performance, safety, and design perspective, but also brings about challenges in its development.

**Keywords:** Fly-by-wire, sailplane

### How it came to the fs36 Fly-by-Wire?

As our last project, the fs35 Harpyie, neared its end, it was time to start making plans for the next project. At the same time, we found out that we had the chance to apply for a grant which supports innovative aviation projects from the Luftfahrtforschungsprogramm (LuFo, Aviation Research Program). The program is run by the Bundesministerium für Wirtschaft und Energie (BMWi, Federal Ministry for Economy and Energy). This led to two ideas: The first, the fs36 Velo, revolved around an elastic wing leading edge which would act as a slotless high-lift device for sailplanes. The second idea, the fs36 Fly-by-Wire, would serve as a demonstrator for fly-by-wire technology in sailplanes. Although both proposals were accepted, we decided after some discussion to pursue the latter idea. For this project, we have the support of the Institut für Luftfahrtsysteme (ILS, Institute for Avionics) of the University of Stuttgart, which is responsible for the fs36's flight computer and the software.

### Our Goals

Our primary goal is the implementation of a fly-by-wire control system in a sailplane. The mechanical control elements will be replaced by cables and actuators, which enables fully electric manipulation of control surfaces. As fly-by-wire opens up many possibilities in the field of safety and performance, which we will exploit and demonstrate, we decided to develop and build our own wings.

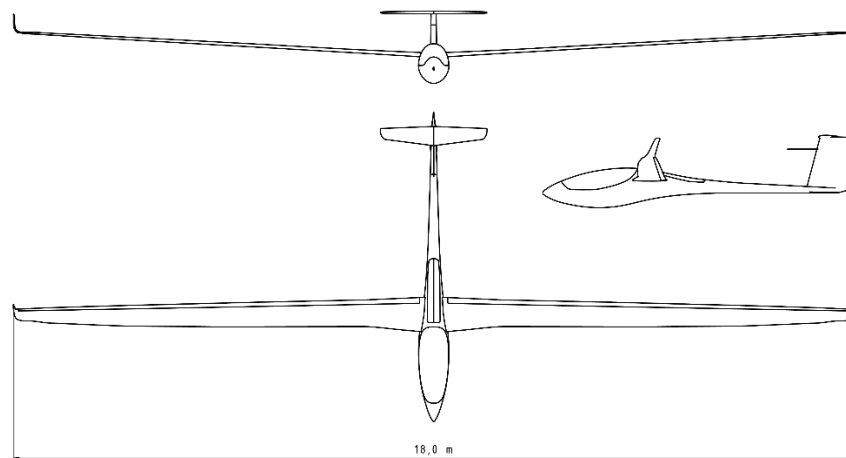


Figure 13: 3-view drawing of the fs36

**For more safety in aviation**

Data from the Bundesstelle für Flugunfalluntersuchung (BFU, Federal Bureau of Aircraft Accident Investigation) show that circa 49% of all fatal accidents are caused by entry into an uncontrollable flight attitude due to pilot error. Conventional safety features, such as modern crash cockpits, minimise injury to the pilot in the event of a crash. Our approach is to prevent accidents before they happen. We plan on integrating aids, such as a stall or even a full envelope protection, with our fly-by-wire control system in the future. The flight computer will then be able to actively intervene during flight, which is standard for airliners. Other functions, such as collision and airspace avoidance systems will also be possible.

### Necessary steps and challenges in the design

As mentioned earlier, new possibilities are opened up by fly-by-wire from a design and competitive perspective. The space inside the airplane is utilised quite differently. Among other things, the flight computer, cabling, actuators, input sensors, and the battery system have to be integrated in the fuselage. Even though the flight computer is programmed by the ILS, the overall system still poses new challenges. For example, the battery system has to be redundant and possess enough fire protection, since the failure of this system would lead to the failure of the whole system. Even the effect of the CFRP skin on the electrical system has to be analysed. Furthermore, the failure rates of each component have to be determined to calculate the failure rate of the overall system.

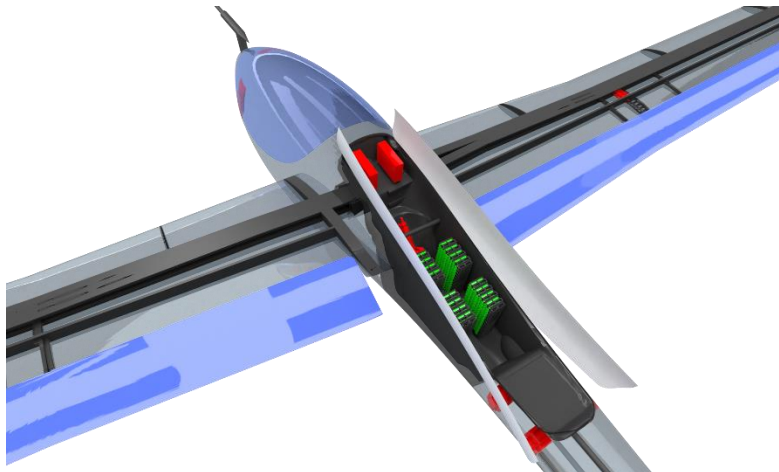
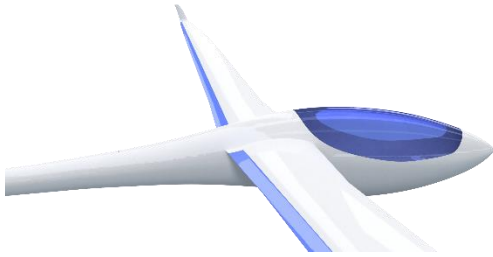


Figure 14: Depiction of the battery packs, actuators and flight computer in the fuselage

### Inspiration from the past: fs34

Besides the challenges inherent with a fly-by-wire system, there are also additional advantages. New designs for the wings are possible. In one of our previous projects, the fs34, we attempted to implement a Fowler flap, which enables the pilot to change the wing area in flight. With flaps extended, the airplane will have a comparable wing area to other high-performance sailplanes, allowing it to thermal equally as well. With flaps retracted, the airplane's best gliding speed is higher than that of its competitors due to its higher wing loading and lower drag.

Unfortunately, the fs34 couldn't be built because a mechanical realisation of the flap system was unfeasible due to multiple reasons, such as space and structural concerns. Fly-by-wire offers a solution to this issue. Unlike with a mechanical system, fly-by-wire does not have the restrictions of the former in the areas of space and kinematics. Paired with a very thin profile, we will be able to demonstrate the advantages of such a control system. These include an optimal deflection of the flaperons based on the current flight attitude.



*Figure 3: Flaps retracted*

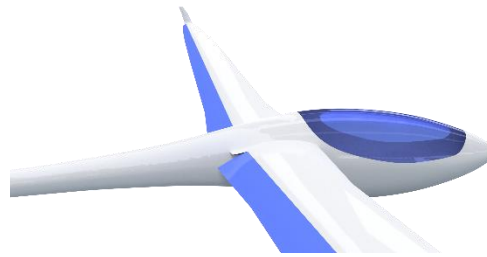


*Figure 4: Flaps extended*

The fs36 will have a wingspan of 18 m and a wing area of approx. 10 m<sup>2</sup> with flaps extended. When the flaps are retracted, the wing area will be reduced to approx. 8,5 m<sup>2</sup>.

### **The current status**

Currently, we are still occupied with pre-development. Much progress has been made regarding determination of system integrity and redundancy. Furthermore, we are working closely with the Luftfahrtbundesamt (LBA, Federal Aviation Office) to set out guidelines and specifications, with which the fs36 and all following fly-by-wire sailplanes will be certified.

Apart from computer-aided design work, we have built a test piece to validate the design and to gain experience for the actual building of the wing. A second test piece of the outer wing is to follow suit. At its current state, each wing is to have four individually controllable flaps. Each flap will have up to two flaperons on its trailing edge. These are manipulated by actuators built into the flaps.



*Figure 5: Wing test piece*

We have also built a test piece for use at the Institute for Aerodynamics and Gasdynamics' (IAG) laminar wind tunnel. With this, we were able to compare the calculated performance of the wing's profile with those in real-life conditions. This is accompanied by further aerodynamic work on other areas, such as the wing root and winglet designs.

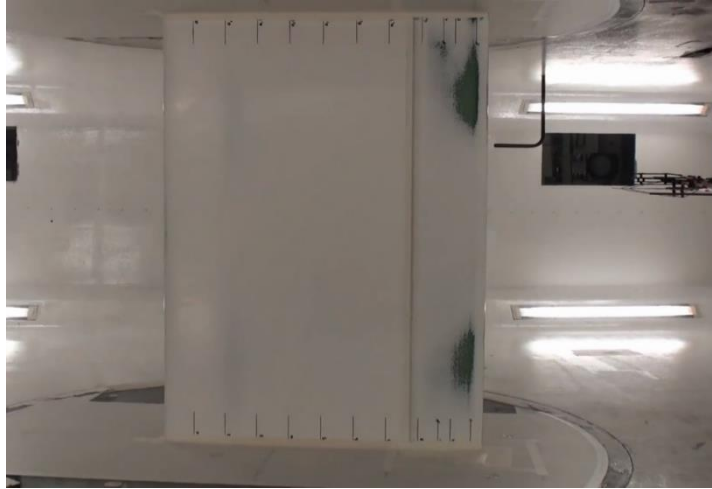


*Figure 6: Test piece inside the laminar wind tunnel*

To test whether parts would fit inside the fuselage and how to best integrate them, we laminated a fuselage mock-up of the Ventus 3 at the Schempp-Hirth plant in Nabern.

Gefördert durch:



aufgrund eines Beschlusses  
des Deutschen Bundestages

## icaré 2 wtp – Fly with light and control by thrust

Werner Scholz<sup>1</sup>, Johannes Schneider<sup>2</sup>, Andreas Strohmayer<sup>2</sup>, Stefan Notter<sup>3</sup>, Walter Fichter<sup>3</sup>

<sup>1</sup>*SFL GmbH, Stuttgart, Germany, scholz@sfl-gmbh.de*

<sup>2</sup>*Institute of Aircraft Design (IFB), University Stuttgart, Germany*

<sup>3</sup>*Institute of Flight Mechanics and Controls (iFR), University Stuttgart, Germany*

**Abstract:** The history of the solar-electric motor-glider icaré II is summarized, leading to the current usage as a test platform for demonstration of asymmetric thrust yaw control. Components of the experimental control system and the main control modes are described and the current and future state of this research program is outlined.

**Keywords:** solar powered aircraft, distributed electric propulsion, yaw control, wingtip propeller, flight test.

### Introduction

In June of 1995, the institutes of the faculty of aerospace engineering at the University of Stuttgart succeeded into building a practicable solar-powered aircraft when icaré II made its maiden flight. This aircraft was destined for the Berblinger Prize of the city of Ulm, which was won by this university team later that summer. In addition, the icaré project represented the cumulative efforts of many participating students, staff members, sponsors and further supporters and was already the topic for approx. 40 student thesis works in the years 1994 to 1996.

This project was later awarded with the Ostiv Prize in 1997 but the icaré team members, despite a steady change of participants, continued to operate this unique aircraft up until today. In the following years, many original components of the electric propulsion systems were updated and as soon as FAI introduced solar powered aircraft as a new class, world records were flown with the icaré. In parallel this aircraft remained in the focus of research and student thesis works and since 2017 a new topic was opened with a modification where additional propellers have been installed on each wing tip.

The main motivation here is to show the ability for distributed propulsion systems to actively control the aircraft and to analyze different flight modes which become possible with this additional control system. This effort is conducted at the Institute of Aircraft Design (IFB) and the Institute of Flight Mechanics and Controls (iFR), both at the University Stuttgart and is supported by SFL GmbH, also from Stuttgart, Germany.

### History

The solar powered motor-glider icaré II was built to fulfil the requirements of the Berblinger Prize 1996. The two main tasks were to show a self-launch with electric propulsion up to an altitude of 300 m AGL and to demonstrate the ability to produce enough power with the solar generator to sustain flight altitude at a solar irradiation of only 500 W/m<sup>2</sup>, representative of a European summer day. It has to be remembered that at that time this needed to be realized with Nickel-Cadmium batteries and silicone solar cells with about 17% efficiency, both representing the state of the art at that time. The icaré II succeeded to demonstrate all these tasks and won that competition, In addition it proved to be a usable powered sailplane which could be rigged and operated similar to other composite sailplanes, thereby representing another step of evolution which saw the experimental solar planes like the Solar Challenger of Paul MacCready and then the Sun Seeker of Eric Raymond at earlier evolution stages. Figures 1a and 1b show icaré II during its first self-launch and solar powered flight during the Berblinger competition.

After replacement of the batteries against more modern Lithium based cell systems and after a non-official record flight without usage of thermals or other updrafts over more than 300 km, further modifications in the drive train were implemented. Icaré then came into focus of the record pilot Klaus Ohlmann who soon started to fly world records with this aircraft for the new generated solar powered aircraft class of FAI. Figures 2a and 2b depict the pilot and icaré in the region of Southern France, where the majority of these records had been flown.

Starting in 2017, a new development started for the icaré project with a first installation of additional propulsion units at the wing tips, were electric motors now drive small propellers to add the possibility to control the aircraft around the yaw axis using differential thrust. Figures 3a and 3b show this modification which made icaré the first aircraft capable to simultaneously fly with light and to control by thrust.



Figure 1a. first self-launch of icaré II in 1996



Figure 1b. solar flight at Berblinger Prize



Figure 2a. world-record pilot Klaus Ohlmann



Figure 2b. icaré in Southern France



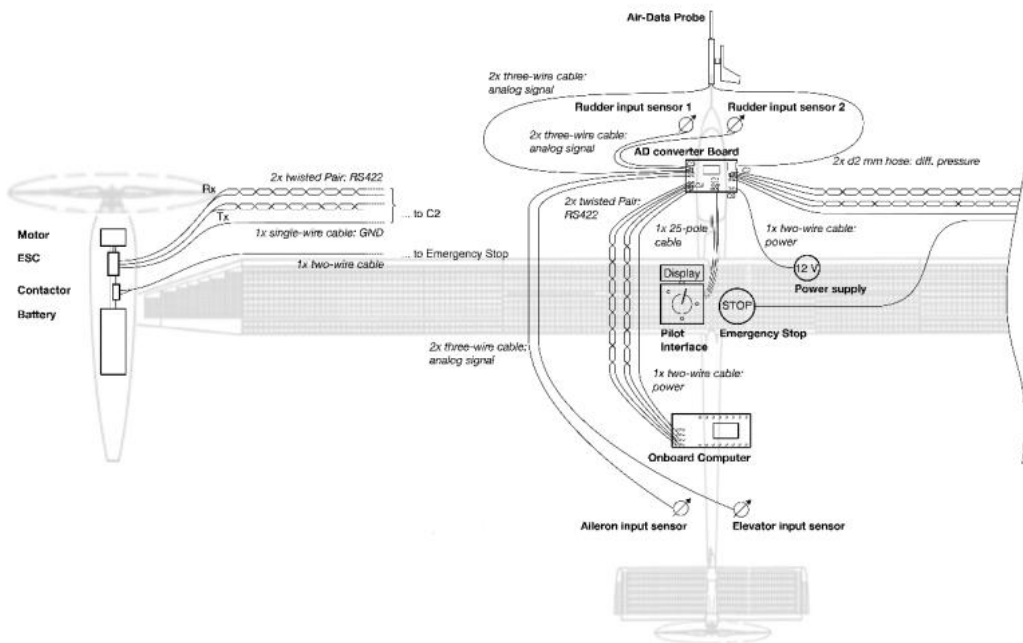
Figure 3a. flight with wing tip propellers



Figure 3b. additional propeller pods

### Experiment setup and Results

The modification with the wing tip propellers includes installation of a flight data acquisition system to measure relevant flight parameters and to allow an on-board computer to activate different flight modes with the wing tip propellers for yaw control. Figure 4 shows a diagram of the additional system components which were installed into icaré II.



**Figure 4. Wing tip propeller modification – systems overview**

The wing tip pods were developed using commercially available elements for the propulsion system, which were not coupled to the main solar-electric propulsion system, as these pods were not designed for propulsion but for control purposes. Figures 5a and 5b show the design and inner components of the pods.

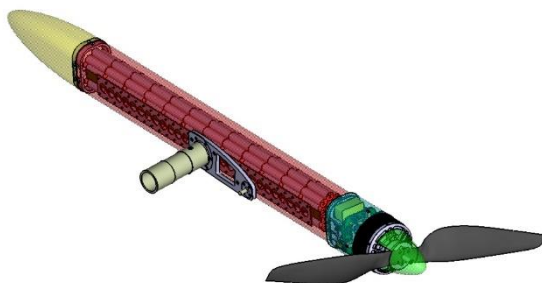


**Figure 5a. wing tip propeller pod design**

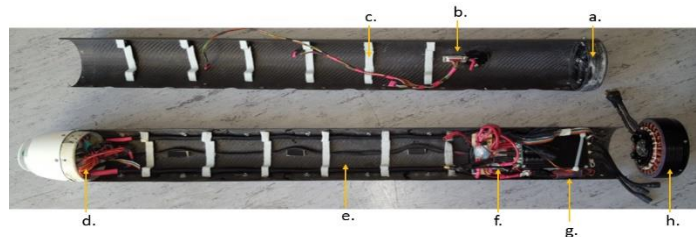


**Figure 5b. wing tip propeller pod components**



**Figure 6a. cockpit side-stick installation**



**Figure 6b. wing tip pod display unit**

Figures 6a and 6b show the additional control and display elements in the cockpit. A sidestick installation mounted on the left side of the instrument panel allow the pilot to manipulate the differential thrust in the different operational modes and a display unit installed to the right side of the instrument panel offers data for the pods and other parts of the data acquisition system to the pilot.

The following modes were developed and put into flight test one after another:

- data acquisition system test and parameter identification: here the additional flight test components were first taken into operation and several parameter identification maneuvers were demonstrated and documented with the system; this data was then used to create a representative aero-physical model of icaré in a Simulink model which was then later used to develop the different yaw control modes
- manual mode: in this mode, the pilot directly controls the power setting of both wing tip propellers – stick forward increases the thrust, left or right increases the thrust so that the aircraft yaws to the left or right side
- rudder-coupled mode: as the flight test acquisition system also measures all pilot inputs on the primary flight control systems, this mode now uses the rudder position to modulate the asymmetric thrust, i.e. from the pilots perspective, this modes increases rudder efficiency by adding the wing tip pod component to the normal rudder efficiency
- aileron-coupled mode: her the principle is similar to the rudder-coupled mode, but now the lateral stick position is used to command asymmetric thrust; for the pilot this creates now an aircraft handling behavior which nearly allows to control turns without usage of rudders
- automatic doublettes: this mode allows the pilot to create a yaw doublette by just pressing a button, which then starts an according sequence of asymmetric thrust inputs in order to offer a better reproduceable input for later parameter identification
- automatic sideslip control: in this most automated mode the system uses the measured sideslip angle from a nose-boom air-data probe to use the asymmetric thrust to control the aircraft to fly a pre-set sideslip-angle; for a straight flight path this is obviously set to zero, for turns up to approx. 10° bank angle, the pilot adjusts the sideslip angle accordingly (due to the very strong roll-yaw coupling, icaré needs a considerable yaw angle with outward angling yaw string to fly a coordinated turn)

First analysis of the results of the flight test campaigns shows that such yaw control by asymmetric thrust is a practicable usable additional control option for aircraft configurations with distributed propulsion elements and additional tests on a sub-scale unmanned version of the electric powered e-Genius experimental aircraft of University Stuttgart further explore more control modes. The final figure 7 shows icaré II and the full-scale e-Genius in formation as both aircraft keep on expanding the range of research work with electric propulsion and flight control systems in Stuttgart.



**Figure 7. Flight of icaré II and e-Genius experimental aircraft in formation**

## References

<sup>1</sup>J. Schneider, M. Frangenberg, S. Notter, W. Scholz, W. Fichter, A. Strohmayer, 2020: Integration of propelled yaw control on wing tips, Proceedings of „Deutscher Luft- und Raumfahrtkongress 2020“, DGLR.

## Status report about AlpTherm\_2 as a fully revised convection model

Bruno Neininger

*MetAir AG, Switzerland, bruno.neininger@metair.ch*

**Abstract:** The convection model ALPTHERM (or Toptherm, Regtherm as follow-ups) are in use for soaring weather forecasts by several national weather services in Europe since 1993. A fully revised new version AlpTherm\_2 was under development since 2014 and has now reached a maturity that should allow operational applications starting next year. This presentation is describing the new architecture and is giving an outlook. Since the spatial resolution (100 m horizontal) is much higher than for the sub-regions defined in the original ALPTHERM, the resulting forecasts might also be interesting for paragliders.

**Keywords:** soaring, gliding, paragliding, convection, post-processing GFS.

### Introduction

When the first version of ALPTHERM was launched in 1993 [1, 2], computer programs running on PCs were limited to 640 kB RAM, floppy disks had a capacity of 1.44 MB, and hard disks of – maybe – 30 MB, and actual weather data was not that easy to access as it is today. Nevertheless, the original version of ALPTHERM and derivatives are still in use at national weather services and widely observed by the gliding community (distributed e.g. via [3]). Encouraged by colleagues and students interested in soaring weather, the author of this article began to think about new options for a second generation AlpTherm\_2. The basic idea was to use as much useful input (initial and boundary conditions) from the global circulation model GFS [4], supplemented by those sub-scale processes, where the complex topography and surface properties are important for the development of thermals. This new version should be fully three dimensional (the original ALPTHERM was "one-and-a-half-dimensional" for selected regions), should represent any slope or other hot spots also in flat terrain (e.g. low albedo, enhanced evaporation over forests, or cooling towers), applicable to any region of the world.

During the more than 20 years, the global general circulation models (GCMs) [5] and many local area models (LAM) such as AROME in France, ICON-DE in Germany, and COSMO-1 in Switzerland [6] have evolved enormously. Platforms like [7] are offering detailed weather forecasts based on different GCMs worldwide for free. This raises the question if there is still a need for a special convection model.

All these models for different scales are focusing on dynamical processes, i.e., they are solving the Navier-Stokes equations for generating a best-possible wind field, and hence reasonable temperature and humidity fields on a scale of 10 to 20 km (most advanced GCM) or one kilometre (LAM). However, for fulfilling this priority they are forced to make compromises in resolving the terrain, causing known deficiencies [8]. It is widely discussed in the literature, that convection is still a challenge. 'Convection allowing schemes' is the most advanced stage, meaning that based on a resolution of 1 km horizontally, the development of thunderstorms can be simulated. This is still far away from resolving slope winds and thermals on a scale of 100 m.

On the other hand, statistical approaches using machine learning, connecting data from glider and paraglider flights with meteorological data, were successful in regions with high gliding activity [9].

However, there are still important gaps and shortcomings:

- Neither GCM nor LAM are producing routine output for detailed local convection.
- Even the most advanced machine learning cannot give reliable advice for regions with insufficient data coverage (recorded flights over different seasons) and for weather conditions that were not used for the learning algorithm (the daily weather has many parameters ...).
- There is a gap between 'good old tephigram-exercises' and advanced LAMs, i.e. the skill of most pilots using the first is limited (also by the time needed for such a pre-flight analysis), and having an own LAM is out of reach even for organisations such as aeroclubs or competition organisers.

Therefore, it was decided that an advanced algorithm serving as a post-processor for existing models could still fill these gaps. A second application is (self-)teaching, because the different processes such as the influence of the snow-limit can be studied 'hands-on'.

### Methodology

Both the old and the new AlpTherm are not classical meteorological models solving equations on a Eulerian grid. Instead, the near-surface air is heated or cooled according to the available net heat (short- and longwave in and out, evaporation/condensation, and ground heat flux, resulting in net sensible and latent heat fluxes). Then these pockets of air are moving to their equilibrium level (katabatic downward flow when cooler than the ambient air or rising along slopes and as thermals when warmer (including humidity via the virtual temperature). This 'Lagrangian approach' is applicable when the situation is not highly dynamic, i.e. is especially suitable for weak wind situations as they are preferred anyhow for paragliding. Of course, the quality of the result is depending on sufficiently good estimates of the above mentioned heat fluxes, needing reliable surface properties like albedo, Bowen-ratio, or ground heat flux on the 100-m-resolution. In contrast to GCM and LAM, this algorithm is focusing on the local, mainly vertical, exchange of air between the surface and the free atmosphere, putting less emphasis on the wind field.

However, the new version will be capable (see table 1) of estimating "internal wind", i.e. wind that is resulting from the small-scale pressure gradients developing between the 'cells' (see figure 1 and explanatory text), and can integrate "external wind", i.e. entering and exiting air masses according to the GCM in which AlpTherm\_2 is embedded.

**Table 1: A list of features that are already implemented (left), or under development (right)**

<ul style="list-style-type: none"> <li>✓ global coverage (can be adapted to any region)</li> <li>✓ semi-automatic data download including SRTM topography</li> <li>✓ albedo (and partly Bowen-ratio) from MODIS images</li> <li>✓ improved downscaling from GFS using SYNOP data</li> <li>✓ flexible for other data sources (other than SRTM topography, GFS, SYNOP-stations, and MODIS imagery)</li> <li>✓ surface energy exchange on 100 m resolution</li> <li>✓ improved night-time inversions in valleys</li> <li>✓ fully Lagrangian formulation of slope-winds and thermals</li> <li>✓ aggregating results in cells of 1 to 5 km size (1 km used here)</li> <li>✓ resulting regional lifting and subsidence</li> <li>✓ realistic cloud bases and cloud tops</li> <li>✓ 10 minutes temporal resolution</li> <li>✓ less than 10 minutes runtime for the examples in figs. 2 &amp; 3</li> </ul>	<ul style="list-style-type: none"> <li>➤ individual clouds within the cells, including wind-influence</li> <li>➤ thermal horizontal wind following the pressure gradients</li> <li>➤ influence of the wind on the quality of thermals</li> <li>➤ improving the energy budget over lakes and snow</li> <li>➤ improving the Bowen-ratio (latent heat flux e.g. over forests)</li> <li>➤ cloud shadows from cumuli generated by the algorithm</li> <li>➤ validation for different cases with known soaring activity</li> <li>➤ operational production and dissemination (needs partners)</li> </ul>
---	--

It is not possible to explain all the details of the algorithm here, but figure 1 is explaining the concept. More details will be published when also all the items on the right-hand-side of table 1 are finished and tested.

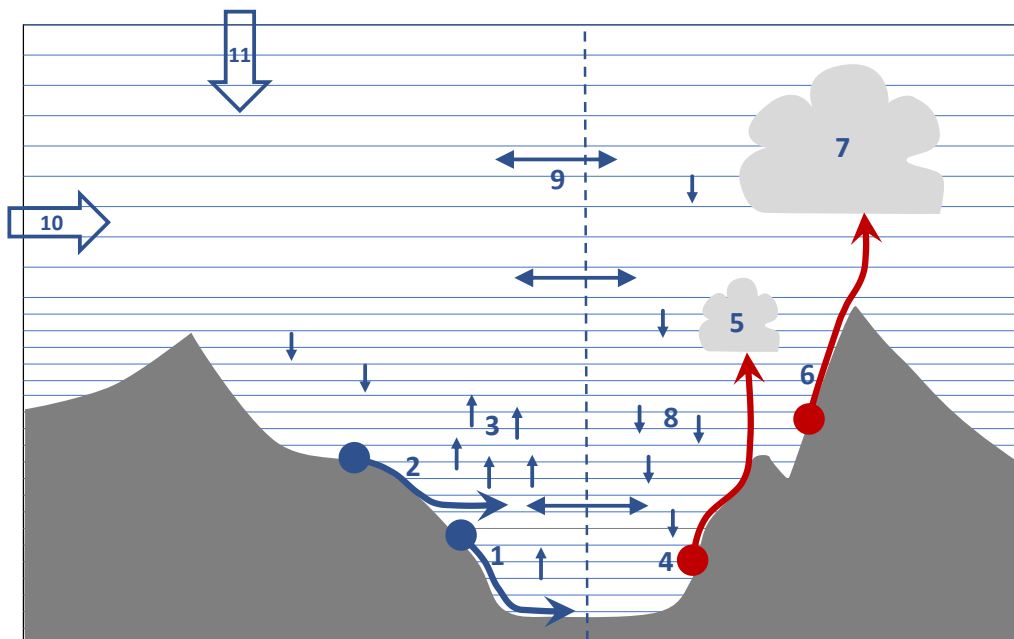


**Figure 1: The basic mechanisms implemented in AlpTherm\_2. The items 1 to 11 are explained below**

Explanations to figure 1: The thin horizontal lines are indicating the vertical levels with a thickness of 50 m below 3'000 m AMSL, followed by 100 m spacing up to 5'000 m, 200 m up to 10'000 m, and 500 up to 16 km (flexible, i.e. can be re-defined in the parameter file). The dotted vertical line is indicating a cell-boundary (symbolically, in the model this spacing is 1 km (scalable up to 5 km), i.e. on the scale of the figure there would be more of these aggregating 'cells'). (1) is depicting a cooled pocket of air sinking into the lowest cell. (2) is another katabatic movement, finding its equilibrium level (virtual potential temperature) above the valley-bottom. (3) is showing the resulting lifting in the column of cells when mass is added below. (4) is a heated pocket of air on the sunny slope, following the slope to some 'release point', then generating a cumulus (5) with a cloud base that is corresponding to the moisture in the rising pocket of air. (6) is another heated pocket of air with a higher origin, leading to a higher cloud base of (7). (8) is the resulting subsidence within the column of cells when air is removed below by upslope winds and thermals. (9) is symbolising the horizontal exchange between the cells, following the pressure differences between the cells. (10) and (11) are indicating the external forcing by the horizontal wind and large-scale subsidence or lifting. All these processes are updated every 10 minutes (interpolated within the hourly GFS-data for the external forcing).

More details (not shown in the figure): The incoming shortwave radiation ('sunshine') is calculated directly from an astronomical formula and the orientation of the 100-m-surface-pixels. It is reduced according to the net incoming radiation by upper-level clouds from the GFS-grid ( $0.25^\circ$  lat/long, interpolated to the cells). The backscatter is then calculated using the albedo from recent satellite imagery (MODIS Terra or Aqua with about 250 m resolution). The outgoing long-wave-radiation (terrestrial infra-red) is calculated using the estimate of surface temperatures and adjusted to the average value in GFS. Similarly, the incoming long-wave-radiation is taken from GFS as the averages on the GFS-grid, but downscaled using the altitude-dependence found by linear regression within the GGS grid. Similar downscaling is done for the fraction of latent heat. All these inputs could also be taken from a LAM such as COSMO. However, at this stage, free access to data had priority. The same is true for the topography and the surface properties, where using SRTM and MODID imagery was a compromise as well.

## Results

The figures 2 and 3 are showing two results after applying the algorithm to a region of 200 km (west-east) times 150 km (south-north) for the 1<sup>st</sup> of April 2021 with mainly clear-sky-conditions and still snow down to about 1500 m AMSL. Figure 2 is showing the initial lifting or sinking near the surface (items 1 and 2 in figure 1), i.e. the mass of air [values in  $10^6$  kg or Gg per pixel] that was moved to the next higher or lower 50-m-level during the last 10 minutes before 09 UTC (11 LT = CEST). Figure 2 is showing the aggregation of all these movements as changing column masses between 11:50 and 12:00 UTC. Yellow to red pixels (cell size of 1 km) are showing increasing mass columns, while light to dark blue is showing loss of mass according to the mechanisms summarised in figure 1.

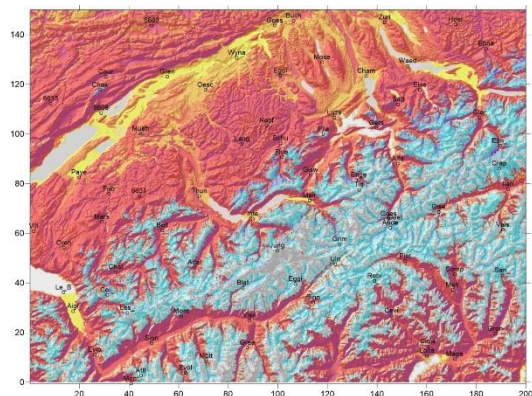


**Figure 2: Vertical mass flux [Gg] on the level of the surface pixels ( $100 \times 100 \text{ m}^2$ ) within a 10-minute timestep. See more explanations in the text.**

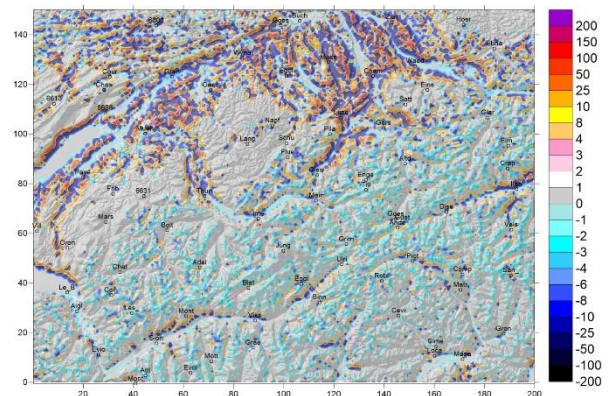


**Figure 3: Loss and gain of mass [Gg] in the columns of cells ( $1 \times 1 \text{ km}^2$ ). See more explanations in the text.**

It is obvious that the mass flux displayed in figure 2 can be translated to slope-winds when applying a 'typical thickness' for these flows. Similarly, figure 3 is indicating those expositions where most mass converged over slopes and crests during the afternoon regime. Earlier, when cooling is still dominating, this picture is inverted, i.e. the dominating convergence is then by the cold-air-flow into the valleys. In a next step, these horizontal mass differences (causing

altitude-dependent pressure differences) will be relaxed by local horizontal winds (2<sup>nd</sup> item listed on the right-hand-side in table 1) that can be superposed to a wind field from a GCM or LAM. However, this is not trivial, since some of the processes represented in AlpTherm\_2 are already included in the wind-field of a LAM.

Not shown here yet are those results that are directly quantifying the thermal lift on slopes and in released thermals, and the cumuli generated when condensation occurs. This is because this last step of the algorithm needs to be checked and calibrated first by comparing with observations. This last version of the algorithm was just finished one day before the deadline for this extended abstract. Hoping to present more during the conference.

### Discussion and Outlook

The present version of the post-processing algorithm AlpTherm\_2 has shown that thermal convection during a diurnal cycle on a scale of 100 m near the surface can be estimated with the computing power of a notebook computer. The already short runtime of 10 minutes for the example shown here (for the duration 03 to 18 UTC) might further be reduced by using a faster 'gaming PC' and by optimising some time-consuming parts, which was not at all a priority until now.

There is still a long way to go when AlpTherm\_2 should become operational either within a meteorological service, or for user groups such as gliding competitions, clubs or by individual enthusiasts. However, discussions about applications should be possible during winter 2021/22. Some planned improvements as listed in table 1 and first validations will be done during the next few months.

Since the performance of GCMs has reached a level, where the soaring potential can be assessed directly from these products [10], AlpTherm\_2 might not be a necessity for planning long-distance flights by glider pilots. However, paragliders are seeking more detailed information that can be generated using this algorithm.

This presentation will hopefully trigger discussions about possible collaborations for the use and dissemination.

### References

- [1] Liechti, O. and Neining, B. (1994). ALPTHERM - A PC based model for atmospheric convection over complex topography. Technical Soaring, Vol. 18, No. 3, July 1994, pp. 73. (*ALPTHERM\_1994\_reprint\_2005.pdf* in [11]).
- [2] Liechti, O. (2012). A readers comment in TS 36/4: (*TS\_36\_4\_Readers\_Comment.pdf* in [11]).
- [3] pc\_met selfbriefing system from the DWD: <https://www.flugwetter.de> (annual charges apply).
- [4] <https://www.ncdc.noaa.gov/data-access/model-data/model-datasets/global-forecast-system-gfs>
- [5] Peter Bauer, Alan Thorpe, Gilbert Brunet, 2015: The quiet revolution of numerical weather prediction. Nature, Vol. 525, doi:10.1038/nature14956. <https://www.nature.com/articles/nature14956>, plus a copy in [11]
- [6] <https://www.meteoswiss.admin.ch/home/measurement-and-forecasting-systems/warning-and-forecasting-systems/cosmo-forecasting-system.html>
- [7] <https://www.windy.com>
- [8] S. Westerhuis, O. Fuhrer, R. Bhattacharya, J. Schmidli, Ch. Bretherton, 2020: Effects of terrain-following vertical coordinates on simulations of stratus clouds in numerical weather prediction models. Quarterly Journal of the Royal Meteorological Society, DOI: 10.1002/qj.3907.
- [9] <https://www.meteo-shv.ch/home/footer/news/paraglidable.html>
- [10] B. Neining and A.J. de Orleans-Borbon, 2021: A climatology of soaring conditions in Eurasia, in this conference.
- [11] Electronic supplements in <https://drive.switch.ch/index.php/s/TpJYwCqoVVE2KQ> with PW 'OSTIV\_2021'.

## On the influence of moisture on the strength of thermals:

### A large-eddy simulation case study

Oliver Maas and Dieter Etling

*Leibniz University Hannover, Institute for Meteorology and Climatology, Germany, maas@muk.uni-hannover.de*

**Abstract:** Thermals in the atmosphere are driven by buoyancy forces due to density differences between air parcels and their environment (Archimedes principle). Here we present some estimates on the contribution of moisture on the strength of thermals based on numerical simulations with a large-eddy-simulation model (LES).

**Keywords:** thermals, moisture, large-eddy simulation.

#### Introduction

There has been some debate in recent years within the soaring community on the contribution of atmospheric moisture content on thermals, especially if moisture might be even the dominating factor on thermal strength. The arguments are based mainly on measurements of temperature and moisture (in terms of specific humidity) inside and outside thermals obtained by glider equipped with instruments. But as the temperature and moisture differences between thermals and their environment are quite small, this question has not been answered by measurements without doubt. Here we present a complementary approach based on numerical simulations for a field of thermals in the atmospheric boundary layer as heated from below. In order to quantify the effect of the moisture content of rising thermals on the vertical velocity (updrafts), vertical profiles of temperature and specific humidity have been varied systematically by applying different values for latent heat flux (moisture flux) and sensible heat flux (temperature flux) as forcing at the earth surface. In order to quantify the contribution of moisture on the strength of thermals, various data on temperature, specific humidity and vertical velocity have been extracted from the 3-D simulations.

#### The influence of moisture in Archimedes principle

The vertical acceleration (A) of air parcels in the atmosphere is based on Archimedes principle which can be formally expressed by the buoyancy force (B) as:

$$B = \rho_p A = -g(\rho_p - \rho_e), \quad (1)$$

where  $g$  is gravity ( $9.81 \text{ m/s}^2$ ),  $\rho_p$  the density of an air parcel and  $\rho_e$  the density of its environment.  $A = dw/dt$ , where  $w$  is the vertical velocity and  $t$  is time. The air density  $\rho$  is defined by air pressure  $p$ , air temperature  $T$  and moisture content (specific humidity  $q$ ) through the ideal gas law:

$$p = R\rho(1 + 0.6q)T, \quad (2)$$

where  $R$  is the universal gas constant. Inserting (2) in (1), the vertical acceleration can be expressed by air temperature  $T$  and specific humidity  $q$  approximately by:

$$A = g \frac{(T_p - T_e)}{T_e} + g0.6(q_p - q_e) = A_t + A_q. \quad (3)$$

It is common to combine the last two terms in (2) to form the so-called *virtual temperature*  $T_v$ :

$$T_v = T(1 + 0.6q). \quad (4)$$

By using (4), the vertical acceleration  $A$  provided by buoyancy forces (3) can also be written as:

$$A = g \frac{(T_{vp} - T_{ve})}{T_{ve}}. \quad (5)$$

In a dry atmosphere ( $q = 0$ ), thermals are driven by the temperature differences between the thermal and its environment, where updrafts are generated for  $T_p > T_e$ . In a moist atmosphere ( $q > 0$ ), moisture differences between thermals and their environment provide an additional acceleration, where updrafts are supported for  $q_p > q_e$ , i.e. air parcels are moister than their environment. To provide an example of the magnitudes of the vertical acceleration due

to temperature differences ( $A_t$ ) and due to moisture differences ( $A_q$ ) let us assume typical values as found in moist thermals (see Figure 17):  $T_p - T_e = 0.2$  K,  $q_p - q_e = 0.2$  g/kg = 0.0002. Then we have:  $A_t = 0.007$  m<sup>2</sup>/s,  $A_q = 0.0012$  m<sup>2</sup>/s and  $A_q/A = 0.15 = 15\%$ . Hence moisture (specific humidity) contributes to the strength of thermals but is not the dominating factor.

It is also common to introduce a new temperature measure called “potential temperature”, designated by the Greek symbol  $\theta$  (theta), as this is a conserved quantity for adiabatic processes. Hence the vertical stratification in the atmosphere can be easily identified by profiles of  $\theta$ , as  $\theta(z)$  is constant for adiabatic (neutral) stratification and decreases with height in unstable conditions. Examples for profiles of potential temperature  $\theta$  and virtual potential temperature  $\theta_v$  are displayed in Figure 1.

### Numerical Setup

The numerical simulations were conducted with the **Parallelized Large-eddy simulation Model PALM**, developed at the Leibniz University Hannover, Germany (Maronga et al., 2020). Classical simulation methods, that are e.g. used for the numerical weather forecast, only simulate the mean flow, such as the mean wind speed and mean temperature profile. Large-eddy simulation (LES), however, is a simulation method that explicitly resolves the largest eddies (turbulent motions) of the turbulent lower atmosphere (the boundary layer). Hence, the properties of updrafts and downdrafts can be investigated.

We performed five simulations with different Bowen ratios  $Bo$  and different humidity differences  $\Delta q$  between the boundary layer (BL) and the overlying free atmosphere (FA), see **Table 1**. The thermals are driven by a typical daytime surface heat flux of  $Q = 200$  W/m<sup>2</sup>, which is the sum of the sensible heat flux  $Q_s$  and the latent heat flux  $Q_L$ . A high Bowen ratio  $Bo = Q_s/Q_L$  occurs if the surface is dry and most of the heat flux is used to heat up the near-surface air. A low Bowen ratio represents a wet surface and most of the heat flux is used for evaporation, so that the humidity of the near-surface air increases. The humidity difference between the BL and the FA is varied from 0 g/kg to 11 g/kg, as can be seen in the profiles of specific humidity in **Figure 15**. The height of the thermals is limited by an inversion layer, starting at  $z = 1000$  m. The inversion height  $z_i$  increases to more than 1000 m during the simulations because the temperature in the BL increases, see **Figure 15**. The domain size in all cases is  $L_x = 8192$  m,  $L_y = 5120$  m and  $L_z = 3300$  m, so that several convection cells fit into the domain. The grid spacing is 32 m in all directions, which is enough to resolve thermals that have a typical diameter of several 100 m. The simulations ran for 2 h physical time, the profiles are averaged over the last 15 minutes and the vertical cross sections are obtained from the last time step. With this grid spacing and domain size, the simulations can be performed on a modern notebook and do not require a supercomputer. In order to keep this investigation simple, we chose temperature and humidity values in such a way that no cumulus clouds will form and we assume that there is no background wind.

### Results

**Figure 16** shows vertical cross sections of potential temperature, virtual potential temperature and specific humidity as deviations ( $\theta'$ ,  $\theta'_v$ ,  $q'$ ) from the respective horizontal mean value for the case Bo1\_dq6. Two large updrafts with a distance of about  $2.3 z_i$  can be identified. As can be seen in **Figure 16a**, these updrafts are relatively warm near the surface, but are relatively cold near the top of the BL. **Figure 16c** shows that the humidity excess of updrafts is highest at the top of the BL but it is nearly zero near the surface. The high humidity differences  $q'$  at the top of the updrafts adds buoyancy so that relatively cold updrafts (negative  $\theta'$ ) can still be positively buoyant (positive  $\theta'_v$ ). Beside the updrafts, warm and dry air is entrained from the FA into the BL (top left and right), which enhances the humidity excess but diminishes the temperature excess of updrafts.

**Figure 17a** shows vertical profiles of the mean temperature excess and the mean virtual temperature excess of all updrafts for the case Bo1\_dq6. In order to investigate only updrafts that are usable for soaring, we included only updrafts with a vertical velocity  $w > w_*$ , where  $w_* = \left(\frac{g}{T_0} z_i B_0\right)^{\frac{1}{3}}$  is the convective velocity scale, which indicates a typical updraft velocity for a given surface buoyancy flux  $B_0 = \left(w'\theta_v'\right)_0$ , surface temperature  $T_0$  and inversion height  $z_i$ . It can be seen that the temperature differences between updrafts and their environment are in general very small (only about 0.1 K). The temperature excess decreases from more than 0.2 K below 200 m to less than 0.1 K in the middle of the BL. At  $z = z_T = 941$  m (or  $0.73 z_i$ ) the temperature excess is zero. However, at that height the updrafts are still positively buoyant (have a positive virtual temperature difference  $\theta'_v$ ) due to the humidity difference between the updrafts and their environment (shown in **Figure 17b**). The buoyancy of updrafts becomes zero somewhat higher at  $z = z_B = 1106$  m (or  $0.85 z_i$ ). The humidity excess of thermals is highest at the top of the updrafts, not because they gain humidity during their ascend but rather because the surrounding air is dryer at that height due to the

entrainment of dry air from the FA. Temperature and virtual temperature differences become negative at the top of updrafts, reaching values of  $-0.3$  K.

The heights for zero temperature excess  $z_T$  and zero buoyancy  $z_B$  of updrafts for all five cases are listed in Table 1. The updrafts reach zero buoyancy at about  $0.85 z_i$ , relatively independent of the Bowen ratio  $Bo$  and the humidity difference  $\Delta q$  between BL and FA. However, the height of zero temperature excess of updrafts  $z_T$  varies significantly and can be as low as  $0.57 z_i$  for the case with  $Bo = 0.1$  (wet surface). Note that in this case the updrafts are generally weaker (indicated by a small  $w_*$ ), because most of the available surface heat flux is used for evaporation (latent heat flux), which is ineffective in generating buoyancy. A high difference between  $z_B$  and  $z_T$  is achieved for wet surfaces ( $Bo = 0.1$ ) and high humidity differences between BL and FA ( $\Delta q = 11$ ) and nearly no difference between  $z_B$  and  $z_T$  is achieved for  $\Delta q = 0$ . Hence, the contribution of humidity on the buoyancy of updrafts is only dominant, if dry air is entrained from the FA into the BL. For very dry surfaces ( $Bo = 10$ ) or a low humidity difference between BL and FA ( $\Delta q = 0$ ), humidity effects play a minor role. In this case, the temperature excess of updrafts vanishes relatively late at  $z_T = 0.80 z_i$  ( $Bo = 10$ ) or  $z_T = 0.82 z_i$  ( $\Delta q = 0$ ).

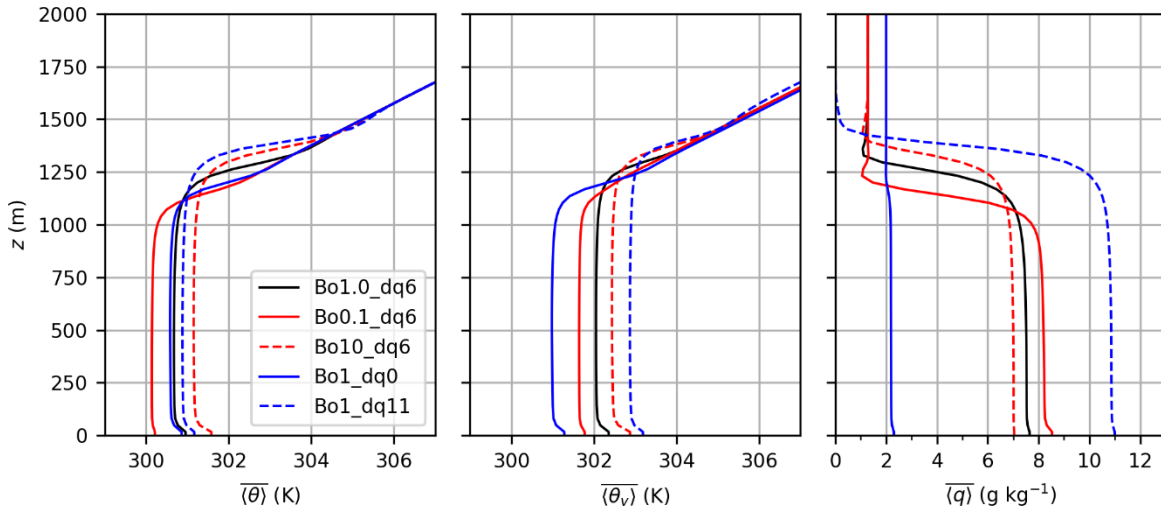


**Figure 15: Horizontal and temporal averaged profiles of potential temperature  $\theta$ , virtual potential temperature  $\theta_v$  and specific humidity  $q$  for the five cases Bo1.0\_dq6 (reference), Bo0.1\_dq6 (wet surface), Bo10\_dq6 (dry surface), Bo1\_dq0 (no humidity difference between BL and FA) and Bo1\_dq11 (high humidity difference between BL and FA).**

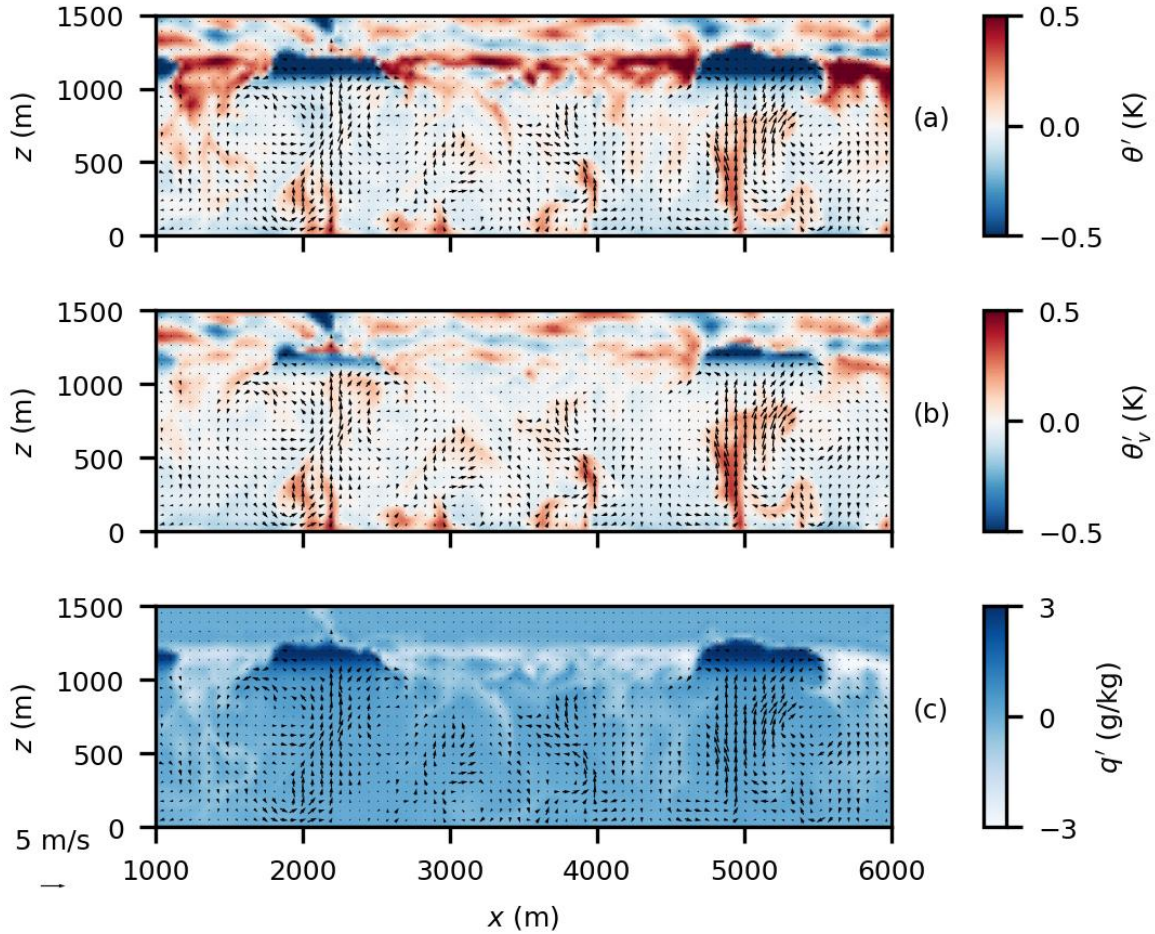


**Figure 16:** Vertical cross sections of potential temperature excess  $\theta'$  (a), virtual potential temperature excess  $\theta'_v$  (b) and specific humidity excess  $q'$  (c) for the case Bo1\_dq6. Arrows indicate flow velocity.

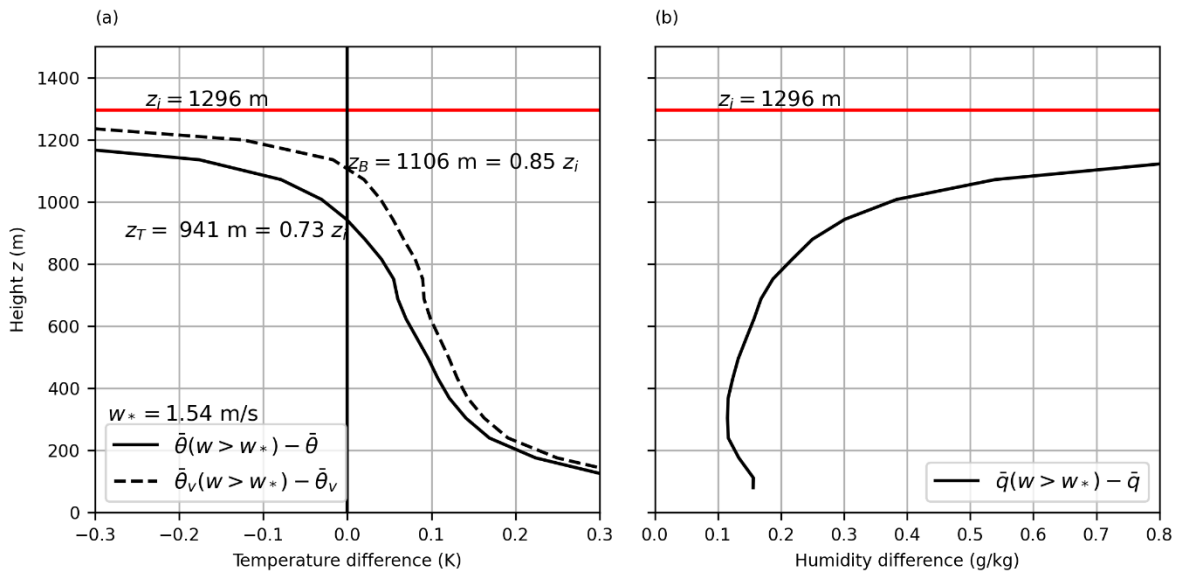


**Figure 17:** Vertical profiles of temperature excess and virtual temperature excess (a) and humidity excess (b) of all updrafts that are stronger than  $w^*$  for the case Bo1\_dq6.

**Table 1: Overview of the five simulated cases with Bowen ratio  $Bo$ , specific humidity difference between BL and FA  $\Delta q$ , typical updraft velocity  $w_*$  (convective velocity scale), inversion height  $z_i$ , height at which updrafts ( $w > w_*$ ) have zero temperature excess ( $z_T$ ) or have zero buoyancy ( $z_B$ ).**

Case	Bo	$\Delta q$ g/kg	$w_*$ m/s	$z_i$ m	$z_T$ m	$z_B$ m	$\frac{z_T}{z_i}$	$\frac{z_B}{z_i}$	$\frac{z_B - z_T}{z_i}$
Bo1_dq6	1	6	1.54	1296	941	1106	0.73	0.85	0.12
Bo0.1_dq6	0.1	6	0.99	1168	664	958	0.57	0.82	0.25
Bo10_dq6	10	6	1.87	1360	1091	1203	0.80	0.88	0.08
Bo1_dq0	1	0	1.51	1200	984	997	0.82	0.83	0.01
Bo1_dq11	1	11	1.58	1392	1014	1201	0.73	0.86	0.13

### Conclusions

With this study we showed that large-eddy simulation is a suitable method for the investigation of thermals, as the spatiotemporal properties of thermals can be extracted while the boundary conditions can be controlled and systematically changed. The results show that updrafts become neutrally buoyant at about  $0.85 z_i$ , more or less independent of Bowen ratio and humidity difference between the boundary layer and the free atmosphere. However, the temperature excess of updrafts becomes zero at heights between  $0.57 z_i$  and  $0.82 z_i$ , with lower values for small Bowen ratios and high humidity differences. As humidity-driven buoyancy partly replaces temperature-driven buoyancy, humidity effects do not lead to stronger thermals but rather lead to colder thermals, for a given surface buoyancy flux. For a given surface heat flux, the strongest updrafts are achieved at high Bowen ratios (dry surfaces). The entrainment of dry air from the free atmosphere into the boundary layer significantly affects the importance of humidity in the upper part of updrafts. Interesting research topics for the future could be to study the effects of clouds, vegetation or wind on the structure of thermals.

### References

Maronga, B. et al., 2020: Overview of the PALM model system 6.0, *Geoscientific Model Development*, 13, 1335–1372, <https://doi.org/10.5194/gmd-13-1335-2020>, <https://gmd.copernicus.org/articles/13/1335/2020/>, 2020.

## Examination of the Microburst Incident in Istanbul, July 2017

Ali Osman MUT<sup>1</sup>, Fatma Betül DEMİR<sup>1</sup>, Hande TEMUR<sup>1</sup>, Zafer ASLAN<sup>2</sup>

<sup>1</sup>Istanbul Technical University, Graduate Institution, Maslak, Istanbul-TURKEY

<sup>2</sup> Istanbul Aydın University, Florya, Istanbul-TURKEY

[muta@itu.edu.tr](mailto:muta@itu.edu.tr), [demirfa@itu.edu.tr](mailto:demirfa@itu.edu.tr), [handetemur@hotmail.com](mailto:handetemur@hotmail.com), [zaferaslan@aydin.edu.tr](mailto:zaferaslan@aydin.edu.tr)

**Abstract:** Microburst and hail storms are severe meteorological events that negatively affect people, living things and life in many ways. Hail, rains, severe storms cause various losses of life and property depending on their duration, severity and size. The microburst with hail that occurred with the storm on 27 July 2017 caused a lot of material damage in Istanbul. In this study, synoptic analyses have been done, skew t diagrams, the meteorological parameters of the event day were evaluated and analyzed. WRF model was utilized to simulate the downburst event occurred in Istanbul. For simulation, European Centre for Medium-Range Weather Forecasts (ECMWF), ERA5 data set which is a reanalysis data at 0.25° horizontal resolution from 1979 to near present was used as initial condition. Simulation is done with two domains with different horizontal solution of 27 km, 9 km for two different microphysics schemes. The WRF outputs of meteorological variables causing convective movements were evaluated. In order to perform the statistical analysis of the downburst event, WRF, ECMWF model outputs will be compared with the measurement data and will be used to create linear models according to error rates. Statistical mode will be extracted using ARMA, ARIMA and linear regression methods. Model performances will be compared according to the error rates of the models obtained in this process. The models will be used to predict characteristic parameters such as wind intensity of the downburst event using measurement and numerical weather forecast model outputs. In addition, in the case of convective motion, indices such as the Richardson number will be calculated.

**Keywords:** Microburst, hail, CB, convective, downburst, outburst, downdraft, WRF, statistical analysis, ERA5, ARMA, ARIMA, Linear Regression

### Introduction

Microbursts are a well-known atmospheric intense phenomenon, they have been the subject of several observational and numerical studies since the pioneering work of Fujita [1978] (Ferrero et al, 2013). Microbursts are short-lived intense downdrafts that are forced by thermodynamic cooling and hydrometeor frictional drag produced by cumulonimbus clouds (Leigh and John, 1999). They have localized intense downdraft which descends to the ground can result in a violent divergent outburst wind near surface (Zhang, 2013).

In this study, the microburst phenomenon that took place in Istanbul on July 27, 2017 was analyzed. Around 18:00, the dark clouds covering the city fell to the ground first as hail and then as rain. Approximately 20 minutes of hail and rain damaged hundreds of homes, businesses and vehicles. Eurasia Tunnel was closed, planes could not take off from Atatürk Airport, and sea transportation was paralyzed. Many people were injured. It was reported that 30-40 kilograms of rainfall were recorded in 20 minutes with the storm and hail.

### Methodology

Synoptic charts provided from the Wetter3 website at 1200 UTC to investigate the structure of synoptic scale weather systems for the purpose of examining the downburst incident that occurred in Istanbul on 27<sup>th</sup> July 2017. In addition skew-t diagram, satellite view and radar images evaluated to understand what condition caused the microburst with hail in Istanbul.

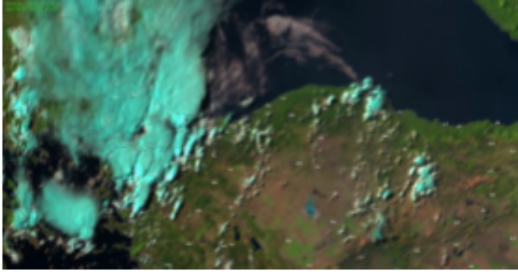


**Figure 1.** *Natural Colour RGB satellite view at 1500UTC, 27th July 2017*

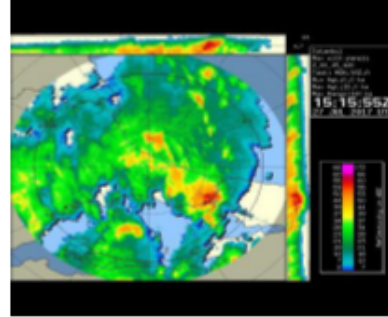


**Figure 2:** *Radar view 27 Jul, 17 1515 UTC*

The boundary conditions which generate the WRF model is downloaded from the European Centre for Medium-Range Weather Forecasts (ECMWF), ERA5 data set which is a reanalysis data at 0.25 horizontal resolutions from 1979 to near present. For the simulations ERA5 data sets (pressure level data, surface level data, and sea surface temperature data) are downloaded from Climate Data Store (CDS) for the case date 27 July 2017 by six hour time steps. Simulation is done between 09Z to 21Z with an interval of 15 minutes. The area affected by the downburst incident is defined with three domains with different horizontal resolution of 9 km, 3 km and 1 km from outer domain to inner domain. Parameterization is an important factor to simulate a selected event and improve the model performance of the model. To simulate the downburst event in presented study, Yonsei University, Kain-Fritsch and Milbrandt schemes are selected as PBL physics, Cumulus physics and Micro physics respectively. Domains prepared for the simulation are shown in below figure.

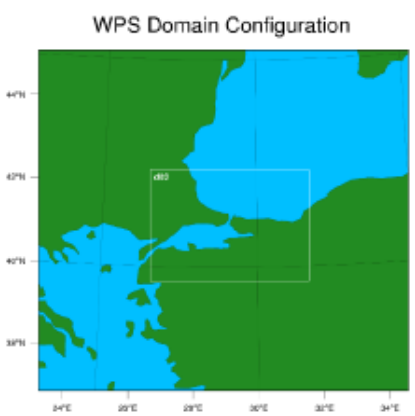


**Figure 3: Domain Configuration**

Due to the chaotic nature of the atmosphere, the estimation of wind parameters is quite difficult. However, numerical weather forecast models can give very successful results in determining these parameters. However, due to the initial sensitivity and dynamic nature of the models, the determination of initial conditions and parameterization methods is of great importance. The main purpose of using numerical weather prediction models in the study to be carried out is that the sounding data is obtained much earlier than the time of the event. Therefore, the ability to represent the event has decreased considerably. However, erroneous measurements due to the effect of the sounding balloon downburst event or the decrease in representation due to the effect of strong winds are separate causes. At this stage, using numerical weather forecast models provides a great advantage. However, since it is not possible for these models to give as good results as the measurements, the most effective data will be used as input in the statistical model after the error rates are compared with the surface measurement data and sounding data.

## Results

A microburst with hail occurred on 27<sup>th</sup> July 2017, in Istanbul. The extreme rains that occurred with the storm, hail and maximum wind values exceeding 50 knots affected life negatively. According to the synoptic analysis, a low pressure system coming from the west of Turkey and the convergence line at 500 hPa came over Istanbul and increased the convective movements. The 75% humidity at 700 hPa strengthened the unstable atmosphere conditions. Satellite and radar images show high clouds and high cloud content. This weather condition caused that severe weather phenomenon.

To understand the weather condition and its physics and evaluate meteorological conditions WRF model, statistical analyses and linear model were conducted.

WRF model results, statistical analysis and comparing both WRF and Linear model results will be forwarded in the further report.

## References

- Atlas D., Ulbrich C.W., Williams C.R., 2004. Physical Origin of a Wet Microburst, Observations and Theory. *J Atmos Sci*, 61, 1186-1196
- Chay M.T., Albermani F., Wilson R., 2005. Numerical and analytical simulation of downburst wind loads. *Engineering Structures*. 28, 240-254
- Chay M.T., Letchford C.W., 2002. Pressure distributions on a cube in a simulated thunderstorm downburst, Part A: stationary downburst observations. *J. Wind Eng. and Ind. Aerodyn.* 90, 711-732.
- Choi E.C.C., 2004. Field measurement and experimental study of wind speed profile during thunderstorms. *J. Wind Eng. and Ind. Aerodyn.* 92, 275-290
- Das K.K., Ghosh A.K., Sinhamahapatra K.P., 2010. Investigation of the axisymmetric microburst flow field. *J. Wind and Eng.* 7, 1-15.
- Ferrero E., Mortarini L., Manfrin M., Solari M. and Forza R., 2013. Physical simulation of atmospheric microbursts. *Journal of Geophysical Research: Atmospheres*, 1.1002/2013JD021243
- Vasiloff S.V., Howard K.W., 2008. Investigation of a Severe Downburst Storm near Phoenix, Arizona, as Seen by a Mobile Doppler Radar and the KIWA WSR-88D. *Weather and Forecasting* 24: 856-867.
- Toker E., Ezber Y., Şen Ö.L. (2021). Numerical simulation and sensitivity study of a severe hailstorm over Istanbul. *Atmospheric Research*, 250 (2021) 105373.
- Yair Y., Lynn B., Yaffe M., Ziv B., Shpund J. (2021). Observations and numerical simulations of the October 25th, 2015 supercell thunderstorm over Central Israel. *Atmospheric Research*, 247 (2021) 105165.
- Cao Y. (2020). Modelling and Simulation of Microburst. *Proceedings of the 2020 International Conference on Aviation Safety and Information Technology*. 363-369, 2020.

## E-ROP electric and rotary engined hybrid plane

Dipl. Ing. Stefan Senger, Prof. Dr. Ing. Rainer Klein

*Advantec GmbH, am Technologiezentrum, 86159 Augsburg and Duale Hochschule Baden-Württemberg (DHBW) Mosbach*

### Abstract:

Electric flight efforts produced significantly more development projects in the last 10 years, than in the beginning of electric flight. These developments affect both, manned and unmanned systems. All developments so far have a major problem, that is the energy density of the electrical storage device, that the aircraft has to carry. The project deals with the optimization of the design of a hybrid drive system consisting of batteries and a range extender for long-distance capability.

**Keywords:** electric flight, hybrid propulsion system, battery development, range-extender

### Introduction

In order to be able to operate an electric aircraft in a meaningful way, the designer must keep an eye on two parameters. 1. a very good aerodynamics and 2. the lowest possible flight mass of the overall system. The very good aerodynamics are necessary in order to achieve the lowest possible energy consumption in cross-country flights. It is imperative, that the flight mass is as low as possible, as every kilo of flight mass costs additional energy, lifting to cruising altitude. These two requirements basically contradict each other in the case of electric drives in aircraft, because in order to be able to fly as far as possible, you currently have to carry a lot of battery weight, which is counter-productive in reaching cruising altitude. Hybrid-electric drives can represent a way out of this misery, since the energy required for long journeys can be taken from a fossil fuel with a multiple of energy density.

### Methodology

In order to prove, that long distance flights can be carried out with a hybrid system, an already existing airframe was used, which has excellent aerodynamics. This cell comes from the E1 -Antares aircraft manufactured by Lange Aviation. The E1 Antares is a well-known electric motor glider with a purely electric range of about 170km with its batteries in the wing. In order to significantly increase the range with a hybrid drive, it was necessary to almost completely redesign the configuration of the aircraft. As before, the batteries are also housed in the wing. However, in cooperation with Prof. Rainer Klein, a battery system with a higher energy density was developed from LI-cells with the format 18650. This battery fits into the existing receptacles in the wing. On the fuselage side, the configuration had to be changed, so that the previous folding engine in the back compartment was replaced by a “front electric sustainer system<sup>3</sup>” in the nose. The space in the rear is thus free for the installation of a range extender with a maximum continuous electrical output of 12 KW. The range extender consists of a Wankel-generator-unit with a controlled inverter, that puts the output voltage on the high-voltage rail of the drive battery.

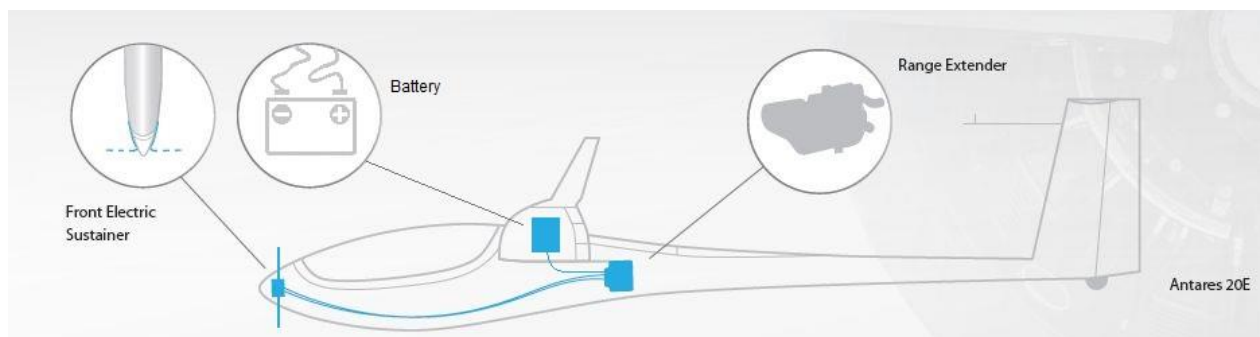


Figure 1: Configuration of electric propulsion system of E-ROP motorglider

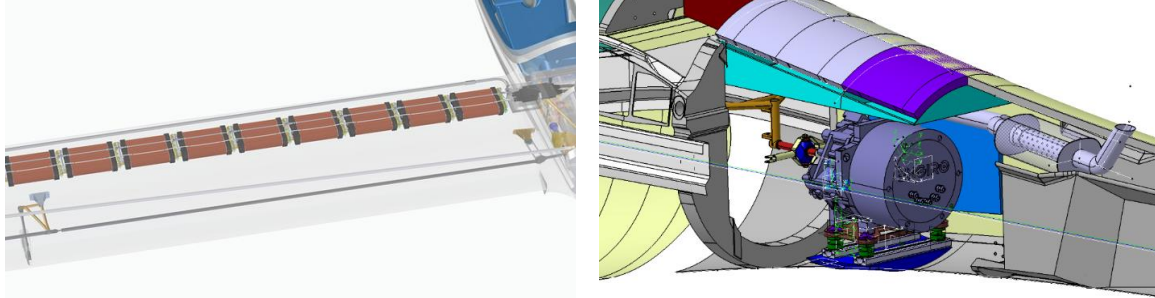


Figure 2<sup>1</sup> and 3: placement of battery and placement of range extender in the back compartment

**Result**

The current status of the project is, that the test vehicle has been upgraded to such an extent, that the first flight will take place in summer 2021. The drive train is already installed without integrating the range extender. Instead, there is a battery with approx. 4 KWh in the rear with which gives a range of approx. 80km. As soon as the battery development of the new wing battery is completed, it will add another 18KWh to the overall energy budget. This will then increase the range to 450km. In the last step the REX will be integrated, to widen the range up to 2000km. The last test for a thermal runaway of the battery string at DHBW, that is relevant for EASA approval is still pending. After successful completion, the integration of the battery string in the wing can be performed. To this end, Prof. Klein carried out extensive experiments on the charging and discharging behavior of various cell types. The fire behavior in the event of a thermal runaway in our module design was also examined in detail. It could be shown that there is no chain reaction within a battery module.

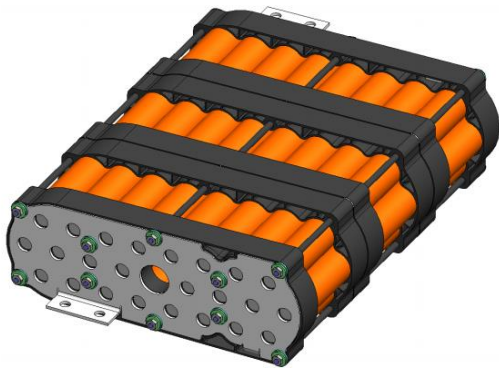


Figure 4: new Battery design with 18650 cells

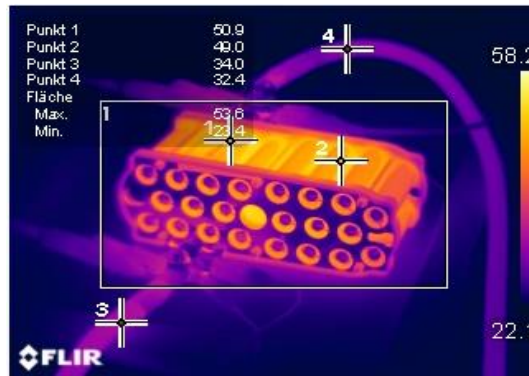


Figure 5<sup>2</sup>: Continuous Discharge of a 22p Block at 130A



Figure 6: E-ROP at “roll out” 1st of June 2021 at Unterwössen, Germany

**References**

1. Lange Aviation, Zweibrücken – [www.lange-aviation.com](http://www.lange-aviation.com),
2. Duale Hochschule Baden-Württemberg (DHBW) Mosbach, 3.LZ-Design d.o.o Logatec, Slovenia

## Experimental Verification of the *PROPWING* Propulsion System – First Tests of a Model Motor Glider

Jan Pytka<sup>1</sup>, Andrzej Rypulak<sup>1</sup>, Zbigniew Czyż<sup>1</sup>, Robert Bąbel<sup>1</sup>, Kinga Gierczak<sup>1</sup>  
Jarosław Pytka<sup>2</sup>, Rafał Kliza<sup>2</sup>, Kamil Hryć<sup>2</sup>

<sup>1</sup>*Military University of Aviation, Institute of Navigation, Dęblin, Poland*

<sup>2</sup>*Lublin University of Technology, Faculty of Mechanical Engineering, Lublin, Poland*

**Abstract:** The *PROPWING* is a custom name for a new propulsion concept, particularly beneficial for sailplanes and motor gliders. The concept assumes a number of small electric propelling systems installed in each wing of a sailplane. A complete propelling system is located inside the wing, thanks to its small dimensions and cubature. The presented system is expected to be a remedy for some problems that arises during starting a classic propelling system, that is commonly used today on motorized sailplanes. Thanks to almost immediate start of the propellers, there will be no altitude loss in the flight. Moreover, it is expected the design could improve maneuverability in flight. The paper presents results recorded by the onboard telemetry system during the test flights as well as a short pilot's report after the flight.

**Keywords:** Sailplane propulsion, *PROPWING* system, flight testing, RC test model airplane.

### Introduction

The idea of integrating a sailplane wing with a single or multiple motor – propeller systems has been presented during the 2018 OSTIV Congress in Hosin, the Czech Republic. Some question of general nature arise, how the system works and how much is the additional drag by the openings in the wings and the propellers that co-incident with the airfoil<sup>1</sup>. Since then, the authors continued research in the field of experimental verification of the proposed propulsion system. A powered sailplane model was built with the *PROPWING* system, consisting of four electric motors, two in each wing of the model. Flight tests have been carried out. The model flies and obtained promising flight results. A certain drawback was the incorrectly selected propellers, while commercially available ones were used.

The aim of this study was flight testing of the *PROPWING* concept using a RC motor glider.

### Methodology

A radio controlled model airplane was used for flight tests. It was a 1400mm motor glider with electric drive with a pushing propeller. For the purpose of the present study, in order to compare the model's flight performance with the *PROPWING* system and the basic propulsion system, four *PROPWING* units were installed, two in the right and left wing. The original propulsion system with a central engine with a pusher propeller remained in the model, while during tests of the *PROPWING* system, this propeller was disassembled. Four miniature electric brushless motors were used to drive the version with the *PROPWING* system. Openings for engines and propellers were made in the rear part of the wing profile so as to interfere with the profile as little as possible and that none of the elements protrudes beyond the profile outline. The spacing between each hole was 50mm. In the prototype model airplane, no open-and-close mechanisms were installed in the openings in wings. Figures 1 and 2 show one wing of the test model aircraft together with in-wing electric motors and propellers. Two-blade propellers of 3" diameter and a constant pitch of 2,5" were used.

The onboard instrumentation system was developed and installed in the model, its task was to measure flight parameters and send them to the ground, to the operator's station. The instrumentation consisted of the following components and systems:

- miniature autopilot system
- GPS receiver
- barometer sensor for altitude measurement;
- static and dynamic pressure sensors;
- inertial navigation system sensors: accelerometers and gyroscopes;
- a radio telemetry system.

The instrumentation was a miniature, low weight system since the test model was a relative small and light. Integration of the instrumentation was a challenge due to small space in the fuselage of the model airplane. Figure 3

includes details of the on-board instrumentation system used in the test model airplane. Figure 2 shows the test model with the PROPWING system, during a test flight.

The flight tests were carried out twice. The first time without using a speed sensor in relation to the incoming air streams AS and the second time using a sensor. The results of the first tests turned out to be unreliable due to the flight of the model at an unstable speed. The second time a constant AS speed of 10 m/s was set for the test. Figure 4 shows the test model airplane in flight and flight trajectories are depicted in Figure 5.



Figure 1. One wing of the RC model with two PROPWING units

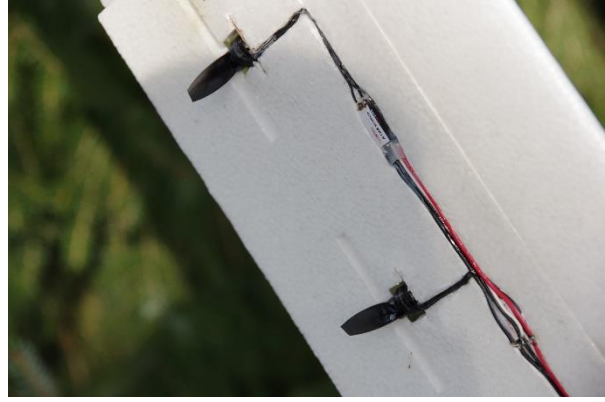


Figure 2. Details of the PROPWING units in test model's wing

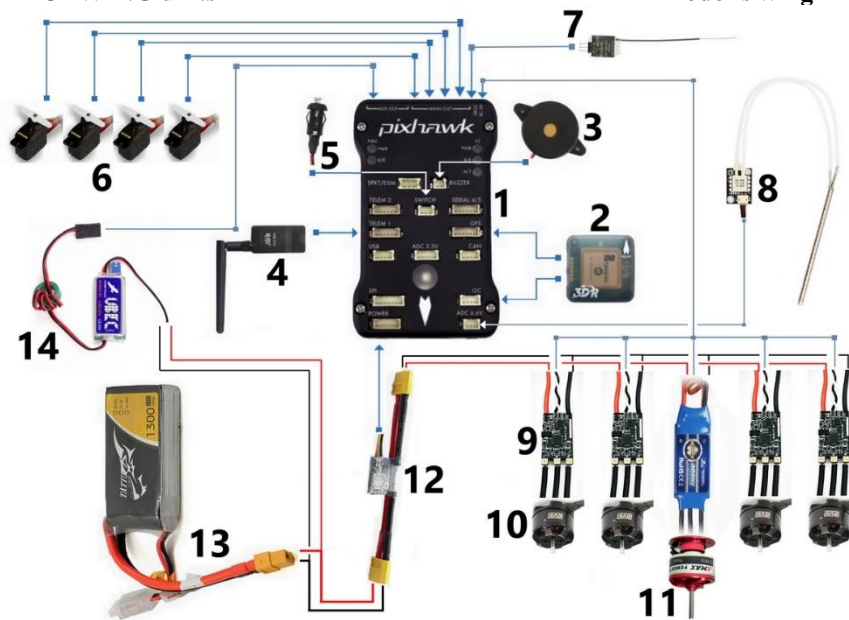


Figure 3. Instrumentation of the test model airplane. 1. Pixhawk autopilot 2. GPS module and external compass 3. Buzzer informing about autopilot status 4. Telemetry module 5. Emergency button arming the motors 6. Servos (4 pieces) 7. RC receiver 8. AS speed sensor and Prandtl tube 9. ESC regulators controlling the motors in the wings (4 pieces) 10. Brushless motors installed in the wings (4 pieces) 11. Main drive motor with ESC regulator 12. Voltage and current sensor 13. LiPo 3S 1300mAh 75C battery 14. BEC 5V 3A module



**Figure 4. The test model airplane in flight**



**Figure 5. Trajectories of the test flights**

### Results

Four parameters are of interest: air data – flight altitude, airspeed and rate of climb as well as supply current value<sup>2</sup>. They are discussed below.

Analyzing the graph in Figure 6, it can be seen that the speed of the research model during the study oscillated within the 10m / s limit, as it was specified in the pre-flight mission parameters. The initial increase in speed was the result of flying the model from its current position to the starting point of the mission.

As it can be seen from the graph in Figure 7, the altitude was for most of the test flight approx. 100m above the start level. Focusing on the stage of increasing the height autonomously, it can be seen that the model achieved a 35m altitude in 20s, which gives a climb speed of 1.75m/s .

The climb rate was determined by means of the GPS sensor. The graph in Figure 8 shows that the maximum climb rate during the test flight was 5,12 m/s. For most of the flight, this parameter did not exceed 2.5 m/s. The average value in this range is 1.63m/s, which is close to 1.75m/s measured with a barometric sensor.

The power consumption by the PROPWING system (Figure 9) depended largely on the maneuver performed by the model. However, current consumption by the original propulsion system of the model has been included in Figure 10. It is visible, the values are considerably lower than those for the PROPWING propulsion system.

According to the test pilot report, a lower airspeed of the test model airplane was found in the *PROPWING* propulsion configuration at the same throttle stick setting compared to a classic propulsion system. The model had sufficiently large thrust, however, to maintain the airspeed needed to obtain the appropriate lift force required more power. The test model airplane retained its longitudinal and transverse stability properties in both propulsion configurations. During test flights with the propulsion system installed in the wings, the rudder and the ailerons proved slightly less effective. An important issue was the high level of high-frequency noise generated by 4 drive motors compared to the classic propulsion system.

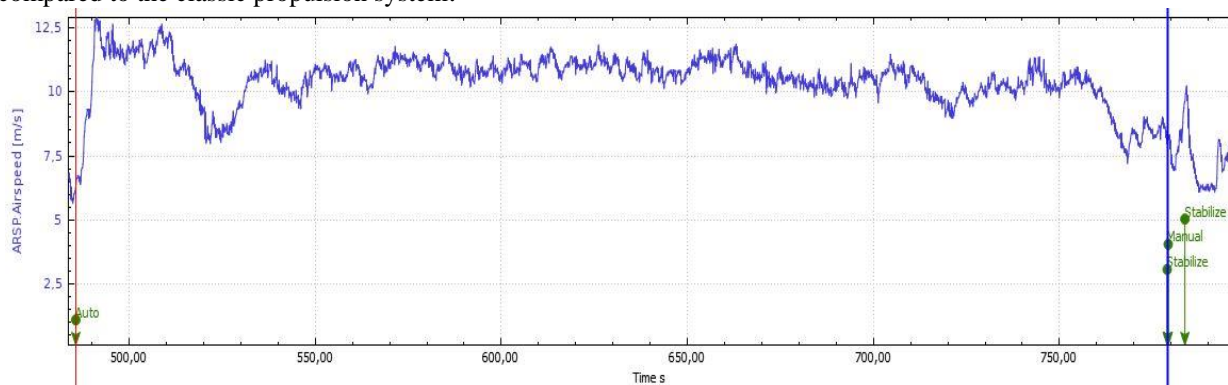


**Figure 6. Airspeed measured during the test flight**

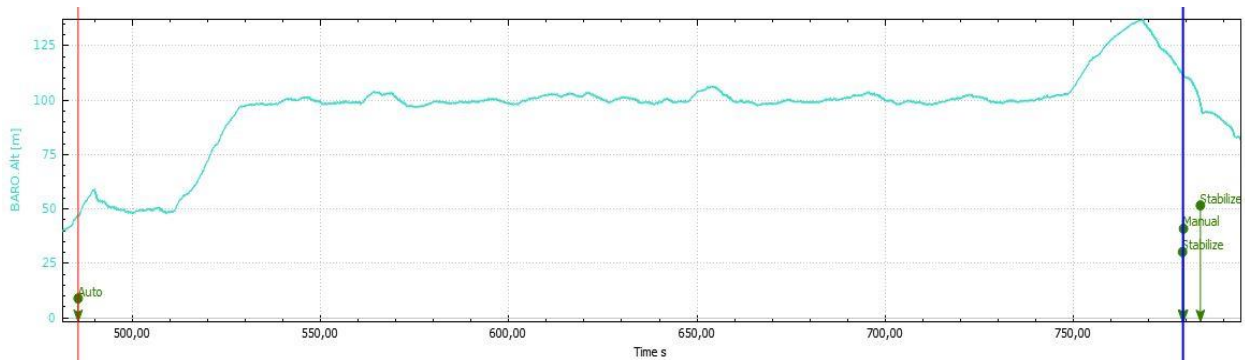


Figure 7. Flight altitude vesus time of the test flight

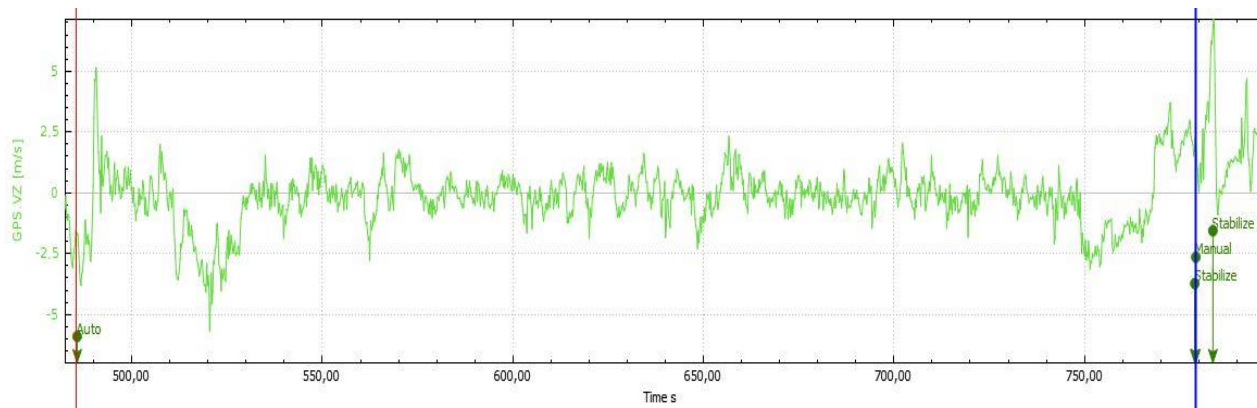


Figure 8. Climb rate during the test flight

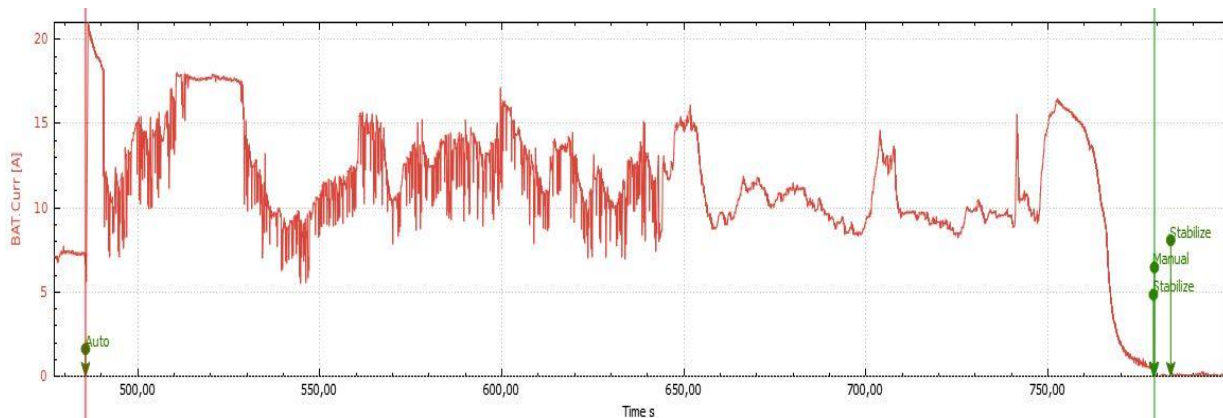


Figure 9. Current consumption by four *PROPWING* units during the test flight

### References

- <sup>1</sup>Pytka, J., Gnapowski, E., Rypulak A., Kasprzak, P. and Pytka, J “Sailplane wing integrated with a motor – propeller system,” Proc. XXXIV OSTIV Congress, Hosin, Czech Republic, July 2018.
- <sup>2</sup> Pytka J. A., Rypulak A., Michałowska J., Pytka J.D., Błażejczak D., Gnapowski E., Laskowski J.” Flight Testing of the *PROPWING* Airplane Propulsion Concept.” 7th International Workshop on Metrology for AeroSpace (MetroAeroSpace) IEEE 2020 : proceedings / Institute of Electrical and Electronics Engineers.- Piscataway, NJ : Institute of Electrical and Electronics Engineers (IEEE), 2020.- 538 s.- ISBN 978-1-7281-6637-7, .- ISBN 978-1-7281-6636-0

## CREATeV: An Exploration of a Solar-Powered, Ultra-Long Endurance UAV

Amir Ray Ramesh<sup>1</sup>, Korbin C. Mallette<sup>1</sup>, Hyunwoo Kim<sup>1</sup>, Bill Bissonnette<sup>1</sup>, Götz Bramesfeld<sup>1</sup>

<sup>1</sup>Ryerson University, Department of Aerospace Engineering, Toronto, Canada. [kmallette@ryerson.ca](mailto:kmallette@ryerson.ca)

**Abstract:** Over the past four years, the Clean Renewable Energy Aerial Test Vehicle (CREATeV) solar-powered UAV has accumulated 23 hours of flight testing. Throughout this testing an evaluation of the solar charging system was completed. Flight test results show that, to allow for multi-day flight endurance changes to the vehicle are required. A new wing has been manufactured that results in the reduction of weight by 20%. To further increase the endurance of the aircraft, a remodeling of the propeller was completed that allows a 3~4% propulsive efficiency gain. Understanding the aircraft's propulsion efficiency and solar charging, combined with the reduction in weight, increases the theoretical endurance of the vehicle, and moves the team closer to its goal of setting the world record for the longest flight of an autonomous aircraft.

**Keywords:** Ultra-Long Endurance, Unmanned Aerial Vehicle, Solar Power, UAV Manufacturing.

### Introduction

Currently the world record for the longest autonomous flight is held by the Airbus Zephyr project at 25 days, 23 hours, and 57 minutes [1]. The CREATeV team aims to break this record using a 6.28m, 12kg, solar-powered unmanned aerial vehicle. The CREATeV vehicle, shown in Fig. 1 below, features a lightweight fibreglass and carbon fibre laminate structure, and a 96-cell solar array. To date, the original flight test vehicle (FTV) has completed a total of four test flights, the longest of which lasted 10.5 hours during November in Ontario, Canada. The following paper will provide an update on the previously published extended abstract written in 2018 [2], and will describe the ongoing efforts to minimize the structural weight of the vehicle, the efforts to improve solar energy intake during flights, and the efforts to maximize the efficiency of the propulsion system.



Figure 1. The CREATeV vehicle in flight on November 11, 2020.

### Prototype Flight Testing

The four flight tests completed with the CREATeV vehicle have a combined 23 hours of flight time. The first flights took place in 2019, without the solar array installed, and focused on validating the structural design assumptions, and tuning the control systems for future flights. In 2020, the solar array was installed and testing primarily focused on developing and testing the performance of the in-flight charging system. The most recent flight focused on performing a variety of maneuvers to generate a performance baseline, and pushed the aircraft's endurance to the limit. Unfortunately, high wind speeds, wind gusts, and the presence of thermals led to large scatter in the reduced data. Future flight tests will incorporate the suggestions in Ref. 3 to investigate the in-flight performance of the vehicle.

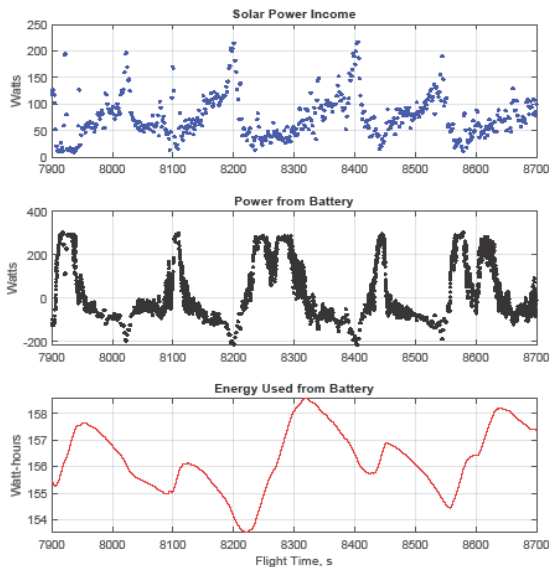
**Solar Charging**

To ensure the solar system does not suffer damage throughout ultra-long flights, the solar cells are installed directly onto the upper wing skin. To reduce the risk of damaging solder joints when the wing experiences bending, the solar cells are connected in arrays using strain relief connectors. The cells are then mated to the upper wing skin with the use of double-sided tape, and covered with clear iron-on film [4]. While this covering results in small efficiency losses, it protects the cells from debris, scratching, and provides an extra layer of adhesion to the rigid wing skin.

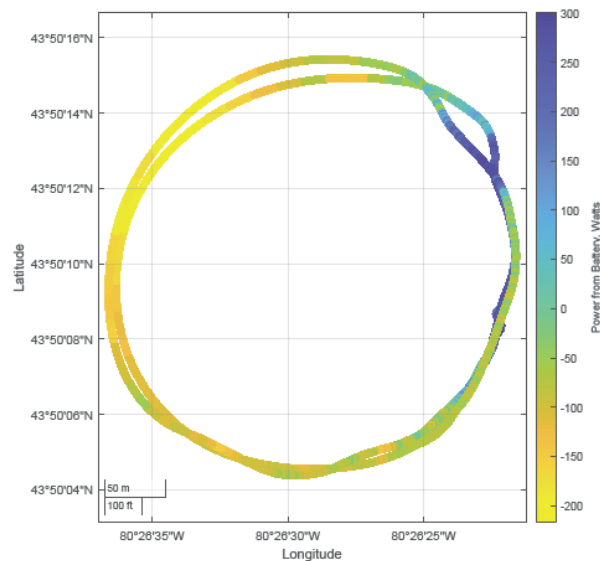
During installation of the cells to the wing skin, care is taken to avoid damage. To reduce damage caused by handling the individual cells, arrays are soldered in sets of four before being transferred to the wing on a flat tray. Finally, the cells are sealed in place with the aforementioned clear film. This installation procedure takes only a few minutes to complete per cell, thus minimizing the time the solar cells are exposed to the environment and potential damage.

Prior to recent flight testing, an in-depth analysis of the solar charging capabilities was conducted and outlined in the previous extended abstract [2]. At the time, wind conditions were not accounted for, however, data from flight testing has shown that the wind conditions during flight have caused issues with solar charging. With the geometry of the wing’s upper surface causing the solar cells to be tilted slightly aft, the solar charging is maximized when flying away from the Sun. If flying with the wind coming from the Sun’s direction, the vehicle will spend less time in ideal charging conditions.

While the solar and wind conditions were not ideal due to winter flying in Ontario, Canada, in-flight battery charging was demonstrated during both flights in 2020. Figure 2a below shows an 800 second segment of data from the flight on November 4, 2020. The top plot shows power income from the solar array, the second plot shows power drawn from the battery. Periods of negative wattage indicate charging. The third plot shows a time integral of the battery wattage, indicating the energy drawn from the battery. Improved charging capabilities can be seen when flying away from the direction of the sun, for example at times 8200 and 8400.



a. An 800 second segment.



b. Two clockwise loiter circuits.

**Figure 2. Recorded flight test data from the CREATEv vehicle showing in-flight charging of the onboard batteries. Throughout the test shown, the solar irradiance was measured as 400-600W/m<sup>2</sup> normal to the ground. Negative power from the battery indicates periods where the vehicle is charging the onboard batteries.**

Figure 2b further describes this result by displaying the battery charging, in Watts, during the completion of two clockwise loiter circuits completed by the CREATEv vehicle during the most recent flight test in November, 2020. Each location along the flight path has a corresponding latitude, longitude, time of day, roll angle, pitch angle and heading. During the two loiter circuits shown, the sun was to the southwest, and the wind was originating from the southwest. Positive values of power, shown by the blue flight path sections, indicate sections of flight where the batteries are discharging. Discharging occurs primarily when the aircraft flies towards the sun, or during instances where high throttle settings are required. The negative values, shown by the yellow flight path sections, indicate advantageous positions for the aircraft's solar charging system and result in a net power gain. In these segments, the aircraft is flying away from the Sun, which is a favorable position for the vehicle to maximize solar intake provided the shown wind direction.

Based on this observation, a model to predict the net power gains during specific loiters is being developed [5]. This model accounts for the attitude of the aircraft throughout a loiter circuit and calculates the available solar energy and power required for trimmed, turning flight. This model can then be used to determine the optimal loiter radius to maximize the net power gains, depending on the time of day and year, latitude, and wind.

### **Manufacturing and Weight Optimization**

After flight testing the vehicle in 2019 and 2020, it was determined that the vehicle's weight needed to be decreased by 20% in order to remain airborne long enough to beat the world endurance record. To do so, a new wing was designed and constructed in Spring 2021. This vehicle, constructed using the new wing, is referred to as Flight Test Vehicle 2 (FTV2), with FTV1 being the initial, flight-proven prototype.

For the manufacturing of FTV2, a lighter wing was required while maintaining similar performance to FTV1. The new wing structure not only had to meet strength and stiffness requirements for design loading and aeroelastic performance, but also ensure the solar cells mounted on the upper skin stayed intact. Defining the limit state criteria for solar panel failure was not readily determinable (i.e., deflection level that causes cracking in panels or tearing of solder joints). Therefore, an allowable stress design (ASD) approach was adopted. Maximum deformations (spanwise curvature, rotation and in-plane skin deformation) from FTV1 were calculated based on the design loads and available material properties. These were set as the limits for deformations of the new design to reduce the risk of damaging solar cells.

To accomplish this, the following design changes were made during the construction of FTV2:

- Fibre directions are re-orientated along the principal stress axis for better structural efficiency.
- A lighter carbon fibre weave is utilized for the inboard wing skin.
- The wing skin for the outboard sections are manufactured using fibreglass instead of carbon fibre.
- The spar caps have been redesigned to be incorporated directly into the skin, and make use of unidirectional carbon fibre instead of a 0/90 weave.
- The entire spar web is made using a foam core instead of Balsa wood. This provides a more consistent spar density across the entire span.
- The lower skin of the vehicle is constructed using a thinner core material, and the upper skin is constructed using a thicker core material.
- A lighter carbon fibre weave is utilized for the construction of the ribs and necessary structure.
- During construction, care is used to maintain the proper fibre to epoxy-resin ratio and to minimize the weight of the joining epoxy.
- Each of these changes allow for a leaner design which decreases the CREATEv vehicle's weight closer to the target weight for the record flight attempt.

### Propulsion and Propeller

The propulsion system of the CREATEv vehicle was also identified as a system where improvements could be made. To do so, a parametric study of existing wind tunnel data for Aero-Naut folding propellers was conducted. Previously, the aircraft utilized a 20-inch Aero-Naut CAM folding propeller, selected based on wind tunnel testing data conducted at Ryerson Applied Aerodynamics Laboratory of Flight (RAALF). Because of the need for a greater degree of CREATEv's propeller-motor optimization, research was conducted for the analysis into a scaling relation of Aero-Naut CAM folding propeller performance through parametric studies of published wind tunnel data [6].

Due to a unique geometric profile of every Aero-Naut propeller, challenges were encountered in determining proper performance scaling effects. Nevertheless, a predictable trend was observed between a propeller's pitch-to-diameter ratio ( $P/D$ ) and its performance, and a performance prediction method was established. Based on the  $P/D$  ratio, the performance of Aero-Naut CAM folding propellers was estimated using a 4<sup>th</sup> order polynomial fit. Using the operating flight conditions of the CREATEv vehicle, an iteration method was developed to calculate estimated propeller and overall propulsive efficiencies for varying propeller diameters and  $P/D$  ratios. The resulting analysis showed a theoretical optimum  $P/D$  ratio of 0.846 with propeller diameter of 17 inches.

Compared to the existing propulsion system used on the CREATEv vehicle, the increase of overall propulsive efficiency is estimated to be 3~4%. While the magnitude of the efficiency increase may seem marginal, the impact on performance gain of CREATEv's ultra-long-range capability is expected to be significant.

### Summary

Over the last four years, the CREATEv vehicle has been gradually improving towards its goal of setting the world record for the longest flight of an autonomous aircraft. Twenty-three hours of flight testing have been completed that have identified the need for a solar charging model, more accurate predictions of the power required, and improved propulsion system efficiencies. Recently, the manufacturing of a new flight test vehicle is being completed that will allow for 20% weight savings, and a 3~4% efficiency improvement is possible with a remodelled propeller. In the coming summer of 2021, multi-day flight tests are planned, along with further development of the solar charging model and the power prediction methods.

### Acknowledgements

The authors would like to thank the generous support from Ryerson University, Kenneth M. Molson Foundation, Natural Sciences and Engineering Research Council of Canada (NSERC), Record Technology and Development, Advanced Mobility Products Inc., MI Concept + Design, Columbiad Launch Services, and the communities of the York Soaring Association and the Toronto Electric Model Aviation Club. The authors would also like to thank the past and present members of the CREATEv team, including Dr. Travis Krebs, Alton Yeung, Michael Melville, Devin Barcelos, Lydia Habib and Kanwar Johal.

### References

- [1] Airbus, "Zephyr: Pioneering the Stratosphere", [Online] Available: [www.airbus.com/defence/uav/zephyr.html](http://www.airbus.com/defence/uav/zephyr.html) [Accessed 06/10/2021].
- [2] Bissonnette, B., Krebs, T., Melville, M., Bramesfeld, G., 2018: An Ultra-Long Endurance Solar Powered Unmanned Airplane, XXXIV OSTIV Congress.
- [3] Oettershagen, P., Melzer, A., Mantel, T., Rudin, K., Stastny, T., Wawrzacz, B., Hinzmann, T., Leutenegger, S., Alexis, K., Siegwart, R., 2017: Design of Small Hand-launched Solar-powered UAVs: From Concept Study to a Multi-day World Endurance Record Flight, *Journal of Field Robotics (JFR)*, vol. 34, pp. 1352-1377.
- [4] Horizon Hobby, Hangar 9, "UltraCote Lite, Transparent Clear", [Online] Available: <https://www.horizonhobby.com/product/ultracote-lite-transparent-clear/HANU964.html> [Accessed 06/15/2021]
- [5] Ramesh, A.R., Mallette, K.C., Habib, L., Bissonnette, B., Bramesfeld, G., 2021: An Evaluation of Solar Charging Optimization for Ultra-Long Endurance Flight, *Proceedings of CASI Aero 2021*.
- [6] Caccamo, M., Dantsker, O.D., Beters, R.W., Selig, M.S., 2020: Performance Testing of Aero-Naut CAM Folding Propellers, *Proceedings of the AIAA Aviation 2020 Forum*

## Laminar separation bubbles at unsteady inflow conditions – a status report

Michael Greiner, Werner Würz

*University of Stuttgart, Institute for Aerodynamics and Gas Dynamics, Germany, greiner@iag.uni-stuttgart.de*

**Abstract:** Spectra of atmospheric turbulence have been measured during cross-country flights with a sailplane. The spectra have been analyzed with respect to the different phases of the flight. As a basis for experimental and numerical investigations, specific properties have been determined, such as dissipation rates and frequencies/amplitudes of AoA-gusts. Based on this data, wind tunnel measurements on the effect of free stream turbulence upon laminar separation bubbles have been carried out. Unsteady surface pressures and boundary layer velocity profiles have been measured for different turbulence levels and AoA-gusts.

**Keywords:** free stream turbulence, laminar separation bubbles, in-flight-measurement

### Introduction

Laminar separation bubbles (LSB) play an important role in the design of natural laminar flow (NLF) airfoils. The prevention of laminar separation is a defining factor for the upper surface contour and the possible laminar run. Evidently LSB are susceptible to free stream turbulence (FST). If airfoil design could take into account the specific level of FST, advantages could be gained from the reduced size and drag penalty related to LSB. This investigation seeks to quantify the effect of increased inflow turbulence upon laminar separation bubbles.

### In-Flight Measurements: Test Setup

In soaring conditions thermals introduce turbulent energy at large scales into the convective layer of the atmosphere. This energy is passed on to smaller scales until it is dissipated into heat. Between introduction of kinetic energy and dissipation a spectrum with a  $-5/3$  exponential slope is shaped according to Kolmogorov's hypothesis [1]. The effect of free stream turbulence on boundary layers has been scope of various investigations [2], but there is little information on the level of turbulence  $Tu$  in soaring conditions [3, 4]. There are two scales of turbulence that are of interest. (1) low frequency turbulence or gusts, which act as AoA-fluctuations upon the pressure distribution, and (2) high frequency turbulence or increased turbulence level, which act through the mechanisms of receptivity directly upon the initial amplitudes of TS-waves.



**Fig 1: Boom with x-wire, attached to sailplane wing**

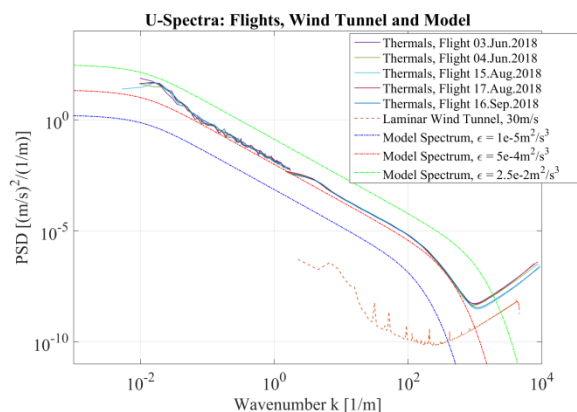


**Fig 2: Power spectral densities of turbulence averaged in thermals, in the Laminar Wind Tunnel and model spectra according to [1]**

In order to investigate both phenomena in the wind tunnel, a solid data base of typical FST is required. For this purpose, a measuring system was set up and installed on a 20m sailplane (ARCUS), which recorded  $u$ - and  $v$ -components of the inflow by means of a custom built  $x$ -wire-CTA. The  $x$ -wire was installed on a boom 1.3m upstream of the wing leading edge (Fig. 1). The CTA signals were recorded by a  $\Sigma\Delta$ -A/D-converter, DC coupled as well as AC-amplified by a factor of 300. Sampling rate was 105kHz, and maximum continuous operation was 8 hours. The special properties

of the  $\Sigma\Delta$ -converter renders an anti-aliasing filter obsolete, since there is a sharp cut-off at the Nyquist frequency, which suppresses efficiently the CTA-specific, increasing electronic noise. Additional measurements such as dynamic and static pressure, temperature and humidity were taken at a sampling rate of 0,2kHz. Those data allowed to correct the calibration of the CTA for ambient temperature and wear of the wires. Dynamic g-loads were also measured at the tip of the boom to exclude the influence of vibrations on the CTA readings. The whole installation was tested and calibrated in the Laminar Wind Tunnel (LWT) in Stuttgart. In flight, spectra could be gained up to 5kHz, covering a significant part of the dissipative subrange, before the CTA-specific noise prevails (Fig. 2).

In the 2018 season the equipment was airborne on 13 days along the Swabian Alb, of which five days proved to be evaluable, resulting in 22 hours of typical cross country flight data. A range of different weather situations and average climb rates up to 3m/s are covered, as well as thermals described by pilots both as smooth and rough.

### In-Flight Measurements: Results

To facilitate statistical analysis, the continuous data stream was divided in sections of four seconds and power spectral densities (PSD) and dissipation rates were determined. According to the GPS-track, the sections were identified as thermalling, or as flying straight ahead, or were left uncategorized. Regarding the thermalling category, dissipation rates and power spectral densities show only little scatter during each flight as well as between the flights. (Fig. 2). When consecutive thermalling sections are regarded as a whole, and CTA data is downsampled, PSD could be derived down to frequencies of 0.01Hz. At that frequency flight mechanics can be assumed to become dominating. In general, all the thermalling PSD agree very well with model spectra of [1] (Fig 2). Compared to the LWT, integral turbulence intensities ( $15\text{Hz} \leq f \leq 5\text{kHz}$ ) in thermals are consistently higher by a factor of 60.

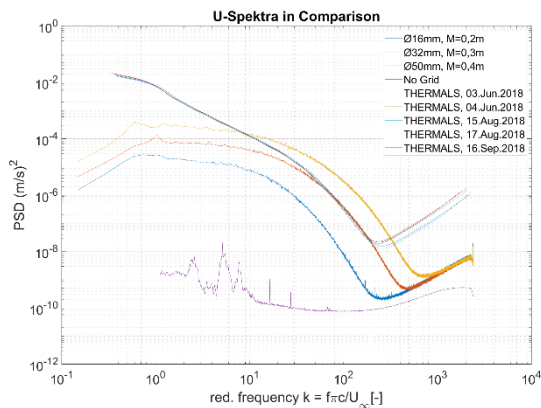


**Fig 3: In-flight spectra compared with Wind Tunnel Spectra behind grids (measurements by J. Romblad)**

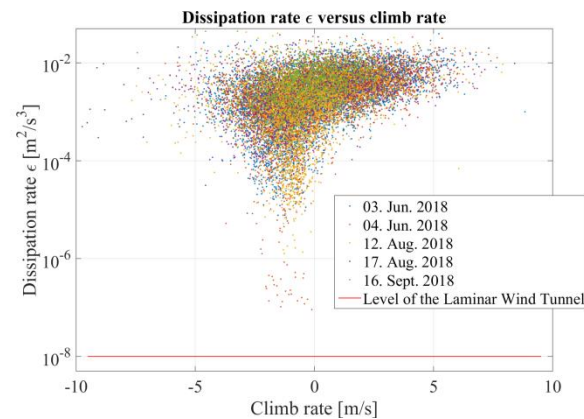


**Fig 4: Dissipation rate as a measure of the turbulent energy plotted versus the climb rate**

The spectra found during flight match well with turbulence spectra that can be achieved in the LWT by means of passive grids (Fig. 3). While large eddies are difficult to create in the wind tunnel, the small scale turbulence within the frequency range ( $0.5\text{kHz} \leq f \leq 3\text{kHz}$ ) of the TS-waves can well be reproduced.

Outside the thermals, on the straight legs, it is difficult to coin general statements about the magnitude of the free stream turbulence, because the flight path may have crossed up- or downdrafts, or dead air. Therefore, Fig. 4 shows the dissipation rate as a function of the climb rate, where each 4s-section of every flight is represented by a dot. It is obvious that low dissipation rates are only found where the glider sinks with about its polar sink rate. This means that all up- and downdrafts go along with higher turbulence intensities. The smallest dissipation rates are still significantly higher than those in the LWT.

To investigate low frequency AoA variations in the wind tunnel, complementary to the turbulence grids, a second wing is installed upstream of the main wing, pitching in a sinusoidal manner (Fig 5) as a gust generator. This requires representative combinations of frequency and amplitude. There is no use in applying FFT or wavelet transforms to the flight data, when only single frequencies are applicable in the wind tunnel. Comparable to transition counting in material testing, the AoA time signal was fractioned into a sequence of AoA steps. Each step corresponds to half an oscillation, peak to peak. The nodes were chosen such, that large amplitudes were favored, but not on the prize of

frequency. This leads to a range of amplitudes for every frequency (Fig 6), from which suitable values could be chosen for the experiment.

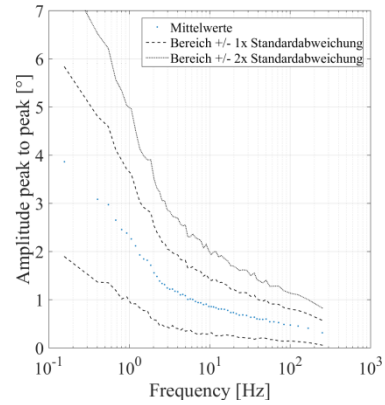
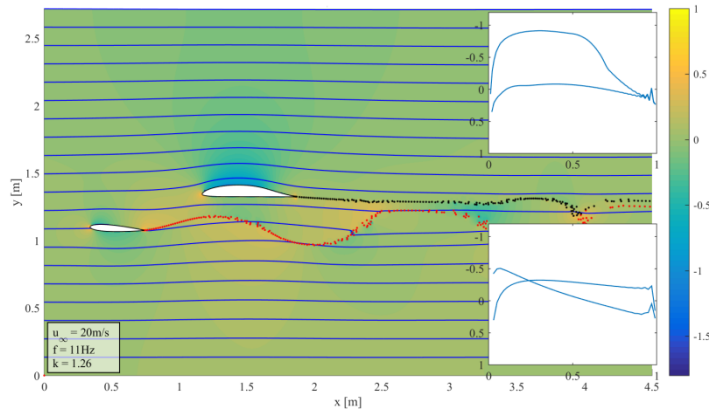


**Fig 5: Creation of AoA variations by means of an oscillating wing upstream of the main wing**

**Fig 6: Range of amplitudes of AoA fluctuations at different frequencies**

### Windtunnel Experiments: Setup

The aim of the in-flight measurements was to provide data of the FST for experimental and numerical simulation. Since LSB become relevant at low speeds and high AoA, the reference cases for further studies were derived from the typical speed and turbulence-data measured in thermals (Table 1). An AoA-amplitude of  $\pm 0.6^\circ$  covers 83-92% of all gusts at the regarded gust frequencies. The turbulence intensities given in Table 1 refer to the spectra of the LWT with and without grids within the range of 15Hz - 5000Hz. For the alignment of the experiment with the atmosphere, the spectra need to fit in the range of the TS-frequencies (Fig. 3). The average and the spread within each flight is well covered by the three grids.

	In-flight	Experiment	Non-dimensional
chord length $c$	0.5m	0.7m	Re = 0.88e6
airspeed $U_\infty$	30m/s	19m/s	
kin. viscosity $\nu$	1.7e-5 m <sup>2</sup> /sec	1.5e-5 m <sup>2</sup> /sec	
turbulence intensities (LWT, 15Hz-5000Hz)	0.066%, 0.16%, 0.33% (only in the experiment: 0.002%)		
AoA-frequencies	12.6Hz, 18.9Hz, 25.2Hz, 31.5Hz, 37.8Hz	6Hz, 9Hz, 12Hz, 15Hz, 18Hz	$k = \pi r c / U_\infty =$ 0.66, 1, 1.33, 1.66, 2
related AoA amplitudes	$\pm 0.6^\circ$		

**Table 1: Reference flight case and relevant AoA fluctuations.**

For the wind-tunnel experiments an airfoil was derived from an actual sailplane application airfoil with flaps. The flap was fixed in positive flap setting and stretched to reduce gradients in the turbulent boundary layer, while the forward section was shrunk in order to reduce the rectifying effect on the generated gusts. Care was taken not to alter the stability properties of the boundary layer upstream of the LSB. The model was equipped with 65 static pressure ports on the upper surface and in the leading edge region, 21 of which are located within the predicted range of the LSB. For the measurement of unsteady pressures up to 3kHz, 32 ports are also connected to piezoresistive pressure sensors within the model. A high precision hotwire traversing probe is used to determine boundary layer velocity profiles.

Increased intensities of small scale turbulence at reduced frequencies of 20 to 400 can be simulated by means of grids. Larger scale turbulence with reduced frequencies up to 2, i.e. AoA fluctuations, are generated by an oscillating NACA0012 ( $c=0.4m$ ) upstream of the test model. It is precisely timed and actuated by an CNC servo motor. The effectiveness of the gust generator was demonstrated on the basis of resulting pressure distributions. An amplitude of  $\pm 6^\circ$  of the NACA0012 corresponds to an AoA oscillation of  $\pm 0.6^\circ$ .

**Windtunnel Experiments: Measurements**

An extensive test matrix has been set up and carried out (Table 2). These measurements have provided ample data, which will now be evaluated and compared with numerical results. The unsteady pressures and the boundary layer velocity profiles allow a comparison with LST methods. Special attention will be drawn to the cases with gusts. As an example Fig 7 shows amplification rates for different gust frequencies calculated from phase averaged surface pressures. The magnitude and the spatial extend of the amplification rate for the most amplified Fourier coefficient change with increasing gust frequency.

Turbulence intensity	Gusts	Boundary Layer Velocity Profiles			Variation of Re	Variation of the gust amplitude
		for $\alpha=1,5^\circ$	for $\alpha=0,7^\circ$	for $\alpha=2,3^\circ$		
0,0015%	none	✓	✓	✓	✓	
0,066%	none	✓	✓	✓	✓	
0,16%	none	✓	✓	✓	✓	
0,33%	none	✓	✓	✓	✓	
0,0015%	6, 9, 12, 15, 18Hz	9Hz, 15Hz	-	-	✓	✓
0,16%	6, 9, 12, 15, 18Hz	9Hz, 15Hz	-	-	✓	✓

**Table 2: Program of the first wind tunnel measurements**

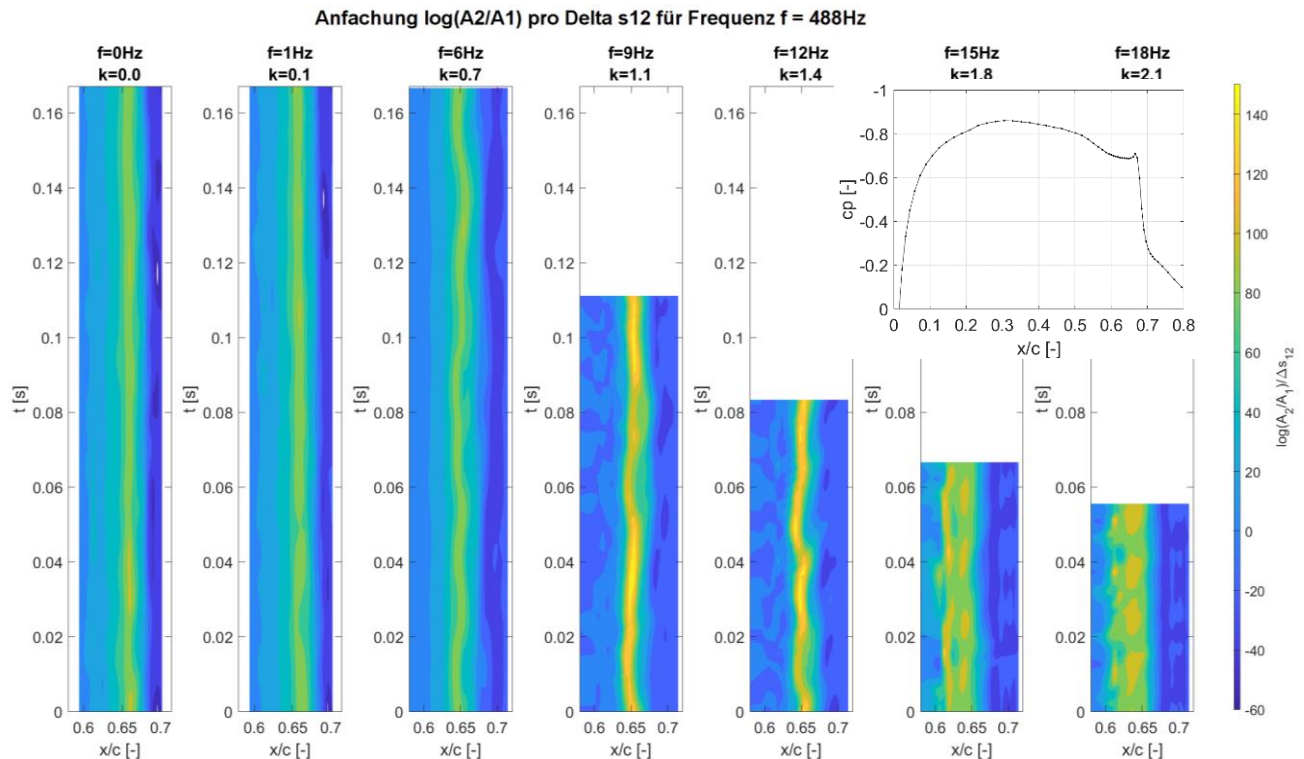


**Fig 7: Amplification rates across the separation bubble for different gust frequencies**

### Conclusion

Inflow turbulence has been recorded in the convective boundary layer of the atmosphere during cross-country flights with a sailplane. Measured spectra cover the scales from the phygoid to the dissipation range, and were used to characterize the free stream turbulence. Based on these results, wind tunnel experiments were conducted to investigate the effect of free stream turbulence on laminar separation bubbles. Analysis of wind tunnel data is in progress, and will lead to improved airfoils design methods, which will benefit sailplanes and wind turbines.

### References

- <sup>1</sup> Pope SB (2000) Turbulent Flows, Cambridge University Press, Cambridge
- <sup>2</sup> Bertolotti FP (2001) Effect of atmospheric turbulence on a laminar boundary-layer, Technical Soar., Vol. XXV:154-159
- <sup>3</sup> MacCready PB (1962b), The inertial subrange of atmospheric turbulence. J Geophys Res 67:1051– 1059. <https://doi.org/10.1029/JZ067i003p01051>
- <sup>4</sup> Popelka L, Matějka M, Zelený L, Uruba V (2014) CTA measurement of longitudinal velocity fluctuations and its spectra in thermal convection atmosphere and lee-wave condition using sailplane in-flight experiment. XXXII OSTIV congress, Leszno

Gefördert durch:



Bundesministerium  
für Wirtschaft  
und Energie

aufgrund eines Beschlusses  
des Deutschen Bundestages

## Sink Polar Analysis for Unmanned Aerial Gliders using the USAF Datacom

Fares El Tin\*, Inna Sharf†, and Meyer Nahon‡  
 McGill University, Montreal, Quebec, H3A 0G4

### Abstract

WITH recent advancements in research on Unmanned Aerial Gliders (UAGs), autonomous soaring is becoming more reliable and capable of significantly extending flight time and range of aerial vehicles. By exploiting available atmospheric energy, in the form of thermal updraft or ridge lift, UAGs can gain altitude while preserving on-board energy. The most common form of atmospheric lift, thermal updraft, has been the focus of most research investigating the automation of both the exploration and exploitation phases of soaring. The former concerns locating thermals around a certain region, during flight, while the latter is focused on successfully entering, remaining within, and exiting the thermal. Several previous works have shown the potential of autonomous soaring using thermal updrafts [1–3]. Throughout all phases of autonomous soaring, the key element that is relied upon by the guidance strategy is netto-variometer measurements.

Netto-variometer provides a measure of the local vertical velocity of the airmass surrounding the aircraft, by comparing the rate of change of the aircraft energy, against the natural sink rate of the aircraft at the current airspeed. The latter is obtained from the sink polar of the aircraft, which describes a functional relationship between its sink rate and airspeed. Therefore, prior to the implementation of any autonomous soaring algorithms, a characterization of the sink behavior of an aircraft is required. In previous works, doing so has involved performing multiple flight tests, on days with reasonably calm wind conditions, at a range of airspeed, and post-processing flight data to obtain filtered estimates of sink and airspeed. This tedious procedure has limited the choices of platforms for autonomous soaring implementation, which resulted in most researchers relying on the same platform for flight testing (as is the case with the works referenced here relying on the SB-XC RC glider).

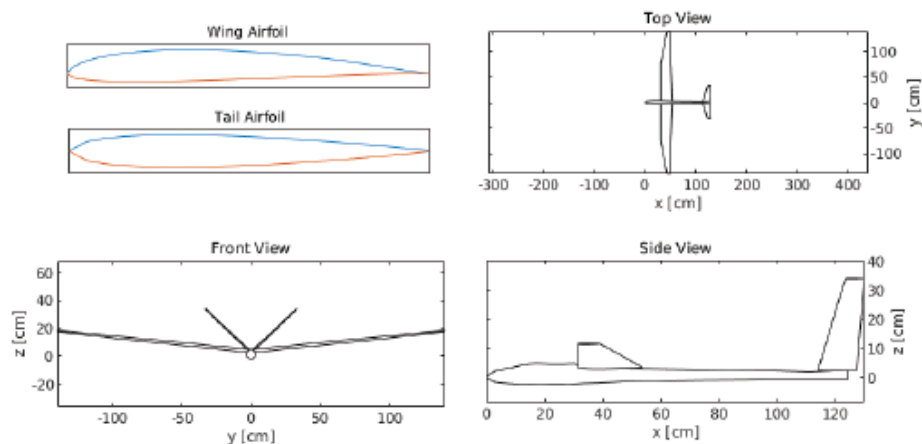


Fig. 1 One of the platforms used in this work, Magellan 2.8 m wingspan RC glider, as seen by DATCOM [4].

This paper aims to evaluate the formulation of a preliminary sink polar for a given aircraft by using the USAF Stability and Control Digital DATCOM [5]. Digital DATCOM implements aerodynamic analysis, using a combination of theoretical and analytical methods, to estimate stability and control derivatives based on the geometry of the aircraft

\*Ph.D. Student, Mechanical Engineering, fares.eltin@mail.mcgill.ca

†Professor, Mechanical Engineering, inna.sharf@mcgill.ca

‡Professor, Mechanical Engineering, meyer.nahon@mcgill.ca

at desired flight conditions. Figure 1 shows an illustration of the geometry of an RC glider used in the DATCOM analysis. By using these aerodynamic coefficients in equilibrium flight, sinking velocity in steady gliding flight can be computed for a range of airspeed, and thus a sink polar can be generated numerically. This allows us therefore to quickly generate a sink polar for use with autonomous soaring algorithms without requiring the collection and post-processing of experimental flight data for a given platform. Furthermore, the DATCOM sink polar could also be used to benchmark the quality of an experimental sink polar, should one be obtained, by serving as a baseline predictor of sink behavior for the desired platform.

In this paper, two sink polars are generated for two distinct platforms using both DATCOM and flight test data. Analyses of the results from both methods show that good agreement between both sink polars, especially as sink rate varies with airspeed, with DATCOM results tending to underestimate true influence of drag on the aircraft.

### References

- [1] Edwards, D. J., "Autonomous Locator of Thermals (ALOFT) Autonomous Soaring Algorithm," Tech. rep., Naval Research Lab, 2015.
- [2] Depenbusch, N. T., Bird, J. J., and Langelaan, J. W., "The AutoSOAR Autonomous Soaring Aircraft part 2," *Journal of Field Robotics*, Vol. 35, No. 4, 2018, pp. 435–458.
- [3] Acevedo, J. J., Lawrance, N. R., Arrue, B. C., Sukkarieh, S., and Ollero, A., "Persistent monitoring with a team of autonomous gliders using static soaring," *IEEE/RSJ International Conference on Intelligent Robots and Systems*, 2014, pp. 4842–4848.
- [4] Sahrn, S., "drawDATCOMaircraft," 2021. URL <https://www.mathworks.com/matlabcentral/fileexchange/34035-drawdatcomaircraft>.
- [5] Williams, J. E., and Vukelich, S. R., "The USAF Stability and Control Digital DATCOM Vol. 1," Tech. rep., USAF, 1979.

## A Design Study on the Application of Slotted, Natural-Laminar-Flow Airfoils on 18-Meter Sailplanes.

Leonard Metkowski and Mark Maughmer

*The Pennsylvania State University, University Park Pa, United States*

**Abstract:** A performance analysis along with a cross-country speed analysis were performed for an 18-meter flapped sailplane equipped with slotted, natural-laminar-flow airfoils. The slotted natural-laminar-flow airfoil (SNLF) can obtain higher than traditionally expected maximum lift coefficients with a simple flap, while still retaining low drag coefficients during cruise. While sectional drag coefficients for SNLF airfoils may be slightly higher than modern NLF airfoils, (due to an increase in wetted area from the slot), a sailplane equipped with a series of SNLF airfoils needs less wing area and is thus hypothesized to have lower total drag. The higher-than-traditional maximum sectional lift coefficient of the SNLF airfoil allows for the wing area to shrink to lower cruise drag yet retain similar minimum-sink rates when compared to modern flapped sailplanes. Initial computational analyses indicate that the SNLF airfoil can increase both performance and cross-country speed for modern flapped sailplanes.

**Keywords:** Slotted, natural-laminar flow, airfoil design, sailplane design.

### Introduction

Aerodynamic optimization of modern sailplanes can be significantly challenging, often characterized by the attempt to be both aerodynamically optimum in two very different flight regimes. High lift coefficients and low wing loadings lower the sink rate at low speeds and enhance performance needed for climbing in thermals, while the opposite tends to be beneficial in high-speed glide where profile drag is dominant. It is therefore best to have a blend of these characteristics in order to maximize cross-country speed in a wide variety of atmospheric conditions. It is here where the design of a new class of airfoil, the slotted, natural-laminar-flow airfoil (SNLF), appears to provide beneficial characteristics for use in sailplane design [1].

The SNLF airfoil is characterized by two elements with a slot separating the fore element from the nested aft element, Fig 1. Long runs of laminar flow exist across both elements which significantly lower the profile drag, though wetted area is increased in comparison to a traditional laminar flow airfoil due to the additional area of the slot between the two elements. The slot, while adding area, acts as a blowing mechanism at higher angles of attack, leading to higher maximum sectional lift coefficients than would be possible with traditional single element airfoils. The fore element exists entirely in a favorable gradient while the rear element is used for pressure recovery. The favorable gradient over the fore element allows for fully laminar flow on both the upper and lower surfaces. The aft element has fully laminar flow on the lower surface and is laminar on about half the upper surface with transition occurring prior to recovering the pressure to free-stream velocity. The aft element operates in the wake of the main, and thus its pressure distribution does not vary much with lift coefficient. While several SNLF airfoils have been created (S414, S204, and S103), and a few experimentally verified, none have yet to be tailored specifically for a sailplane [2,3,4].

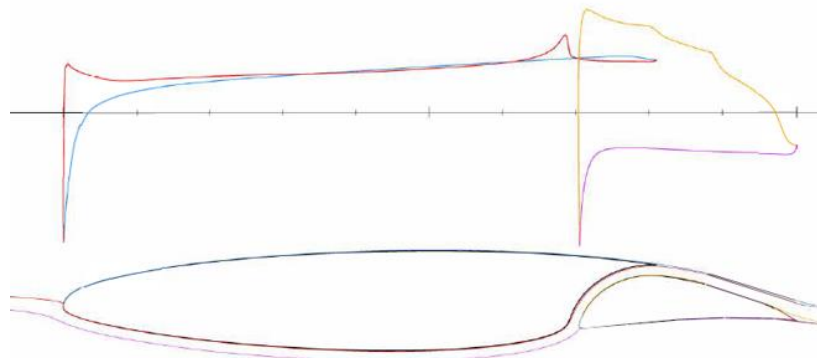


**Fig. 1** A slotted, natural-laminar-flow airfoil.

### Design Requirements

The design process of an aircraft wing is iterative in nature, with planform requirements driving airfoil design as is the opposite true [5]. This paper purely serves to investigate whether an SNLF airfoil tailored for a sailplane is likely to enhance performance and may serve as start for the iteration process by providing initial airfoil design specifications. Sailplanes in particular are no different than any other aircraft in that they too require iterative wing and airfoil design and, in some ways, present more complex design challenges than a traditional point design aircraft. This is in part due to the large range of speeds, and thus Reynolds numbers, observed in flight. Often Reynolds number and lift coefficients can vary widely, with Reynolds numbers as low as  $0.7 \times 10^5$  at the wing tip in climb and as high as  $3.0 \times 10^6$  at the wing root in cruise.

In an attempt to constrain the design space, it was determined both a SNLF wing along with a traditional NLF airfoil would be compared on an 18-meter glider. Fuselages, horizontal stabilizers, and wing design characteristics (such as quarter chord wing sweep, winglets, etc.) were held constant. The addition of the SNLF airfoil allowed for a smaller wing area while keeping climb rate constant, and thus changes to the wing planform were made to lower the aircraft's total drag. While induced drag was accounted for on both the SNLF and NLF gliders, it was not optimized for the SNLF case. A similar circumstance existed for the winglet on the SNLF glider, which also was not optimized. Wing chord was allowed to fluctuate for the SNLF airfoil in an attempt to lower the profile drag contribution in high-speed cruise, Fig. 4. The NLF airfoils used were from the most recent generation of modern production sailplanes.

Due to their recent inception, the SNLF airfoil family is quite small with only a few available for computational comparison and even fewer with experimental testing, Fig. 2. A SNLF airfoil for use on sailplanes has yet to be designed, and thus, lift coefficients, drag polar bucket width and depth, and profile drag coefficients were pulled from experimental data supplied from reports on existing airfoils. Maximum lift coefficients were determined using experimental data from the S414. It should be noted that the S414 is a rotor-craft airfoil, and significant improvement should be expected from a sailplane tailored version. Further constraints were made to simplify the design process, including a constraint that kept stall speeds of both aircraft equivalent.

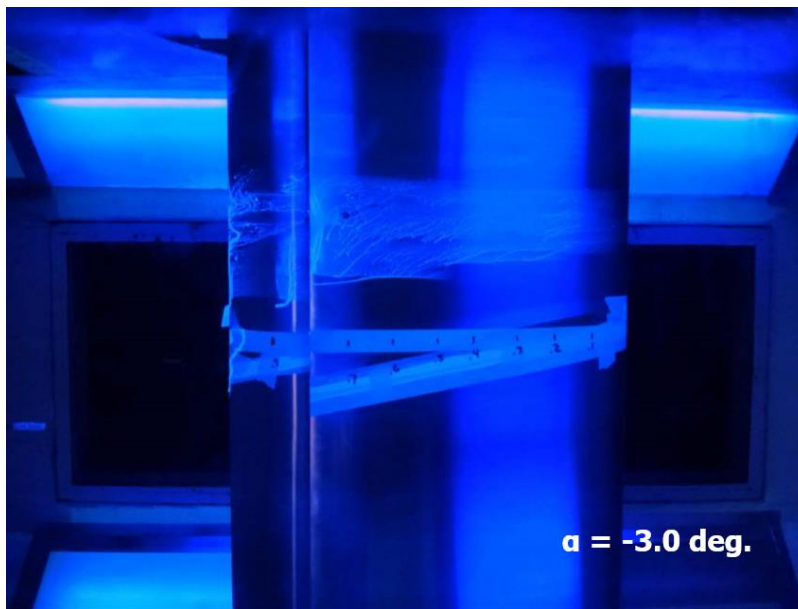


**Fig. 2 Experimental testing of the S414.**

As mentioned earlier, it was found that a SNLF class glider benefited from a reduction in wing area due to the airfoils having a significantly higher  $c_{l,max}$ . Experimental values were around 50% higher when compared to modern NLF airfoils, Figure 3. To reduce the wing area, the chord was decreased while the span held to 18 m. This decrease in chord added significant challenges in generating accurate polar data, with a reduction in chord leading to a decrease in Reynolds number for all wing stations across all speeds. It is well known that airfoil aerodynamics can become complicated and counter-intuitive as Reynolds number starts to approach values less than 300,000. There is also a lack of experimental data for Reynolds numbers less than 500,000 for SNLF airfoils. Best guesses were made to generate representative polar data in these areas.

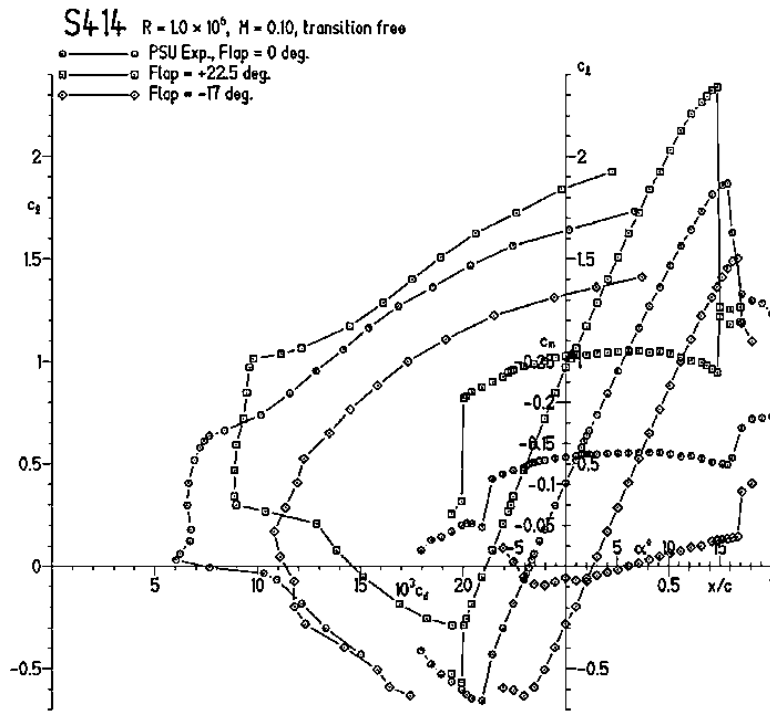


**Fig. 3 The S414 airfoil with flaps at  $Re = 1.0 \times 10^6$ .**

To further understand the aerodynamic performance benefits and the design space of a SNLF glider, several airfoil polars were generated as candidates using data from other existing SNLF type airfoils. Lift and drag polars were generated using both experimental and computational data from the S103, S414, and S207 airfoils. Drag coefficients were held constant (in agreement with experimental data) while lift coefficients were moved to more appropriate values for sailplanes. This likely created an overestimation in the profile drag contribution from the SNLF airfoil due to the lack of data from low-Reynolds number case designed airfoils. It also allowed for accurate modeling of the width and depth of the drag bucket in addition to its movement with flaps.

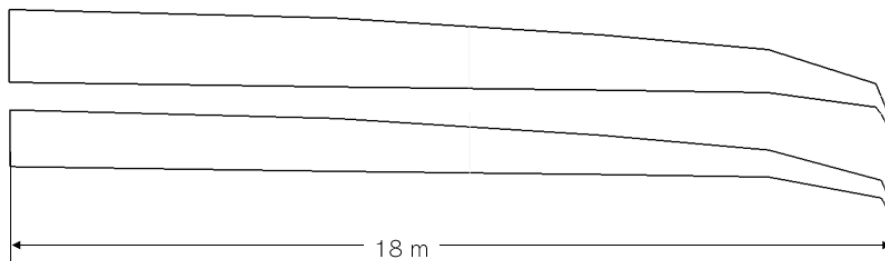


**Fig. 4 Planform comparison of the SNLF glider vs the modern glider.**

### Results

Results were computed for both the aerodynamic efficiency (lift to drag ratio) of each glider along with the average cross-country speed. Lift to drag ratio is a good indicator of performance, but average cross-country speed is a much better metric for how a sailplane will perform under contest conditions. To predict these values, glider polars were calculated using an in-house tool called PGEN (Polar Generator) [6]. PGEN uses Horstmann’s multi-lifting-line method along with an airfoil table look-up method for profile drag computations in order to predict the airframes

aerodynamic performance [7]. Figure 5 and 6 show computational results from PGEN compared to flight test data. The polar comparisons for both the SNLF glider and the modern sailplane are shown in Figure 7.

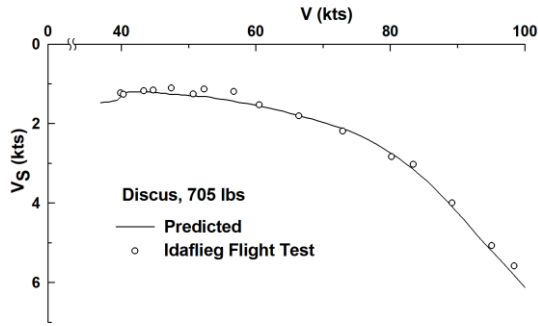


Fig. 5 Discus Polar, Predicted and Flight Test.

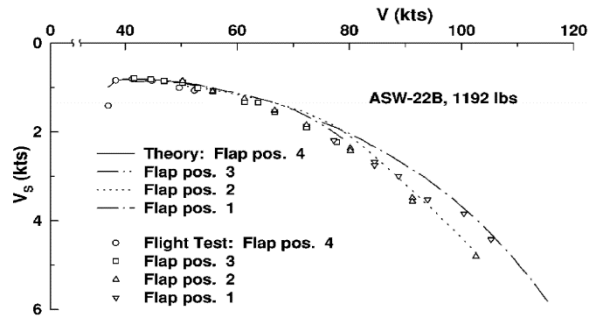


Fig. 6 ASW-22B Polar, Predicted and Flight Test.

A second program called ACCS (average cross-country speed) uses differing thermal strengths and radii to predict the average speed attainable on a cross-country task. While the code may not perfectly predict actual cross-country speed, it does accurately assess which aircraft configuration performs better. The results for the modern production glider and the SNLF glider are shown below in Figure 8.

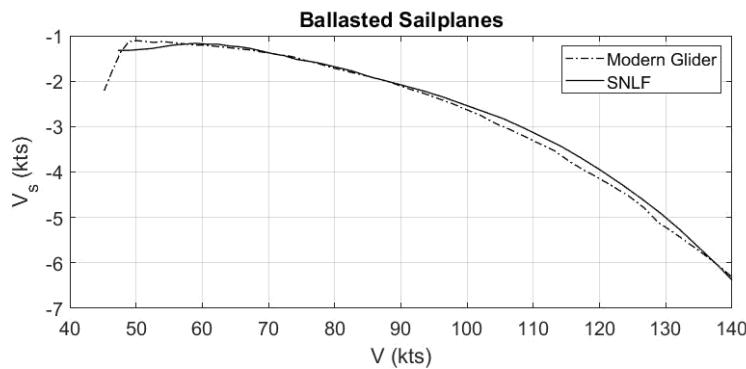


Fig. 7 Aerodynamic Polar for Ballasted Modern Glider vs. SNLF Glider

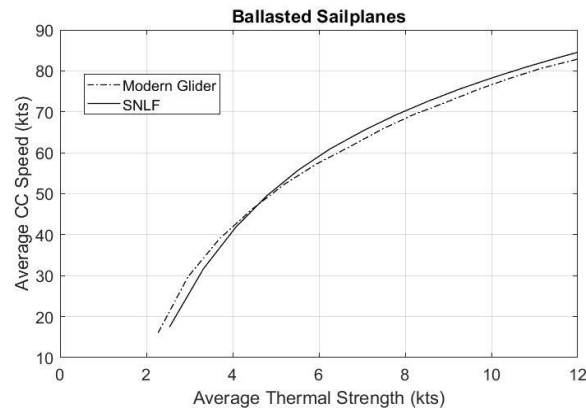


Fig. 8 Average Cross-Country Speed for Ballasted Modern Glider vs. SNLF Glider

### Conclusions

The advent of the SNLF airfoil provides a unique opportunity where enhancements in airfoil design could lead to aerodynamic improvements if properly tailored for sailplane applications. The SNLF glider showed the potential for

improvements over the current generation of gliders. Maximum lift coefficients of SNLF airfoils can be as much as 50% higher than the current generation of modern NLF airfoils. Drag coefficients are around 45% higher for the current SNLF class of airfoil, but could be expected to decrease with a sailplane tailored design. While the polars used for computational comparison have yet to be realized, they represent a realistic and most likely conservative estimate of a low Reynolds number sailplane SNLF airfoil.

## References

- <sup>1</sup> Somers, D. M., "Laminar-Flow Airfoil," U.S. Patent 6,905,092 B2, June 2005.
- <sup>2</sup> Somers, D. M., "An Exploratory Investigation of a Slotted, Natural-Laminar-Flow Airfoil," NASA/CR-2012-217560, 2012.
- <sup>3</sup> Somers, D. M. and Maughmer, M. D., "Design and Experimental Results for the S414 Airfoil," U.S. Army Research, Development, and Engineering Command TR-10-D-112, 2010.
- <sup>4</sup> Somers, D. M., "Design of a Slotted, Natural-Laminar-Flow Airfoil for Business Jet Applications," NASA CR-2012-217559, 2012.
- <sup>5</sup> Maughmer, M. D., Timothy, S. S., and Willits, S. M., "The Design and Testing of a Winglet Airfoil for Low-Speed Aircraft", AIAA Paper 2001-2478, 2001.
- <sup>6</sup> Kunz, P. J., "Development of a Software Package for the Assessment of High Performance Sailplanes," M.S. Thesis, Department of Aerospace Engineering, Penn State University, University Park, PA, 1997.
- <sup>7</sup> Horstmann, K. H., "Ein Mehrfach-Traglinienverfahren und seine Verwendung für Entwurf und Nachrechnung nichtplanarer Flugelanordnungen," Institut für Entwurfsaerodynamik, Rept. DFVLR-FB 87-51, German Aerospace Research and Test Establishment, Braunschweig, Germany, Dec. 1987.

## Microbiological examination of aeroplane control elements

Inga Weisheit

*Akaflieg Braunschweig e.V. inga@phkw.de*

*Interessengemeinschaft deutscher akademischer Fliegergruppen e.V.*

**Abstract:** The goal of this study was to develop the addiction of substances of aeroplane control elements and microorganism. Microorganism are ubiquitous and the use of controlelements is very high. The study examines the common microorganism like *Escherichia coli*, *Bacillus subtilis*, *Enterococcus faecalis*, *Staphylococcus aureus*, *Aspergillus brasiliensis*, *Candida albicans*. Certain materials will be privileged infected by fungus, like smooth hard plastic or leather. The addiction between Bacteria and materials of the control elements were not available, there is only a correlation between Bacteria and Fungi.

### Introduction

Microorganisms may exist in colony of single celled or low celled form. They are ubiquitous, also they occur on surfaces of control elements which are permanently used. These control elements are produced from different Materials like hard plastic, synthetic foams or wood. They decompose organic into inorganic matter, besides they are used for antibiotic production, food production or environmental protection. They also can evoke infectious disease. How well microorganisms attach to the control element is mainly effected by the material of the control elements. The present work handles the most common bacteria and fungi, which are easy to culture. *E. coli* and *E. faecalis* occur in intestines of warm-blooded animals. *B. subtilis* occurs in the upper layers of soil, in the air and is thought to be a normal gut commensal in human bodies *S. aureus* occurs in food, stretch of water, or human mucosa. *C. albicans* occurs on human mucosa, too. *A. brasiliensis* can be found in the upper layers of soil and forms mould on food. The present work aims to examine correlation between control element materials and the presented microorganisms.

### Methodology

For the present work contact plates for surface sampling by CarlRoth were used. The plates are composed of two sides with different composition. One side, PCA, Tryptic Soy Agar for reliable total germ count and on the other side RBCplus, for detection of yeasts and moulds. Agar is obtained from red algae, a jelly-like substance. It will be used as a growth medium, mixed with other nutrients in which microorganism can be cultured. Agar was gently pressed with both sides onto the surface that had to be tested. After that, the carriers were incubated at 25°C for 2-3 days. After the incubation colonies were counted. The data was processed with IBM SPSS, a program for statistic data analysis.



Fig.1: Agar with bacteria colonies for count



Fig.2: Agar for detection of yeast and moulds

The colonies were counted as colony forming units (cfu) and their colour was noted. Depending on the colour of the colony, the type of microorganism is different. Measured by means of the following table, the colonies were analysed.

Tab.1: Table to evaluate the grown colonies

**MICROBIOLOGICAL TEST**

CASO (37 ± 2 °C / 22-48 h, and \*: 4 - 5 d, respectively)

Test strain	Growth	Colour
<i>Escherichia coli</i> ATCC 25922	Good	red
<i>Bacillus subtilis</i> ATCC 6633	Good	red
<i>Enterococcus faecalis</i> ATCC 19433	Good	red
<i>Staphylococcus aureus</i> ATCC 6538	Good	pink-red
* <i>Aspergillus brasiliensis</i> ATCC 16404	Good	White, becomes black
* <i>Candida albicans</i> ATCC 102231	Good	weiß-hell

RBCenr (25-30 °C / 5 d)

Test strain	Growth	Colour
Bacteria	inhibited	-
<i>Aspergillus brasiliensis</i> ATCC 16404	Good	White, becomes black
<i>Candida albicans</i> ATCC 102231	Good	white - light

**Results**

The result of the project shows a correlation between fungi and bacteria grow. All in all the more fungi grew the more bacteria grew and otherwise. Also there is another correlation between surface material and microorganisms, which means that the growing of microorganisms is effected by the surface of control elements. Overall there were 25 samples tested in that project. So the conclusions are more a general tendency than absolute results.

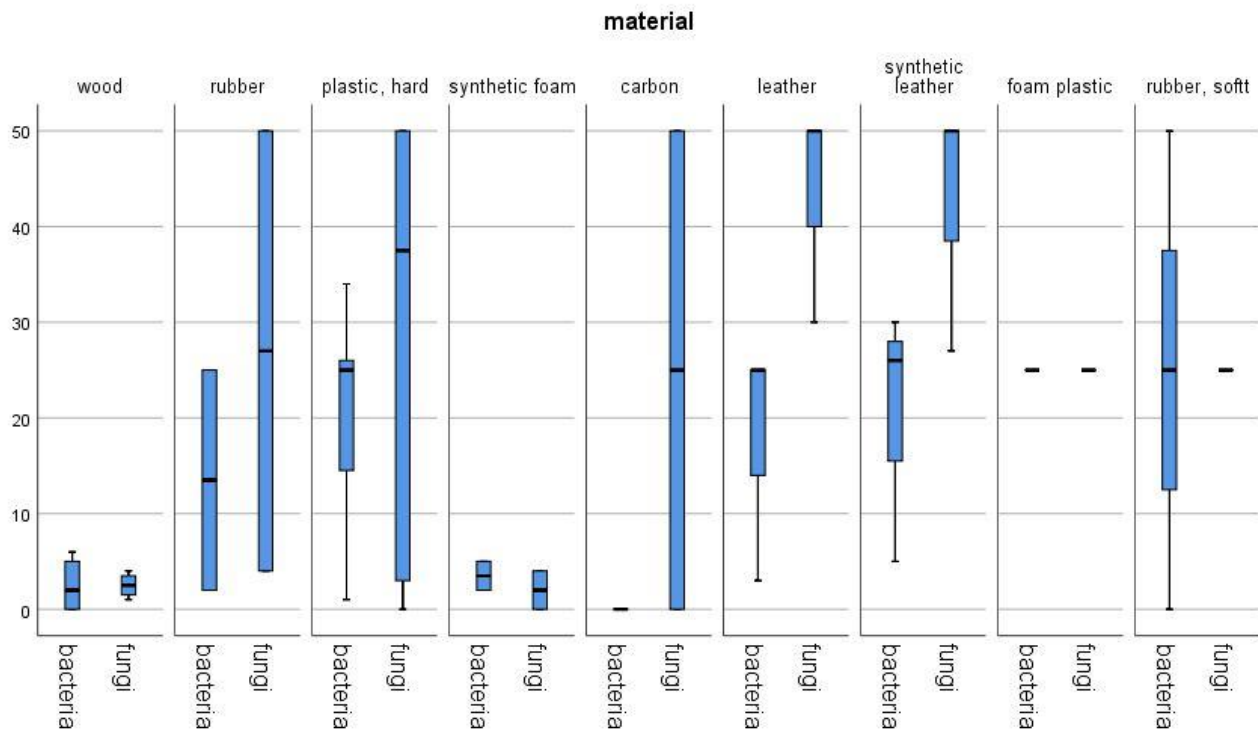


Fig.3: box plot of all colonies reference to the material

Figure 3 shows a leptokurtic distribution at wood and synthetic foam surface. The interquartile range shows a low statistical spread. Also the whisker are close to the box. On the other hand, plastic (hard) and rubber shows a high statistical spread. After that, the correlation between fungi and bacteria is tested, also the correlation between the tested materials and fungi or bacteria. It can be said, that there is only a correlation between Bacteria and Fungi.

The research project shows a low infestation of bacteria and fungi at wooden control elements as well as synthetic foam. Otherwise hard plastic and leather show much more infestation. Fungi are growing better in comparison to bacteria. All in all it is more important to clean the control elements than choosing the right surface material.

## References

Product Data Sheed of ROTI®DipSlide CASO-TTC/RBCenr by Carl Roth GmbH + Co. KG

-<https://www.spektrum.de/lexikon/biologie-kompakt/mikroorganismen/7607>; 24.06.21

-Ja'nosVarga, Sa'ndorKocsube', Bea'taTo'th, Jens C. Frisvad,Giancarlo Perrone, Antonia Susca, Martin MeijerandRobert A. Samson;Aspergillus brasiliensissp. nov., a biseriaterblackAspergillus species with world-wide distribution; International Journal of Systematic and Evolutionary Microbiology (2007), 57, 1925–1932

-M. AnaulKabir, Mohammad Asif Hussain, andZulfiqarAhmad; Candida albicans: A Model OrganismforStudyingFungalPathogens; International ScholarlyResearch Network, ISRN Microbiology, Volume 2012, Article ID 538694, 15 pages, doi:10.5402/2012/538694

## Experiences from Flight Testing in the Idaflieg

Tessa Weigelt <sup>1</sup>

<sup>1</sup> Idaflieg e.V., Germany, tessa.weigelt@idaflieg.de

**Abstract:** In the Idaflieg students from all over Germany get the opportunity to learn how to design, to build and to fly sailplanes and small motorplanes. Especially the home build prototypes enable them to gain unique knowledge and experiences. Also, the flight testing is completely in the hand of the students. From maiden flight to certification, they have to overcome many challenges and receive the opportunity to learn a lot. This presentation will give a look inside the current projects in flight testing.

**Keywords:** Idaflieg, flight test, homebuild aircraft, Akaflieg, student group

### Introduction

The Idaflieg is the national association of the „German Academic Flying Groups“ (in German “Akademische Fliegergruppe “ for short: “Akaflieg”). It connects the individual Akafliegs together and ensures the knowledge transfer between them. Since 1922 students have shared their common passion for aviation under the theme “Research, building and flying“. More than 150 aircraft prototypes have been designed, build and tested by students themselves. The Akafliegs shaped the history of sailplane design in Germany with lots of innovative prototypes. Today the focus is especially on the practical education of the students alongside their university education.



**Figure 1. Idaflieg prototypes on flight test campaign at Aalen-Echingen**

Over years a new prototype is designed and built but after that there is not just the fun part of flying it. A well-organized flight test starts long before the preparations in the cockpit and ends after the detailed documentation. The main motivation behind this is to complete the certification process while ensuring the highest possible safety. For this the limits of the aircraft need to be explored based on the certification specifications. By doing this the students learn a lot about their prototype and step by step the flight manual is created. The presentation shows in detail how flight testing in the Idaflieg works and considers the experiences with the current prototypes and what the students learned from it.

### Background

Every Akaflieg has more than one project at the same time. First there is the maintenance of the older prototypes to keep them in good condition and to hold them in honor, then there are the new ideas and projects which must get from head to the paper or CAD and lastly next to the sailplanes undergoing maintenance there is a new prototype growing in the workshop. Sometimes it is not easy to concentrate all the good ideas to one goal and get everything under one roof, but every flying prototype shows that it is worth it. An innovative idea is not well thought out in a day and after the frame is set, the design has to be well thought out in detail. Also, the construction is a challenge day by day and the at first inexperienced students have not to give up in the light of the many smaller and bigger problems. When the aircraft in the workshop is near in completion and the maiden flight is getting closer, the topic of flight testing becomes more important. The maiden flight is the greatest day for everyone who has worked on the project from the beginning till the end. It is a multiple generations project, and every generation of students earned their own very special experiences with their project phase. After passing this highlight the project is far from over the flight testing begins.



**Figure 2. The Mue 31 of the Akaflieg Munich on the hands of her crators**

### Current projects

The flight testing of the current prototypes takes mostly place on the Idaflieg Summer Camp. This is the three-week annual meeting of the Idaflieg for flight performance and characteristics measurements as well as research projects and the prototype testing. The exchange of knowledge, the good infrastructure as well as support from internal and external resources advances every single project. In recent years to work closer together and to learn from each other has become always more important. The current projects in flight test on the last Idaflieg summer camps in 2019/2020 were the following:

The **AK-8**, is a standard class high performance sailplane with an elliptical leading edge. After a landing damage the AK-8 had her second maiden flight in 2009. With new winglets all necessary flight tests for the certification were completed last year. The **B13e**, is a side-by-side two-seater with an electrical front sustainer with retractable four blade propeller. The motorglider had her first electrical flight in 2019 and was tested for the motor performance and their effect on the flight performance. The **D-43**, a training two-seater in side-by-side configuration, could prove her good-naturedness in the flight testing since her maiden flight in 2014. The **fs35**, the newest Idaflieg prototype, is a towing motorglider and had her maiden flight in 2019 and could complete a big milestone in the flight testing on the last summer camp: the first tows which stands out with an impressive climb rate.



**Figure 3. AK-8 of Akaflieg Karlsruhe**



**Figure 4. B13e of Akaflieg Berlin**



Figure 5. D-43 of Akaflieg Darmstadt



Figure 6. fs-35 of Akaflieg Stuttgart

The **Mü 31**, is a high-performance sailplane with an aerodynamically optimized wing-fuselage junction. After her maiden flight in 2017 the essential flight tests like flutter and spinning were performed. And last but not least, the **FVA-29**, a self-designed electrical sustainer for sailplanes in an ASW 28-18, on which the students test the integration of the whole system to earn knowledge in electrical flying. In the presentation the most important methods employed in the flight test campaigns will be detailed, for example the airspeed calibration, spinning and flutter tests.



Figure 7. Mü 31 of Akaflieg Munich



Figure 8. FVA 29 of FVA Aachen

Over all the projects stand out for their uniqueness and are connected by the mindset to explore and improve how we fly. The goal of the collaboration is to learn from each other and to create the environment for professional flight testing as well as to hand over the collective knowledge to the next generation. With the hope that also the next 100 years students get the possibility to design, construct and test their prototypes.

## References

Idaflieg e.V: Idaflieg Berichtsheft 2020 – Nr. 46.

Idaflieg e.V: Idaflieg Berichtsheft 2021 – Nr. 47

[www.idaflieg.de](http://www.idaflieg.de)

[www.akaflieg-karlsruhe.de](http://www.akaflieg-karlsruhe.de)

[www.akaflieg-berlin.de](http://www.akaflieg-berlin.de)

[www.akaflieg.tu-darmstadt.de](http://www.akaflieg.tu-darmstadt.de)

[www.akaflieg-stuttgart.de](http://www.akaflieg-stuttgart.de)

[www.akaflieg-muenchen.de](http://www.akaflieg-muenchen.de)

<http://www.fva.rwth-aachen.de>

## Proceedings in the Development of a Crashworthy Glider Cockpit

Till Lindner<sup>1</sup>, Christian Rolffs<sup>1</sup>, Niklas Dierksen<sup>1</sup>, Rahmi Öküz<sup>1</sup>, Sven Scheffler<sup>2</sup>, Oliver Dorn<sup>2</sup>

<sup>1</sup>Akademische Fliegergruppe Hannover e.V., Germany, <sup>2</sup>CraCpit; till.lindner@akaflieg-hannover.de

**Abstract:** In the joint LuFo Project CraCpit a single seat glider cockpit is designed with FE-Methods to sustain the loads in a crash scenario. In this part of the project a single seater glider designed without a designated crash-cockpit is retrofitted with structures to maintain structural integrity and limit peak accelerations acting on the pilot. The crash scenario is determined by flight tests and evaluation of accident reports. A FE-model (finite element) of an Astir CS is then build. The unmodified reference model is then compared to multiple retrofitted frame elements to identify the optimal stiffness increase per weight, showing significant improvement. Together with the Munich team consisting of Akaflieg München and Lehrstuhl für Carbon Composites (LCC), a drop test of the crash cockpits is planned.

**Keywords:** Safety, Crashworthiness, Cockpit, Emergency Landing

### Introduction

Crashworthiness of glider cockpits has improved with the 2008 amendment of CS 22.561, asking for higher static loads without damage in emergency landing conditions, which is generally accepted in the community. However, there is still a large number of sailplanes flying that were developed for the former less strict emergency landing conditions, that is 6g of acting at 45° rearward and upward on the nose. This value seems rather low when compared to more real world high-risk crash scenarios: By evaluating 78 accident reports of the Bundesstelle für Flugunfalluntersuchung (BFU), 48% of reported accidents happen nose-first at a steep flight path and high velocity, resulting in 94% of all reported fatalities. These numbers agree well with the statistics reported in [1]. To gather input parameters of this highest-risk-scenario that can be applied in a dynamic FE Simulation, flight tests entering a spin at safe altitude were carried out at the Idaflieg Sommertreffen. The typical pitch angle and downwards velocity measured with an IMU and GPS are shown for a 15 m standard class sailplane in Figure 18. The values of  $\theta=20\dots60^\circ$  and  $w < 25$  m/s are valid for all 5 measured types and share the periodic characteristics.

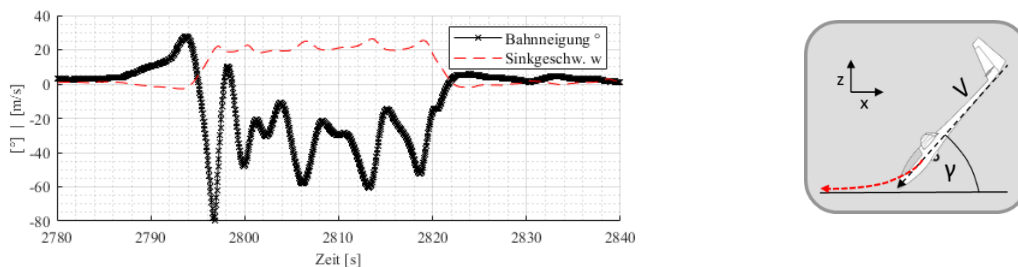


**Figure 18: Typical pitch angle and downwards velocity in the inertial reference frame and resulting crash scenario (right)**

As a first approximation of survivability in such a scenario an ideal constant deceleration after impact is assumed. With an allowed deformation distance of  $s=440$  mm (from nose to control bulkhead on an Astir CS) and 20 m/s impact velocity this leads to the expression:  $a = \left(\frac{1}{2} \times \frac{v^2}{s}\right) \div 9.81 = 46 g$  over a duration of 44 ms. Note that the deformation of the ground is not yet considered. If the sliding path shown in Figure 18 (red) can be ensured, such a crash is to be placed in the “area of moderate injury” after [2]. With proper design it should thereby be possible to reduce fatalities significantly. The fact that this idealised estimation of survivability is not true in the real world comes from two main reasons: i) The structural integrity is lost after impact due to buckling and a severe bending moment on the canopy cutout. ii) Few types make use of the available deformation space in the nose. This has been recognised by previous works [1,3,5]. Further, the subsurface may contribute to whether and how structural failure occurs. If penetration into the soil takes place, the damage pattern is different from that if the aircraft is deflected by hard soil. This is investigated by the Munich team.

**Methodology**

By means of technical drawings, material samples and 3D scanning a detailed FE Modell shown in Figure 2 has been built in Abaqus. All main structural components such as fibre layup, bulkheads, stringer and glued joints are considered. Dummy masses of the tail section and elastic beams with correct eigenfrequency substituting the wings are included. The load case identified above is implemented as follows: 45° flightpath angle at 20 m/s and no sideslip. Note that the idealised equivalent static loads are severely higher to the 9 g, 45° emergency landing condition in CS22.

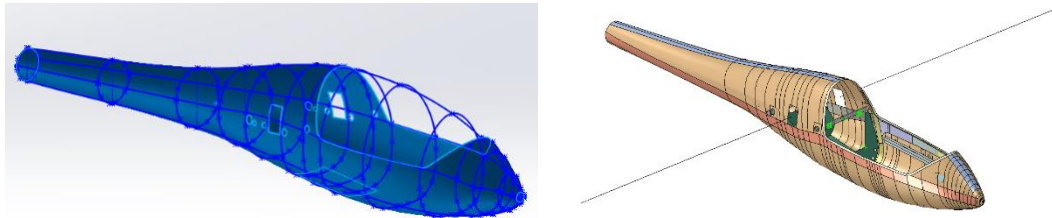


**Figure 19: 3D scanning results, parametric reconstruction and resulting structural model of Astir CS**

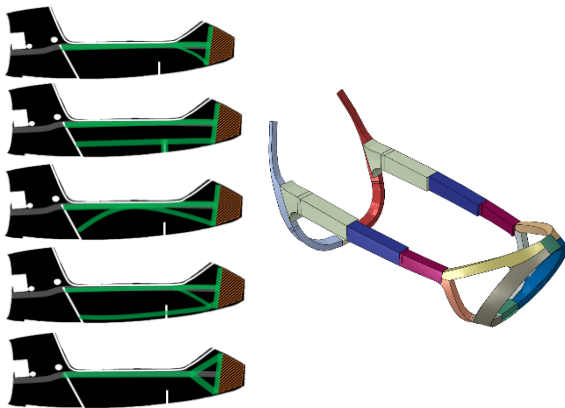


**Figure 20: Iteratively tested retrofitted frame concepts (left) and final design (right, thickness exaggerated)**

With a baseline model working, different cage-like structures shown in

Figure 3 are retrofitted in the digital cockpit. Two external constraints were applied: No control mechanisms in the existing cockpit are modified, resulting in limited available space. Furthermore, the additional weight is kept below 10 kg. The resulting design choice based on crude, but sufficiently fast simulations is shown on the right. For the results presented in the following chapter a more detailed FE-Model is used.

This dynamic explicit simulation consists of more than 48000 elements. The CRP is modeled as conventional shell elements (S4R) with a Hashin damage initiation criterion and stiffness degradation to zero. At a simulation time of 0.2 seconds the solution takes 33 h to compute on a 8 core cluster. Mechanical properties of the GFK material most used in the fuselage shell are estimated with:

$E_1$ [MPa]	$E_2$ [MPa]	$\nu$	$G_{1/2}$ [MPa]
50000	5000	0.3	2900

With the outer contour of the frame structure agreed, a full scale demonstrator was additively manufactured and test fitted in an Astir CS. This revealed necessary details that have to be addressed in the manufacturing model such as the bottom seam of the cockpit and the position of the emergency exit lever. All in all, the path from 3D scan, FE-model, retrofitted elements and rapid prototyping proved to be viable and expandable to different types.

The comparison of the simplified FE solution for the retrofitted and the original Astir are shown in **Figure 4**.

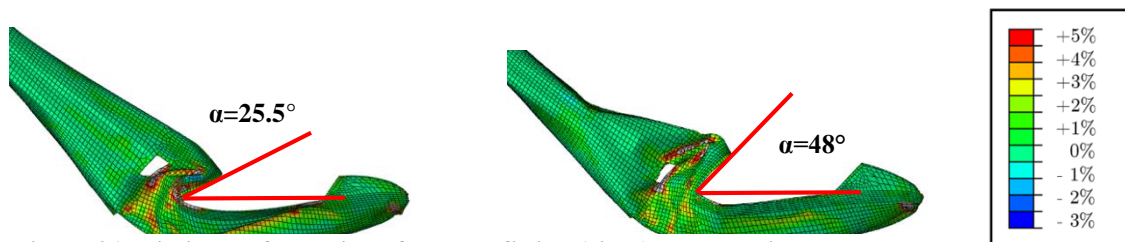
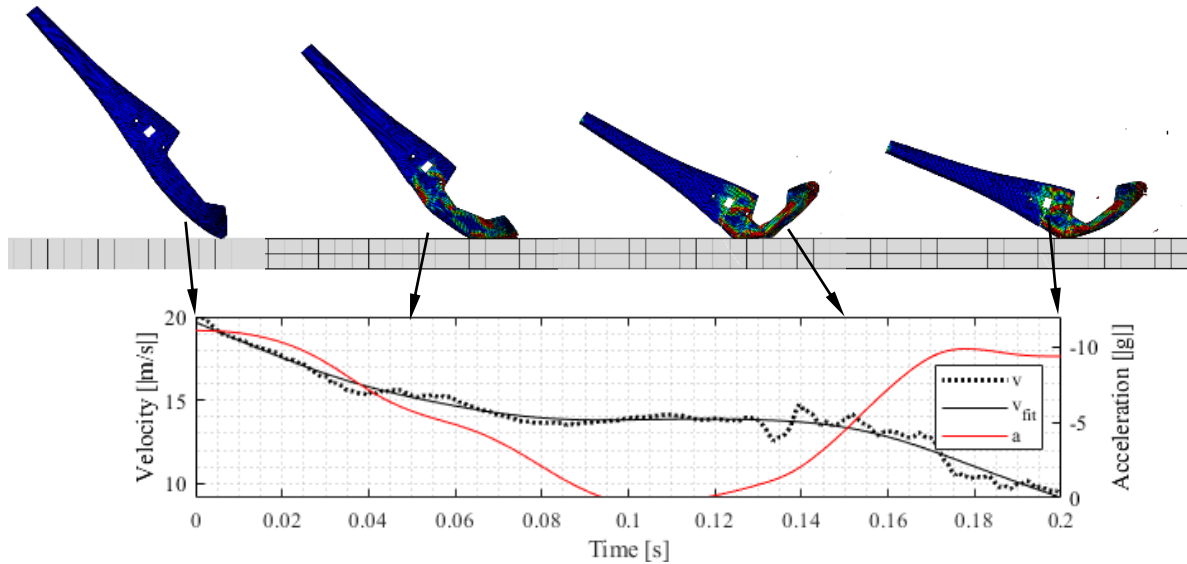


**Figure 21: Limited deformation after retrofitting (right) as shown in reduced FE-Model used for iteration. Colours show relative strain**

**Results**

A time-series of the detailed FE-Simulation described above are shown in **Figure 5**. Buckling is less severe and the rear part of the cockpit stays intact. However, the fuselage still fails in an unacceptable way, not maintaining a safe volume.



The red curve in Fehler! Verweisquelle konnte nicht gefunden werden., indicating the global deceleration magnitude of a mass behind the pilot, shows a rather low peak deceleration of ca. 10 g. This is mainly because the initial velocity at 45° is split in two components, a ground-parallel motion and a downward motion. With the current numerical setup, the fuselage is deflected on the ground surface and maintains its horizontal velocity, only decelerating due to friction. Only the vertical movement is reduced quickly by energy dissipation in the deformation, making it the dominant factor of acceleration magnitude. This issue is further addressed by means of plastic deformation in the impact surface by the Munich CraCpit team. However, this observation shows how effective a guided deflection towards sliding upon impact is. This can be introduced by means of keel beams [4] and forward angled bulkheads.

At the current state of design, the structural integrity of the cockpit is still lost, as seen in **Figure 6**. The point of failure has merely shifted from the rearward canopy cutout to buckling of the hull at the point of max. unsupported length, as one would expect. This will be addressed in modifications of the fibre layup, which in its current state weights below 5 kg.

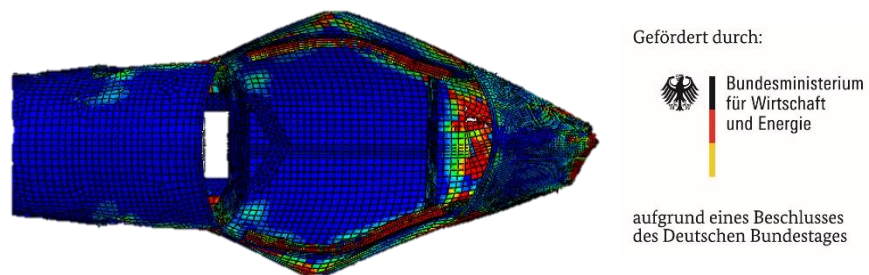


**Figure 22: Buckling of reinforced Astir CS Cockpit. Colours showing matrix compression failure (from blue to red)**

**References**

- [1] Sperber, M.: Untersuchung des Insassenschutzes bei Unfällen mit Segelflugzeugen und Motorseglern- Forschungsauftrag-Nr. L-2/93-50112/92, TÜV Rheinland GmbH - Institut für Verkehrssicherheit - Abteilung Luftfahrttechnik, Köln, 1998.
- [2] Shanahan, D.: Human Tolerance and Crash Survivability, Injury Analysis, RTO-EN-HFM-113, Carlsbad, USA, 2004.
- [3] Hurley T., Vandenburg J.: Small Airplane Crashworthiness Design Guide, Phoenix, Simula Technologies, 2002.
- [4] Schuster U., Wolf K.: Improvement of Sailplane Crashworthiness trough Keel Beams with Silicone Cores, Technical Soaring Vol. 38, 28. April 2014, S. 16-26.

## Optical deformation measurement of a two-seater cockpit under emergency landing conditions during a quasi-static load test

Lajos Fohlmeister<sup>1</sup>, Till Julian Adam<sup>2</sup>, Benjamin Schwarz<sup>3</sup>

<sup>1</sup>*Akademische Fliegergruppe Braunschweig, Germany, lajos.fohlmeister@online.de*

<sup>2</sup>*DLR, Institute of Composite Structures and Adaptive Systems, Braunschweig, Germany*

<sup>3</sup>*GOM GmbH, Braunschweig, Germany*

**Abstract:** A static load test required for type certification of the two-seater glider SB 15 was performed. The test shows that the deformation behavior of the two-seater differs from that of single-seat gliders. The dimensioning factor is the deformation of the cockpit frame, which leads to structural failure. Using optical displacement analysis, the deformations can be attributed to two different mechanisms. Based on the experimental results, modification proposals for future cockpit designs are derived.

**Keywords:** Crashworthiness, Load test, Cockpit frame, Deformation, Emergency landing conditions, Crash scenarios, Passive safety, Survival cell, ARAMIS, CS 22.561

### Introduction

Passenger protection in gliders is a high priority in cockpit design. Experience from static and dynamic tests shows that the risk of injuries to the pilots results primarily from a collapse of the cockpit structure itself and less from strong decelerations [1]. Passive safety is ensured by passing a static equivalent load case, proving the strength of the safety cell.

In this safety cell, the cockpit frame as the main load-bearing element is of great importance. A failure of the cockpit frame around the canopy cutout usually leads to a collapse of the cockpit structure itself. Comprehensive works by Segal [2], Röger [3], Sperber [4] and Kämpf [5] show that the cockpit frame buckles outwards during crash landing. The large deformation eventually causes the frame to break. Based on the measured deformations, Waibel [6] proposes a calculation method for cockpit frame dimensioning taking into account the deformation and pre-curvature. The extensive tests lead to a safety cockpit, which is standard in modern gliders and increases occupant protection considerably.

However, all existing tests and results refer to single-seat gliders. There are no findings applicable to two-seat gliders which are becoming more popular [1]. In two-seaters, the longer fuselages in particular result in a higher bending moment due to the long distance between the impact point at the nose and the center fuselage. This bending moment must be carried by the cockpit. The longer unsupported length of the cockpit frame additionally aggravates the stability problem. Therefore, there is a need to understand the failure behavior of two-seat sailplanes in more detail in order to derive improvements for future designs.

### Methodology

To verify passive safety, the Certification Specification requires a load test, which may be performed quasi-statically. In the test, a 45° impact is simulated. Thereby, the force to be verified must act at 45° to the longitudinal axis of the aircraft at a point in front of the rudder pedals. Such a test was performed and the deformation was measured optically during the test.

The test was performed with the fuselage of the SB 15, representing the current state of modern safety cockpits, see Figure 1. The SB 15 is a 20 m class two-seater with the pilots seated behind each other. The design of the crash structure of the SB 15 is based on recommendations from Sperber [4]. The aim of this structure is to maintain the interior cockpit volume necessary for survival and to prevent the cockpit from collapsing.

To achieve this, the canopy cutout is reinforced by a solid cockpit frame (section B-B, Figure 1), which is supported with a metal cross strut between the pilots. The cockpit frame is designed to carry the resulting bending moment and to transfer the loads around the pilots and to distribute them in the center fuselage. Additional stringers on the bottom increase bending stiffness. Two control column bulkheads support the fuselage shell. The installation of the seat shells was omitted for the test.

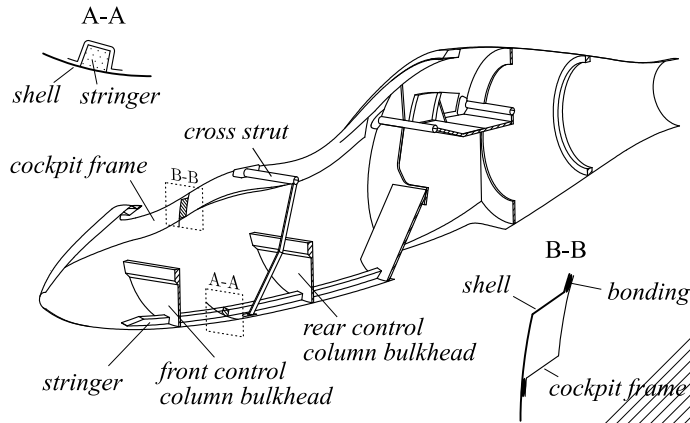


Figure 1. Layout of the crash-structure

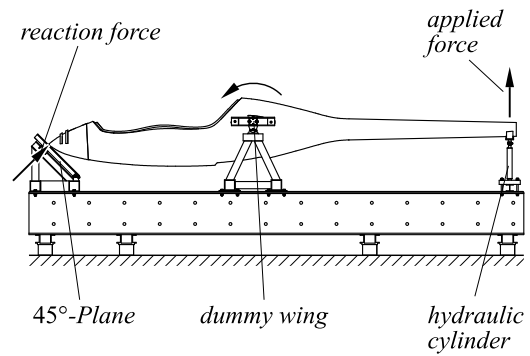


Figure 2. Principle of the load test

In the test, the fuselage was mounted on a dummy wing allowing rotation about the lateral axis, see Figure 2. The rear of the fuselage was pushed up by a hydraulic cylinder causing the fuselage to perform a pitch down motion. As a result, the nose of the fuselage met a 45° plane built up in front of the fuselage. This is where the test force to be verified was generated as a reaction force. According to the certification specification applicable to the SB 15, the force must be equivalent to a deceleration of 6 g.

The deformation was measured by an ARAMIS system by GOM consisting of three synchronized 3D sensors. ARAMIS uses Digital Image Correlation (DIC) to optically record 3D coordinates on a stochastic gray-scale pattern applied to the shell. When the fuselage deforms under load, the movement and deformation of the stochastic pattern is calculated to 3D displacements and deformations against the unloaded reference state. The arrangement of the ARAMIS sensors resulted in a combined 3D measurement volume that included the entire cockpit area. This allows the deformation of the outer fuselage shell to be determined on both sides. In addition, the computationally critical area at the rear end of the cockpit frame was examined in detail by a third ARAMIS sensor with a higher local resolution. The virtual test planning for optimal positioning of the sensors was done in advance in the ARAMIS Professional software.

### Results

The fuselage failed at a load corresponding to a deceleration of 6.14 g. The primary failure observed was a macro-scale laminate rupture in the left rear cockpit frame area, just before the end of the canopy cutout, resulting from severe deformation. The fracture runs through the bonded cockpit frame and through the shell. Further failure occurred at the control column bulkheads, which delaminated locally. In addition, the metal connection of the cross strut to the composite structure was plastically deformed due to the deflection of the cockpit frame.

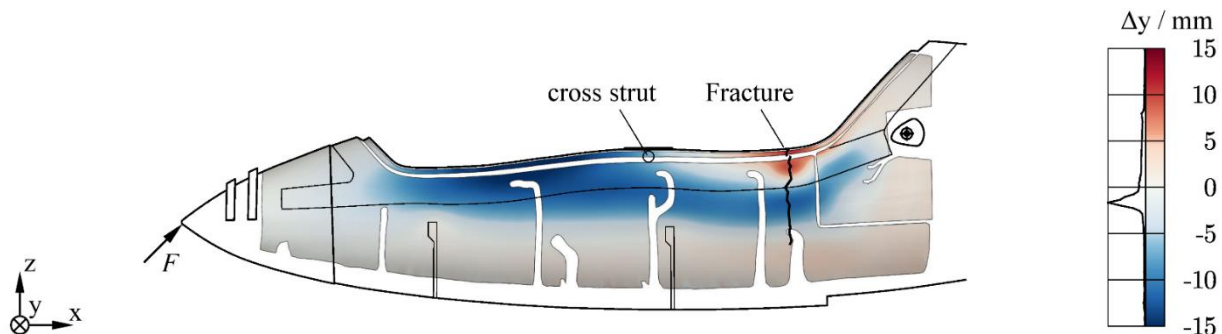
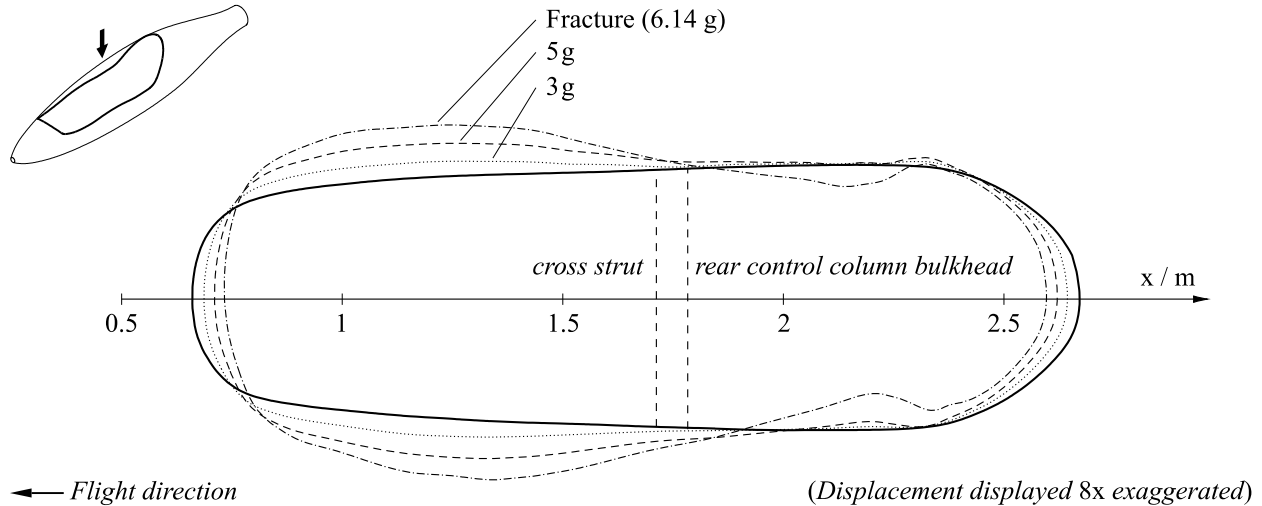


Figure 3. The ARAMIS measurements show predominantly an outward deflection of the hull at a load of 6.14 g. An inward displacement can only be observed in the area of the fracture. (blue: displacement out of the drawing plane, red: displacement into the drawing plane)

Figure 3 shows the measured deformation of the fuselage shell in the spanwise direction immediately before the fracture occurred. A widening of the fuselage shell at the position of the front pilot in the upper area is clearly visible.

The widening extends downward behind the cross tube. Shortly before the fracture, the cockpit frame shows a non-linear inward buckling deformation in the area of subsequent failure. The deformation behavior can be explained using the optical displacement analysis by evaluating the deformation in lateral and vertical direction separately.

The expansion of the cockpit frame in the front region is a result of secondary bending about the vertical axis, resulting from the pre-curvature of the cockpit frame. This behavior is known from single-seaters [6]. In the case of two-seaters, the cockpit frame can be divided into two sections, see Figure 4. The section in front of the cross strut has the greater unsupported length, which is why deformation begins in this area even at small forces and dominates the deformation of the entire frame. The cross strut between the pilots acts like a pivot joint and favors inward deformation in the rear section. Because the unsupported length is shorter in the rear section, stability behaviour is less critical here.



**Figure 4. The measurements show a widening of the cockpit frame in front of the cross strut, leading to an inward deflection in the rear area**

Below the inward buckling area visible in Figure 3, outward deformation can still be observed at the position of the rear pilot. The outward deformation is a consequence of the bending moment about the spanwise axis generated by the test force. Figure 5 shows the deflection of the cockpit frame along the vertical axis. It is clear that the deflection is greatest in front of the rear cockpit frame bend, where the ratio of bending moment to moment of inertia reaches its maximum. The lowering of the frame causes vertical forces in the fuselage cross-section which are comparable to crushing loads in a wing spar and lead to the ovalization of the cross-section. As a result, the fuselage shell deflects outward below the cockpit frame.

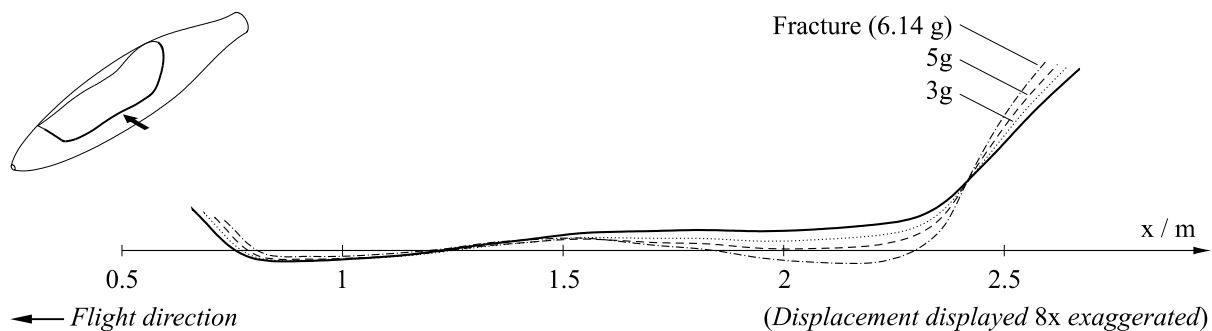


**Figure 5. The downward displacement in the rear area causes crushing loads in the cross-section resulting in an ovalization, which explains the outwards displacement of the fuselage shell**

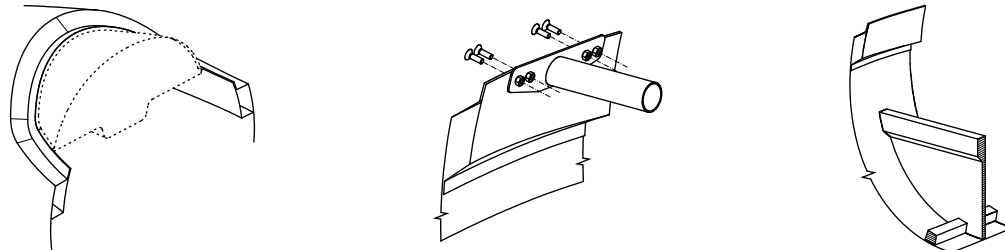
### Conclusion

The test carried out shows that the deformation behavior of two-seater cockpits differs from that of single-seater cockpits due to the pivot joint created by the cross strut. For the calculations, the cockpit frame should in no case be divided into two sections (a front and a rear section), as these would be verified independently, neglecting the pivot

joint. In order to represent the measured effects in a design calculation, nonlinear analysis is required, since the deformation effects violate central assumptions of linear methods. Against this background, it seems reasonable to carry out a load test for new designs.

The measured deformations can also be used to derive suggestions for improvements that increase the load-bearing capacity of the structure with a small increase in weight and which can be transferred to other designs. The goal of the modifications shown in Figure 6 is to reduce the lateral deformation of the cockpit frame.

Previous design



Proposed changes

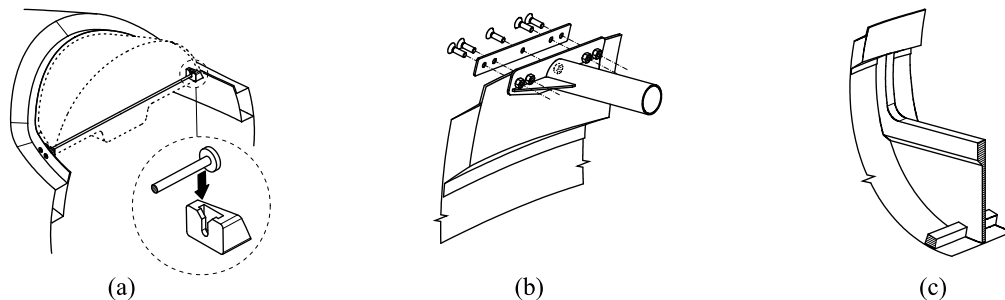


**Figure 6. The proposed changes aim to reduce the lateral deformation of the cockpit frame.**

Critical to the deformation of the frame is the large unsupported length of the front cockpit frame section, which promotes undesirable buckling of the frame in the rear. The length can be reduced by an additional cross strut in the instrument panel, see Figure 5 (a). This inhibits the lateral expansion of the cockpit frame locally, which is already at 8 mm per side shortly before the failure.

Due to plastic deformation the cross strut between the pilots is not able to prevent the widening. A more rigid connection to the composite structure is therefore necessary. This can be achieved by adding a bolted connection in the tube axis, see Figure 5 (b). When making the modification, it must be taken into account that the plastic deformation of the sheet metal has a load-limiting effect with regard to tearing out the bolted connection. With a stiffer connection, there is a risk of the bolts tearing out of the structure. An additional plate should therefore be used to transfer the load over a greater area. To reduce the pivoting joint effect of the cross strut, the aim must be to achieve a rigid connection of the cross tube. This can be achieved by using additional shear transmitting plates or by increasing the wall thickness of the connection.

To prevent buckling below the cockpit frame, additional ring frames should be used. A simple solution would be to extend the existing bulkheads up to the frame, if the available space allows, see Figure 5 (c).

## References

- <sup>1</sup>European Aviation Safety Agency, 2008: Comment response document to notice of proposed amendment 2007-12, "Cockpit crashworthiness"
- <sup>2</sup>Segal, A.M., 1989: Aircraft (full-size glider) crash-worthiness impact test, Technical Soaring, Volume XIV, No. 2, pp. 40-46
- <sup>3</sup>Röger, W., 2007: Safe and Crashworthy Cockpit, Fachhochschule Aachen, Fachbereich Luft- und Raumfahrttechnik
- <sup>4</sup>Sperber, M., 1998: Untersuchung des Insassenschutzes bei Unfällen mit Segelflugzeugen und Motorseglern, Tech. Rep. FA-Nr. L-2/93-50112/92, TÜV Rheinland
- <sup>5</sup>Kämpf, K-P., Crawley, E.F., Hansman, J., 1989: Experimental Investigation of the Crashworthiness of Scaled Composite Sailplane Fuselages, Journal of Aircraft, Volume 26, No. 7, pp. 675-681
- <sup>6</sup>Waibel, G., 2000: Designing a crashworthy cockpit sill, Technical Soaring, Volume XXIV, No. 4, pp. 109-112

## An Integrated Flight Dynamic Model for Flexible Aircraft

Michael Melville<sup>1</sup>, Götz Bramesfeld<sup>1</sup>, Julia Cole<sup>2</sup>

<sup>1</sup>Ryerson University, Department of Aerospace Engineering, Toronto, Canada, michael.melville@ryerson.ca

<sup>2</sup>Bucknell University, Department of Mechanical Engineering, Lewisburg, Pennsylvania, USA

**Abstract:** An investigation was performed into the benefits of aeroelastic tailoring on the energy harvesting capabilities of an aircraft penetrating an atmospheric gust. A potential flow based aeroelastic solver was coupled with a flight dynamic model to capture the longitudinal motion of the aircraft as it traversed through the gust. It was shown that more flexible configurations provided improved energy harvesting characteristics. The aft movement of the aircraft center of gravity due to flexibility was shown to assist in the energy extraction process, in addition to the lifting motion of the fuselage as the wing bending increases.

**Keywords:** Aeroelasticity, unsteady aerodynamics, flight dynamics, gust analysis

### Introduction

Small aircraft, such as unmanned aerial vehicles (UAVs) or high-altitude, long-endurance (HALE) aircraft, have had their designs evolve over the last several decades to incorporate slender, more flexible structures. The use of composite materials in these designs allows for high strength but low mass fractions, contributing to the highly flexible nature of these vehicles. While the use of flexible composite structures presents design challenges in terms of the aircraft flight dynamic behaviour, there are also unique opportunities to improve aerodynamic performance through aeroelastic tailoring. Aeroelastic tailoring is a passive approach commonly used with composite structures in which composite plies are placed and oriented in a specific manner to achieve a desired structural response. The application of aeroelastic tailoring can result in an overall reduction in aircraft mass as well as an improvement to the aerodynamic performance. Lupp and Cesnik [1] used aeroelastic tailoring to quantify improvements to the average cross-country speed of a sailplane. By varying the cross-sectional stiffness across the wingspan, improvements to the average cross-country speed of 2-3 m/s were observed. Melville [2] used aeroelastic tailoring to quantify the energy extracted from an atmospheric gust and how the wing performance is further improved with varying elastic axis locations. Aeroelastic tailoring has been shown in literature to provide appreciable performance improvements, warranting further investigation into its use within an aircraft design.

This paper presents a coupled aeroelastic and flight-dynamic model to investigate the aerodynamic performance improvements of a flexible aircraft encountering atmospheric gusts. A potential flow model capable of accurate induced drag predictions at a fraction of the surface resolution, when compared to a conventional vortex lattice method, is coupled with a structural and flight-dynamic model to quantify the possible performance improvements of an aircraft penetrating a gust. Aeroelastic tailoring is used through a simplified case study to determine design configurations that maximize performance increases.

### Methodology

The present method uses the potential flow based aeroelastic solver from Melville et al. [3] coupled with a flight dynamics model to predict the response of an aircraft penetrating a gust. The aerodynamics in this model are predicted using the advanced potential flow model of Bramesfeld [4], while the structural dynamics are modelled using an explicit finite difference representation of the Euler-Bernoulli beam equations, shown by Ironside et al. [5]. This method has shown good agreement with both commercial finite element software and existing numerical methods.

The flight-dynamics model for the present method considers only the longitudinal motion since only aircraft in initially unaccelerated flight encountering symmetric gusts will be studied. The fuselage is assumed to produce no lift, and thus the applied forces that govern the fuselage motion consist of the elastic reaction forces and moments from the wing and the aerodynamic forces and moments from the tail. The wing motion is governed by the structural dynamic equations outlined in Refs. 3 and 5, where the wing is assumed as a cantilevered beam that is rigidly fixed to the fuselage. The entire aircraft is free to pitch and translate in the lift and streamwise directions based on the longitudinal equations of motion and the resulting aerodynamic forces and moments from the aeroelastic solution. The goal of the flight-dynamics model is to capture the vertical and pitching motion of the aircraft when penetrating a gust, as well as

the changing forward velocity. Since an aircraft experiences a change in drag when traversing through a gust, these changes in drag results in an increase or decrease in the forward velocity [6].

**Verification**

The flexible vehicle flight dynamic model was verified against results from ASWing [7] for a theoretical HALE aircraft. The aircraft properties are described in Table 1, where  $\beta$  is a scaling factor for the wing stiffness. For the verification case, the aircraft was prescribed to fly at 10 m/s through a 75 m 1-cosine gust with a peak magnitude of 1 m/s, with the wing structure described with  $\beta = 1$ . It should be noted that for this comparison, the fuselage was modelled as a point mass in ASWing and the present method. The subsequent flight dynamic response was thus governed by the integrated aerodynamic forces rather than the elastic reactions at the wing/fuselage interface.

**Table 1. Specifications for theoretical aircraft**

Main Wing		Tail		Fuselage	
Span (m)	32	Span (m)	5	Length (m)	10
Chord (m)	1	Chord (m)	0.5	Linear Mass (kg/m)	0.2
Airfoil	NACA0012	X Offset (m)	10	Payload Mass (kg)	50
Bending Stiffness (Nm <sup>2</sup> )	$6\beta \times 10^4$	Z Offset (m)	2.5	Payload Location (c)	0.25
Torsional Stiffness (Nm <sup>2</sup> )	$3\beta \times 10^4$	Bending Stiffness (Nm <sup>2</sup> )	$\infty$		
Elastic Axis Location (c)	0.55	Torsional Stiffness (Nm <sup>2</sup> )	$\infty$		
Mass Axis Location (c)	0.25	Linear Mass (kg/m)	0.45		
Linear Mass (kg/m)	0.75	Mass Axis Location (c)	0.25		
Mass Moment of Inertia (kgm)	0.075				

The results presented in Figs. 1-4 show good agreement between the present method and ASWing. Slight differences are observed in the lift coefficient and tip deflection responses, as seen in Figs. 1 and 2. The differences seen in the lift coefficient response, specifically at the peak around 6 seconds can be attributed to the differences seen in the velocity response of Fig. 4 and tip deflection response in Fig. 2. Since a slightly lower peak velocity is predicted by ASWing as the aircraft is traversing through the gust, a larger effective angle of attack due to the gust is created, thus increasing the overall lift coefficient. Additionally, a slightly larger tip deflection change below the equilibrium point is observed; the resulting velocity experienced by the wing due to this downward kinematic motion is increased, creating an increased effective angle of attack and thus increase in overall lift. In general, the longitudinal response of the theoretical HALE aircraft is predicted quite well in comparison to a similar fidelity method in ASWing, providing confidence in using the method moving forward for more extensive gust analyses.

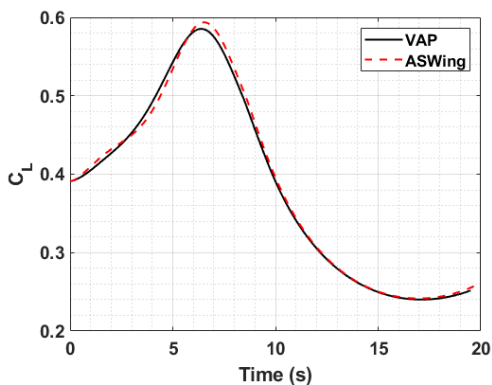


**Figure 1. Lift coefficient response of HALE aircraft.**

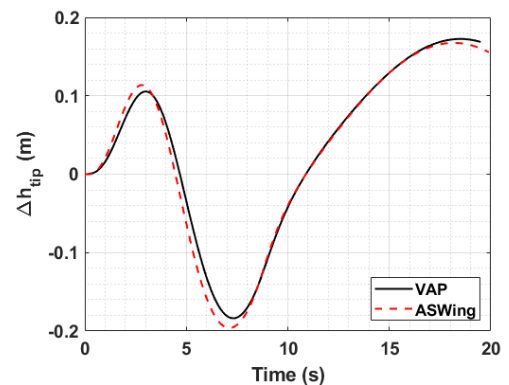


**Figure 2. Change in tip deflection from equilibrium position.**

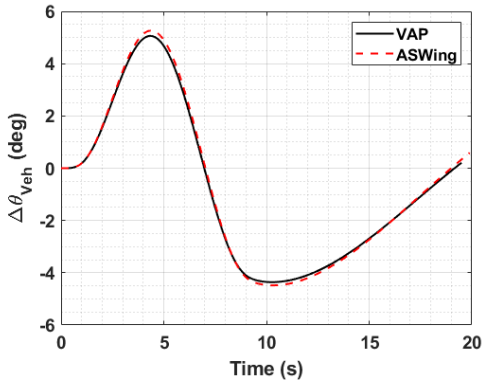


**Figure 3. Change in aircraft pitch from trim state due to 1-cosine gust.**

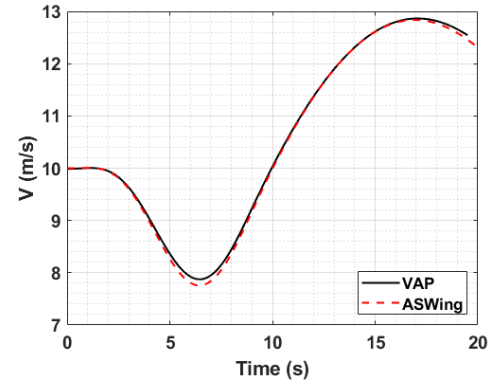


**Figure 4. Total vehicle velocity variation over time.**

### Case Study

A simple case study was performed to investigate the effects of varying stiffness on the gust energy extraction capabilities. A brief note should be made on the contributions to the energy state of a flexible aircraft before continuing. The total energy state of is described by the following:

$$E_{tot} = U_{pot} + U_{elastic} + T \tag{1}$$

where the first term represents the gravitational potential energy, the second term represents the elastic strain energy to due wing bending and the final term captures the kinetic energy of the aircraft. The elastic strain energy is a term included here that is not seen in the description by Mai [6]. In terms of an energy balance where total energy is conserved, both potential and elastic energies are exchanged for kinetic energy. The exchange of potential energy results in an increase in the total kinetic energy of the vehicle, while the elastic energy exchange results in an increase in kinetic energy of the wing as it begins to flap down or a decrease in kinetic energy as it flaps up. The energy altitude increase from a gust encounter can then be computed as follows:

$$z_e = \frac{E_{(tot)_f} - E_{(tot)_i}}{m_{tot}} \tag{2}$$

where the numerator represents the change in the total energy of the aircraft between the final and initial states (i.e., at the beginning and end of the gust) and the denominator is the total aircraft mass.

For the presented case study, the same aircraft as presented in Table 1 was used with some minor changes. The elastic axis and mass axis of the wing were moved to coincide with one another at 0.45c and the gust length was changed to 50 m with a 1 m/s peak amplitude. The aircraft remained at a freestream trim velocity of 10 m/s. Three different configurations were investigated: a highly flexible ( $\beta = 1$ ), a moderately flexible ( $\beta = 3$ ) and a stiff configuration ( $\beta = 10$ ). The energy altitude gains reported herein are for one gust length.

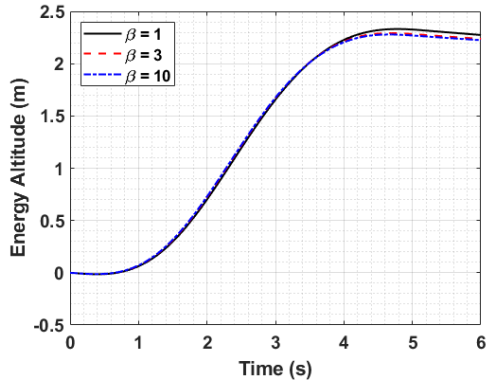


**Figure 5. Energy altitude gain of three configurations**

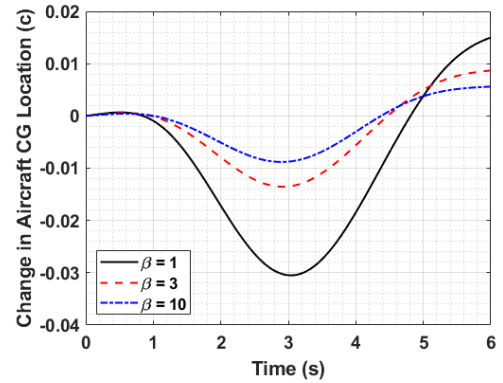


**Figure 6. Center of gravity location variation throughout gust**

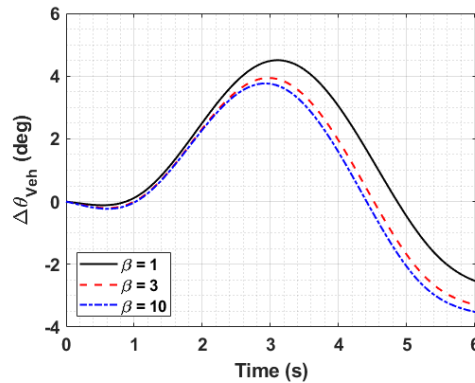


**Figure 7. Aircraft pitch variation throughout gust**

Figure 5 shows the energy altitude gains through the gust for each flexibility configuration. For the highly flexible, moderately flexible, and stiff configuration, energy altitude gains of 2.27 m, 2.23 m, and 2.22 m, respectively, were observed. The results here indicate that having a more flexible aircraft is more beneficial for gust energy harvesting; this is consistent with the results reported by Mai [6]. From the most rigid case of  $\beta = 10$  to the most flexible case of  $\beta = 1$ , a 3% increase in the energy altitude gains is observed. With very little penalty in terms of weight, careful consideration of composite fiber placements can net one significant performance gains. The mechanism through which these performance gains are achieved is through two parts. First, the more flexible configurations experience larger changes in the chordwise location of the aircraft center of gravity, as indicated in Fig. 6. Consequently, the aircraft static margin is changing as the wing bends up and down through the gust, resulting in a configuration that is less statically stable, and thus freer to pitch through the gust. These increased pitch responses, shown in Fig. 7, allow the aircraft to climb further, thus increasing its overall altitude and subsequently, energy altitude. This conclusion is also consistent with what is shown by Ref. 6 in which a reduced static margin provided increased energy altitude gains. Additionally, with a more flexible configuration, the elastic energy stored in the wing through the gust is increased; as the gust magnitude diminishes, this stored elastic energy is exchanged with kinetic energy in the wings as they begin to flap down, increasing their overall lift and thus lifting the fuselage upwards.

### Conclusions

A simplified case study was performed to quantify the effects wing flexibility has on the energy harvesting capabilities of an aircraft penetrating an atmospheric gust. Performance gains up to 3% were seen as wing flexibility was increased, holding fixed the elastic and mass axis locations. Further gains are expected to be possible if one allows for the spanwise variation in both the elastic axis and bending and torsional stiffnesses. Further work is to be done to quantify the effects of adding these additional design variables to the aeroelastic tailoring process.

## References

- <sup>1</sup>Lupp, C. A. and Cesnik, C. E., "Aeroelastic Tailoring for Maximizing Sailplane Average Cross-Country Speed," *AIAA Atmospheric Flight Mechanics Conference*, Dallas, TX, June 2015.
- <sup>2</sup>Melville, M., Bramesfeld, G., Kolaci, A., and Alighanbari, H., "Aeroelastic Tailoring for Gust-Energy Extraction," *Journal of Aerospace Engineering*, Vol. 33, No. 4, 2020.
- <sup>3</sup>Melville, M., Kolaci, A., Bramesfeld, G., and Alighanbari, H., "An Efficient Model for Aeroelastic Tailoring of Aircraft Wings Under Gust Loads," *2018 Aerospace Sciences Meeting*, Kissimmee, FL, Jan. 2018.
- <sup>4</sup>Bramesfeld, G., *A Higher Order Vortex-Lattice Method with a Force-Free Wake*, Ph.D. thesis, Pennsylvania State University, Aug. 2006.
- <sup>5</sup>Ironside, D., Bramesfeld, G., and Schwochow, J., "Modeling of Wing Drag Reductions Due to Structural Dynamics in Atmospheric Gusts," *28th AIAA Applied Aerodynamics Conference*, Chicago, IL, July 2010.
- <sup>6</sup>Mai, H. U., "The Effect of Aeroelasticity Upon Energy Retrieval of a Sailplane Penetrating a Gust," *XIXth Congress of OSTIV*, Rieti, Italy, Aug 1985.
- <sup>7</sup>Drela, M., "Integrated simulation model for preliminary aerodynamic, structural, and control-law design of aircraft," *40th Structures, Structural Dynamics, and Materials Conference and Exhibit*, St. Louis, MI, April 1999.

## A climatology of soaring conditions in Eurasia

Bruno Neininger<sup>1</sup>, Alvaro de Orleans-Borbon<sup>2</sup>

<sup>1</sup>MetAir AG, Switzerland, [bruno.neininger@metair.ch](mailto:bruno.neininger@metair.ch)

<sup>2</sup>private, competition glider pilot, organiser of the First Himalaya Soaring Expedition in 1985

**Abstract:** Today's global general circulation models (GCM) have reached a spatial resolution that is sufficient for assessing the daily potential for good soaring conditions all over the world. Within this study, such publicly available archived data was used for an analysis of six soaring seasons for parts of Europe, Africa, and Asia. The motivation was the planning of an expedition by a group of pilots intending to soar along the historical Silk Route from Europe to China, along a total distance of about 9.000 km. The results of this focused climatology should help to plan the route both geographically, and seasonally. The first results are very promising, can be refined by calibrating the method using known long-distance flights, and could as well be applied to other regions of interest.

**Keywords:** soaring, gliding, climatology, seasonal task planning, application of global circulation models.

### Introduction

The sport of soaring has evolved extraordinarily, but the long term vision was there from the beginning, considering what had already been published in 1922 [1] – by then, only a 50 m height gain and a 2000 m glide had been achieved – where the author therein not only recognizes the existence of usable thermals but “...leaves to future developments how to exploit turbulence and varying wind fields”, i.e. what today is known as “dynamic soaring” and exploited by aeromodellers with spectacular performances [2].

During the last century, the mark of excellence within the sport of soaring has correspondingly evolved through profound changes – from duration to distance and speed, each new “challenge horizon” has spawned new theories, generated new tools and gradually changed the pilot’s perspectives.

Somewhat phylogenetically, this evolution is still recognizable during the three main development stages of a modern soaring pilot, first learning to control the sailplane, then using it to extract local energy from the atmosphere (flying in thermals and waves) and finally integrating all this knowledge to fly cross country, including competitions and distance or speed records.

Now a *fourth stage* is timidly but clearly appearing, still without a universal label, loosely defined as long range, adventure, or exploratory soaring and represented by extended, even intercontinental soaring expeditions such as those carried out by Karl Striedeck, Friedrich Schneider, Winfried Boos, and a few other [3].

One such expedition has been planned during the last two years by a group of pilots intending to soar along the historical Silk Route from Europe to China, along a distance of some 9.000 km.

Such a novel undertaking, as in the past, has generated a corresponding need for new planning tools.

One such new tool, the object of this publication, responds to a specific need: how to plan the timing of a multi-month soaring expedition through widely different seasonal, geographical, and meteorological areas, so as to easily assess and visualize the potential daily flying distances and build up the corresponding calendar and logistical framework for the whole expedition.

More precisely: which are the general meteorological conditions to be expected along the route for any given place and day of the year? Will there be sufficient convection (thermals), enabling cross-country flights of several hundred kilometres distance? And most importantly, how much do these conditions vary during each month of the year?

Consulting individual routine weather information along possible routes in past years would not facilitate the planning phase – too much dispersed and widely different information hampers the numerous “what if” considerations, mostly of a logistical nature. One main question thus became how to visually map the varying distance flight potentials to easily absorb the underlying information for planning purposes, based on homogeneous weather data. The method described here offers one solution which could also be applied and tested for other regions with sparse existing information about the potential for long-distance soaring.

## Methodology

Glider pilots are used to consult daily forecasts – maybe up to a couple of days in advance for getting an idea if it will be worth going to the airfield, well knowing the limited reliability of the details in such outlooks. However, when building a climatology (a statistical representation of *past* conditions) the available data is *analysis* data that is much more reliable than a multi-day *forecast*, especially for details such as cloud cover, insolation, or rain (derived from satellite and radar data for the time of the analysis). The analysis or 'assimilation run' of any global circulation model (GCM) is integrating all available measurements worldwide [4]. When analysing retrospectively if a certain day in a certain place fulfilled some basic criteria for good thermal soaring conditions, the answer is relatively simple: enough sunshine to maintain a super-adiabatic layer near the surface for several hours, a temperature and humidity profile allowing the convection to reach sufficient height above the surface, and no disturbing factors such as rain, or excessive wind. All these parameters can be found in archived data of GCMs such as GFS [5], or others (ECMWF, ICON, etc., where the choice of the model is not dominated by the forecasting skill, but by the public availability of high-quality analytical data from the assimilation runs at sufficient resolution).

Some specifications of the downloaded archived GFS analyses are summarised in table 1. This data allowed to assess the soaring conditions for a variety of seasonal ensembles within map-pixels of roughly 50 km size. The applied criteria are summarised in table 2. As a next step, the algorithm combined neighbouring pixels in a desired direction (in this application proceeding eastwards, i.e., to NE, E, or SE), estimating the daily potential eastward flight distance (pfd).

The operation height was calculated based on the vertical profiles of temperature and humidity. In the dry case this is the height where the virtual temperature near the surface was falling below the virtual temperature aloft. Using the virtual potential temperature included the reduced density of moist air, and the adiabatic cooling within the thermals in an elegant way. When condensation occurred (forming Cu), the operation height was limited by the cloud base.

Table 1: Accessed archived data from NOAA [5]	Table 2: Selected data and applied criteria
Coverage of the packed (grib2) data: global	Selected region: 30° to 60° North / 0° to 120° East
File size for each 3-hour-period: 50 to 100 MB	Used vertical levels: 21
Spatial resolution: 0.5° lat/long	Used profile parameters: temperature, dew point, wind
Temporal resolution: 3 hours	Used surface parameters: radiation balance, sunshine duration, temperature, near-surface temperature gradient, dew point, wind, precipitation
Number of vertical levels <sup>1</sup> : 35	H: Minimum operation height above average terrain: 1.000 m
Number of profile parameters <sup>1</sup> : 15	M: Assumed minimum speed when H is sufficient <sup>2</sup> : 60 km/h
Number of surface or integrated parameters <sup>1</sup> : 42	B: Assumed average speed in best conditions <sup>2</sup> : 120 km/h
Downloaded months: March to September 2014 to 2019	W: Maximum allowed wind speed within H: 50 km/h
	R: Maximum rain within any 3-hours-period: 2 mm

<sup>1</sup> typical for the data for the year 2018; growing numbers between 2014 and 2019

<sup>2</sup> The net travel speed was scaled between M and B proportional to H; tail- or nose-wind was added or subtracted thereafter.

## Results

The daily results were aggregated per month for a visualisation of these statistical quantities on maps: (i) The average pfd per pixel (i.e. for local flights within the pixel); (ii) the average pfd towards the east (combining pixels in eastern, north-eastern, and south-eastern direction); (iii) the percentage of days where a daily eastward flight of at least 500 km distance should have been possible, (iv) the percentage of days with visible convection (cumuli), and (v) the percentage of days where rain or wind was the limiting factor. The figures 1 to 4 are showing a few examples; the whole collection of maps (both as PDF and as KMZ for Google-Earth) can be downloaded from the electronic supplement [6].

First conclusions from this set of preliminary results:

- From a European perspective, the soaring conditions are much better and starting earlier east of the Bosphorus.
- Even in June, conditions are improving east of about 15° longitude (negative influence from the Atlantic?).
- The region between the Black Sea and the Caspian Sea might be a barrier.
- The relatively humble results for Europe are indicating that the chosen criteria (table 2) are rather conservative, i.e. the conditions could be even better than these maps are suggesting (see the discussion).

flying eastwards [km] in March 2014-2019

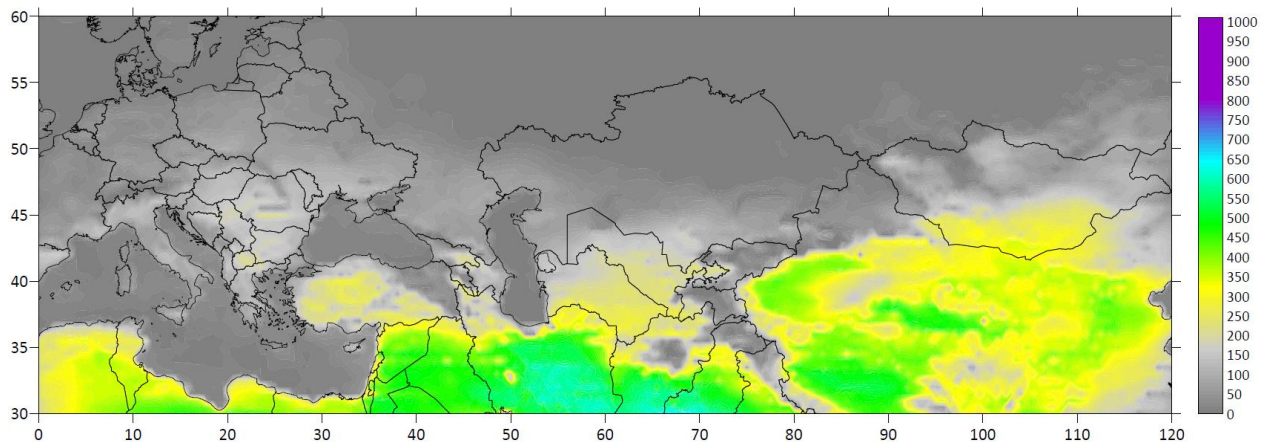


Figure 1: Already in March, the soaring conditions east of the Bosphorus are becoming acceptable.

percentage of 500 km flights in all June 2014 to 2019

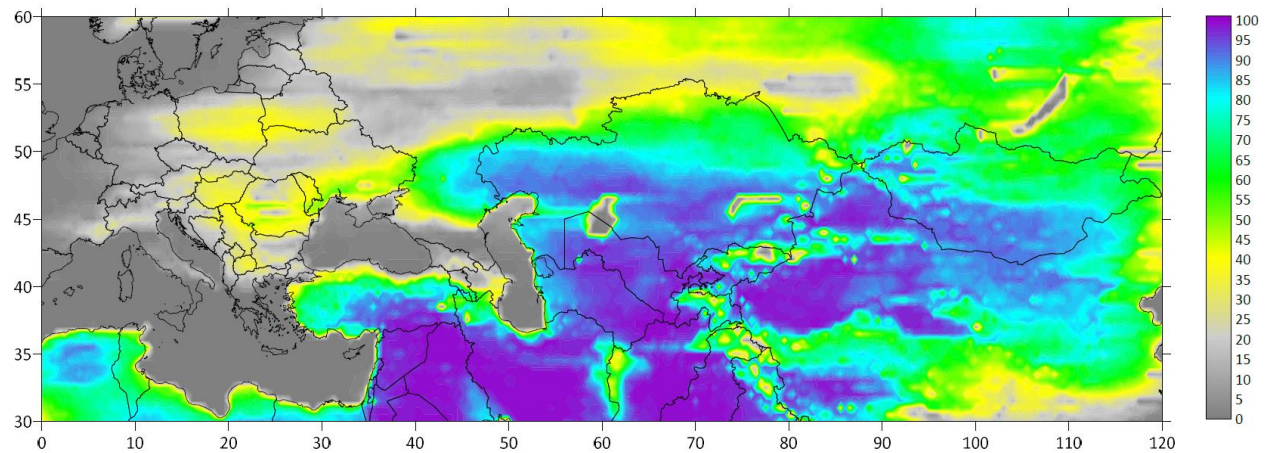


Figure 2: In June, most regions east of the Bosphorus are offering 500-km-flights more often than every second day, with a wide gap east of the Black Sea (see the average pfd's with up to 1000 km per day in [6]).

percentage of Cumuli during active Convection in all May 2014 to 2019

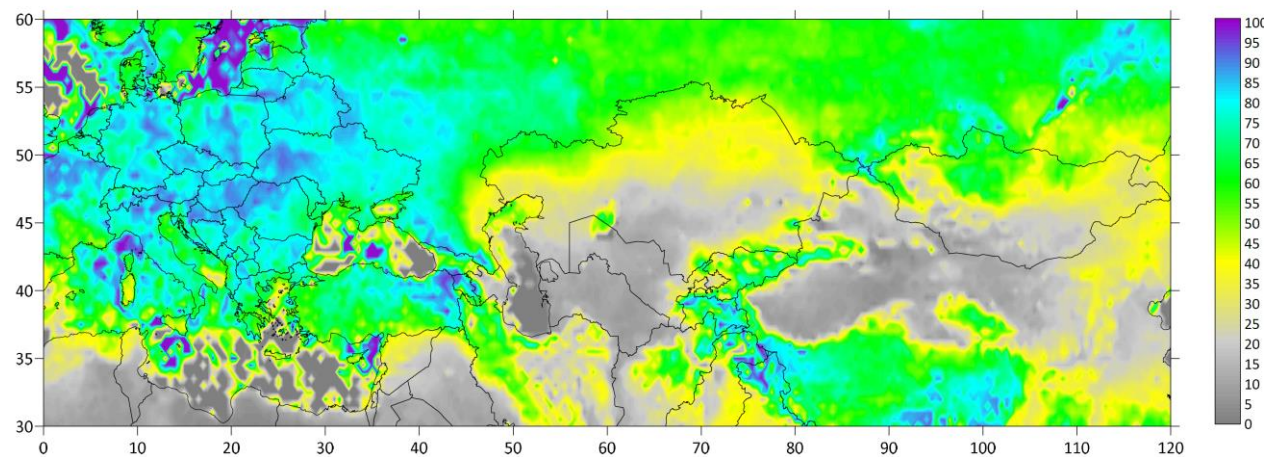
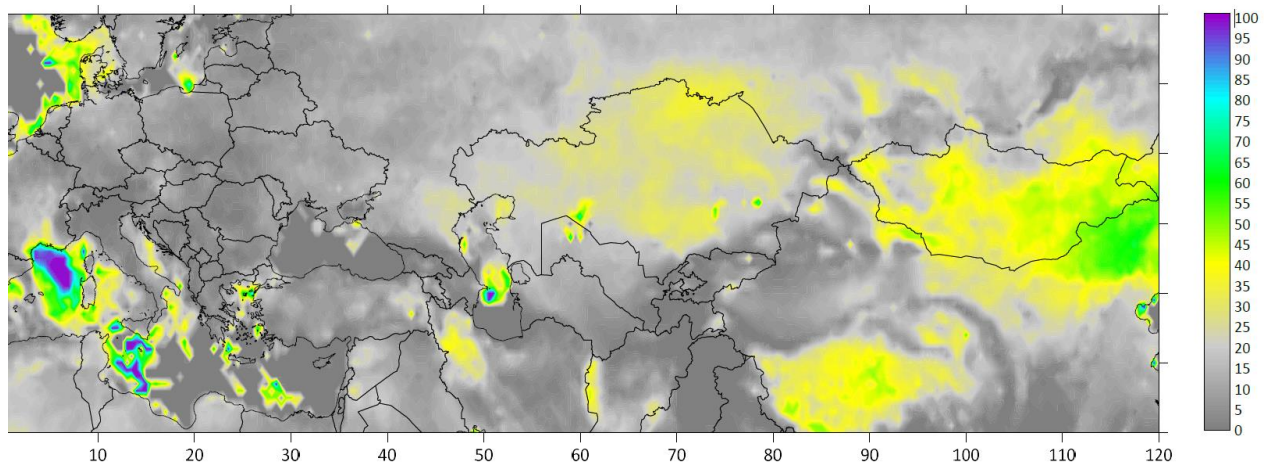


Figure 3: Within the blue to purple regions, thermals are marked by cumuli during more than 75 % of the days, while over the yellow and grey dry regions, this is far less the case.

percentage of Limitation by Wind all May 2014 to 2019



**Figure 4: One example of a map showing wind as the limiting factor, i.e. yellow to green means that about 30 to 60 % of the days, thermals were most likely disrupted by too much wind (> 50 km/h according to table 2). This deterioration is already included in the overall results as shown in figures 1 and 2. An interesting detail (not relevant for this study) is the obviously high frequency of 'Mistral' near 5° longitude.**

### Discussion

Of course, all these results are depending on the defined criteria (table 2) and do not yet consider details like mountain effects such as enhanced thermal activity [7], slope winds, or lee-waves. However, the average terrain elevation of the pixel was included in the calculations, and the primary inputs like the radiation budget, humidity, etc. are already represented in sufficient resolution by the GCM itself, disqualifying e.g., zones with sea-breeze. For all these neglected influences it can be stated that they are rather leading to an underestimation of pfd's than to an overestimation. On the other hand, this purely meteorological climatology is ignoring important practical aspects like political borders, non-flying areas either by legal or safety reasons, etc. However, it would be relatively simple to bring them in. For the moment, such non-meteorological considerations must be considered manually for a concrete planning.

In order to adjust the criteria for achieving an even better estimate of seasonal soaring conditions, validations by recorded long-distance flights would be most valuable. For doing this, the results for specific days could be picked out and compared with competition results, or record flights. The main aim of this paper is to show that useful data is accessible, and the way to informative map products is not that complicated. The high performance of today's GCM – even for decisions for five days in advance - was already demonstrated by the successful flight around the world by the Solar Impulse adventure [8]. The authors of this article are ready to share the tools developed during this short study, aiming to improve the criteria and the algorithm by comparing with real flights, or applying them to other regions. Any feedback is welcome.

### References

- [1] Kurt Wegener, 1922: Vom Fliegen. Verlag Oldenbourg, Part 1, Chapter 16. <http://d-nb.info/57868506X>
- [2] The 882 km/h Sailplane and Dynamic Soaring, 2017 (<https://www.youtube.com/watch?v=nv7-YM4wno8>) and the pdf in [6].
- [3] Winfried Boos, 2018: Comme Les Cigognes, und andere Segelfliegergeschichten eines Genusspiloten. Private print that will be re-printed upon request.
- [4] Peter Bauer, Alan Thorpe, Gilbert Brunet, 2015: The quiet revolution of numerical weather prediction. Nature, Vol. 525, doi:10.1038/nature14956. <https://www.nature.com/articles/nature14956>, plus a copy in [6]
- [5] <https://www.ncdc.noaa.gov/data-access/model-data/model-datasets/global-forecast-system-gfs>
- [6] Electronic supplements in <https://drive.switch.ch/index.php/s/TfDwbYfhus5TAwM> with PW 'OSTIV\_2021'.
- [7] Bruno Neining, 2021: Status report about AlpTherm\_2 as a fully revised convection model, in this conference.
- [8] <https://aroundtheworld.solarimpulse.com/eng>

## Wave Flying Experiences - Examples of Observations and its Interpretation

Carsten Lindemann

*Freie Universität Berlin, Germany, carstenl@zedat.fu-berlin.de*

**Abstract:** This report contains experiences of thermal waves, gravity waves and lee waves in Central Europe mostly of the season 2019/2020. An example of a Central Europe Morning Glory, thermal waves of different levels connected to clouds, and mountain waves will be presented. All these waves were detected by glider pilots and are now being forecasted.

**Keywords:** Thermal waves, mountain waves, and model examples

### Introduction

Gravity waves and thermal convection present a normal physics of the lower atmosphere from the surface level up to the stratosphere. The combination of both is a general feature of mountain waves having the laminar wave structure and underlying rotors. The so named Thermal Waves were detected in the 60ties of the last century having wavy structure without being connected to any obstacle. Examples will be given.

### Examples of wavy structures

#### The Hattingen Morning Glory

A sudden rapid wave like cloud system was observed on Christmas day in NW Germany – for discussion. Two photos and a time lapse sequence will be presented.



**Thermal Waves or waves in areas of no obstacles or mountains Obstacle**

#### Cloud Obstacle Thermal Waves

Individual waves formed at singular cumulus seem to move with the wind at top of convection. Principle of mechanism and examples will be shown.

#### Cloud street waves

Generally thermal waves were separated into thermal waves at isolated clouds and thermal waves connected to cloud streets, which approximately rectangular to the upper wind. The latter is indeed a very rare situation. Most of the

thermal waves observed with cloud streets found and flown by glider pilots in Germany had an upper wind field with an essential wind shear but nearly a very low wind velocity within the convection layer. the upper wind field seem to form the convection streets below and not the lower (mostly about 2-10 kts) wind in these cases.

### **Free oscillations at different levels**

#### **By a second upper inversion**

Several wave bands were found in satellite pictures and there was a convection layer below. But no flights reaching the wave clouds were documented. Two inversions were detected by radio soundings. The first inversion limited the convection layer with or without cumulus clouds and a second inversion some hundreds of meters above reaches into the wind shear.

#### **By a humid layer**

The observer is sometimes surprised when looking for satellite pictures showing parallel bands of clouds perpendicular to the upper wind and no flight report is documenting this by using such bands. Wind shear values seem to be sufficient for cloud street waves. The bands were formed at humid layers. They are more humid waves than thermal waves.

### **Experiences**

Some shear und inversion values will be given. Some flights were done for detecting waves but with no success.

### **Lee Waves**

There were about 50 flyable days during the winter season of 2019/2020 in the area of Altvatergebirge/Hruby Jeseník (CZ) and at Harz mountains in Germany. Most flights are done regularly at Jeseník, because of the position of the airfield (Mikulovice) to the higher mountains, and of more favorable wind directions.

It could be found that maximum altitudes were mostly gained by classical mountain wave parameter so as published by WMO. But there were several cases with nearly no wind shear and even wind velocity decrease with altitude, the latter more at Hruby Jeseník.

Some of the cases with wind conditions decreasing with altitude had strong lower wind from ground up to altitude approximately near to the mountain heights producing a wave *forced* more by the by the obstacle itself and not by the oscillation ability by the atmosphere. This forced wave extended further upward for thousands of meters into layers with nearly no wind. This seems to be valid only for higher mountains and not for the lower ones. These observations result in a statement:

***The lower the mountain the more the classical parameters of wind shear and temperature inversion must be fulfilled. Higher mountains can produce waves by a strong wind field in lower layers.*** This was detected and measured by gliders.

### **Models**

Some characteristics of models forecasting waves will be presented for two days at Harz.

### **References**

Carsten Lindemann, 1970: Leewellen in der Flugmeteorologie, Abhandlungen Band 89 Heft 4 Institut für Meteorologie der FU Berlin

Herbert Horbrügger, 2012: „Thermikwellen“ DM 2011 Lüsse, Report at Schwerewellenseminar in Göttingen

## Ascend Mount Everest via paraglider?

Edward Hindman

*The City College of New York, Earth and Atmospheric Sciences Department, USA, ehindman@ccny.cuny.edu*

**Abstract:** On 23 July 2016, 8,051 m Broad Peak in the Karakorum range of the Himalayas was ascended by Antione Girard through soaring flight with a paraglider. I analyzed the flight record to determine the glider performance and wind conditions and used the results with the soaring meteorology of 8,848 m Mount Everest to investigate the possibility of a similar ascent of Everest from Tibet. A safe ascent and descent appear possible in late April and early May during the almost daily convective period when the summit-level winds are from the northwest and less than 15 m/s. I identify necessary diplomatic and logistical preparations and propose solutions.

**Keywords:** Soaring Mt. Everest, Himalayan soaring meteorology, Himalayan paragliding.

### Introduction

From the Rongbuk Monastery, at the base of Mt. Everest in Tibet in late April and early May 1996, I made surface measurements and observations during a trans-Himalayan meteorological expedition [1, 2]. They revealed strong convection. I and my colleagues investigated the possibility that this convection could enable a soaring ascent of Everest by gliders using a numerical model initialized by local measurements [3]. On the few days with the warmest and driest surface conditions and no stable layers aloft, cloud-free thermals were predicted strong enough to carry a glider to the summit. To date, no soaring ascent has been attempted to my knowledge. But on 23 July 2016, 8,051 m Broad Peak was ascended via paraglider [4]. This flight inspired the following study of the possible soaring ascent of Mt. Everest via paraglider.

### Methodology

#### *Paraglider glider performance*

I used SeeYou to analyze the file recorded aboard the paraglider during the Broad Peak flight. The flight consisted of three segments: launch to the base of the peak, the climb of the peak and the final glide to landing. For the first two segments, I determined the average forward speed and climb rate and for the last segment the glide speed. I used these values along with wind data from the Tibet-side of Mt. Everest to compute the expected flight path to and from the Everest summit.

#### *Meteorology*

Broad Peak is located in the dry, land-locked western region of the Himalayan Mountains. Mt. Everest is located in the eastern Himalayas between the moist plains of India and dry plateau of Tibet. The soaring ascent of Broad Peak was during the optimum climbing period, June and July. Similarly, the soaring ascent of Mt. Everest would be during April and May when most climbing ascents are made.

Knowledge of the surface winds and winds aloft is essential for safe flights. The wind speed must be less than the forward speed of the paraglider for the craft to advance. I used wind measurements made by Chinese meteorologists to identify safe flight periods. They made rawinsonde measurements from Old Tingri in Tibet near the base of Mt. Everest during May 1979, reported in [3] and wind measurements in May and June 2006 [5] at the monastery where I made measurements. Our surface measurements agree.

### Results

The area of the proposed flight on the north side of Mt. Everest is illustrated in Figure 1. The left image, extracted from the 1988 U. S. National Geographic Society map, illustrates the topography. The right image was constructed from that map. The **red line** in both images identifies the common ridge line.

I determined the winds in Figure 1 as follows. A north-flowing, shallow, down-valley ‘glacier wind’ [5] is common beginning around 12 local standard time (LST) at the north Everest base camp, the proposed launch and landing site. At the nearby ridge, a 2.6 m/s across-valley wind [5] should enhance a thermally produced upslope flow. I used SeeYou to calculate an across-valley wind of 2.6 m/s from the Broad Peak flight record; SeeYou resolved the drift of the craft during circling flight while ascending in thermals. As in the approach to Broad Peak, the upslope flow is expected to enable a slow, ascending flight toward Everest. The 10 m/s wind at Bei Peak and the 15 m/s wind at the

Mt. Everest summit were taken from the Chinese rawinsonde measurements displayed in [3]. The 15 m/s wind is near the maximum value to allow the paraglider to glide from the Everest summit safely back to the launch site.

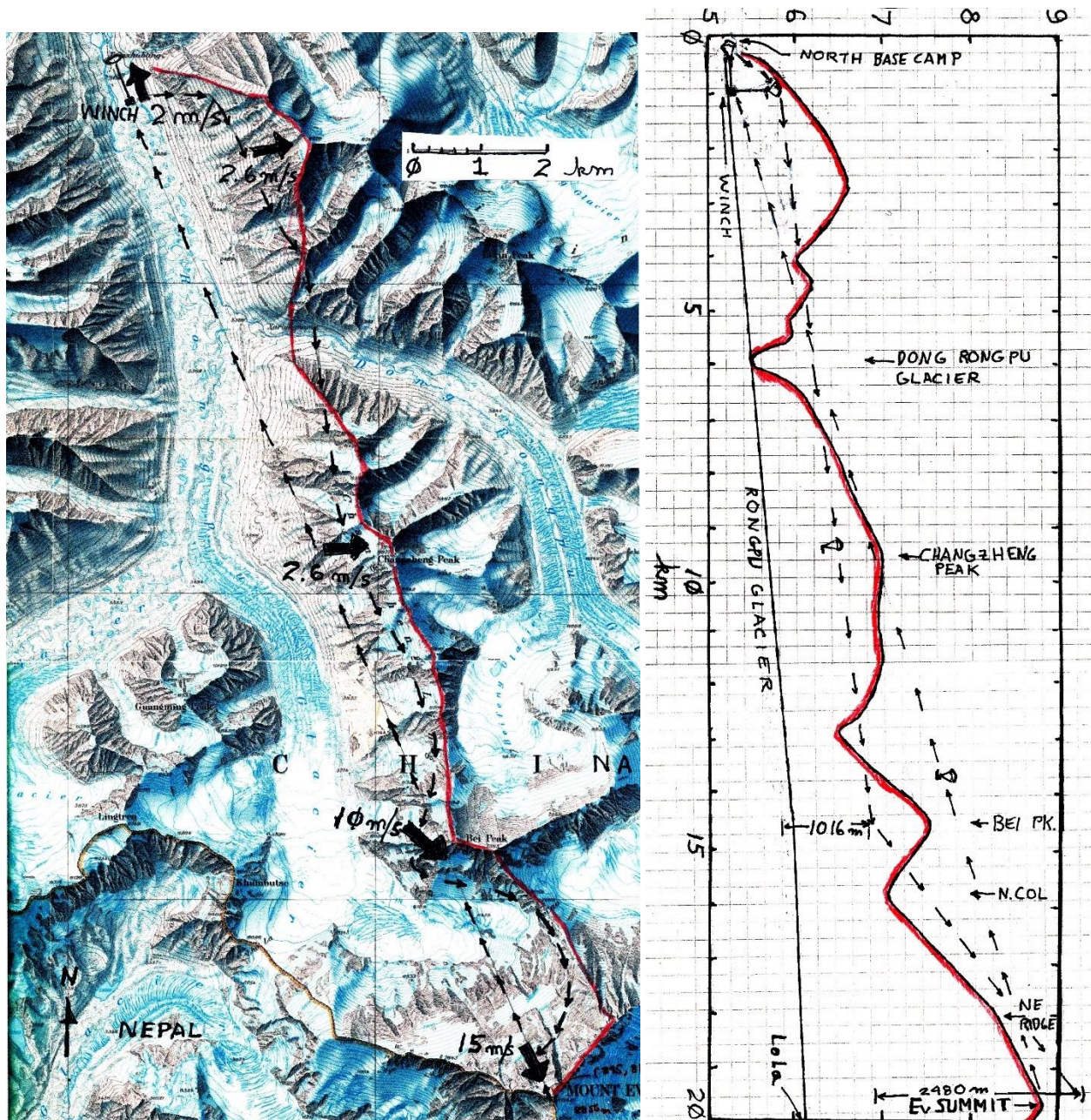


Figure 1. Left: the topography of the north-side of Mt. Everest. Right: the cross-section along the red ridge common to both images. The solid arrows are the expected winds and the dashed arrows identify the expected flight path.

The expected flight path to the Mt. Everest summit is illustrated in Figure 1. A winch would be used to launch the paraglider above the shallow ‘glacier wind’. The first segment from launch to abeam of Bei Peak is a distance of 14.5 km (Figure 1, right). This path is similar to the path along the slopes above the Baltoro Glacier from launch to the base of Broad Peak which is 47 km in length. The first segment of the Broad Peak flight began at an elevation of 4704 m and ended at an altitude of 5720 m at the base of the first thermal at the beginning of the ascent. The altitude gain was 1016 m and the average forward speed and climb rate were, respectively, 4.5 m/s and 0.1 m/s. These values are

expected to be achieved by the paraglider flying toward Everest along the slopes above the Rongpu (Rongbuk) Glacier. Using the forward speed value over the 14 km segment results in a flight time of 0.86 h from launch to Mt. Everest. The second flight segment from Bei Peak to the Everest summit is a distance of 5 km (Figure 1, right), a distance similar to the distance during the ascent of Broad Peak. This segment follows the ridge line from Bei Peak crossing the North Col and ascending the NE Ridge to the summit. The Broad Peak values are used to construct the path: the average forward speed was 0.81 m/s and climb rate was 0.41 m/s. The Broad Peak path began at an altitude of 5720 m and ended at 8200 m for an altitude gain of 2480 m. The resulting path, shown in Figure 1 (right) clears the Everest summit. Using the 0.81 m/s forward-speed value over the 5 km segment results in a flight time of 1.7 h.

The third flight segment, from the Everest summit to landing back at the base-camp launch site, is a distance of 20 km. The maximum glide speed from the Broad Peak summit to the base of the first thermal was 24 m/s. Flying at this speed into a worst-case 15 m/s headwind will take 0.62 h to return to the launch site.

Thus, the total flight time over the proposed flight from the Everest north base camp to the summit and return is  $0.86 + 1.7 + 0.62 = 3.2$  hours.

### Discussion

The proposed 3.2 h paraglider flight would occur during a 3-to-4 hour convective period. I determined the period as follows. The surface wind measurements at the Rongbuk Monastery [2, 5] show the surface convection begins about 10 LST and the onset of the downvalley ‘glacier wind’ begins at about 12 to 13 LST. Additionally, the images in Figure 2 taken from the Monastery on 28 April 1996 [1] illustrate convective clouds formed between 09 and 12 LST and dissipated between 15 and 18 LST. My notes describe the conditions: “1200 LST- Increasingly strong flow toward Ev, stirring up dust at Monastery with cumulus overhead swirling violently. Cumulus with ~8000 m bases forming upwind then enveloping the summit! 1300 LST- do wash in warm sun watching 8000 m based cumulus form upwind Everest...’Soar Everest’ day from the north”.



0900 LST



1200 LST



1500LST



1800 LST

**Figure 2. Convective cloud development and dissipation over the Rongbuk Valley in Tibet on 28 April 1996. LST is local solar time, Z + 6h.**

In Figure 2, the proposed launch site is seen behind the tip of the Monestary prayer flag support. Comparing the 0900 and 1200 LST images, convective clouds are seen forming in Nepal along the 7000 m ridge separating Tibet and Nepal. These clouds often deepen quickly in the afternoon as documented by climbers (e.g. [6]) obscuring the summit. So, the convective period that should enable soaring flight is, conservatively, 10 to 14 LST.

To insure a safe flight, there must be careful and thorough preparations. First, short flights should be made from the base camp to learn if soaring is possible. With experience, flights along the ridge to the Dong Rongpu Glacier can be attempted. In the event of a forced landing, the flight path is along the main trail from base camp to advance base camp (ABC). Flights beyond this point along the main Rongpu Glacier to the northwest face of Everest would be over untrekked ground. A forced landing should be possible just east over the ridge on the trail to ABC. The camp is east of the North Col at the head of the East Rongpu Glacier (Figure 1-left).

The meteorological systems are in place to support the proposed flight. A series of automatic weather stations was installed in May 2019 from the base of Everest to the South-summit on the Nepal-side [7]. These stations are capable of transmitting wind measurements in real-time. Real-time cloud images of the region can be received every 10-minutes from the HIMAWARI-8 geosynchronous meteorological satellite. Numerical weather predictions are made for the region every-three hours by the READY.ARL.NOAA.gov.

The diplomatic and airspace clearances should be accomplished by imbedding the proposed flight in a possible Chinese study to expand the meteorological measurements made by H. Zhou and colleagues [5]. Also, a sport expedition might support the proposed flight. Tibet's first paragliding competition was conducted near Lhasa in October 2018. The FAI-Hang Gliding and Paragliding Commission may be a conduit to paragliding in Tibet.

Logistics can be handled through a trekking agency based in Lasha. For example, Himalayan Glaciers.

### Conclusions

The soaring ascent of 8051 m Broad Peak via paraglider [4] produced flight and meteorological data that I used to explore a similar ascent of 8848 m Mt. Everest from Tibet. I constructed a flight path from these data including launch to the base of the peak, ascent of the peak and glide back to the launch site. The flight would likely take 3.2 hours to fit within the approximately 4 h daily convective period during late April and early May. I identify the necessary preparations: diplomatic and airspace clearances, meteorological and logistical support and the practice flights.

### References

- <sup>1</sup>Hindman, E. E., 1999: Soaring weather at the top of the world, *Tech. Soar.*, **23/2**, pp 52-57.
- <sup>2</sup>Hindman, E. E. and Upadhyay, B. P., 2002: Air pollution transport in the Himalayas of Nepal and Tibet during the 1995-1996 dry season, *Atmos. Environ.*, **36**, pp. 727-739.
- <sup>3</sup>Hindman, E. E., Liechti, O. and P. Lert, 2002: Soar Mt. Everest, *Tech. Soar.*, **26/4**, pp 114-123.
- <sup>4</sup>Hindman, E. E., 2021: 8051 m Broad Peak ascended via paraglider, *Tech. Soar.*, in review, 16 pp.
- <sup>5</sup>Zou, H., and colleagues, 2008: Local wind system in the Rongbuk Valley on the northern slope of Mt. Everest, *Geophys. Res. Lett.*, **35**, 7 pp.
- <sup>6</sup>Venables, S., 1989: Everest Kangshung Face, *Rupa & Co.*, pgs. 151, 152, 156, 175.
- <sup>7</sup>Matthews T, et al., 2020: Going to extremes: installing the world's highest weather stations on Mount Everest. *Bull. Am. Meteorol. Soc.*, **101/11**, E1880–E1890.

## Satellite Observation of a Deep Convective Storm Top at Kastamonu, Turkey - A Case Study.

Sema ÇİL<sup>1,2</sup>, Haneen Qusay Adeeb<sup>1</sup>, Rusul Abd Al-munaf Al-bayati<sup>1</sup>

<sup>1</sup>Istanbul Technical University, Atmospheric Sciences, Istanbul, Turkey [sema.cil@itu.edu.tr](mailto:sema.cil@itu.edu.tr)

<sup>2</sup>TSMS, Turkish State Meteorological Service, Department of Remote Sensing, Ankara, Turkey

**Abstract:** Overshooting tops of storms and pre-environment of occurrence, their initiation, and mature stage of them are analysed with various geostationary satellite images from MSG. In addition to satellite observations, radar reflectivity and synoptic analysis of the atmosphere are also utilized to enhance the knowledge about the intensity of storm. The results display the severity of storm for the area of interest. For further cases, MTG (Meteosat Third Generation) satellites with lower temporal resolution (more frequent images every 5 min) and higher spatial resolution will be a crucial tool for both weather forecasters and meteorologists for understanding convection.

*Keywords:* Convective storm, cold ring, Cloud top height, Overshooting top

### Introduction

Thunderstorms are one of the major hazardous meteorological phenomena, especially deep convective storms with overshooting tops can produce severe weather conditions such as heavy rainfall, damaging winds, large hail, and tornados. However, the complex nature of convective processes sets specific limitations to their observation, analysis, and forecasting. Thus, the assessment of their characteristics is essential for an effective national climate and weather prediction service. This study aims to analyse a moist convective thunderstorm on 13th September 2018 at Kastamonu, Turkey. On this thunderstorm, the city centre of Kastamonu had heavy rainfall approximately 50mm/h and got large hail on walnut-size had approximately 3cm diameter in only 20 minutes (14.45 UTC – 15.05 UTC) period. According to local authorities, 2357 houses and 8908 vehicles damaged in varying severity in the city centre.

### Methodology

The lifecycle of the deep convective storm is analysed in three phases as Pre convective environment, Initiation of convection, Mature stage of convective storms, which is recommended by Convection Working Group (CWG) – EUMETSAT. The methodology, which is taken into deep consideration on this case study, adopted from the studies of Setvák et al., 2010, and Setvák et al., 2008 from the literature.

The data provided by EUMETSAT - Meteosat Second Generation (MSG) satellite is utilised to analyse the characteristics of this thunderstorm. However, direct satellite observations are not sufficient to analyse the vertical structure of the storm since satellite sensors are not capable of examining the inner characteristics of cloud. Therefore, variant channel, RGB satellite images and the satellite-derived products like NWCSAF and radar products are used in this analysis. Moreover, synoptic analyse of the atmosphere and automatic station observations from that region were included to study for a better understanding.

### Results

In Figure 1, the reddest pixel value at the squared area on IR 10.8 - 14.45UTC image indicates that the top of OT's brightness temperature (BT) is around 210K. This value of BT with relatively warmer than the surround of it and the cold (or enhanced)-U/V area beyond that is an indicator of a severe thunderstorm. In Figure 2, MAX reflectivity value on Samsun Radar at 14.48UTC measured as 70 dBz which corresponds to extreme severe thunderstorm conditions which produce heavy rainfall and large hail. These observations show the severity of thunderstorm and mention as an indicator of heavy rainfall and large hail which causes extreme damages in 20 minutes.

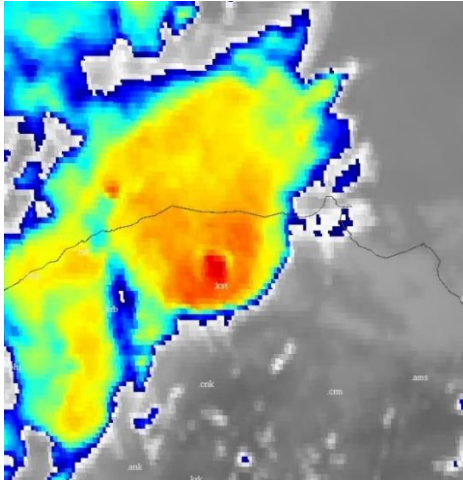


Figure 1: 14.45 UTC – IR 10.8 image from MSG

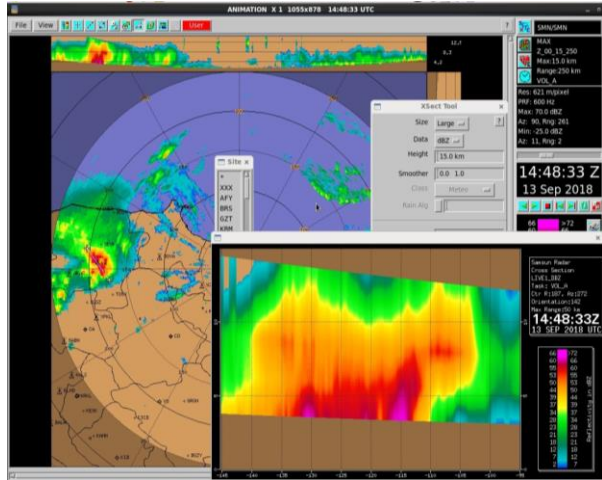


Figure 2: Cross Section of MAX reflectivity image of SMN Radar at 14.48UTC (©TSMS)

The importance and usefulness of remote sensing tools for both tracking storms and analyse afterward are the main results of this project. Soon, MTG (Meteosat Third Generation) satellites with lower temporal resolution (more frequent images every 5 min) and higher spatial resolution will be a crucial tool for both weather forecasters and meteorologists for understanding convection.

## References

- <sup>1</sup>Setvák, M., Lindsey, D. T., Novák, P., Rabin, R. M., Wang, P. K., Kerkmann, J., ... & Štřástka, J. (2008, September). Cold-ring shaped storms in Central Europe. In EUMETSAT Meteorological Satellite Conference (pp. 8-12).
- <sup>2</sup>Setvák, M., Lindsey, D. T., Novák, P., Wang, P. K., Radová, M., Kerkmann, J., ... & Charvát, Z. (2010). Satellite-observed cold-ring-shaped features atop deep convective clouds. *Atmospheric Research*, 97(1-2), 80-96.
- <sup>3</sup>Bluestein, H. B., Lindsey, D. T., Bikos, D., Reif, D. W., & Wienhoff, Z. B. (2019). The Relationship between Overshooting Tops in a Tornadoic Supercell and Its Radar-Observed Evolution. *Monthly Weather Review*, 147(11), 4151-4176.
- <sup>4</sup>Bedka, K., Murillo, E. M., Homeyer, C. R., Scarino, B., & Mersiovsky, H. (2018). The above-anvil cirrus plume: An important severe weather indicator in visible and infrared satellite imagery. *Weather and Forecasting*, 33(5), 1159-1181.

## Discovering the Tropical Gravity Wave

Jean-Marie Clément<sup>a</sup>

**Abstract:** During the November 2019 gliding camp in Atacama (Chile), we discovered that gravity and convergence waves can occur with extremely weak winds, so weak that they were insufficient to produce ridge lift. The strength of the lift sometimes strongly increased with the altitude, all without any turbulence, even inside the rotor clouds around 6.000 m. We did not have specific tools to predict these waves but the "standard" *SkySight*<sup>b</sup> software could help a lot. This lecture shows what we found and the numerous questions that arose around this phenomenon, and we invite experts to continue with research campaigns.

### INTRODUCTION

The November 2019 gliding camp in the Atacama Desert was originally intended to discover the volcanic thermals above the volcanoes, using a rented Stemme S10 with an atmospheric Limbach engine. The first flights did not meet our expectations. Since we could not take off early in the morning for technical reasons, the conditions were already dying when we arrived. At noon, the beautiful cumulus with bases up to 8.000 m already started fraying down. We were facing the "*Bolivian Winter*". The local population knew this phenomenon, but there was no aeronautical data or report. More on <https://topfly-aero.com/index.php/category/atacama-2019-en/>.

### ON-SITE EXPERIMENTATION

We then decided to exploit the weak afternoon westerly breeze, which was blowing 10-15 kt when the north-east wind from Bolivia was not blowing. The ridges did not work because of either the conical shape of the volcanoes or the very irregular and broken shapes of the other mountains. We then decided to check for the presence of the convergence lift on the lee side of the perfectly conical volcanoes. That was rather tricky because this side is in Bolivia, theoretically prohibited airspace, totally unlandable, the altitude of the ground being 4.500 - 5.000 m, with escape cols around 4.500 m. For safety reason, we had to keep the engine running, even if not climbing above 5.000 m (which is the service ceiling of the Limbach engine). Good surprise, the convergence worked perfectly, as in the books, allowing reaching the altitude of the volcano, around 6.000 m. We then tried the other volcanoes, there are dozens all around, they all worked the same way, every cone was producing a convergence, without any turbulence. But hardly reaching more than 6.000 m with 10-15 kt westerly wind and 4.500 m ground altitude.

We then decided to investigate more accurately every time we had a forecast of light westerly flow in altitude, or the presence of jet streams often 500 km to the South, even sometimes 1.000 km away. The convergence lift converted into wonderful and incredibly powerful and calm gravity waves and hydraulic jumps. For health safety reasons, we decided to stop climbing at 8.000 m, once abandoning 7,6 m/s with lenticulars approximately 4.000 m above us, see fig.1. All in tropical light clothing, extremely comfortable living, no turbulence, very light wind (25-30 kt at this altitude can be considered as weak). We repeated this type of flying as much as we could, flying thermals at 6.000-7.000 m only when "desperate".



Fig.1 - 26 Nov 2019, 7.534 m. The top of the volcanoes is 6.000 m

Volcano Sairecabur, looking North. Wind 32 kt / 293°

<sup>a</sup> Retired Engineer Arts et Métiers, Paris, specialist in fluid mechanics, world level glider pilot, multiple world record holder, expert in wave experimentation and flying, author of the book "*Dancing With the Wind*".

<sup>b</sup> Designed by Matthew Scutter, a professional computer scientist and world top glider pilot, presently the only (and therefore the best) wave prediction software.

The most difficult activity has been the forecast of the dynamic lift. The tropical aerology is totally unknown to gliding meteorologists. We could not get help from our friends in Europe, just one recommendation: "*look carefully at weak signals*". The Atacama tropical air mass can produce gigantic wave systems with very weak flows.

During one month (November), we have not seen one single front passing, at least according to our standards, i.e. clouds, rain and wind. The sky remained desperately blue during 30 days; the wind on the ground in Calama was everyday the same, a typical mountain breeze regime from East or West with 180° rotation every morning around 11 am and 10 pm. See Fig.2.

The conventional geopotential maps at 500 hPa were unusable, simply because the ground is at 500 hPa. Getting altitude wind forecast and wave prediction was however possible thanks to SkySight, with whom we made a contract. This was by far our best source of information, together with the public websites showing the jet streams. We in fact discovered that, even though we never had any strong flow above the flying area, the presence of jet streams 500 to 1.000 km to the South was generating a totally different behaviour of the air mass. We do not know why, but it worked.

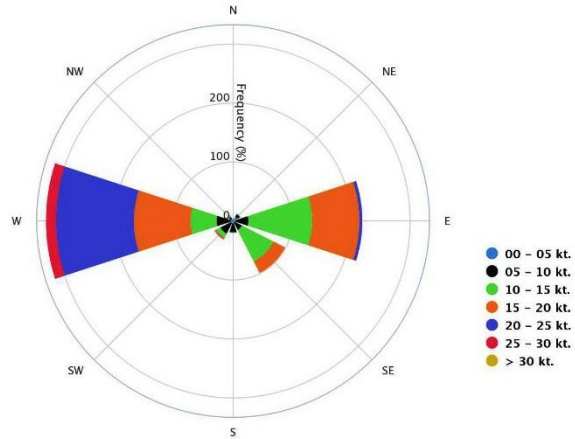


Fig.2 - Windrose November 2018, Calama airport (alt. 2.300 m)

## POST-EXPEDITION ANALYSIS AND REFORECASTING

Since the day-to-day life and the organization of the expedition in a so harsh environment did not allow us to investigate immediately about the many surprises we found, I decided to ask two experts in computer science and meteorology to make the re-forecasting of the six particularly interesting wave days. Matthew Scutter and Ezio Sarti<sup>©</sup> of Meteowind made a huge work allowing us to analyse the in-flight findings from our office in Europe one year later, as if we were there.

Among the many surprises we could see, two were particularly amazing:

1. The temperature was always 11 to 14°C higher than the one of the soundings. See fig.3, December 1<sup>st</sup>, 2019.  
Can that be related to the air mass travelling above the overheated desert for 250 km? Can that be related to the compression resulting by lifting the airmass from sea level to 4.500 m average, thus reducing the section by 40%. See fig.4. Or a combination of both? Or an unlikely lack of initial data of the model?
2. The actual QNH at Calama airport (2.300 m AMSL) was permanently 10-14 hPa higher than the one of the GFS data base.

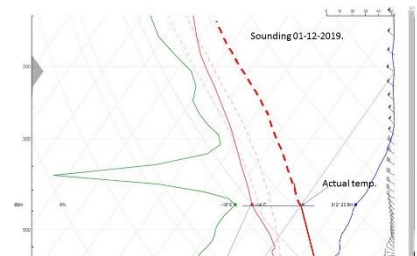


Fig.3 Sounding of 1<sup>st</sup> Dec. 2019, and actual temperature

The QNH and the temperature should be linked, the cause might be the same.

This results in an extreme stability of the airmass, as it appears on the annotated Skew-T diagram, and certainly contribute to the unusual power and easiness of the gravity waves and the hydraulic jumps.

## CONCLUSIONS

The tropical gravity wave can be an extremely powerful, easy, safe and comfortable phenomenon for glider pilots who want to combine exotic holiday and beautiful flying. However, its forecast is tricky and depends on many other factors than only wind, temperature and gradient.

<sup>©</sup> Ezio Sarti, <http://www.meteowind.com/>, is a meteorological expert certified by the WMO. He manages a team of computer experts who recently developed a forecasting software very similar to SkySight.

The purpose of this lecture is both to show to the public how beautiful these waves are and to invite the experts and the meteorological organizations to investigate on how they develop and how to predict their formation. We offer our know-how for organizing research campaigns in San Pedro de Atacama using motorized gliders.

The main issues to be solved for a future research campaign remain:

- Getting a clearance to overfly Bolivian airspace up to FL 280 using gliders with conventional supplemental oxygen delivery systems or even FL 340 when using a pressurized breathing system.
- Getting a reliable pressurized oxygen breathing system and installing it in a S10 or equivalent motorized glider.
- Getting a turbocharged self-launching glider or tow plane.
- Finding an agreement with San Pedro municipality and Chilean Civil Aviation Directorate in order to make San Pedro airfield safe and secured during the night.

Contrary to the QNH and the temperature, the wind forecast of either models GFS and WRF used by MeteoWind and SkySight were corresponding to our actual observations.

This is a real enigma that will be exciting to solve, also and above all regarding the phenomenon of the warming of the upper layers of the atmosphere: "Is there something that escapes the current models?".  
Can gliding meteorology help finding solutions?

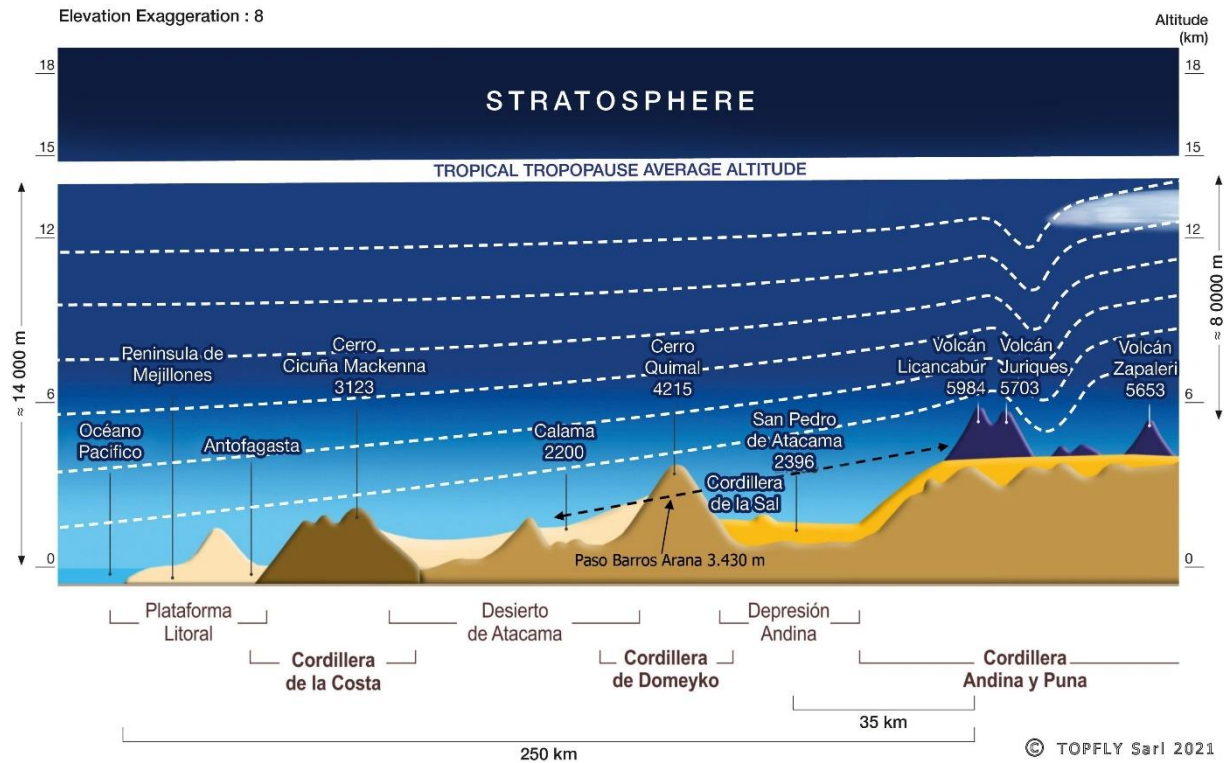


Fig.4 Topographic cross section of Atacama Desert along the Tropic of Capricorn, from the Pacific Ocean up to the volcanoes and the Bolivian Altiplano. The section of the atmospheric westerly flow is reduced by 40% in 250 km, between an overheated ground and the supposedly constant altitude of the stratosphere.

## Two birds with one stone (and one trailer)

Michael Greiner

*University of Stuttgart, Institute for Aerodynamics and Gas Dynamics, Germany, greiner@iag.uni-stuttgart.de*

**Abstract:** The manufacturers of sailplanes cannot rely on quantum leaps in aerodynamics or material science. New ideas are required to uphold the desire for buying new sailplanes.

There have been trends discernible in recent years, such as increasing wing loading, or offering different outer panel panels for different spans. Although the flexibility has been valued by pilots to a high degree, it seems the possibilities of these options soon will be exhausted. With a fresh approach and a new concept, the combining of different spans in one sailplane can be driven to an even higher extend, which in return offers advantages over the present approach in other respects, too.

However, such a new concept requires new solutions in various aspects to achieve a harmonious sailplane again. The challenges and possible solutions are discussed.

**Keywords:** Flexible span, wing junction design, vertical tail design, wing fuselage junction,

### Introduction

Glider manufacturers continuously have to convince potential customers to spend a large amount of money on their products. The most convincing argument is setting new performance benchmarks in the given competition classes. Airfoil aerodynamics seems to have achieved a level, where only minuscule improvements can be achieved. Sources of parasite drag are now addressed by CFD or more complicated installations (wing-fuselage junctions, tail-junctions, retractable tailwheels, etc.). However, the major trends over the last twenty years are:

- Increasing wing loading (performance)
- Propulsion, relieves the glider pilot from his most nearby worries, and is a field where a manufacturer still can measurably outperform the competition (convenience).
- 18m-class offers an attractive compromise between performance and handling (performance, convenience).
- Alternative outer panel panels for two spans, e.g. Standard/18m, 15m/18m, 18m/21m (flexibility)
- Small open class with spans between 21m and 23m (performance, convenience)

The instant success of some of these developments were surprises to the more conservative observer: like the 18m-wingtips for a standard class glider or the 21m-open class glider. Neither development was a promising contender for competitions. However, they offered an attractive new compromise of performance, handling and price. The same applies to the 18m-class, which became so popular, that no major manufacturer can afford to look outperformed in this class. If these trends were successful, how can they be extended even further, to offer even more options for performance and handling?

### The Concept

The challenge is to find design features that offer new and attractive possibilities to the customer. Starting point was the idea of a sailplane with the option of two span-configurations, that are even further apart than nowadays, say 18m and 26m. Today span variations are realized by means of different/additional sets of outer panels. Both spans cannot be too different, otherwise – with a junction far out – an unacceptable wing planform would arise in at least one configuration, or – with the junction further in – a lot of wing has to be build doubly for the different spans. In any case, the inner panel is excessively over-dimensioned for the small span. Therefore, the maximum practical span increase so far is  $\psi=18m/15m=1,2$ . Exception to the rule is the Slingsby T-59D, for which inner panels of 1.5m were available to alternatively extend the span from 19m to 22m [1], which gives only a slight span increase of  $\psi=1,16$ . However, extending or shortening the inner end of the wing or mould is a common approach for a permanent span change, which has been applied for various prototypes (Dick Butler's ASW17S, Akafliegs' SB10, D-41, fs33) and

even for a number of modern production sailplanes. The fs29 telescopic wing is a very special case. As the taper usually is very small near the root, this solution is almost self-suggesting.

This solution is also feasible for a variable span wing, with a high span increase. The wing for the small span configuration can be extended with inner panels, which can either be rigged or left out (fig 1). The planform of the inner panels is a rectangle, or more general a parallelogram. For this investigation, a sailplane for 18m and 26m has been studied. A conventional flapped 18m wing was combined with the fuselage of a self-launching 18m sailplane. The additional inner panels had a span of 4m each. The tailcone was extended by about 45cm, while the cockpit was stretched by 30cm for c.g. reasons. Wing loads were calculated for the usual CS22 load cases with the numbers from table 1. The mass distribution of the wing was not iterated, as this is only a concept study. The calculated vertical wing bending loads showed, that the loads upon the outer wing panels are very similar in both span configurations. This means that the strength of the structure is exploited in both spans. In the conventional design with alternative outer wing tips, the strength of the inner wing is larger than necessary, when the smaller wing tips are rigged (fig 2). This causes the small configuration of a conventional design to be unnecessary heavy.

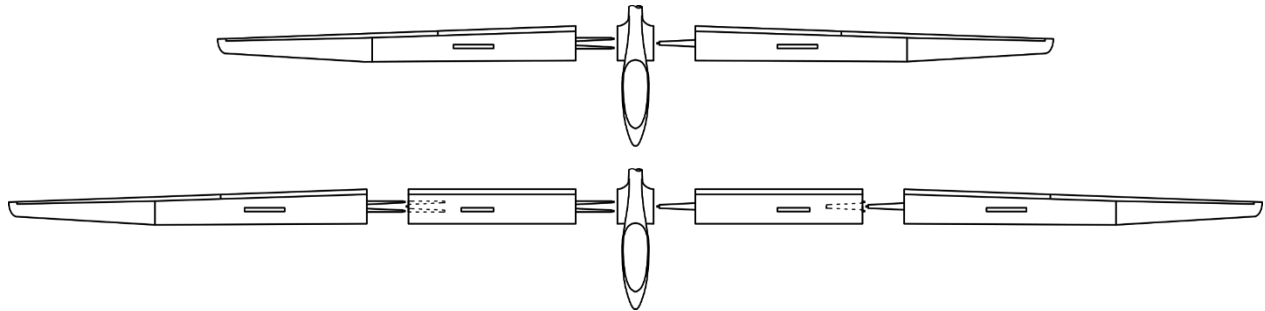


**Fig 1: Sketch of a sailplane with 18m/26m span. Variability through the inner panels**

Span	18m	26m
Wing area	10,4m <sup>2</sup>	16,6m <sup>2</sup>
Max. mass	600kg	850kg
Max mass of non lifting parts	380kg	380kg
Max wing loading	58kg/m <sup>2</sup>	51kg/m <sup>2</sup>

**Table 1: Basic parameters**

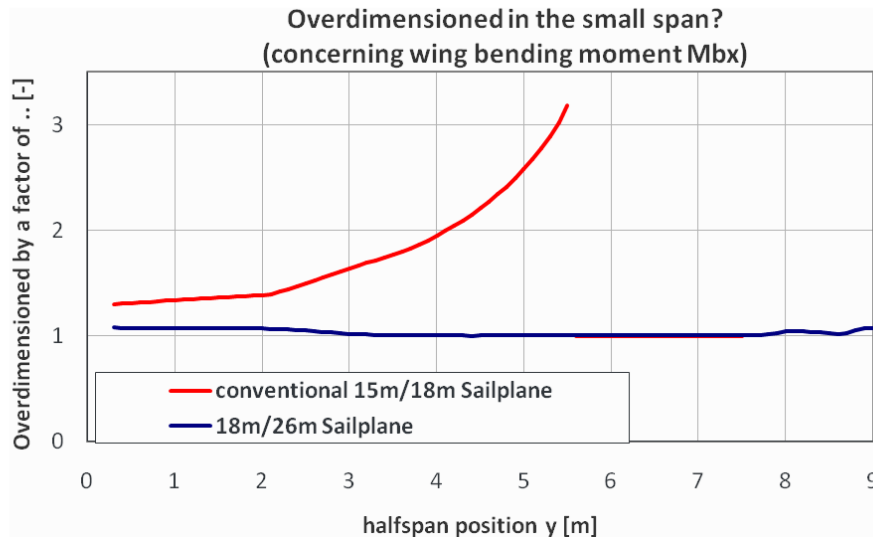


**Fig 2: Ratio between the vertical wing bending moments in the large span and in the small span configurations experienced by the same structure.**

### The Horizontal Tail

The horizontal tail design benefits from two aspects: Compared to a fixed wing design, the flaps provide some margin for the operational range of the horizontal tail airfoil. Second, the tail volume  $V_H/V_W$  uses the wing reference volume, which increases roughly linearly with  $\psi$ . Therefore, it is possible to find a good compromise for the horizontal tail design, with an extension of the tailcone by 45cm. With this measure, the horizontal tail volume is certainly large for the 18m class, but still within the statistical data cloud for various other sailplanes [2].

### The Vertical Tail

Concerning the vertical tail, the vertical tail volume  $V_V/(Sb)$  is normalized by the product of wing area and span, which increases roughly with  $\psi^2$  [2]. This makes it difficult to find an acceptable size of the vertical tail for both spans with respect of harmony of controls, rudder authority (for spin recovery), and no excessive wetted area. A solution could be a vertical tail extension, below the horizontal tail, at the tail wheel, or an exchangeable rudder. This raises the question if such a tail extension can be certified and is suitable for everyday use. However, junctions and automatic hook-ups are standard features nowadays, and the pilot is already expected to rig his glider in a sensible manner, e.g. not with different span extensions left and right. Trim weights for spinning, which could constitute a c.g. hazard are also regularly handled in operation with appropriate procedures. Certainly it is not a shortcoming if the glider remains flyable with an incorrect vertical tail configuration.

### The Junctions between Panels

For the junctions there are new boundary conditions. The fork/stub of the outer panels must connect with each other and the fuselage in between. The outer side of the inner panel must provide an interface, that allows the outer panels to be mounted. The simplest solution is probably, when all bending loads are transferred by nose pins on the narrow sides of the fork/stub, while the main pins only serve as a loss protection. It requires appropriate pockets and a locking pin in the inner panel, which receives the outer panel fork/stub.

Designing the inner panel inner junction will pose challenges, because the loads of a 26m-wing have to be transferred within root ribs the size of an 18m glider. Most of the designer's trouble is connected with shear loads (shear stress in bondings, loads upon the fittings). The shear loads within the stub/fork can easily be reduced by making them longer. This not even increases their weight, because at the same time it reduces the required wall thickness. These forks/stubs are longer than the fuselage is wide, and reach into pockets of the opposing root rib. Again the main pin only serves as a loss protection.

### The Wing Fuselage Junction

Another demanding design task is the wing fuselage junction. Resulting from the two possibilities to rig the glider, the inner panel not only must have a rectangular planform, but also must have the same airfoil on both ends. This limits the design options for wing fuselage junctions, as no fuselage related changes of the airfoil or of the angle of incidence can extend into the wing. Different solutions are possible. The most feasible compromise would be to move the root rib junction 5cm to 10cm further away from the plane of symmetry. From an aerodynamic standpoint, more would be desirable, but it creates unwanted bending moments in the fuselage behind the lift and drag pins, and also costs precious space in the trailer. On the other side, having the junction further outside, would allow to apply a wing-body fairing at the wing nose [3]. With current designs, the gap of the junction close to the fuselage prohibits the use of such fairings.

### The Wing Control Systems

If a flaperon design is incorporated with several flaperons, that make specific deflections, the design of the control system must be designed for both spans. Important aspects are roll control, low-drag and high lift during circling and a landing flap setting. A save way to achieve this in both configurations is to reduce the spread between the inner panel flaperon and the inner flaperon of the outer panel. The design of the airbrakes needs more attention. With the airbrake on the usual location of the 18m-wing – for good effectiveness and without wake upon the horizontal tail – it will be quite far out in 26m-configuration. In order to keep the horizontal bending moments and the torsional deformation on a normal level, this airbrake should not be larger than required for 18m-span. Various options are possible to achieve sufficient effect in 26m-span: An additional airbrake on the inner panel, a more pronounced landing flap setting on the inner panel, or to couple the flap on the inner panel with the airbrake control, such that extending the airbrake deflects the flap positive. The latter is probably the simplest solution.

Most of the proposed solutions have in some way already been realised in existing designs.

### Result

The goal was to find a way to design a sailplane that can be flown in two span configurations, with a large difference between the spans  $\psi=26\text{m}/18\text{m}=1.44$ . The motivation is not to achieve a higher performance, but to offer the customer advantages and a combination of characteristics, he cannot find in present sailplanes.

With 18m, the glider is as quickly and easily rigged as every other glider in the class. Neither on ground nor in the air weight has to be carried, that is unnecessary for the 18m-configuration. In 18m it is a handy glider.

With 26m it is a fully-fledged open-class glider. The heavy inner panels only need to be handled for this configuration.

The concept also offers advantages to the manufacturer. It is a new feature, that is not available so far. No wing area needs to be built twice for a single sailplane. A certain chance to “recycle” existing moulds, such as fuselages of sailplanes in the 18m to 23m range, or 18m-wings. The 18m wing mould can still be used for smaller gliders. The rectangular inner panels without twist or airfoil change only need one mould for both sides.

### References

<sup>1</sup> Geistmann, D., 1994: Segelflugzeuge in Deutschland, Motorbuch-Verlag, p 270.

<sup>2</sup> Thomas, F., 1999, Fundamentals of Sailplane Design, College Park Press, pp.130-147

<sup>3</sup> van Oudheusden, B.W., Steenaert, C.B., Boermans L.M.M., 2004, Attachment-Line Approach for Design of a Wing-Body Leading Edge Fairing, Journal of Aircraft, Vol. 41, No. 2

## Inflight Measurements of Control Surface Deflection in Circling Flight

Kai Rohde-Brandenburger<sup>1</sup>

*DLR, Institute of Aerodynamics and Flow Technology, Braunschweig, Germany,  
kai.rohde-brandenburger@dlr.de*

**Abstract:** Test flights with the research sailplane Discus-2C DLR were conducted. Control surface deflections, airflow data and sink rates were measured at different bank angles, to gain data for the validation of simulation tools. The data is shown and the averaged values for each bank angle are plotted. The data is prescribed and the measured sink rate over the bank angle is compared with the sink rate derived from the straight flight polar.

**Keywords:** *Circling flight*, sailplane, flight test, sink rate, control surface deflection.

### Introduction

Circling flight is an important part in the design of sailplanes or other slow flying and circling aircraft. While flying cross country, up to above 50% of the time can be spend circling in thermal updrafts, and even in competitions 30% of flight time [2] is spend circling. The sink speed while circling is important for climbing in thermals, influencing the climb rate directly and therefore even small improvements have big effects to the overall cross country speed.

The circling polar can be derived from the straight flight polar (3). This calculation is neglecting the locally varying inflow conditions due to rigid body rotation. This is causing an unevenly distribution of airspeed and angle angle of attack and therefore a change in Reynoldsnumber and angle of attack for each part of the plane. The deflections of the control surfaces, needed for a steady and trimmed circling flight are also neglected in the simple calculation from straight flight polar. In order to improve the circling flight of modern sailplane designs, prediction tools are needed which are capable of these effects in circling flight. These tools are improved in the recent years, but need to be validated using flight test data from circling flight. Measurements with the research aircraft Discus-2c DLR were conducted, to collect data of the deflection angles of the control surfaces and to measure sink rates and airflow conditions at stabilized circling flights. The data measured can be used to validate prediction tools for future sailplane designs, especially simulations of the control surface deflections under fully trimmed circling conditions.

### Methodology

The measurements for one bank direction (left or right) were done in a row. Before and after the circling test sections to one direction, a straight flight with zero degree bank angle was performed to compensate the measurement for air mass movements and calibration of the sensors.

The plane was weighted with the pilot on July 23rd 2019 and trimmed to the center of gravity wanted. The measurements were conducted on two days, July 24th and 25th 2019 on the Braunschweig research airport. The test flights started in calm morning airmasses and the sailplane was towed to FL95. The measurement time for each test section was between 90 to 130 seconds. The speed for each test point was calculated beforehand, to have all measurements near to  $C_L=0.85$ . This resulted in prescribed indicated airspeeds for each bank angle, varying from 95-118km/h CAS.

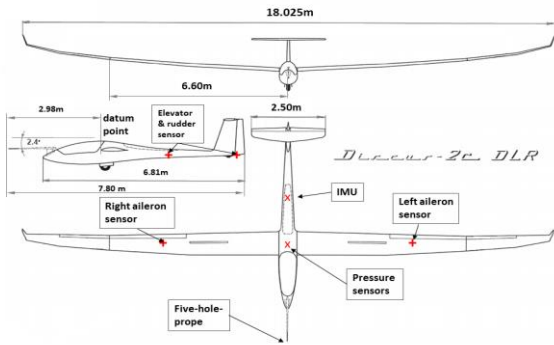


**Figure 1. Geometry of the Sailplane and Sensor Positions**

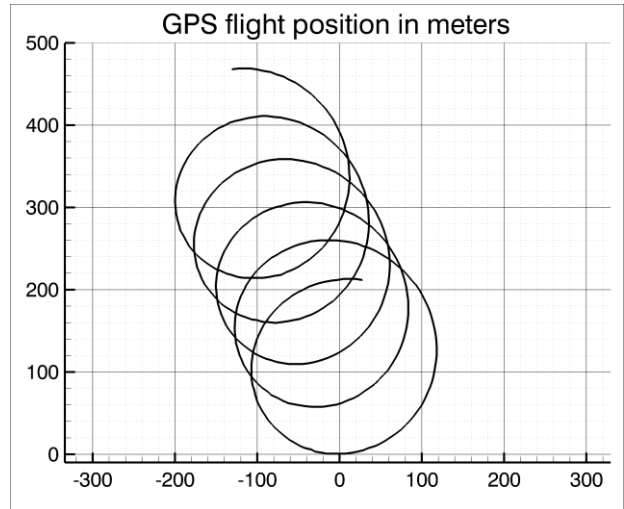


**Figure 2. Example of a 50 degree circling flight section in 2 D.**

The measured airflow data has to be corrected, due to induced velocities of the rigid body motion in circling flight. The data of the control surfaces are measured very close to each control surface, to avoid influences of temperature or deforming of the cables or the push rods. The rigid body motion was measured with an IMS (Inertial Measurement System).

**Results**

Measurements in circling flight could be succesfull conducted with the Discus-2c DLR. The measurements show small variations in rudder deflections and airflow. Values for 27 different bank angles from -54.2 degree to +50.3 degree could be measured.

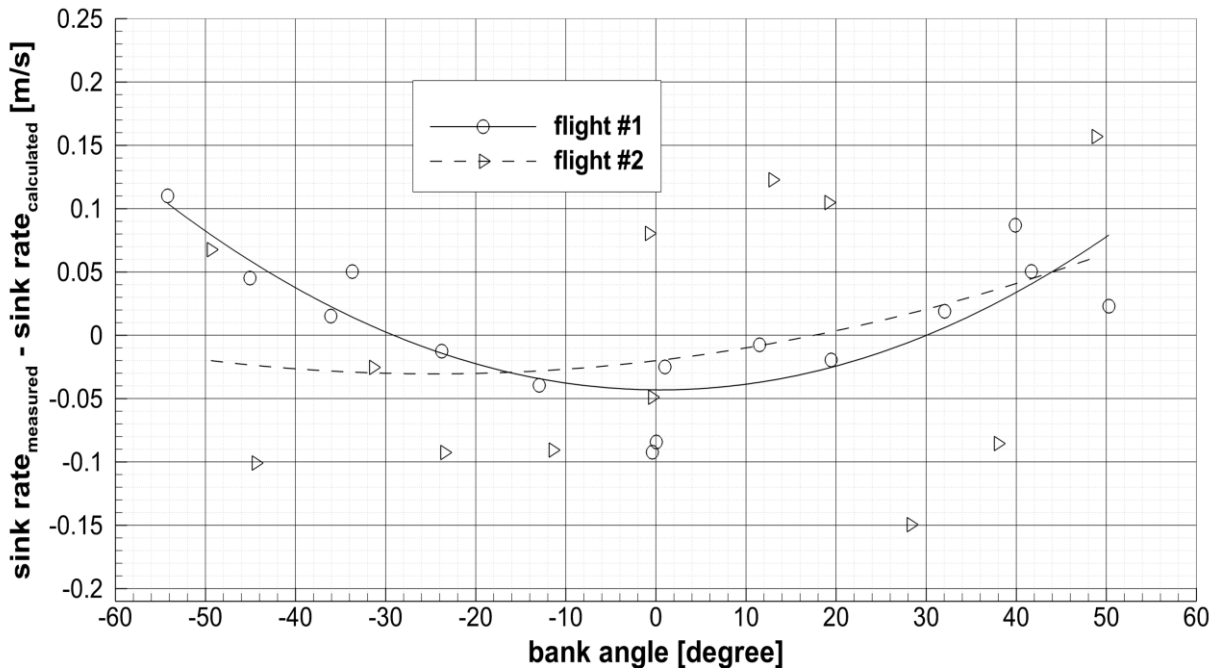


**Figure 3. Differences in measured and calculated sinkrates for circling flights of the Discus-2c DLR**

Averaged values for each test section are calculated and detailed measurement data for each section is shown.

The calculated sink rates for banked flight from the measured straight flight polar and the measured sink rates at bank angle are plotted. The differences between the calculated and the measured sink rates in flight number 1 show less drag and therefore less sinkrate for the Discus-2c DLR in circling flight than calculated from the straight flight polar. This may come from Reynoldsnumber effects, which is neglected in the simple calculation from straight flight polar.

Because sailplanes spend in most cases over 30% of flighttime in circling flight, even small changes in sinkrate can make a big influence to the cross country speed possible. Optimizations of sailplane designs for circling flight are only possible with simulation programs which can take these effects into account. The measured values will be used to validate these programs.

## References

<sup>1</sup>Müller, B., 1982, Design study of a sailplane with fowler flaps (German) DFVLR, Inst. f. Aerodynamik

<sup>2</sup>M. Maughmer, J. Coder, C. Wannemacher, W. Würz, 2017: The Design of a New Racing Sailplane: A New Thermal Mix Model and the Role of Transitional CFD, AIAA AVIATION Forum, Denver, Colorado

<sup>3</sup>Thomas, F., 1985: Fundamentals of Sailplane Design, Motorbuch Verlag Stuttgart, 2. Auflage

## Morphing Shell Design of a Sailplane with a Morphing Forward Wing Section

Fabian Sturm, Mirko Hornung

*Technical University of Munich, Institute of Aircraft Design, Germany, fabian.sturm@tum.de*

**Abstract:** A sailplane with a morphing forward wing section offers a promising performance increase compared to current designs. The morphing shell has to fulfill requirements that differ from those of a conventional shell. It shall adopt the desired aerodynamic shape even in between the ribs which impose the deformation onto the shell. Low actuation work for morphing is favorable and the shell must not buckle or fail under global wing bending. Monolithic balanced ply laminates show promising behavior and are therefore chosen as a baseline. Discrete design variables are fiber angle, ply thicknesses and fiber material.

A number of monolithic shell laminates are analyzed with classical laminate theory with regard to membrane and bending stiffnesses. To evaluate all requirements a FEM simulation of a representative wing segment with two rib spacings is performed for six relevant load steps. Deformation work, buckling behavior, actuator reaction forces and aerodynamic performance of resulting airfoil shapes is analyzed from that.

**Keywords:** *Morphing Wing, Variable Geometry, Composite Design, FEM*

### Introduction

Sailplanes operate in a wide range of airspeeds, from low-speed circling in thermals to high-speed cruising. The objective is to maximize the average cross-country speed. State of the art are airfoils with hinged trailing edge flaps to operate within the laminar-low-drag-bucket over the whole range of lift coefficients from  $C_L = 0.2$  to  $C_L = 1.5$ . Airfoils that have the upper corner of the laminar-low-drag bucket at a higher lift coefficient allow to reduce the wing area. Maintaining the mass, the wing loading increases and keeping the span constant results in a higher aspect ratio. As a result, the profile drag is lower and high lift-to-drag ratios can be achieved at higher airspeeds. To achieve this, a morphing forward section can be combined with a conventional trailing edge flap, which results in a maximum lift coefficient of up to  $C_L = 1.8$  [1]. During flight, the airfoil shape can be switched from low- to high speed configurations like an airfoil with a conventional flap. Airfoils and a wing for an 18 m span sailplane with this concept have been designed and numerically optimized by Achleitner et al [2]. Performance calculations show a significant speed increase and higher lift-to-drag-ratio, compared to a conventional state-of-the-art sailplane. The low-speed performance and landing speed can be maintained.

The concept of the wing structure is shown in Figure 1. The morphing shell is supported by a discrete number of compliant mechanisms (CM), which act as elastically deformable ribs, which are created by means of topology optimization [3] [4]. They impose a specific kinematic deformation onto the shell, to achieve the aerodynamic target shape of the airfoil. The shape of those ribs is the result of a topology optimization with the objective to achieve a precise output deflection from a given input deflection. On the upper side, the morphing shell is attached to the primary wing structure, on the lower side there is a structural gap, which allows lateral displacement. The gap is aerodynamically sealed with a Mylar tape, comparable to the sealing of trailing edge flaps. By this, the leading edge maintains its shape during morphing. The input deflection can be either applied on the compliant mechanisms or on the lower side of the morphing shell.

Three different concepts for morphing wing shells have been investigated by Sturm et al [5]. Based on these results, the monolithic shell layout has been developed further and the requirements are stated more precisely:

The morphing shell shall provide an aerodynamic shape that leads to acceptable drag coefficients and acceptable maximum lift coefficients. This shall be achieved for the whole morphing shell, especially in between compliant mechanism ribs and for all relevant flight conditions with their aerodynamic loads. The morphing deformation shall require as little work as possible. The morphing shell must not buckle below limit load for the whole load case envelope. It must have sufficient static and fatigue strength to transfer aerodynamic loads and bear morphing deformations over the whole service life without failure. It does not need to transfer global bending or torsion loads of the wing.

From that it seems favorable to have a high bending stiffness in spanwise direction and a low bending stiffness in chordwise direction. However, bending and shear stiffness shall be high enough to prevent buckling. As the global bending deformation and strains of the wing's primary structure are imposed on the morphing shell, the upper side of the morphing shell is pre-strained with compression strain and especially prone to buckling for load cases with positive load factors. A low membrane compression stiffness in spanwise direction is favorable to reduce compression stress on the upper side.

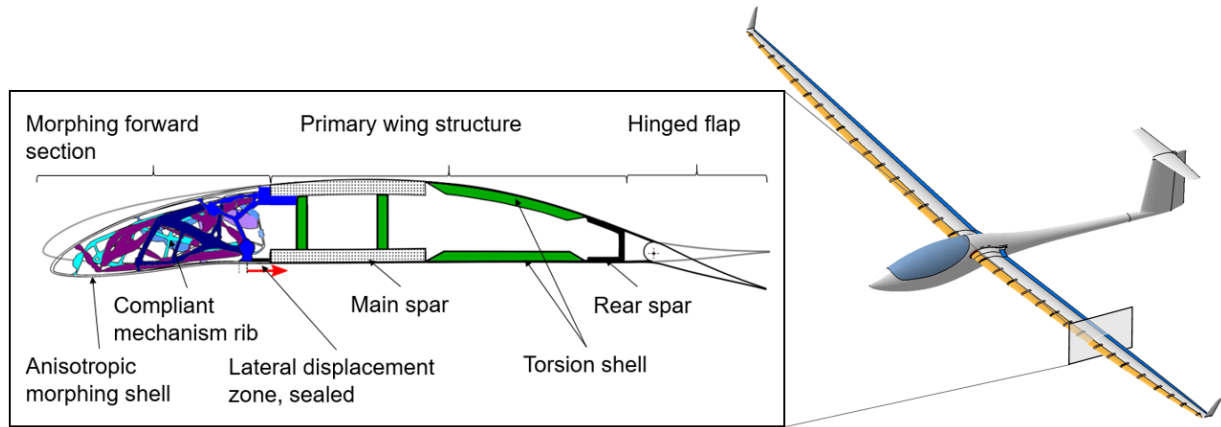


Figure 23 Structural concept of a sailplane with a morphing forward wing section

### Methodology

First, a number of available shell laminates is investigated on a flat-shell-level. For this, the engineering constants for membrane and bending Young's moduli are calculated using classical laminate theory (CLT). Balanced laminates with paired plies of opposite fiber angles are investigated to effectively create laminates with a reduced membrane stiffness in x-direction compared to pure UD 0° laminates. Also shear stiffness increases with increasing fiber angle up to a maximum at 45°. The shell laminates are modeled with composite materials and their elastic properties for a fiber volume ratio of 50%. The shell models are built up as symmetrical balanced laminates with low density polypropylene fiber core plies with 200 g/m<sup>2</sup> to increase the second moment of area and bending stiffness as proposed in [5]. An outer ply with a 25 g/m<sup>2</sup> 45° GFRP woven fabric ply is used with every laminate as a crack arrestor. The UD plies are stacked in an alternating way with the positive and negative ply angle.

The analysis on wing level is done with FEM (ABAQUS CAE 2018) using a static geometrical non-linear solver. By this large deformations and rotations as well as post-buckling behavior can be analyzed. A representative 3000 mm inner wing segment of an 18 m span sailplane with two trapezoids and one airfoil is investigated. It is modelled as a FEM shell model with the morphing section and the wing spar area, omitting the rear primary structure as shown in Figure 24.

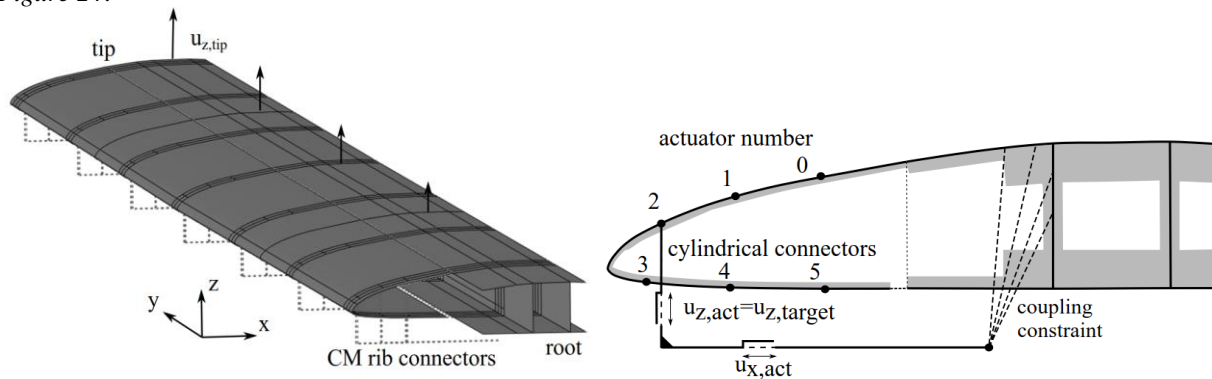


Figure 24 FEM shell model of morphing forward section (left), CM-rib actuation points with connectors (right)

In total, 12 different laminates with either CRFP or GFRP plies are investigated, both with a spanwise CM-rib spacing of 300 mm and 500 mm. This leads to either 7 or 11 CM-ribs, each with 6 actuation points. Bending displacements coming from a separate global wing analysis are applied on the wing spar and the vertical target morphing deflections are applied relative to the main spar with cylindrical connector elements. Six ideally stiff connectors distributed on the morphing shell represent the CM rib actuation points. An aerodynamic pressure is applied uniformly on the forward morphing shell.

Six load steps are applied on the model, that represent jig-shape (step 1), cruise-flight (step 2), thermaling-flight (step 3+4) and a pull-up maneuver (5+6) with their corresponding airfoil morphing configurations. They are derived from a preliminary study on the primary structure [6].

The difference of internal energy of the morphing shell is measured between unmorphed and morphed configuration for each case to determine the required deformation work. On each CM actuator location, the connector total force (CTF) is measured to determine the reaction forces on the CMs. Buckling is investigated by identifying the nonlinear shell displacement and nodal rotation.

On two discrete cross-sections in between CM-ribs, at  $y_1=1050$  mm and  $y_2=2550$  mm, the deformed shell model is analyzed. The nodal coordinates of the forward section are de-rotated and normalized, as well as stacked to the designed rear part of the airfoil to get a complete 2D airfoil. Global wing twist is not regarded in this study, but only deformation within one cross-section. Aerodynamic performance of these airfoils is then investigated with XFOIL.

**Results**

The results of the CLT analysis of flat-plate laminates show the expected decrease of membrane and bending stiffness anisotropy with increasing balanced fiber angle. Also, the shear stiffness increases with increasing fiber angle. Remarkable is the steep gradient of stiffness in x-direction with change in fiber angle. This has to be considered with regard to manufacturing tolerances. The impact on the requirements of a morphing shell can not be evaluated from these results.

From the FEM analysis of the wing segment, there is no significant difference in internal energy for the two spanwise CM-rib spacings with a constant laminate. The deformation work of the CM-ribs however has not yet been considered. The deformation work increases with increased wing bending deformation for all configurations. Laminates with CFRP fibers and those with  $\pm 45^\circ$  fiber angle require most deformation work. Increasing the thickness of the core plies significantly increases deformation work.

The connector forces on the CM actuation points vary both in spanwise and chordwise direction. In general, those CMs that support the leading edge have to support the highest loads. With more wing bending deflection and stiffer laminates, the connector forces increase.

In *Figure 25* a nodal rotation contour plot is shown on the left side, where buckling can be identified visually. On the right, the load step where buckling is identified is shown for all laminates and spanwise rib spacings. The horizontal line represents limit load for a pull-up load case at load step 6. Those laminates with balanced fiber angles of  $30^\circ$  or higher and those with a thicker core plies resist buckling until load step 6.

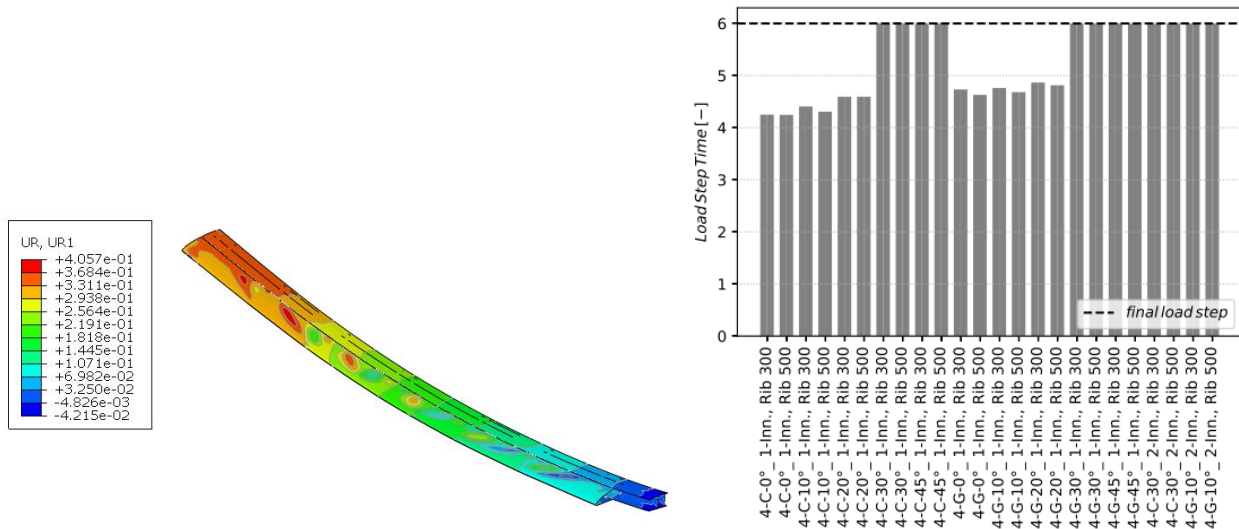


*Figure 25 Nodal rotation URI for visual buckling identification layup 4-C-0° 1-Inn., iib 500, step-6 pull-up (left), load steps with visible buckling occurrence of all laminates (right)*

In *Figure 26*, the resulting deformed airfoils of one cross-section are shown. On the left, the geometry for each load step is plotted together with the target geometry. For the thermaling load steps 3+4 and the pull-up maneuver steps 5+6 the leading edge is bent upwards. For the cruise flight load step 2 there is no visual difference. On the right the lift and drag polars from an analysis with XFOIL are plotted. The  $c_l$ - $\alpha$  curves of the deformed airfoils are congruent to those of the target airfoils up to high lift coefficients. For the cruise flight load step 2 the laminar low-drag-bucket of the deformed airfoil is narrower than desired, within the laminar low-drag-bucket the drag coefficients are very

close to those of the target airfoil. With the upward bent leading edge, the desired maximum lift coefficients are not reached.

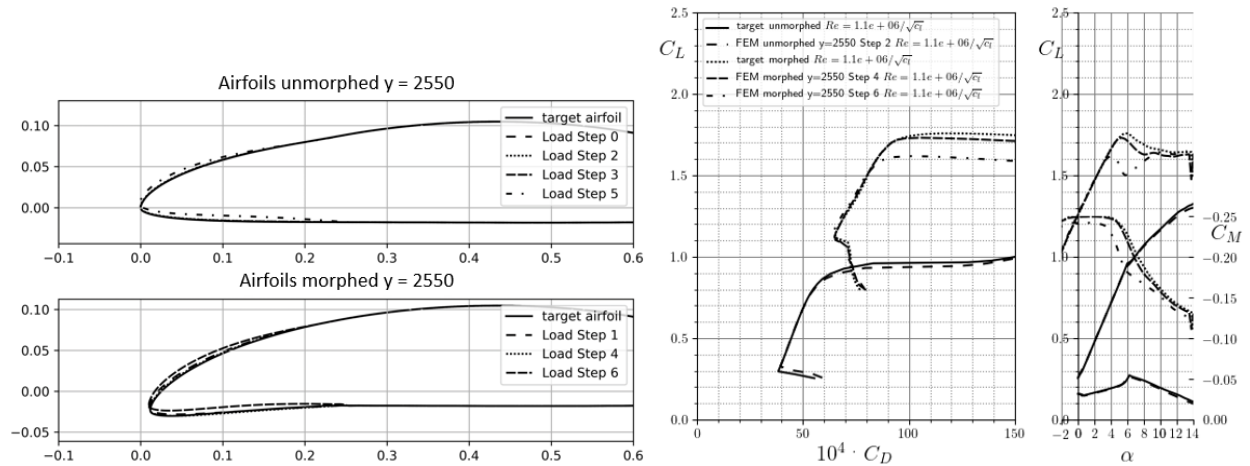


Figure 26 Deformed airfoils of cross-section  $y=2550$  with layup 4-C-30° 1-Inn., rib 500 (left), airfoil polar diagrams (right)

This contribution has been submitted as an article for Technical Soaring with the title “Design Study of Monolithic Morphing Shells for a Sailplane with a Morphing Forward Wing Section”

Gefördert durch:



aufgrund eines Beschlusses  
des Deutschen Bundestages

## References

- [1] Weinzierl, M., Achleitner, J., and Baier, H., “Highly Extensible Skin of a Variable Geometry Wing Leading Edge of a High-Performance Sailplane,” *Technical Soaring*, Vol. 39, No. 1, 2015, pp. 4–9.
- [2] Achleitner, J., Rohde-Brandenburger, K., Rogalla von Bieberstein, P., Sturm, F., and Hornung, M., “Aerodynamic Design of a Morphing Wing Sailplane,” *AIAA Aviation 2019 Forum*, American Institute of Aeronautics and Astronautics, Reston, Virginia, 06172019, p. 4.
- [3] Reinisch, J., “Synthesis of Compliant Mechanisms for Morphing Wings with Nonlinear Topology Optimization,” Master's Thesis, Technical University of Munich, Institute for Aircraft Design, 2019.
- [4] Reinisch, J., Wehrle, E., and Achleitner, J., “Multiresolution Topology Optimization of Large-Deformation Path-Generation Compliant Mechanisms with Stress Constraints,” *Applied Sciences*; Vol. 11, No. 6, 2021, p. 2479. doi: 10.3390/app11062479.
- [5] Sturm, F., Achleitner, J., Jocham, K., and Hornung, M., “Studies of Anisotropic Wing Shell Concepts for a Sailplane with a Morphing Forward Wing Section,” *AIAA Aviation 2019 Forum*, American Institute of Aeronautics and Astronautics, Reston, Virginia, 06172019, p. 4.
- [6] Illenberger, G., “Numerical Investigations on the Static Aeroelasticity of a Sailplane with a Morphing Forward Wing Section,” Semester Thesis, Technical University of Munich, Institute for Aircraft Design, 2019.

## A numerical method for kinematic and structural optimization of sailplane mechanical flight control systems

Oswaldo Palomba Neto<sup>1</sup>, Gregori Pogorzelski<sup>2</sup>, Alexandre Muniz Neves<sup>2</sup>

<sup>1</sup>Universidade Federal de Santa Maria, Centro de Tecnologia, Brazil, [oswaldo.neto@acad.ufsm.br](mailto:oswaldo.neto@acad.ufsm.br)

<sup>2</sup>CENIC Engenharia e Comércio, São José dos Campos, Brazil

**Abstract:** A numerical method for the design and optimization of sailplane mechanical flight control systems is presented. The approach is based on the minimization of a cost function that takes into account both, the system's handling qualities and structural performance. Results obtained by the application of the method to a new sailplane currently under development are presented indicating that the implemented tool can be successfully employed to sizing and handling improvement.

**Keywords:** Numerical optimization, flight control systems, handling.

### Introduction

To provide enhanced handling qualities to a sailplane it's essential to provide light stick forces and a smooth motion on the entire range of surface deflections. Due to all the non-linearities of a mechanic flight control system the early design can be very strenuous, the present paper provides the results of a numerical method approach on a currently under development sailplane. All the relevant components (bell-cranks, push-pull rods, torque tubes, stick, etc.) are modeled as rigid elements connected by coherent geometrical and kinematic constraints allowing the relative positioning and orientation of the components to be computed for any aerodynamic surface or stick deflection. Static equilibrium is also enforced between elements to compute acting loads. The optimization problem is solved by taking into account design constraints related to stick forces, deflection limits, neutral control surface or stick position, and also motion symmetry.

### Methodology

The numerical method was implemented on Scilab/FORTRAN platform using the built-in NSGA-II multi-objective algorithm to perform the optimization [1]. The code it's constituted by two main modules, the kinematic and an acting loads module. A flowchart elucidating the process is shown in Figure 1.

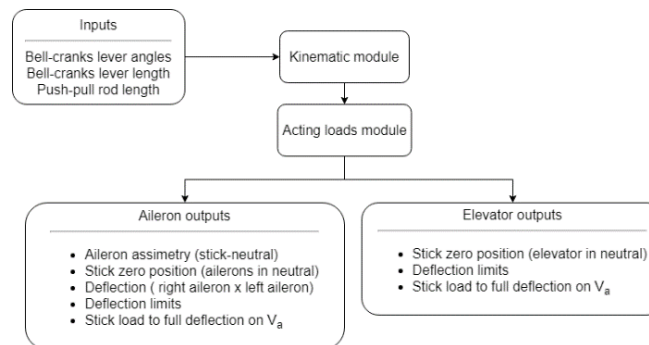


**Figure 1. Optimization process flowchart**

The pivoting elements (bell-cranks, torque tubes, stick, etc.) are defined using as many points as needed, the pivoting axis is also specified in which the rotations are performed, it's assumed that the pivoting elements only perform rotations. The push-pull rods are fully defined by their length and also on which element and point they are connected. The optimizer generates new configurations within the specified range table, on the bell-cranks or torque tube levers, the angle between the bell-cranks lever, and also the length of the push-pull rods.

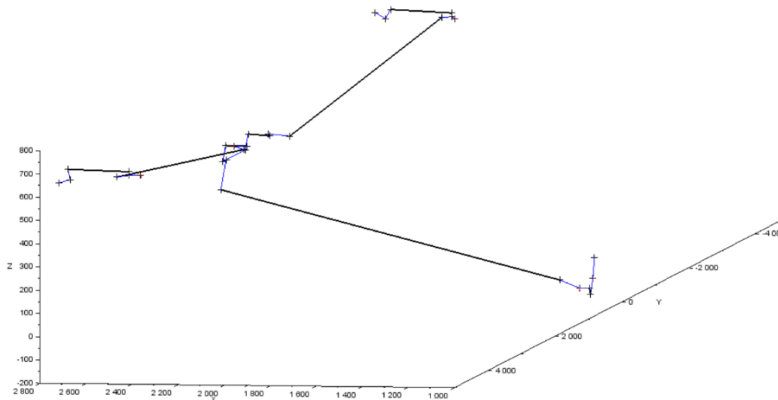


**Figure 2. Aileron control chain**

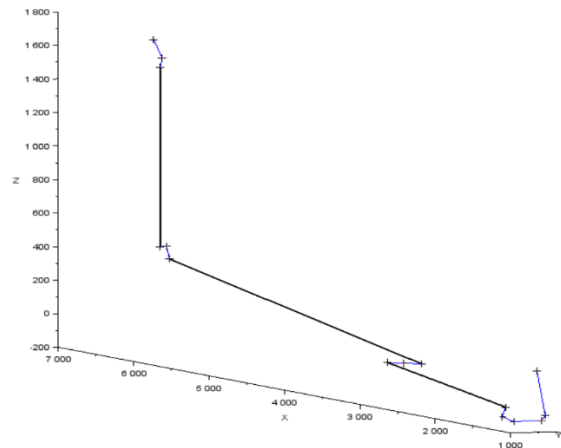


**Figure 3. Elevator control chain**

Figures 2 and 3 presents the control chains on the numerical model, the black bold line represents the push-pull rods, the blue lines the pivoting elements which are defined by the cross black dots.

The configurations generated by the optimizer go through the kinematic module, responsible to ensure the proper connection of all elements composing the flight control system through the entire range of control surface deflection, discarding failed geometry inputs. The method starts by rotating the control surface to the negative limit and iteratively rotating the subsequent pivot element (bell-crank or torque-tube) until the distance between them it's equal to the push-rod length, the equilibrium is done for the ranges in Table 2. If the configuration fails for any deflection is then discarded. The kinematic module provides the following outputs: aileron asymmetry with the stick in the neutral position, stick angle with control surface on neutral, control surface deflection limits, and also the motion symmetry plot of the aileron, further presented in Figure 4.

To all valid configurations, the acting loads module calculates the static equilibrium of all the elements for a previous equilibrium control chain, provided by the kinematic module. The loads are calculated by applying static equilibrium on forces and moments starting from the control surface hinge moment and ending on the pilot force applied on the stick, the hinge moment is provided by previous aerodynamical analysis performed for the model. It's considered that the push-pull rods transmit only axial loads, this assumption can be made by the use of self-aligning bearings and rod-ends, which is the case of the studied sailplane. The acting loads module provides the loads acting on the elements, special attention is given for the pilot stick force to provide equilibrium, used on the cost function. The aileron control chain cost function is computed by the sums of the absolute values of aileron asymmetry with stick in neutral position, the stick angle to get aileron on neutral position, the error on the deflection limits, and the stick load to full deflection on  $V_a$ , speed on A point of the V-N diagram. The elevator control chain cost function is computed by the sum of the absolute values of stick zero position error, deflection limits error, and also the stick load to full deflection on  $V_a$ . Table 1 presents the deflection limits constraints used in the optimization.

Control surface	Lower limit	Upper limit
Elevator	-30	15
Aileron	-20	40

**Table 1. Control surface deflection constraints**

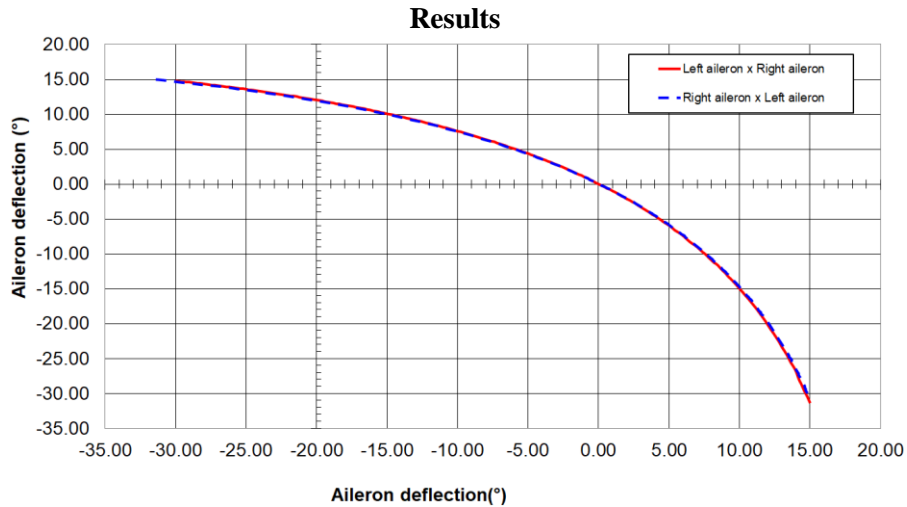


**Figure 4. Optimized aileron deflections**

Figure 4 displays the aileron deflections on both surfaces, the red-filled line presents the left aileron deflection on the x-axis and the right aileron deflection on the y-axis. The blue dotted line presents the right aileron deflection on the x-axis and the right aileron deflection on the y-axis. The two curves matching, indicating the motion symmetry on both sides, negative and positive. Table 2 shows the axial loads on the push-pull rods of the elevator and ailerons controls. It is worth presenting that compensator load relief is not taken into account. Figure 5 presents the result stick deflection vs. elevator deflection.

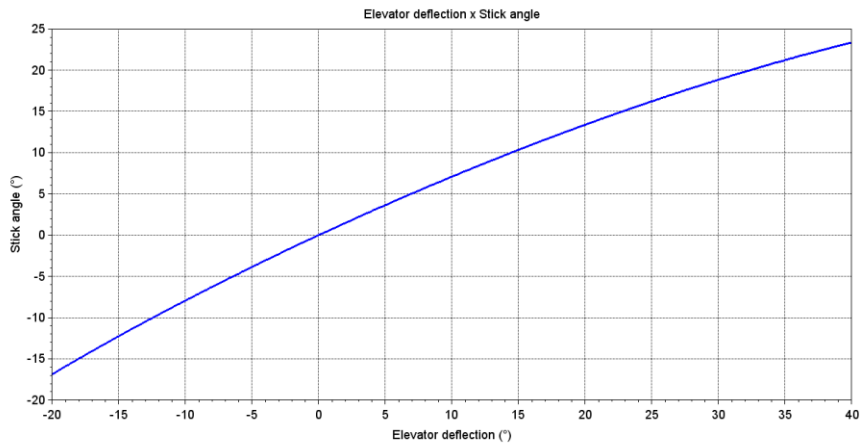


**Figure 5. Optimized elevator deflection**

Control system	Stick axial force (N)
Elevator	309.21
Aileron	204.89

**Table 2. Stick forces to full control surface deflection on  $V_a$**

In conclusion, the aileron and elevator control system mechanisms were successfully optimized. The constraints limits of the control surface deflections were respected and the stick axial force was minimized.

Future suggested work can be allowing translation of pivoting elements, this can be used to optimize conjugated flaperon control systems.

### **References**

<sup>1</sup>Bunks, C., 2012: Engineering and scientific computing with Scilab, Springer Science & Business Media.

<sup>2</sup>Roskam, J., 1989: Airplane Design: Part iv: Layout design of landing gear and systems, DARcorporation.

## Load monitoring for sailplanes utilizing an innovative carbon fibre-based, spatially resolved strain sensor

Jan Condé-Wolter<sup>1</sup>, Philip Johannes Steinbild<sup>1</sup>, Pawel Kostka<sup>1</sup>,  
Tom Ehrig<sup>1</sup>, Anja Winkler<sup>1</sup>, Niels Modler<sup>1</sup>, Florian Sell<sup>2</sup>

<sup>1</sup>*Technische Universität Dresden, Institute of Lightweight Engineering and Polymer Technology, Germany,  
philip\_johannes.steinbild@tu-dresden.de*

<sup>2</sup>*Akademische Fliegergruppe der TU Dresden e.V.*

**Abstract:** Real-time measurement of load conditions becomes more and more relevant to determine mechanical stress and strain during flight in sailplanes. In this paper, a spatially resolved carbon fibre based strain sensor that was developed within the last five years is described. This sensor principle will be adapted and scaled up to meet the requirements for real-time load measurements on a sailplane wing within the research project MonStrain. The aim of the project is to build a full-scale sailplane wing with an integrated carbon fibre strain sensor to enable further research. The project and its aim and approach is also described in detail.

**Keywords:** Load monitoring, strain sensor, carbon fibre

### Introduction

With latest trends in soaring like fly-by-wire technology, automated flap systems, active load reductions and numerous upcoming autonomous flying systems, real-time measurement of load conditions becomes necessary more often. In addition to this, the load data collected on a large scale could be used to calculate new, more realistic load spectra, which form the base for every structural sailplane design and could lead to lower empty masses and therefore to a larger range of wing loading and more flexible or efficient designs in general.

The most commonly used embeddable load measuring systems available on the market are based on strain measurements. Strain can be measured via different measurement principles:

- **Resistive measuring principle:** Resistive sensor types are the most commonly used strain sensors. The classic metallic strain gauge consists of a wire made of constantan that is arranged in a measuring grid. The geometric change resulting from strain alters the electric resistance of the measuring grid. The difference in electric resistance is then measured. Metallic strain gauges show a sensitivity (k-factor) of about 2. To be able to measure these relatively small changes in electric resistance under load, the use of measuring bridges and amplifiers is necessary.
- **Piezo-resistive principle:** Sensors that function according to the piezo-resistive measuring principle show a change in electric resistance when under tensile or compression load. Semiconductor strain gauges are one exemplary sensor type operating according to this principle. For semiconductor strain gauges, silicon in the form of a thin monocrystalline strip or as a vapor-deposited layer is mainly used as the measuring element. The much higher k-factor of over 200 for semiconductor strain gauges are advantageous to metallic strain gauges. Higher sensitivities enable the use of simpler measuring equipment to measure smaller strains. However, the measuring range is lower and the signal is less stable under temperature load.
- **Fibre optic principle:** For the fibre optic measuring principle tuneable or broadband laser light is fed into an optical glass fibre. The reflected frequency spectrum is detected and analysed, not only enabling the measurement of the level of strain but also of the position along the fibre optic sensor (FOS). There are two different sub principles that can be distinguished, a discrete measuring method employing fibre bragg grating, which can be compared to the use of strain gauges, and a quasi-continuous measuring method called optical frequency domain reflectometry.

Although strain is distributed continuously throughout the entire structure, it is typically measured discretely and only on the surface of the structure by means of metallic or semiconductor strain gauges. In order to measure the entire strain field over a wide area, multi-channel measuring systems are necessary for such discretely measuring sensors. The commercially available solution for continuous strain measurement is FOS. However, both fibre optic systems and multi-channel strain gauge-based systems with comparable resolution and measuring field size are very cost-intensive due to the required measuring electronics, take up a lot of installation space, and are disadvantageous regarding the mass of the system.

The use of the described measuring principles and corresponding sensors for the development of sailplanes is state of the art. There are many known examples for the application of classic strain gauges and fibre bragg grating FOS, e.g. the Stemme S10 VTX used by Aachen University of Applied Sciences [1] or the Discus-2c DLR at German Aerospace Center (DLR) [2]. In the context of research aircraft, these technologies allow very accurate strain measurement, but for broader applications, such as autonomous systems, active load reduction, or wide-area structural monitoring, lighter and inexpensive ways to sense continuous strain in flight are needed.

A sensor technology that has the potential to meet these requirements is the novel carbon fibre (CF)-based strain sensor that was developed over the course of the last five years at the Institute of Lightweight Engineering and Polymer Technology, TU Dresden (TUD-ILK). Within the new research project “MonStrain” a wing demonstrator with an integrated CF-based strain sensor is to be developed further from a small length of about 10 cm up to a length of 3 m. The CF-based strain sensor has the potential to measure spatially resolved strain using relatively cheap and lightweight measuring devices.

### Cracked CF Strain Sensor

The application of CF as a sensory element for measuring strain is new compared to the use of strain gauges or FOS. The electric properties of CF under tensile load is subject to different investigations [3-7]. Fundamentally, CF show a piezo-resistive behaviour and thus allow measuring strain alongside the CF via a change in electric resistance. K-factors of about 1.9 can be achieved using standard CF and are thus similar to k-factors of classic metallic strain gauges [4]. However, only the strain that is applied to the entire CF can be measured. Local strains acting on the CF cannot be distinguished from global strains. Local strains can thus only be measured using very short CF which offer low electric resistances and even lower differences in electric resistance under load, complicating the measuring of strains even further.

Larger changes in electric resistance were observed for irreversibly damaged CF, e.g. for cracked CF. This behaviour results from the reversible opening and closure of CF cracks and can be used to measure strain [8]. A first description of a strain sensor using cracked CF was done by Höhne et al. [9]. A CF roving featuring a high Young’s modulus of 900 GPa and a low ultimate elongation of 0.3 % was embedded into a glass fibre-reinforced epoxy (GF-EP) carrier. The carrier was then subjected to an elongation above the ultimate elongation of the CF roving but below the ultimate elongation of the GF-EP carrier. Cracks formed perpendicular to the loading direction within the CF roving. The GF-EP carrier, however, remained intact (Fig. 1).

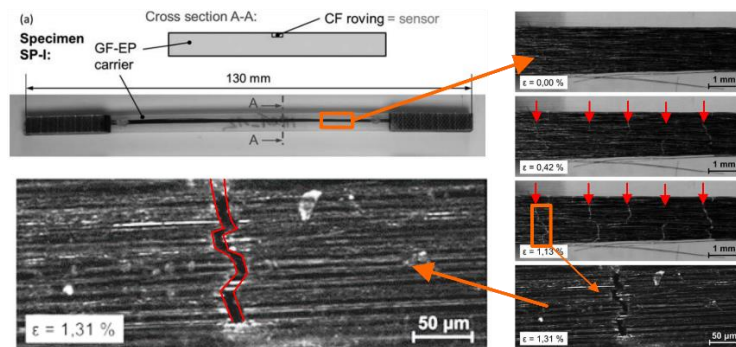


**Figure 1. Glass fibre test specimen (carrier, top left) and microscopy of cracks in CF roving embedded in carrier [9]**

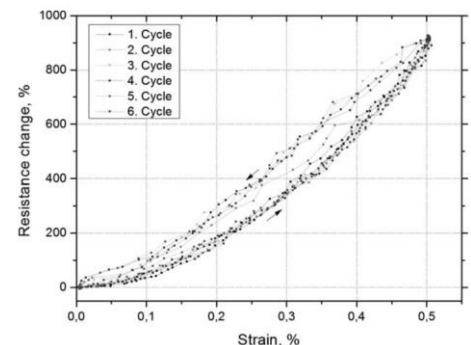


**Figure 2. Characteristic of a CF sensor with fibre cracks [9]**

The electric resistance of the cracked CF roving was measured during cyclic tensile testing of the carrier and showed changes as high as 900 % at strains of 0.5 %, corresponding to a k-factor of about 1,800 (Fig. 2). This significantly higher k-factor enables the use of simpler measuring equipment and makes CF particularly interesting for the use in structural health monitoring.

Since the cracks are almost equally distributed along the CF roving, the high changes in electric resistance resulting from the opening and closure of those cracks can be viewed as spatially resolved. This enables the use of the electric time domain reflectometry (ETDR) to spatially measure the electric resistance, or, to be exact, the impedance of a microstrip line where the cracked CF roving is one conductor respectively. This concept was then detailed and the results were described in [10].

The sensor described in [10] consisted of a transmission line employing a CF roving and a copper strip acting as a second conductor or ground integrated into a GF-EP carrier (Fig. 3). The transmission line was terminated using a

matched resistor. The sensor was clamped in a cantilever arm configuration (Fig. 4) and connected to an ETDR device (D-TDR 3000, Sympuls Aachen GmbH). A force was applied to the unclamped, free end of the carrier (Fig. 4), subjecting the carrier and thus the sensor to bending. By moving the carrier to different clamping positions (55 mm to 11 mm) and measuring the resulting impedance under bending using the ETDR device it was shown, that the sensor could measure spatially resolved strain (Fig. 5). A spatial resolution capability in the low single-digits mm range was confirmed [10].

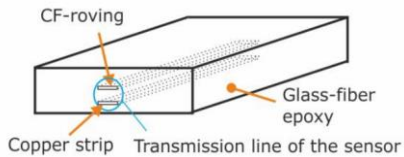


**Figure 3. Schematic setup of the CF strain sensor forming a transmission line [10]**

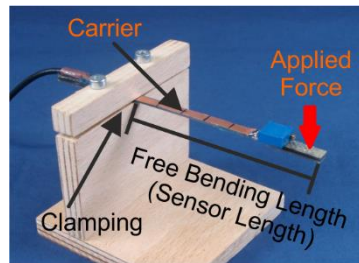


**Figure 4. Clamped sensor in a cantilever arm configuration [10]**

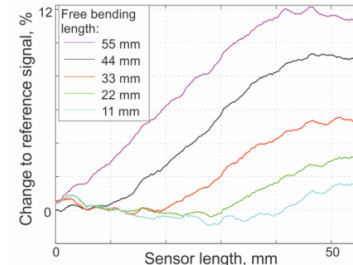


**Figure 5. Resulting ETDR signals for different free bending lengths (sensor length) [10]**

However, the overall length of the sensor in these early studies was limited due to, amongst other things, a high ETDR signal damping and inconsistent impedance along the transmission line. To be able to scale up the sensor length and to use the sensor in a realistic environment, further investigations need to be done which are planned within the research project MonStrain. The next section gives a brief introduction to the project.

### Project Aim and Approach

The aim of the MonStrain project is the development of the CF strain sensor technology towards an utilisation for active load monitoring of large aerospace structures. Since the TUD-ILK has no application-specific experience, it has joined forces with the Akaflieg Dresden e.V (Akaflieg) to meet the requirements from the point of view of glider manufacturers and operators and to develop an application-adapted sensor. The Akaflieg is also providing the sensor specific specifications for application in a sailplane environment (e.g. deformation range of wing bending and torsion, flutter frequencies).

The development in the three-and-a-half year project is divided into three stages:

- **Laboratory scale trials (currently ongoing):** Since the functionality of the CF strain sensor technology has been described [9, 10], other aspects regarding the sensor are tested within the project on a laboratory scale. On the one hand, this includes the determination of measuring range limits such as the validation of the maximum strain range and the realisable measuring length. On the other hand, new potentials like measuring compression with pre-strained sensors and the maximum measuring frequencies for utilisation as a strain sensor for dynamic systems are investigated. These experiments should identify further research questions and necessary steps towards an application-oriented sensor.
- **Upscaling:** The second development step focuses on the main challenge, increasing the measuring length, which is necessary for any application on large structural components. To achieve this, the characteristic impedance must be reduced. This can be achieved by reducing the resistance of the fibre, which is possible, for example, through metallic coatings. The second approach pursued is to reduce the measurement points along the fibre. Through introduction of pre-damage into the fibre, the cracks that act as measuring points should be introduced in a targeted manner and thus reduce the characteristic impedance and increase the measuring length. The results will lead to a large (>1 m) generic beam demonstrator.
- **Sensor integration and validation in a relevant environment:** In close cooperation with the Akaflieg, concepts for integrating the sensor into structures are being developed. Due to the mainly manual manufacturing processes, glider structures are ideally suited as the first demonstrator. The CF strain sensor is to be integrated into an inner sailplane wing, which is also equipped with strain gauges and acceleration sensors for validation (Fig. 7). This allows suitability testing on the ground in relevant strain and frequency ranges.

These three development stages enable the necessary scaling and thus the first use of the novel CF strain sensor technology in environments closer to the application. In subsequent projects, the aim is to integrate the system into a flying demonstrator with the aim of investigating its robustness, suitability for use and performance (Fig. 7).

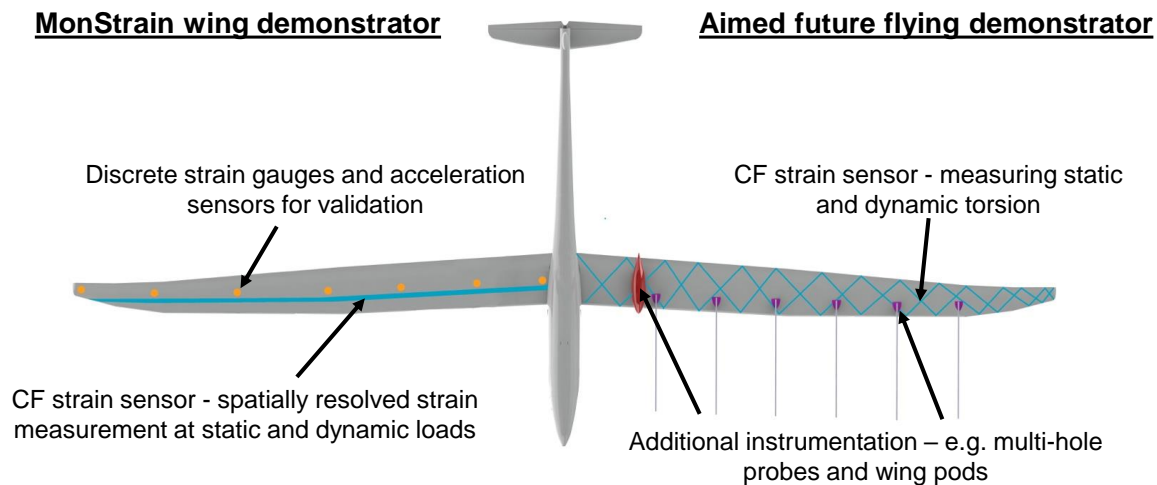


**Figure 7. Left wing: Intended instrumentation of the wing demonstrator for ground tests in the MonStrain project; Right wing: Possible additional instrumentation of the aimed future flying demonstrator**

### Acknowledgment

The authors would like to thank the German Ministry for Economic Affairs and Energy for funding the project MonStrain from 2021 to 2024 within the LuFo VI framework.

### References

- <sup>1</sup>Dahmann, P., 2011: Stemme S10 VTX als multifunktionales Forschungsflugzeug, Proceedings of “Deutscher Luft- und Raumfahrtkongress 2011“, DGLR, Bremen, Germany.
- <sup>2</sup>Viana, M. V. P., 2015: Sensor Calibration for Calculation of Loads on a Flexible Aircraft, Proceedings of “International Forum on Aeroelasticity and Structural Dynamics 2015”, St Petersburg, Russia.
- <sup>3</sup>Wang, X., Wang, S., Chung, D. D. L., 1999: Sensing damage in carbon fiber and its polymer-matrix and carbon-matrix composites by electrical resistance measurement, *Journal of Materials Science*, 34 (11), pp. 2703–13.
- <sup>4</sup>Mäder, T., Nestler, D., Wielage, B., 2011: Strain Sensing Using Single Carbon Fibres, Proceedings of “18th International Conference on Composite Materials, Jeju Island, South Korea.
- <sup>5</sup>Mäder, T., 2014: Neuartige Sensoren zur Erfassung von Dehnungen in Faserverbundwerkstoffen (Structural Health Monitoring), Dissertation, Chemnitz, Germany.
- <sup>6</sup>Owston, C. N., 1970: Electrical properties of single carbon fibres, *Journal of Physics D: Applied Physics* 3 (11), pp. 1615–26.
- <sup>7</sup>Blazewicz, S., Patalita, B., Touzain, P., 1997: Study of piezoresistance effect in carbon fibers, *Carbon* 35 (10-11), pp. 1613–18.
- <sup>8</sup>Abry, J. C., Choi, Y. K., Chateauminois, A., Dallozu, B., Giraud, G., Salvia, M., 2001: In-situ monitoring of damage in CFRP laminates by means of AC and DC measurements, *Composites Science and Technology* 61 (6), pp. 855–864.
- <sup>9</sup>Höhne, R., Ehrig, T., Kostka, P., Modler, N., 2016: Phenomenological investigation of a carbon fibre based strain sensor with spatial resolution by means of time domain reflectometry, *Materialwissenschaft und Werkstofftechnik* 47 (11), pp. 1024–1033.
- <sup>10</sup>Höhne, R., Kostka, P., Modler, N., 2017: Characterization of the spatial resolution capability of a novel carbon fiber strain sensor based on characteristic impedance measurements, Proceedings Sensor 2017, pp. 166–171.

